Forschungszentrum Karlsruhe
in der Helmholtz-Gemeinschaft
Wissenschaftliche Berichte
FZKA 7105

Description of Cherenkov Light Production in Extensive Air Showers

F. Nerling
Institut für Kernphysik

April 2005

Forschungszentrum Karlsruhe
in der Helmholtz-Gesellschaft

Wissenschaftliche Berichte
FZKA 7105

Description of Cherenkov Light Production in Extensive Air Showers

Frank Nerling
Institut für Kernphysik

Von der Fakultät für Physik der Universität Karlsruhe (TH)
genehmigte Dissertation

Forschungszentrum Karlsruhe GmbH, Karlsruhe
2005

Impressum der Print-Ausgabe:

Als Manuskript gedruckt

Forschungszentrum Karlsruhe GmbH
Postfach 3640, 76021 Karlsruhe

Mitglied der Hermann von Helmholtz-Gemeinschaft
Deutscher Forschungszentren (HGF)

ISSN 0947-8620

urn:nbn:de:0005-071050

Description of Cherenkov Light Production in Extensive Air Showers

The subject of this thesis is description of Cherenkov light production in extensive air showers for calculating analytically the Cherenkov light contribution in light profiles measured by air shower experiments using the fluorescence technique, in particular the Pierre Auger Observatory. The ansatz of the developed analytical Cherenkov model is based on parameterisations of the normalised electron energy spectra in shower age and the angular distribution of produced Cherenkov photons with respect to the shower axis. The former is shown to be universal for showers of energies larger than 10^{18} eV, and thus neither depend on primary energy nor on primary particle type, and depends only on the shower age. The latter is motivated by the underlying energy dependent electron angular distribution and takes into account the resultant dependence on shower age, and the height dependence implicated by the energy threshold of the Cherenkov effect depending on the refractive index changing in the atmosphere. Compared to Monte Carlo simulations, this ansatz predicts the Cherenkov light production in extensive air showers of very high energies universally at high accuracy of a few percent within shower-to-shower fluctuations. By this new model, a significant and systematic improvement of prediction is achieved compared to the previous approach. Applying this new analytical description for Auger data analysis results in significant and systematic (depending on viewing angle) differences in reconstructed primary parameters. For this study, the whole available fluorescence data set has been reconstructed and the impact due to the new model is studied on an event-by-event basis. Apart from an improvement of systematic uncertainties in event reconstruction, a larger reconstruction efficiency is expected when using the parameterisation of Cherenkov light production introduced in this work.

Beschreibung von Tscherenkovlicht-Produktion in ausgedehnten Luftschauern

Die vorliegende Arbeit beschäftigt sich mit der Beschreibung von Tscherenkovlicht-Produktion mit dem Ziel einer effizienten analytischen Berechnung des Tscherenkovlicht-Beitrags in longitudinalen Schauerprofilen, die mit Luftschauer-Experimenten, wie dem Pierre Auger Observatorium, basierend auf der Fluoreszenztechnik gemessen werden. Der Ansatz dieses neuen analytischen Tscherenkov-Modells basiert auf Parametrisierungen der normierten Elektronenenergiespektren und der Winkelverteilung der produzierten Tscherenkov-Photonen relativ zur Schauerachse. Es wird gezeigt, daß erstere für Energien oberhalb von 10^{18} eV universal ist, d.h. weder von der Primärenergie noch vom Primärteilchentyp, sondern lediglich vom Schaueralter abhängt. Die Parametrisierung der Photonwinkelverteilung ist motiviert durch die energieabhängige Winkelverteilung der zugrunde liegenden Elektronen und berücksichtigt die resultierende Schaueralter- und Höhenabhängigkeit, wobei letztere durch den mit der Höhe variablen Brechungsindex impliziert wird. Die Tscherenkovlicht-Produktion in ausgedehnten Luftschauern sehr hoher Energien wird mit diesem Ansatz universal und innerhalb der Schauer-zu-Schauer-Fluktuationen mit hoher Genauigkeit von wenigen Prozent im Vergleich zu den Monte Carlo-Simulationen vorhergesagt. Das entwickelte Modell stellt eine signifikante sowie systematische Verbesserung bisher existierender Ansätze dar. Die Verwendung dieser neuen analytischen Beschreibung für die Auger-Ereignis-Rekonstruktion resultiert in signifikanten und systematischen (abhängig vom Beobachtungswinkel) Unterschieden in rekonstruierten Primärparametern. Für diese Untersuchung ist der gesamte zur Verfügung stehende Auger-Fluoreszenz-Datensatz rekonstruiert worden und der Einfluß durch das neue Modell wird Ereignis für Ereignis untersucht. Unter Verwendung der in dieser Arbeit eingeführten Parametrisierung der Tscherenkovlicht-Produktion ist neben der Verbesserung der systematischen Unsicherheit in der Ereignis-Rekonstruktion auch eine größere Rekonstruktions-Effizienz zu erwarten.

Contents

Chapter 1

Introduction

The investigation of relativistic particles, by which the Earth's atmosphere is pounded continously, was initiated by Victor Hess' balloon borne measurements. Measuring the altitude dependence of the discharge rate of electroscopes he discovered the ionising radiation that is now called cosmic rays [Hess 1912]. Soon after this pioneering work cosmic ray research became the frontier in elementary particle physics. Examples are, among others, the discovery of the positron [Anderson 1933], which confirmed the theoretical prediction of anti-matter by Dirac in 1928, and the observation of pions postulated by Yukawa.

High-energy cosmic rays initiate showers of secondary particles in the atmosphere. This phenomenon of extensive air showers was first understood and studied in detail by Pierre Auger and collaborators [Auger 1938], even though Rossi had reported earlier the observation of *"very extensive groups of particles"* that arrived in coincidence [Rossi 1934]. Today the measurement of extensive air showers is subject of intensive research as it is the only way to investigate cosmic rays at the highest energies observed so far.

Almost one hundred years after Hess' discovery there are still many unsolved questions related to the sources and propagation of cosmic rays. To understand the nature and production mechanism of cosmic rays, current activities focus on the precise determination of their energy spectrum and mass composition as well as arrival direction distribution. The investigation of air showers with energies above 10^{20} eV is of particular interest as conventional cosmic ray acceleration models can reach this energy only in extreme astrophysical objects like gamma-ray bursts. On the other hand many models postulating extensions to the Standard Model of particle physics have been proposed to explain the observation of such showers. Although it is experimentally known that showers with energies exceeding 10^{20} eV exist, the data are limited by very low statistics and measurements of different experiments are not consistent. Furthermore, the highest energies observed in extensive air showers exceed 100 EeV, corresponding to more than 400 TeV in the centre of mass reference frame. At these ultrahigh energies, hadronic interactions initiating air showers are not well understood, leading to large systematic uncertainties in the interpretation of air shower data.

The Pierre Auger Project, pursued by more than 250 physicists from all over the world, aims at the detection of ultrahigh-energy air showers with unprecedented precision and statistics. As a large-acceptance hybrid detector, the Auger Observatory combines two complementary techniques: it measures the lateral distribution of charged particles at ground and the longitudinal shower profile in the atmosphere. While a large ground array of water Cherenkov tanks ensures large event rates due to its 100% duty cycle, the atmospheric fluorescence light detection will allow an almost model independent measurement of the shower energy of about 10% of all events. In addition to being a very important calibration tool, the fluorescence telescopes constitute an independent air shower detector providing high quality data for studies where longitudinal profile measurements are vital.

The fluorescence technique is based on observations of the fluorescence light, which is produced by charged particles ionising nitrogen molecules in the atmosphere. The excited nitrogen molecules subsequently return to the ground state in part by emitting light in the near ultraviolet wavelength range. However, charged particles of high energy also emit Cherenkov light [Cherenkov 1934] in this wave length interval. Whereas the fluorescence light is emitted isotropically, Cherenkov photons are produced mainly along the shower axis. Cherenkov photons contribute to the measured light signal but are, due to their angular distribution, not well suited for measuring the shower profile. Therefore, to reliably reconstruct shower profiles from Pierre Auger Observatory fluorescence detector data, one needs to calculate the expected Cherenkov light production in detail and take its contribution into account on a shower-by-shower basis.

This work is dedicated to the investigation of the Cherenkov light production in air showers, whereas the aim is an analytical description, by which the Cherenkov light contribution to the light signal measured by the Auger fluorescence detector can be determined precisely.

After a brief summary of the historical background and introduction to extensive air showers, the unsolved problems concerning ultrahigh-energy cosmic rays are discussed and finally the Pierre Auger Experiment is introduced in Chap. 1. A new analytical scheme for calculating the Cherenkov light produced in air showers has been developed and is presented in Chap. 2. The energy distribution of electrons in extensive air showers has been parameterised. One application is the calculation of total number of Cherenkov photons produced in extensive air showers; both is demonstrated in Chap. 3. Furthermore, a new parameterisation of the angular distribution of produced Cherenkov photons with respect to the shower axis has been derived, as discussed in Chap. 4. By the complete new Cherenkov model, which consists in the analytical scheme based on both of the analytical parameterisations and which has been tested with Monte Carlo simulations, the Cherenkov signal in optical observations based on the fluorescence technique, can be determined analytically. This model has further been applied to the currently available Auger fluorescence data set. In Chap. 5, the impact of the new Cherenkov calculation on the reconstruction of primary parameters is presented and discussed. A summary of the achieved results is presented in Chap. 6. There, also an outlook concerning what should still be investigated is given finally. For completeness, a compilation of further detailed information concerning the presented studies is given in appendix A and B respectively.

Chapter 2

Ultrahigh-energy Cosmic Rays and the Pierre Auger Observatory

After a brief overview of the present knowledge on cosmic rays, it is focused on the region of highest energy cosmic rays ever measured. Presently, measurements in this region of highest energies are of insufficient statistics and the underlying physics is not well understood. Following an overview of most important features regarding extensive air showers, the experimental setup of the Pierre Auger Observatory is described finally.

2.1 Ultrahigh-energy Cosmic Rays

There are numerous review articles on the theoretical and observational status and progress in the field of highest energy cosmic ray research, for instance [Sokolsky et al. 1992, Cronin 1999, Nagano & Watson 2000, Bhattacharjee & Sigl 2000, Boratav & Sigl 2004]. Giving a comprehensive overview of all experiments and their results as well as discussion of some implications the article of [Nagano & Watson 2000] might be one of the most complete reviews. A more recent overview on the experimental situation of ultrahigh-energy cosmic ray research with focus on the Pierre Auger Observatory can be found in [Blümer 2003], for an update of experimental results see [Engel & Klages 2004].

2.1.1 Historical Background

Cosmic rays are primarily nuclei with kinetic energies covering 12 orders of magnitude from a hundred MeV to several hundred EeV. The integrated flux decreases strongly with increasing energy and even spans more than 30 decades, such that numerous particles per $\mathrm{cm}^2 \cdot \mathrm{s}$ reach the Earth at low energies, but only one particle per km^2 and century at the highest energies ever observed. The most accepted mechanism from which the cosmic rays' energies might originate was introduced by Enrico Fermi in 1949, who proposed stochastic acceleration to boost charged particles to relativistic energies [Fermi 1949], even though only strong cosmic shock waves satisfy the required efficiency.

Direct measurements using balloon and satellite experiments have delivered detailed information on the mass composition of cosmic rays at low energy. About 86 % of the primaries

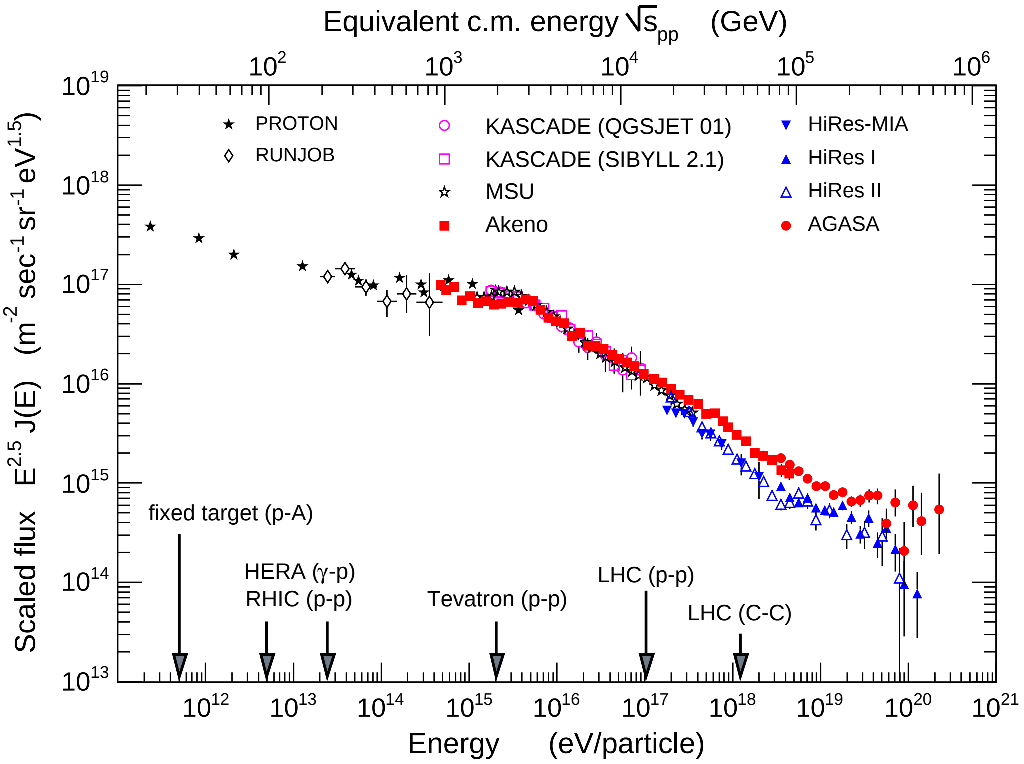

Figure 2.1: Scaled measured flux of cosmic rays - indirect measurements. The PROTON [Grigorov et al. 1971] and RUNJOB [Apanasenko et al. 2001] data are shown to indicate the flux at lower energy. The knee at a few PeV is clearly visible. The primary energies are given in the laboratory system and in the centre of mass reference system. For comparison, the maximum energies of man-made accelerator experiments are indicated. ([Engel 2004])

are protons, 11 % nucleons bound in helium nuclei, 1 % iron (and heavier nuclei up to uranium), and 2 % electrons. Particles of energies in the MeV-range are mostly of solar origin, only above 1 GeV one speaks of cosmic rays. Due to the limited detection area of space-borne instruments, above 10^{14} eV indirect measurements are required. Indirect methods are based on the measurement of the secondary particles that are produced in extensive air showers initiated by primary particles when entering the atmosphere. These secondary particle cascades can be measured by scintillator counters and water Cherenkov detectors as well as by optical air fluorescence and Cherenkov radiation observations.

The intensity of cosmic rays of energies up to several GeV is solar modulated, whereas for higher energies the all-particle distribution follows a non-thermal power-law spectrum

$$\mathrm{d}N/\mathrm{d}E \;\approx\; 1.8\, E^{-\alpha} \; \frac{\mathrm{nucleon}}{\mathrm{cm}^2\,\mathrm{s\,sr}\;\;\mathrm{GeV}/A}\;, \tag{2.1}$$

where E is the total energy per nucleon, $\alpha = (\gamma + 1) = 2.75$ is the differential spectral index of the cosmic ray flux, and γ is the integral spectral index. Theoretically the model proposed by Fermi implies a differential index of $\alpha \approx 2$, whereas the measured one turns out to amount $\alpha \approx 2.8$; this change is often explained to be the cause of propagation through the galaxy.

The differential flux of cosmic rays observed on Earth is displayed in Fig. 2.1; as generally done, it is scaled by a power of the energy, so that possible structures become identifiable. Up to 1 PeV $\alpha \approx 2.75$, from 1 PeV to 100 PeV the measured spectrum steepens to $\alpha \approx 3.05$. This feature of change in slope is referred to as the *knee*.

Within propagation models the *knee* would mainly be caused by the escape of some particles at the galaxy's border, the more as their energy is larger. Accordingly, by some authors the so-called *ankle* at a few 10^{19} eV is interpreted to be the consequence of a cross-over from a galactic to an extra-galactic component, see e.g. [Hillas 1984]. As an additional implication of such models, a heavier composition would be favoured in the region beyond the *knee*, which is confirmed by some experimental data [Ulrich 2003, Kampert et al. 2004], like e.g. the KASCADE[1] experiment [Antoni et al. 2003]. Such an interpretation would also be supported by a proposed re-acceleration process during the particle's propagation through the interstellar medium due to the interaction with supernovae remnants which, as a second order Fermi mechanism is less effective, might accelerate particles up to roughly 1 EeV, the *second knee*. But, an observed heavier composition could also be the result of superposed different spectra as a consequence of different supernovae types.

Apart from such *bottom-up* scenarios also numerous so-called *top-down* models are considered particularly for higher energies. They mainly explain the origin of the highest observed energies based on ideas invoking decays of super massive relic particles or topological defects.

Indeed, Greisen, Zatsepin and Kuz'min predicted a sharp cut-off concerning the cosmic ray flux above about 5×10^{19} eV, implicated by interaction of primary particles with the cosmic microwave background, known as GZK-effect [Greisen 1964, Zatsepin & Kuz'min 1966]. Above the given cut-off energy protons disintegrate mainly via photo-production of pions on account of a Δ-resonance connected with subsequent decay:

$$\begin{aligned} p + \gamma_{3K} \rightarrow \Delta^{+}(1232) \quad &\rightarrow \quad n + \pi^{+} && (33\,\%) \\ &\rightarrow \quad p + \pi^{0} && (66\,\%) \qquad \text{(GZK-effect)} \end{aligned} \tag{2.2}$$

The numbers in parenthesis denote the approximate branching ratios. Another important process of energy loss is Bethe-Heitler pair-production:

$$p + \gamma_{3K} \quad \rightarrow \quad p + e^{+} + e^{-} \qquad \text{(Bethe-Heitler)} \tag{2.3}$$

Heavy nuclei of mass A primarily undergo successive disintegration by scattering on the 2.7 K background radiation and the infrared photons with subsequent pair-production:

$$\begin{aligned} A + \gamma_{3K} \quad &\rightarrow \quad (A-1) + N \\ &\rightarrow \quad (A-2) + 2N \\ &\rightarrow \quad A + e^{+} + e^{-} \quad , \end{aligned} \tag{2.4}$$

---

[1] Karlsruher Shower Core and Array Detector

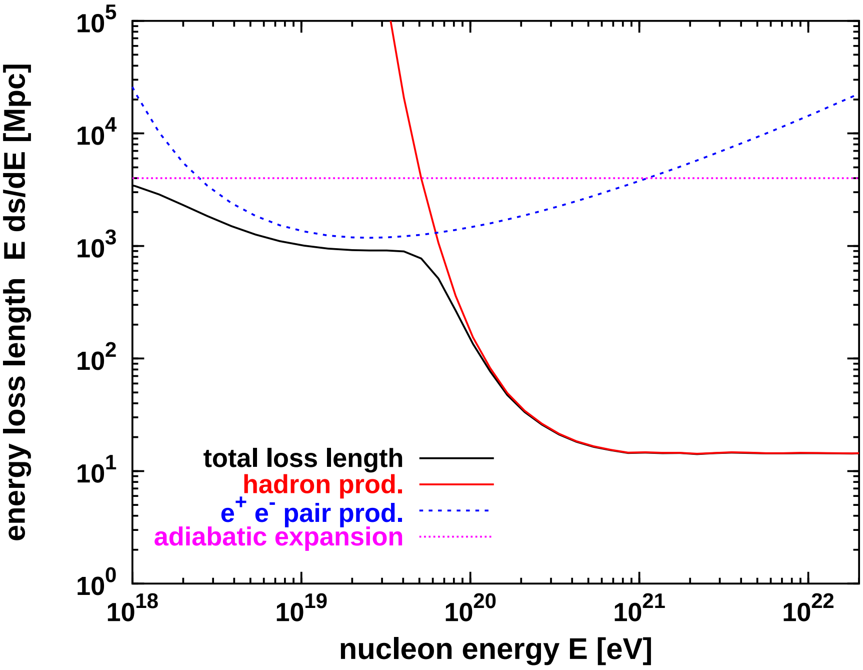

Figure 2.2: Proton energy loss due to the GZK-effect and Bethe-Heitler pair-production, similar for heavier nuclei. ([Stanev et al. 2000])

where N represents a nucleon. The resultant energy loss lengths for both of these predicted processes are illustrated in Fig. 2.2. Provided their sources are at distances larger than roughly 50 Mpc, primary protons of energies larger than 10^{20} eV can hardly reach the Earth. Calculations for heavier nuclei deliver similar limits.

The energy E_{max} attainable by the traditional acceleration mechanism is estimated dependent on the shock velocity b_{s}, charge z of the particle, magnetic field strength B, and the size of the acceleration region L ($\sim$ Larmor radius):

$$E_{\text{max}} = b_{\text{s}}\, z\, B\, L \; . \tag{2.5}$$

In Fig. 2.3 it is shown that accelerating particles to 10^{20} eV is hardly achievable within potential astrophysical sources, the more so possible energy losses by synchrotron radiation are not taken into account. For instance, active galactic nuclei in the Virgo cluster, which is located at $\sim$ 20 Mpc, would be good candidates. Before arriving at the Earth, particles of such extragalactic sources would propagate through the intergalactic and galactic space, meanwhile interactions would cause deflection and energy loss. Charged particles of more than about 10^{19} eV are not deflected significantly neither by extragalactic nor galactic magnetic fields, as long as cosmologically short distances are considered (< 50 Mpc). Consequently, ultrahigh-energy cosmic rays are expected to be distributed anisotropically, the extension of

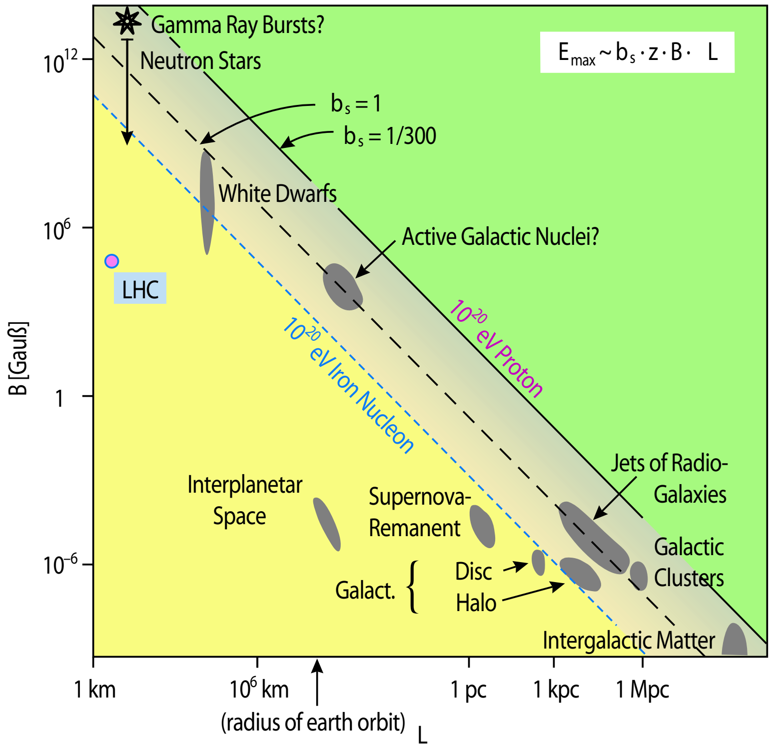

Figure 2.3: Hillas diagram: Size and magnetic field strength for various possible acceleration sites. Objects below the straight lines (Iron of $b_s = 1$ or proton of $b_s = 1$ and $b_s = 1/300$) are not able to accelerate the corresponding particle to 10^{20} eV. (modified version from [Hillas 1984])

the magnetic field in the galactic halo presumed to be smaller than a few kpc [Cronin 1992].

In conclusion, if sources of ultrahigh-energy cosmic rays are uniformly distributed and super-GZK events exist, a window for new physics beyond the standard model opens. For this purpose rather exotic scenarios than traditional *bottom-up* models must be consulted to clarify the puzzle of ultrahigh-energy cosmic rays. Aforementioned *top-down* models predict mainly proton and gamma-ray dominated fluxes and therefore would be excluded if heavier nuclei are dominant. However, separately also shifts of the predicted GZK cut-off due to e.g. violation of Lorentz invariance or dissipating energy through graviton production are discussed. The former can also be the case if there is no cut-off at all and no remarkable fraction of photon primaries.

2.1.2 Extensive Air Showers

In analogy to a fixed-target experiment, one can consider the atmosphere acting as a (inhomogeneous) calorimeter and the incoming cosmic rays as the beam particles. Due to the low density of air, at large altitudes the height of first interaction fluctuates strongly. In the case of heavier nuclei, not all nucleons interact, most of them act as spectators. As indicated in

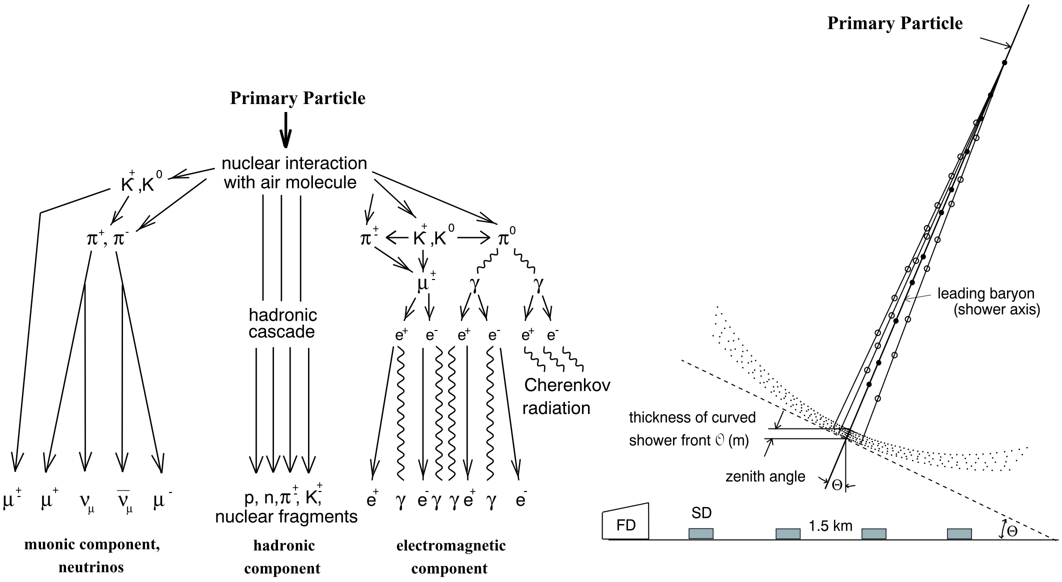

Figure 2.4: Left panel: Extensive air shower development - Scheme of secondary particles production. Right Panel: Sketch of shower front consisting of secondary particles moving towards an air shower experiment.

Fig. 2.4, the most commonly produced particles in the first interaction are pions and kaons of all kinds; however, also etas, strange baryons and resonances are produced.

Subsequently, three shower components can be distinguished, a hadronic cascade, the muonic, and the electromagnetic component. The *hadronic component* is mostly produced by the decay of either strange baryons or resonances, and form the so-called shower core, comprising again mesons and resonances, but also secondary protons and neutrons are produced. Due to their relatively long lifetimes (26 ns), charged pions partly interact with air nuclei or, depending on their energy, decay to muons and neutrinos: $\pi^{\pm} \rightarrow \mu^{\pm} + \nu_{\mu}/\bar{\nu}_{\mu}$.

In this manner the *muonic component* is accumulated. Indeed the daughter muons are also unstable ($\mu^{+} \rightarrow \mathrm{e}^{+} + \nu_{\mathrm{e}} + \bar{\nu}_{\mu}$, $\tau = 2.2\,\mu$s), but implicated by their experienced time dilatation, they mostly reach the ground, unless their energy is smaller than a few GeV; therefore the muonic is also called the hard component of cosmic radiation.

The main decay channel of the neutral pions ($\tau = 8 \times 10^{-8}$ ns) is $\pi^0 \rightarrow 2\gamma$ (98.8 %). The hadronically produced photons undergo e^+e^- pair-production and induce electromagnetic sub-showers, wherefore they are the dominant source of the *electromagnetic component.* In contrast to a purely electromagnetic shower, this contribution is 're-feeded' by the hadronic cascade products, during shower development. Since the electrons[2] and photons of such cascades are easily absorbed, this part is often called soft component.

Hadron induced showers generally penetrate deeper than purely electromagnetic showers and show a larger lateral spread mainly determined by the transverse momentum of hadronic secondaries, typically 0.3 GeV/c.

---

[2] Throughout this work, the notation 'electrons' include e^+ and e^-.

The longitudinal development of extensive air showers is determined by particle production and energy losses. Therefore the matter traversed is the main physical quantity, which in the case of vertical particle trajectories, is given by the vertical atmospheric depth

$$X_{\mathrm{v}}(h) = \int_h^\infty \rho(h)\,\mathrm{d}h \;, \tag{2.6}$$

where ρ is the density of air at height h.

The most numerous component in extensive air showers is the electromagnetic contribution. While traversing the atmosphere, charged particles suffer ionisation energy loss $(\mathrm{d}E/\mathrm{d}X)_{\mathrm{ion}}$, which is described by the Bethe-Bloch formula, see e.g. [Perkins 2003]. Additionally, high-energy electrons undergo radiation loss $(\mathrm{d}E/\mathrm{dX})_{\mathrm{rad}} = -E/X_0$ due to bremsstrahlung, where $X_0 = 37\,\mathrm{g/cm}^2$ [Eidelman et al. 2004] is the radiation length in air. For high energies the former is increases slowly with energy ($\sim \ln E$), whereas the latter is proportional to the particle's energy. The *critical energy* E_{c} is defined as that energy, at which $(\mathrm{d}E/\mathrm{dX})_{\mathrm{ion}} = (\mathrm{d}E/\mathrm{dX})_{\mathrm{rad}}$, in air it amounts about $80\,\mathrm{g/cm}^2$. While electrons above E_{c} lose energy practically throughout radiation processes, below it is mostly due to ionisation. When the mean energy per particle reaches the critical energy, below which energy loss dominates over pair-production, the number of particles decreases and the shower 'dies out'.

From cascade theory Approximation B[3] [Rossi & Greisen 1941] and application of the *superposition principle*[4] it follows for the depth of shower maximum $X_{\max}$ and the number of particles at shower maximum $N_{\max}$

$$X_{\max} \propto \ln E_{\mathrm{p}} \tag{2.7}$$

$$N_{\max} \propto E_{\mathrm{p}} \;, \quad \text{with } E_{\mathrm{p}} \text{ primary energy.} \tag{2.8}$$

For a photon induced shower the longitudinal development can be described by [Greisen 1956]

$$N_{\mathrm{e}}\,(E_{\mathrm{p}}, t) = 0.31 \left(\ln \frac{E_{\mathrm{p}}}{E_{\mathrm{c}}} \right)^{-1/2} \cdot\, e^{t\,(1-1.5 \ln s)} \;, \tag{2.9}$$

where $t = X/X_0$ and $s = 3t/(t + 2\ln(E_{\mathrm{p}} E_{\mathrm{c}}^{-1}))$. The *shower age* s equals zero when the shower is starting, unity at maximum. For $t \to \infty$ it becomes 3 and $N_{\mathrm{e}} < 1$, the shower has 'died out'. The lateral spread of a purely electromagnetic shower can been calculated [Kamata & Nishimura 1957], and the result is typically approximated by a parameterisation called the *NKG*-function [Greisen 1966]

$$\rho_{\mathrm{e}} = C(s) \cdot \frac{N_{\mathrm{e}}}{2\pi r^2} \left(\frac{r}{r_{\mathrm{m}}} \right)^{s-2} \left(1 + \frac{r}{r_{\mathrm{m}}} \right)^{s-4.5} \;, \text{ with} \tag{2.10}$$

$$C(s) = \frac{\Gamma(4.5 - s)}{\Gamma(s)\Gamma(4.5 - s)} \quad \text{(Normalisation)} \;,$$

---

[3] Approximation A is an analytical treatment of transport equations in the limit of very high electron energies, describing a purely electromagnetic (sub-) shower. In Approximation B the ionisation loss is assumed to be constant.

[4] Following the superposition principle, a shower induced by a nucleus of energy E_{p} consisting of A nucleons can in a good approximation assumed to be a superposition of A proton induced showers of E_{p}/A each, see e.g. [Gaisser 1990].

where $\rho_e(r)$ stands for the electron density at distance r from the shower centre, N_e is the total electron number at the given depth level and r_m is the Moliére radius following from theory of multiple scattering. Although the validity of the superposition principle is limited, practical applications show that hadronic showers also can be described reasonably well using (2.9) and (2.11), but the parameters s as well as r_m then lose their original meaning.

An approximative parameterisation, taking into account shower-to-shower fluctuations of the longitudinal development of the number of charged particles in any extensive air showershas been found in the form of the *Gaisser-Hillas*-function [Gaisser & Hillas 1977]

$$N(X) = N_{\max} \left(\frac{X - X_0}{X_{\max} - X_0}\right)^{(X_{\max}-X_0)/\lambda} \cdot e^{(X_{\max}-X)/\lambda} , \qquad (2.11)$$

with X_0 the point of first interaction and $\lambda \approx 70\,\mathrm{g/cm^2}$, motivated by the hadronic mean free path in air[5]. Integrating all charged particles along the shower development delivers a measure of the calorimetric energy [Dozkhenko & Pomanskii 1964]:

$$E_{\mathrm{cal}} = \frac{E_c}{X_0} \int N(X)\,\mathrm{d}X . \qquad (2.12)$$

Particularly for showers initiated by higher energetic nuclei, practically all energy and particles (excepting muons and neutrinos) is finally transferred to the electromagnetic part, and therefore Eq. (2.11) and Eq. (2.12) have universal validity within aforementioned shower-to-shower fluctuations.

2.1.3 Unsolved Problems

In addition to many unsolved problems in understanding of cosmic rays, in particular their sources, acceleration, and propagation, even their flux and composition in and above the ankle region is quite uncertain. In the following the focus is put on measured fluxes, the question of anisotropy, and measured composition information; related discrepancies are briefly discussed.

The observation of a cosmic ray air shower of estimated energy exceeding 10^{20} eV was published for the first time by the historic experiment at Volcano Ranch [Linsley 1962]. At present solely 17 (status mid of 2004) of such ultrahigh-energy cosmic rays, well above the GZK cut-off, have been measured mainly by two experiments, the ground scintillator array AGASA[6] [Chiba et al. 1992] and the HiRes[7] Fly's Eye experiment [Abu-Zayyad et al. 2000, Sokolsky 2002] using the fluorescence technique.

Fig. 2.5 shows a compilation of cosmic ray flux data in the *ankle* region. Mostly the error bars only give the statistic errors. In the following discussions it is mainly restricted to the AGASA and HiRes experiments, which feature the largest integrated aperture and thus provide the best statistics.

---

[5] Indeed the nuclear interaction length in air amounts $\lambda_{\mathrm{air}} = 90\,\mathrm{g/cm^2}$ (STP) [Eidelman et al. 2004].

[6] Akeno Giant Air Shower Array

[7] High Resolution Fly's Eye, successor to Fly's Eye

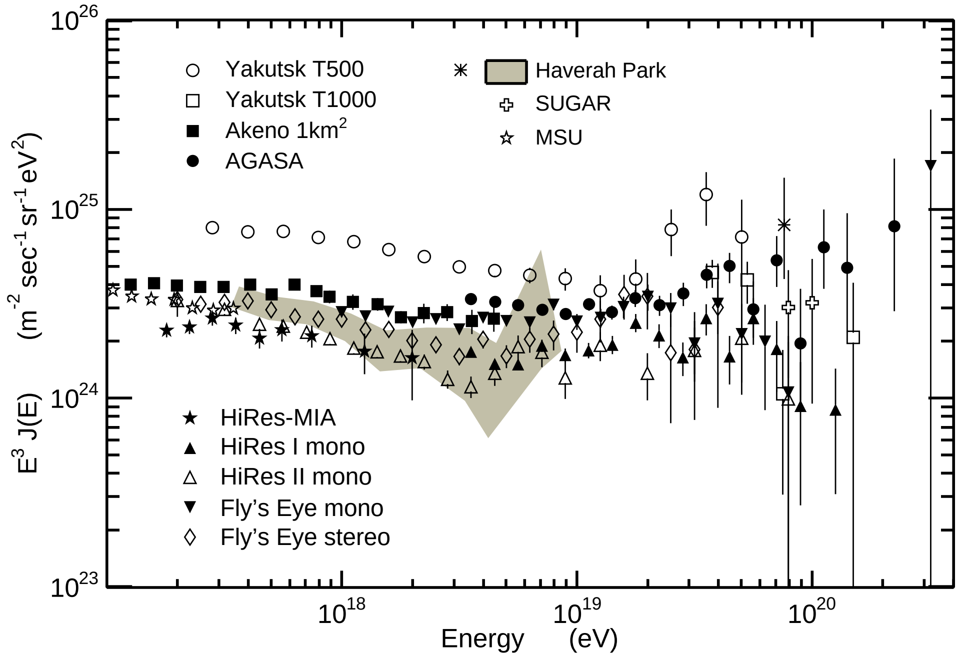

Figure 2.5: Data compilation of cosmic ray flux measurements at very high energy. ([Engel & Klages 2004]) The MSU array data are included to illustrate the connection between high-energy measurements and lower energy data covering the *knee* region. The shaded area represents the (reanalysed) Haverah Park data assuming extreme compositions, fully iron or proton dominated. For references to the different experiments see [Engel & Klages 2004].

For both experiments the measured fluxes are displayed in Fig. 2.6. Their results seem not to be in agreement for the whole energy range. Apart from a relative shift in energy, differences regarding the energy dependence of the flux indicated by the data points occur clearly above 5×10^{19} eV. Before speaking of discrepancy, one should discuss systematic uncertainties.

On the basis of completely different underlying experimental techniques, both of them have different systematics in energy reconstruction to fight with. The surface array AGASA is faced with the systematic uncertainty in energy assignment, which they published to amount $\pm$ 18 % [Takeda et al. 2003a]. This large uncertainty is mainly due to shower phenomenology and the simulation of the observable[8], from which the energy is derived by comparison to Monte Carlo simulations. In the case of the fluorescence technique, as it is used by HiRes, it is the uncertainty in the energy dependent effective aperture. Here, they give as total systematic error for the flux 21 % [Abu-Zayyad et al. 2002] and for the energy reconstruction $\pm$ 17 % [Abu-Zayyad et al. 2002].

Within the uncertainties published by the collaborations, both experiments are in agreement in the energy range up to $10^{19.5}$ eV. But, above 10^{20} eV the different measured fluxes are still incompatible at the level of $\sim 2\sigma$ [Teshima 2003].

---

[8] In ground arrays the energy can be determined by the measured particle (muon and electron) density at a given distance from the shower axis, whereas the best distance for doing so depends on the spacing of detectors [Hillas 2003].

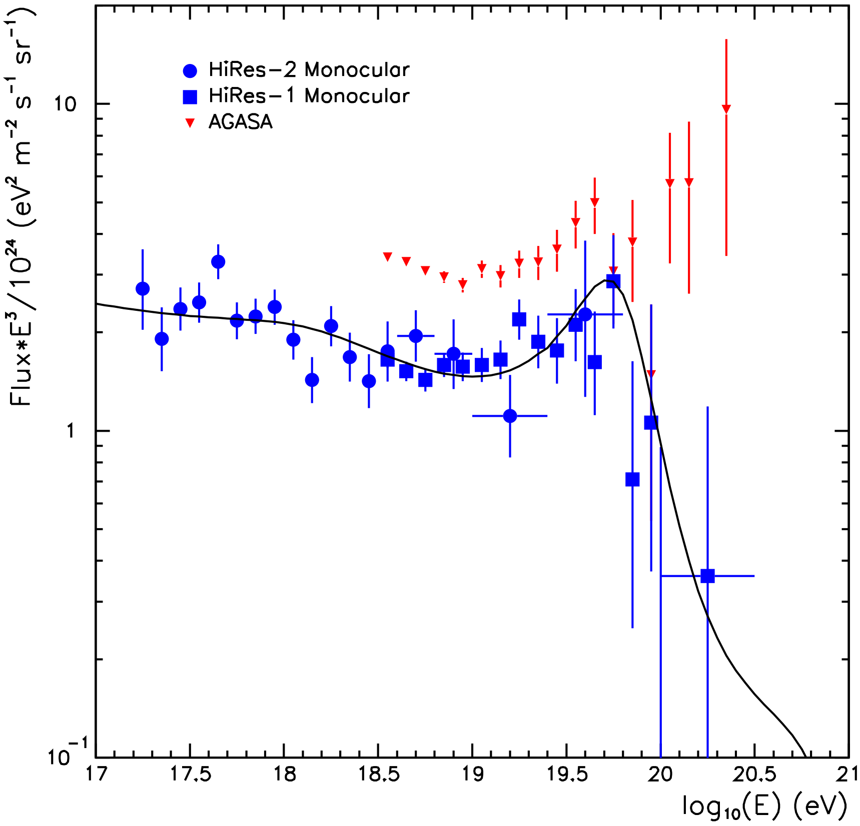

Figure 2.6: Comparison of fluxes measured by HiRes [Bergmann et al. 2003a, Bergmann et al. 2003b] and AGASA [Takeda et al. 1998, Takeda et al. 2003b] with a GZK cut-off prediction, assuming a proton dominated extragalactic cosmic ray flux of uniformly distributed sources. ([Thomson 2004])

The HiRes result is significantly consistent with the predicted GZK cut-off for a proton dominated flux and uniformly distributed sources. In contradiction, the AGASA data do not show any sign of a cut-off.

Presently, there is no evidence for large scale anisotropy, only from the AGASA data a statistically limited[9] excess of incoming showers from direction near to the Galactic Centre has been found analysing their data set above 10^{17} eV [Hayashida et al. 1999]. Anyhow, below energies of $10^{17.5}$ eV as well as above $10^{18.7}$ eV no significant anisotropy exists [Hayashida et al. 1999], which in particular for the higher energies is in agreement with analyses based on the HiRes data set. The HiRes data also do not indicate any clustering on small scales (less than 4 doublets at 90 % confidence level [Belz et al. 2003]), whereas the AGASA data significantly show small angle correlations. The arrival direction distribution of showers with energies above 10^{19} eV as observed by AGASA is shown in Fig. 2.7. The overall isotropy is clearly seen, nevertheless 5 doublets and 1 triplet are found within an angular separation of ∼ 2.5° [Teshima 2003].

---

[9] Presuming a region near the Galactic Centre the access would be significant of $\sim 4\sigma$, but such region is at the angular acceptance limit, and the Galactic Centre is not within the field of view.

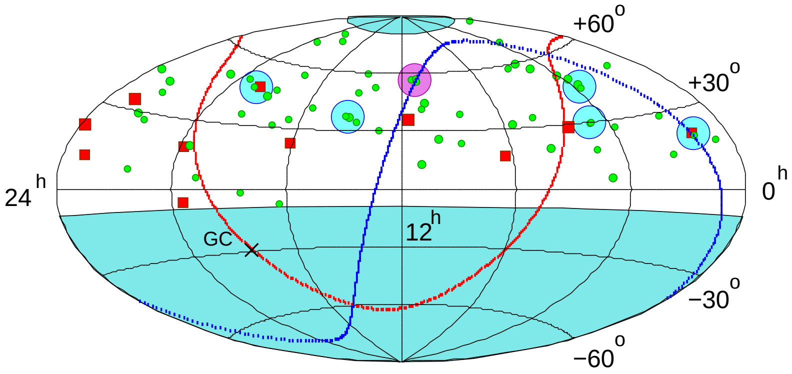

Figure 2.7: Arrival directions of cosmic rays with energies above 4×10^{19} eV. The small squares and cycles represent events with energies above 10^{20} eV and $(4 \text{ to } 10) \times 10^{19}$ eV respectively. The large light circles indicate doublets and the single dark circle a triplet [Takeda et al. 1999]. (modified from [Takeda et al. 1999], available at [AGASA Collaboration 2004])

Information on the mass composition of ultrahigh-energy cosmic rays is, in the case of scintillator arrays, usually derived by comparing muon to electron densities. An alternative approach is the measurement of the depth of maximum X_{max} of the longitudinal shower profile, which can be observed directly with the fluorescence technique or analysing the slope of the lateral distribution of the Cherenkov light. The change from an iron-dominated to proton-dominated composition at about 10 EeV was found by the pioneer experiment based on fluorescence observations, namely Fly's Eye [Bird et al. 1993].

In Fig. 2.8 only the measured X_{max} distribution as measure of composition is shown. For the other composition data, based on particle densities, see [Watson 2004]. As can be seen, above the *knee* the composition seems to become heavier with increasing energy. The measurements show the trend to a lighter composition above the *ankle*. In the case of comparison with air shower simulations applying QGSJET 01 [Kalmykov et al. 1997] as high-energy hadronic interaction model, a proton domination is favoured.

In the range of 10^{18} to 10^{19} eV significant deviation between different data sets and analyses are recognised, which also might be caused by the lack of knowledge of ultrahigh-energy interactions and the subsequent problem of simulating air showers correctly. Further, there seems not to be any indication of considerable fraction of gamma-ray induced showers, but due to low statistics exclusion is limited [Risse et al. 2004], in particular when the pre-shower effect[10] is taken into account [Homola et al. 2003].

However, particularly proton showers fluctuate considerably stronger than iron. That the interpretation of different data sets at ultrahigh energies are model dependent can be seen in comparison with Fig. 2.9. The simulated shower-to-shower fluctuation using QGSJET 01 and SYBILL 2.1 [Engel 1999] respectively are illustrated for proton and iron showers.

In summary, the existence of events with energies exceeding 10^{20} eV is certain. Within the present statistics arrival directions are isotropically distributed. This combination suggests

---

[10] A particle cascade initiated by $\gamma \to e^+e^-$ conversion and subsequent synchrotron radiation (bremsstrahlung) of electrons in the presence of the geomagnetic field above the Earth's atmosphere [Erber 1966].

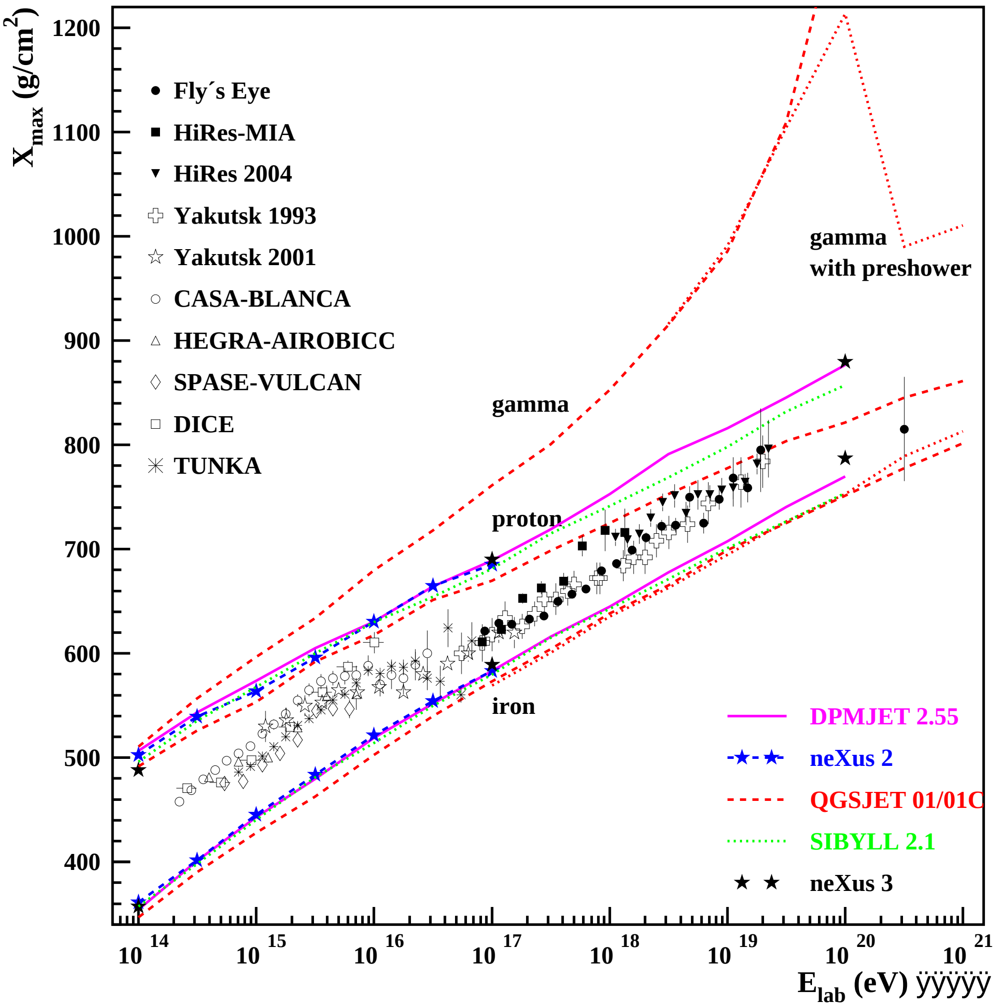

Figure 2.8: Measured distribution of shower maximum of high-energy air showers. The different model predictions are calculated with CORSIKA [Heck et al. 1998]. For the data shown see [Abbasi et. al. 2004] (HiRes 2004), [Boothby 1997] (DICE), and [Prosin 2003] (TUNKA) and references in [Knapp & Heck 2003] respectively, there, also the references of the different interaction models can be found. ([Heck 2004])

new physics as explanation of these observations. Due to the low statistics, *top-down* models cannot yet been excluded by gamma-ray flux limits. Interpretations of present data are strongly model dependent, so that already at the cross-over from the highest to lower energies air shower simulations are not in agreement with the data, and thus still not totally reliable.

In conclusion, to clarify the mysteries of ultrahigh-energy cosmic rays, larger statistics and reliable energy and composition measurements are needed, which also requires new measurement techniques. In parallel, the understanding of extensive air showers, especially modelling hadronic interactions over the whole energy range and for the very forward direction (low transverse momenta), must be improved for correct interpretation of cosmic ray data.

These are the motivations for upcoming experiments, namely the Telescope Array (TA) [Fukushima et al. 2000], the Pierre Auger Observatory [Abraham et al. 2004] and the planned

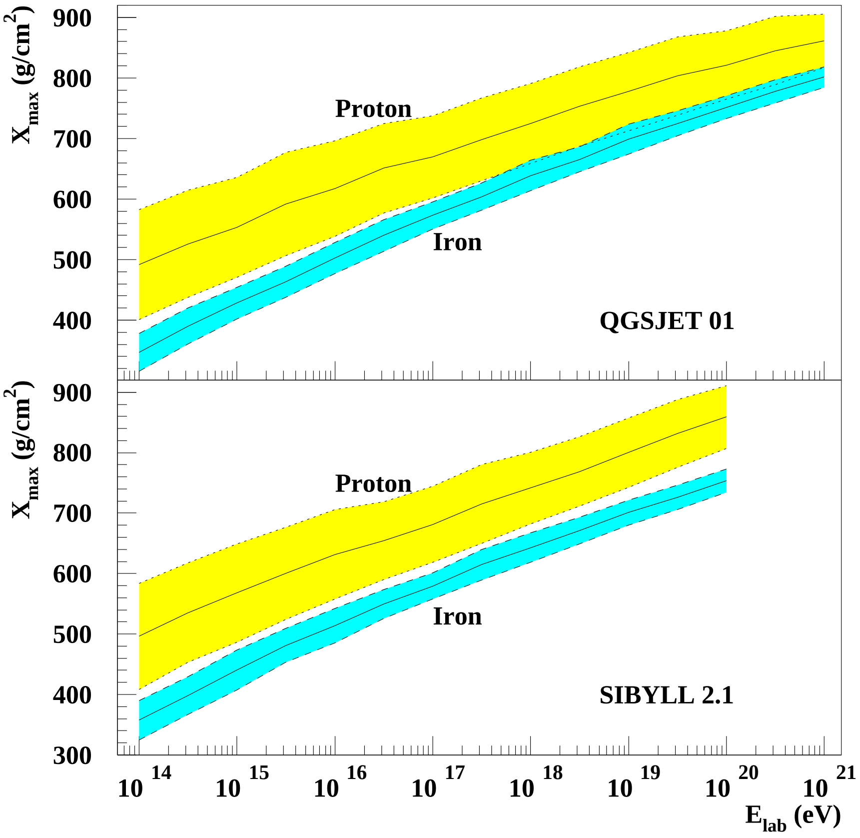

Figure 2.9: Simulated shower-to-shower fluctuations for two different high-energy hadronic interaction models, QGSJET 01 [Kalmykov et al. 1997] and SYBILL 2.1 [Engel 1999], shown for two different primaries, iron and proton. ([Heck 2004])

space-borne Extreme Universe Space Observatory (EUSO) [Pallavicini et al. 2003]. The Pierre Auger Observatory is a hybrid detector, involving both, a huge surface detector array and fluorescence telescopes. Thus, aforementioned systematic uncertainties connected with each method can be cross-checked and reduced remarkably, so that subsequent results may be analysed nearly independent of high-energy interaction models needed for air shower simulations.

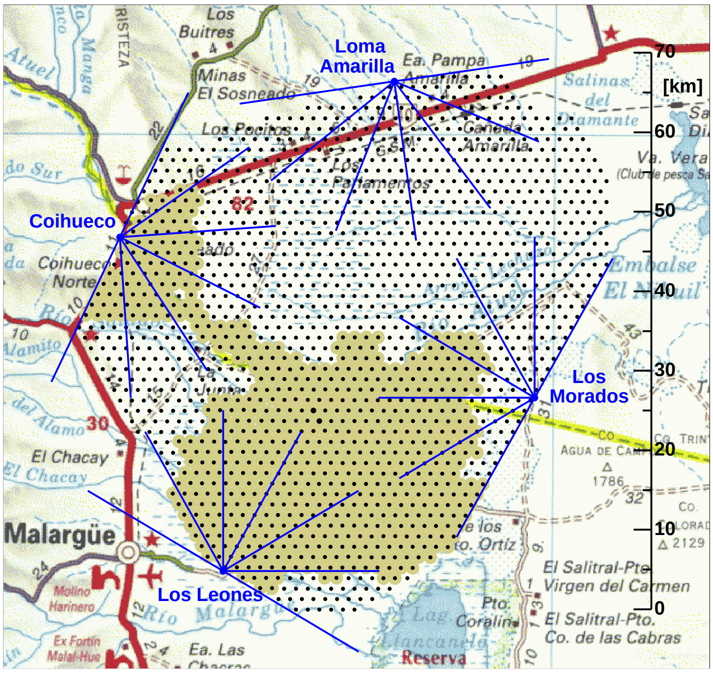

Figure 2.10: Pierre Auger Observatory - Southern Site. The Southern Auger experiment is currently under construction. The black spots indicate 1600 water Cherenkov tanks and in blue 4 fluorescence detector buildings comprising 6 telescopes each are marked. The shaded area demonstrates the status of installed water tanks; apart from 'Loma Amarilla', all fluorescence detector buildings are erected, whereas presently only 'Coihueco' and 'Los Leones' are fully equipped and included in the data acquisition (Status end 2004). ([Oehlschläger 2004])

2.2 The Pierre Auger Observatory

The Pierre Auger Observatory has been conceived to measure the flux, arrival direction distribution and mass composition of cosmic rays above 10^{19} eV up to the highest energies with high statistical significance covering the whole sky. In this manner, it will answer unsolved problems related to the ultrahigh-energy cosmic rays. Presently, the Southern Hemisphere site of the planned pair of experiments is currently under construction and taking data. In the following the discussion is restricted itself to the Southern Pierre Auger experiment.

As a so-called hybrid detector the Pierre Auger experiment merges a large ground array with the fluorescence technique. In doing so complementary strengths are combined, and data analysis benefits from the calorimetry of fluorescence measurement and from the uniformity of the surface detector aperture. The array will consist of 1600 water Cherenkov tanks on a hexagonal grid with 1.5 km spacing, and in total 24 imaging fluorescence telescopes in 4 fluorescence detector buildings observing the atmosphere above the whole surface detector area of $3000\,\mathrm{km}^2$, see Fig. 2.10. The site is located in the Pampa Amarilla near the town Malargüe in the Province of Mendoza in Argentina. The current status of construction is illustrated in Fig. 2.10. Further detailed information can be found in [Auger-DR 1997].

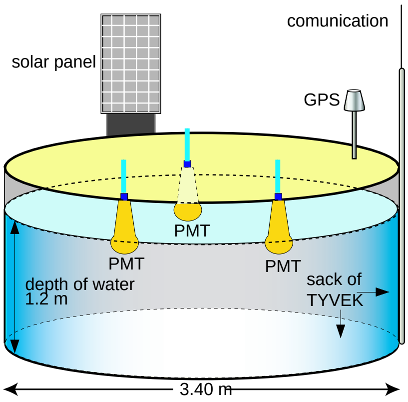

Figure 2.11: Schematic illustration of a single water Cherenkov tank. Electric power is provided by a solar panel and a accumulator battery, communication with the central data acquisition is ensured by microwave radio link.

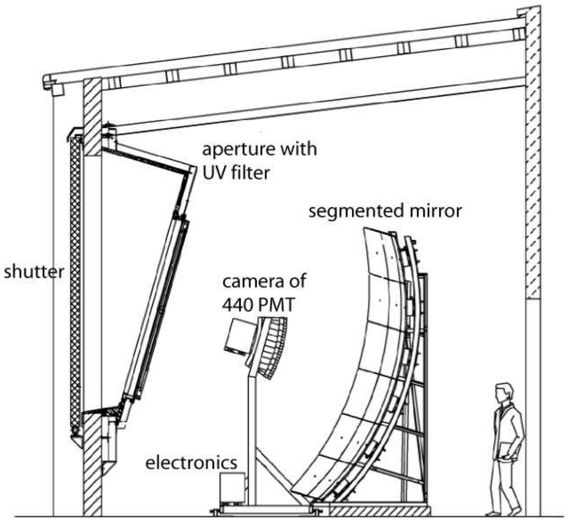

Figure 2.12: Schematic cross-sectional view of a fluorescence telescope showing the aperture and shutter system, PMT camera and spherical mirror.

2.2.1 Surface Detector

Due to the need of long operation time (~ 20 years), water Cherenkov tanks have been chosen due to their robustness and last but not least because of the low costs. In the 12 m^3 volume of ultrapure water, the charged shower particles produce Cherenkov light pulses, which are measured by three 8 inch photomultiplier tubes (PMT). From the time structure of measured PMT pulses, mass sensitive shower parameters can be deduced. For the energy reconstruction based on lateral distributions, the crucial information are integrated PMT signals of triggered tanks (synchronised using GPS), which delivers a measure of the total energy deposit. The trigger conditions are tuned in a way, that starting from a threshold at about 10^{18} eV full efficiency is achieved above 10^{19} eV.

2.2.2 Fluorescence Detector

Each fluorescence telescope has a field of view of $30^\circ \times 28,6^\circ$, thus each peripheral detector building, called 'eye', gives a 180° field of view inwards over the array, as demonstrated by Fig. 2.10. The telescopes are Schmidt optical systems composed of a circular diaphragm defining the aperture of 2.2 m in diameter, UV transmitting filter (~ 300-400 nm) and Schmidt corrector lens, see Fig. 2.12. The camera consist of 20 times 22 PMT having a field of view of 1.5° each, onto which light is focused by the 11 m^2 large spherical mirror. The fluorescence detector is a self-sustaining air shower detector allowing for reconstruction of the longitudinal shower development, and simultaneously, it is very useful for the calibration of the surface detector. Although the fluorescence technique requires many studies of the atmosphere as calorimeter, the energy measurement is much more direct and consequently to a greater extent model independent.

2.2.3 Expected Performance

The expected performance is presented based on the Technical Design Study [Auger-TDR 2002], further work and experiences from the prototype phase. While the surface detector has a duty cycle of 100 %, the calculation of the duty cycle and effective aperture of the fluorescence detector is rather complicated, since weather conditions are always changing. In principle the fluorescence detector can be operated 18 % of the time, however during the run time of the engineering array 10 % were achieved [Abraham et al. 2004].

The aperture of the Pierre Auger experiment calculates to about 7400 km^2 sr for incoming events under zenith angles smaller than 60°. Accepting angles larger than 60° increases the acceptance by 50 % [Cester 2001]. The surface detector reaches full efficiency for primary energies larger than 10^{19} eV. As a result of the arrangement of the experiment, the fluorescence detector is expected to trigger on every event, larger than 10^{19} eV hitting the array, at least by one 'eye' when in full operation. In Fig. 2.13(a) the hybrid (fluorescence plus surface) triggering efficiency in dependence of primary energy is displayed. The calculation has been done for showers of inclination angles smaller than 60° hitting at random positions within the ground array boundary. For this calculation at least one 'eye' and 2 tanks triggered are required [Dawson & Sommers 2001]. Based on the given duty cycle and efficiency, the expected hybrid event rate is derived.

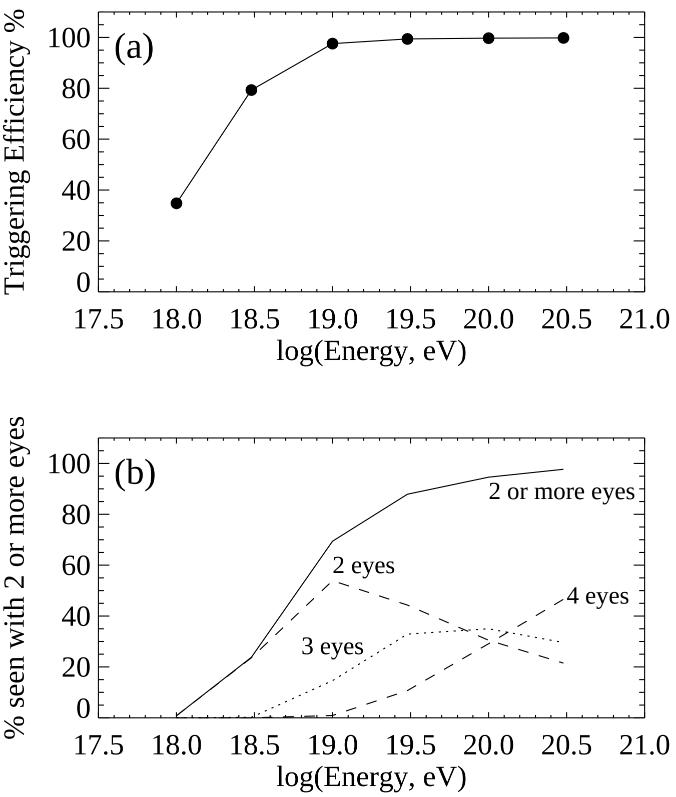

Figure 2.13: (a) Simulated hybrid trigger efficiency in dependence of primary energy for showers with zenith angles $\leq 60°$. (b) Fraction of events triggering more than one fluorescence station. ([Dawson 2004]).

In Tab. 2.1 an estimate of the expected event rate per year is given for the surface detector, the fluorescence detector as well as for hybrid events. In this calculation, the energy spectrum measured by AGASA [Takeda et al. 1998] has been assumed for the part of ultrahigh-energies. For comparison, the corresponding event rates of the HiRes flux [Abu-Zayyad et al. 2000] are given in addition.

As the fluorescence telescopes are grouped into 4 'eyes', the chance for stereoscopic observations is quite good and increases with energy. The situation is illustrated in Fig. 2.13(b). In accordance with this simulation study, almost 70 % of the showers at 10^{19} eV are seen by more

Table 2.1: Expected event rates for one year of operation assuming spectrum suggested by the AGASA experiment, without GZK cut-off. The expected FD rates from HiRes are given for comparison. (from [Cester 2001], modified)

E_{p} [eV]	SD (≥ 5 tanks)	FD / Hybrid (≥ 2 tanks)	HiRes
$\geq 3 \times 10^{18}$	15 000	4700	
$\geq 10^{19}$	5200	520	390
$\geq 2 \times 10^{19}$	1600	160	170
$\geq 5 \times 10^{19}$	500	50	60
$\geq 10^{20}$	100	10	15
$\geq 2 \times 10^{20}$	30	3	4
$\geq 5 \times 10^{20}$	10	1	

than one 'eye'. Apart from a more accurate geometrical reconstruction, stereo observations enable cross-checks of assumed light attenuation in the atmosphere.

The sensitivity of the whole instrument improves with increasing primary energy. The expected energy resolution of the surface detector has been estimated to be about 10 % [Ave et al. 2001], and estimations based on the engineering array running period indicate less than 20 % [Abraham et al. 2004] for showers seen by one 'eye', so-called mono events.

In order to improve the reconstruction of the shower axis, large benefit is achieved by combining pixel timing and amplitude information from one 'eye' with timing information from the ground detector. In such a manner the position of the shower axis in space is determined with a precision comparable to that achieved by stereo observation [Sommers 1995, Dawson et al. 1996]. The hybrid reconstruction precision applying this method is presented in Tab. 2.2. Results presented are based on simulation studies, only statistical median errors are shown. Although the detector is optimised for energies above 10^{19} eV, acceptable reconstruction is expected at energies down to 10^{18} eV.

Table 2.2: Simulation study of the statistical uncertainties of hybrid reconstruction for a single Auger eye (events with zenith angles $\leq 60°$ landing inside the array boundary. In the case of multiple eye events, the information of the one with the longest track length is used. The median errors are given for arrival direction (space angle), energy and depth of shower maximum. ([Dawson & Sommers 2001])

E_{p} [eV]	Δ direc. [deg]	Δ E/E [%]	ΔX_{max} [gcm^{-2}]
	$\sigma_{50\%}$	$\sigma_{50\%}$	$\sigma_{50\%}$
10^{18}	0.50	9.5	21
10^{19}	0.35	4.5	14
10^{20}	0.35	2.5	12

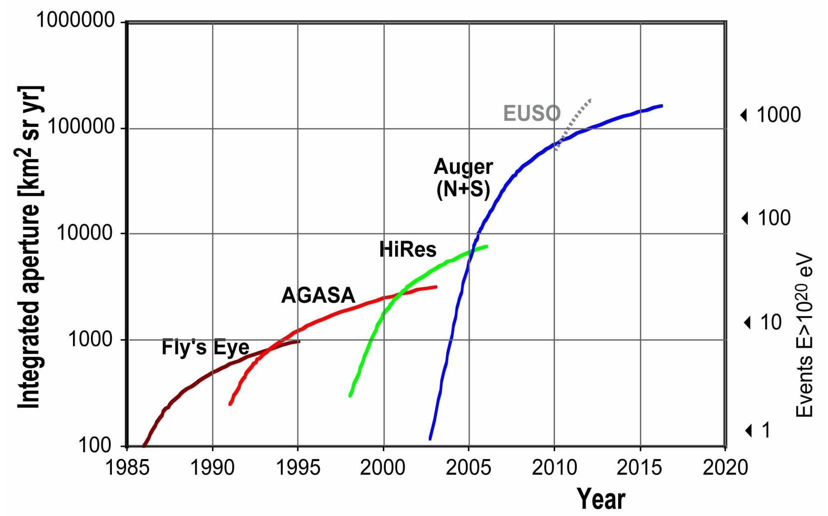

Figure 2.14: Comparison of integrated aperture of current and planned air shower experiments at the high-energy frontier. For completeness, the Fly's Eye experiment is added, so that AGASA and all experiments making use of the fluorescence technique can be compared. (from [Arisaka 2004]).

Using the fluorescence technique, one has to fight with systematic uncertainties, apart from the detector calibration itself, some of the most important sources must be mentioned in this context of discussing resolutions:

- The fluorescence yield is not known very precisely, it is expected to be the source of the largest systematic error.
- Inhomogeneity and instability of our calorimeter in form of the atmosphere makes attenuation and scattering of light on its path from the shower to the detector hard to account for properly.
- The Cherenkov contribution comprised in the measured signal affects the energy integral and distorts the shower profile. If this part of the signal is not taken into account at sufficient accuracy, this can lead to an overestimation of energy and shift the position of shower maximum.
- The fluorescence signal is stricktly speaking only proportional to the electromagnetic shower, a remarkable contribution to the systematic uncertainty is thus expected from the unobserved energy. This effect leads to an underestimation of the energy

Estimations of the combined effect of these systematic uncertainties suggest a contribution in uncertainty of about 20 % [Arisaka et al. 2004].

However, the combination of different methods and increasing event statistics as realised by the Auger project, enables also better techniques to overcome such systematics. Presumed planned projects to be realised, Fig. 2.14 presents the incoming integrated aperture for the next decade, which justifies optimism concerning solutions of riddles going back to the sixties.

Chapter 3

Cherenkov Light and its Role for the Fluorescence Detection Technique

The charged particles of the electromagnetic component of extensive air showers are mostly relativistic. These particles produce Cherenkov light in the atmosphere. In the case of experiments using the fluorescence technique like the Pierre Auger Observatory, one has to subtract this amount of Cherenkov light reaching the detector since it is a not negligible background in the fluorescence detector signal.

3.1 Cherenkov Effect

The emission of Cherenkov radiation is connected to the coherent response of a medium to the passage of a relativistic particle. A comprehensive derivation of the complete mathematical theory can be found e.g. in [Jackson 1975]. Qualitatively one can suppose an electron to be moving relatively slow through a transparent medium. The atoms of the medium near to the passing electron are distorted by its electric field, so that the negative charges of the electrons are displaced to one side of the heavier positive charges of the nuclei of these atoms, like it is shown in Fig. 3.1. Thus the medium gets polarised around the point P, Fig. 3.1a. After the electron has moved to another point P' the atoms near P return to their normal configuration. During the distortion they behave like elementary dipoles and thus the elemental regions along the particle track receive a very brief electromagnetic pulse. However the polarisation field surrounding the electron in this case is completely symmetric in azimuth as well as along the track and consequently there is no resultant field at large distances and therefore no radiation. When the electron is moving faster, comparable to the speed of light in the medium, the picture changes, as shown in Fig. 3.1b. In this case the symmetry along the electron trajectory is no longer preserved and the resultant dipole field appears even at large distances from the track. At each element of the track such field is set up and by this in turn each element radiates a brief electromagnetic pulse. However in general these radiated wavelets from all parts of the track undergo destructive interference and therefore the resultant field at larger distances is still zero. But when the charged particle is moving faster than the phase velocity of light in the medium, at a distant point the wavelets from all parts of the track can be in phase and then there is a resultant field. Assuming the particle's velocity to be $v = \beta c$, then

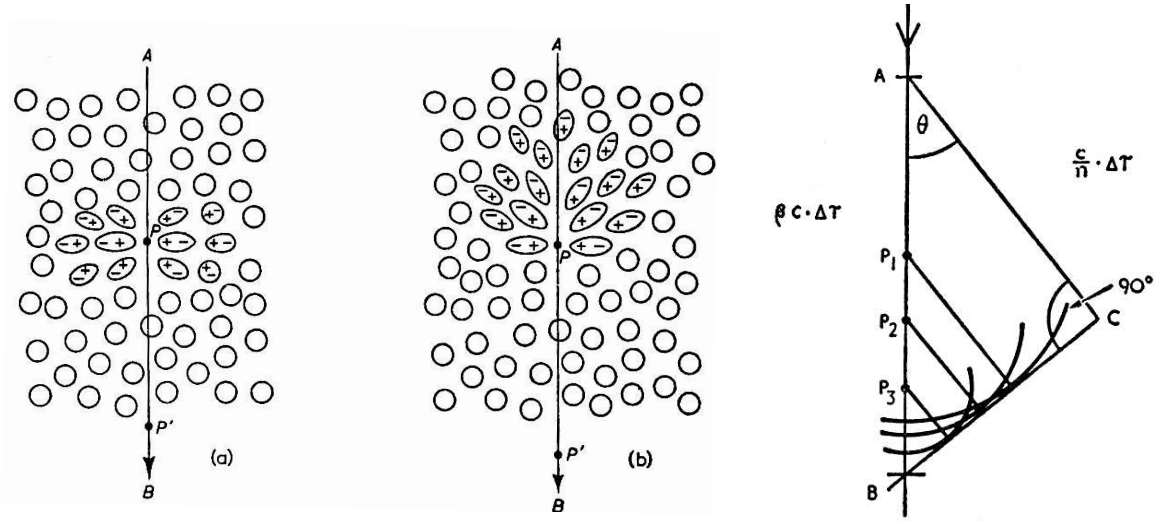

Figure 3.1: Polarisation in a dielectric by the passage of a charged particle (a) low speed (b) high speed, for explanation see text. Right panel: Coherence shown by Huygens construction, for explanation see text. ([Jelley 1958])

in a time $\Delta\tau$ the particle traverses AB and the light a distance $AC = \Delta\tau \cdot (\mathrm{c}/n)$, see Fig. 3.1. In this case by Huygens construction the appropriate wavelets from points P_1,P_2 and P_3 on a track AB are then coherent and build a plane wave front BC. From this qualitative description we obtain two main properties. For a certain medium of given index of refraction $n(\lambda)$, there is a threshold velocity for a charged particle to emit Cherenkov photons of wavelength λ

$$v > \frac{\mathrm{c}}{n(\lambda)} , \tag{3.1}$$

where $n(\lambda)$ is the refractive index of the propagated medium as a function of the photon wavelength λ. Secondly, the angle of emission is given by

$$\cos\theta_{\check{\mathrm{C}}} = \frac{1}{n(\lambda)\beta} , \qquad \beta = v/\mathrm{c} , \tag{3.2}$$

where $\theta_{\check{\mathrm{C}}}$ is the angle with respect to the direction of the particle velocity, which is dependent on the wavelength of the emitted photons as well as on the velocity of the charged particle. In air, the Cherenkov emission angle is close to one degree and increases with decreasing altitude, see Fig. 3.2. For instance, in the atmosphere assuming the refractive index given by Eq. (3.7) one gets for an ultra-relativistic particle $\theta_{\check{\mathrm{C}}} \approx 1.28^\circ$ at 1.2 km, $\theta_{\check{\mathrm{C}}} \approx 1.14^\circ$ at 3.5 km and $\theta_{\check{\mathrm{C}}} \approx 0.99^\circ$ at 6.0 km respectively. From the quantitative treatment the number of Cherenkov photons $\mathrm{d}N_\gamma$ produced by a single relativistic particle per unit length amounts to [Frank & Tamm 1937], see also [Zrelov 1970]

$$\frac{\mathrm{d}N_\gamma}{\mathrm{d}l} = 2\pi Z^2 \alpha \int_{\lambda_1}^{\lambda_2} \left(1 - \frac{1}{n^2(\lambda)\beta^2}\right) \frac{\mathrm{d}\lambda}{\lambda^2} , \tag{3.3}$$

where Z is the charge of the ionising particle in units of e and α is the fine structure constant.

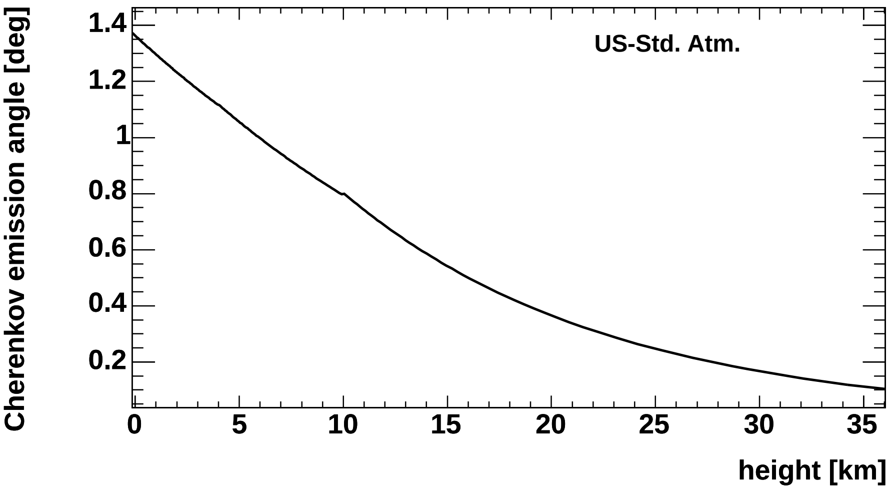

Figure 3.2: Cherenkov emission angle in air is close to one degree, and increases with decreasing altitude. Here, Eq. (3.2) is shown for an ultra relativistic particle and for the US Std. atm. assuming the dependence of the refractive index on height given by Eq. (3.7).

The Role of Refractive Index

For the Cherenkov effect the index of refraction plays an important role as the threshold condition (Eq. (3.1)), the angle of emission (Eq. (3.2)) as well as the number of photons produced (Eq. (3.3)) depend on it. From its definition

$$n := \sqrt{\epsilon\mu} \ , \tag{3.4}$$

with ϵ and μ being the dielectric constant and permeability of a given medium one knows that n depends on wavelength λ. A parameterisation of the wavelength dependence can be found e.g. in [Weast 1986]:

$$(n(\lambda) - 1) \times 10^7 = 2726.43 + \frac{12.288}{\lambda^2 \times 10^{-8}} + \frac{0.3555}{\lambda^4 \times 10^{-16}} \ , \quad \lambda \text{ in Å}. \tag{3.5}$$

From (3.5) it is seen, that the wavelength dependence is rather weak, for instance $n(300\,\text{nm}) = 1.00029$ whereas $n(400\,\text{nm}) = 1.00028$.

In the case of inhomogeneous media like the air also a further dependence occurs. Since the density changes with altitude, also the refractive index does, as shown in Fig. 3.3. There are plenty of investigations on measuring and determining the dependence of n on atmospheric conditions like temperature and pressure, c.f. [Edlén 1966, Owens 1967, Peck & Reeder 1972]. Because of these dependences a precise knowledge of the atmosphere at the experiment's site is necessary also for an accurate Cherenkov light calculation. The present status of the current work of measuring the atmosphere‘s conditions and deriving a realistic atmospheric model by the Auger Collaboration is given in [Keilhauer et al. 2004]. For the work presented here the US standard atmosphere [US-StdA 1976] parameterised by [Linsley 1988] is used, which then, for practical calculations, has to be replaced by a site dependent more realistic atmospheric

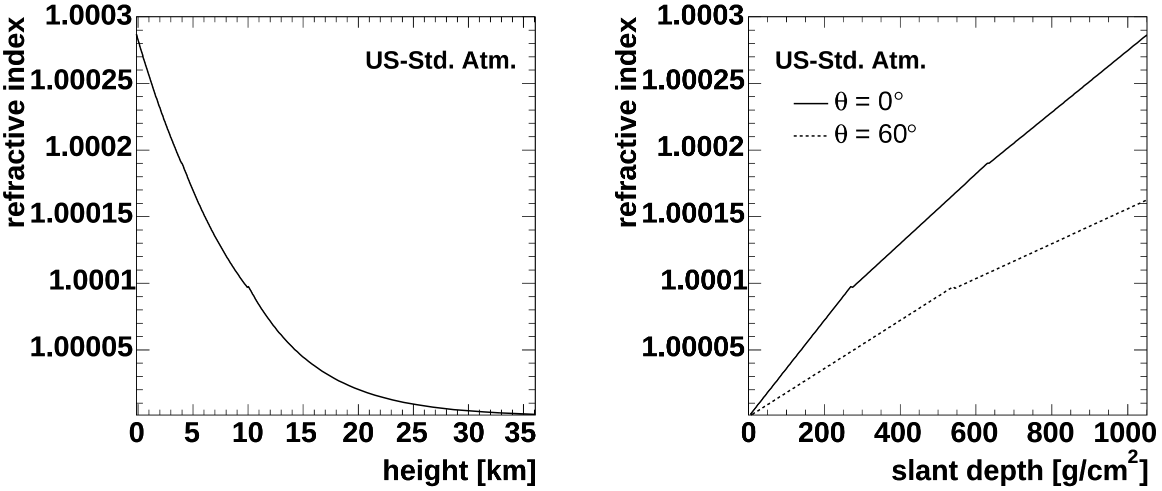

Figure 3.3: Left panel: Height dependence of the refractive index, Eq. (3.7). The index of refraction in air is slightly increasing with decreasing altitude. The dependence is shown for the US-Std. atm. neglecting the wavelength dependence. Right panel: The index of refraction is increasing with increasing slant depth. This dependence is shown here assuming Eq. (3.7) and using Eq. 2.6 for convolution from altitude to atmospheric depth. The refractive index is shown for vertical as well as for an inclined shower axis.

model. For the standard atmosphere, assuming a scaling law, the index of refraction can be approximated [Weast 1986] by the local density $\rho(h)$:

$$\frac{n(h)-1}{n_0-1} = \frac{\rho(h)}{\rho_0} \tag{3.6}$$

The dependence on the atmospheric model used in the following is given by

$$n(h) = 1 + 0.000283\ \rho(h)/\rho(0) \quad \text{(US Std. Atm.)}\ , \tag{3.7}$$

where the wavelength dependence is neglected and the height h is measured relative to sea level.

3.2 Cherenkov Light in Extensive Air Showers

In contrast to the fluorescence light, the Cherenkov light is not produced isotropically, but strongly peaked forward. Therefore one needs to know not only the total number of Cherenkov photons produced, but also their angular distribution. If both quantities are given, the expected background in the fluorescence detector signal due to Cherenkov light is directly computable. One then just has to propagate these direct produced photons through the atmosphere. Depending on the atmospheric conditions a certain amount of photons scatter and are absorbed on their way to the detector. Finally, we expect a Cherenkov contribution in the measured light signal of two different kind, direct and scattered Cherenkov light.

3.2.1 Total Number of Cherenkov Photons

In the case of extensive air showers, almost all of the charged particles are singly charged particles and for the shower development the amount of traversed material is the primary physics quantity. Therefore one has to take into account the density gradient of our inhomogeneous calorimeter, i.e. the atmosphere. One can convert $\mathrm{d}N_\gamma/\mathrm{d}l$ (Eq. 3.3) into atmospheric (slant) depth $\mathrm{d}X(h) = \rho(h)\,\mathrm{d}l$, which is a function of the density $\rho(h)$ depending on the altitude h in the atmosphere. For this purpose, the number of Cherenkov photons produced by a single charged particle of total energy E within extensive air showers per slant depth is defined, and used in the following, as the Cherenkov yield y_γ:

$$y_\gamma := \frac{\mathrm{d}N_\gamma^{(1)}}{\mathrm{d}X}(h,E) = \frac{2\pi\alpha}{\rho(h)} \int_{\lambda_1}^{\lambda_2} \left(1 - \frac{1}{n^2(\lambda)\beta^2}\right) \frac{\mathrm{d}\lambda}{\lambda^2} \,. \tag{3.8}$$

Since in air $n \approx 1$ the integrand of (3.8) can be approximated as

$$\begin{aligned} 1-(\beta n)^{-2} &= 1-\left(1-\frac{m^2c^4}{E^2}\right)^{-1}(1+\delta)^{-2} \\ &\approx 2\delta - \frac{m^2c^4}{E^2} \,, \end{aligned} \tag{3.9}$$

where $\delta = n-1$, m the charged particle's mass, and thus we obtain easily the energy threshold condition for Cherenkov radiation in air:

$$E_{\mathrm{thr}}(h) = \frac{mc^2}{\sqrt{2\delta(h)}} \,. \tag{3.10}$$

The dependence of the threshold energy on the atmospheric model is displayed in Fig. 3.4 and Fig. 3.5 respectively. One should notice that finally not the weak height dependence of the refractive index $n(h)$, but the stronger dependence of $\delta(h) = n(h) - 1$ determines the threshold energy E_{thr}, see Fig. 3.3.

In order to calculate the total number of Cherenkov photons produced by an extensive air shower one has to convolute the fraction of charged particles above the energy threshold E_{thr} for Cherenkov production with the Cherenkov yield y_γ. Thus, the total number of Cherenkov photons $\mathrm{d}N_\gamma$ produced per slant depth $\mathrm{d}X$ in a shower at slant depth X is given by:

$$\frac{\mathrm{d}N_\gamma}{\mathrm{d}X}(X,h) = \int_{\ln E_{\mathrm{thr}}^{\mathrm{e}}}^{\infty} N_{\mathrm{e}}(X)\; y_\gamma^{(\mathrm{e})}(h,E)\; f_{\mathrm{e}}(X,E)\; \mathrm{d}\ln E \tag{3.11}$$

$$+ \int_{\ln E_{\mathrm{thr}}^{\mu}}^{\infty} N_\mu(X)\; y_\gamma^{(\mu)}(h,E)\; f_\mu(X,E)\; \mathrm{d}\ln E \;+\; ... \tag{3.12}$$

where $N_{\mathrm{e},\mu,...}(X,h)$ are the corresponding charged particle numbers as function of slant depth, $E_{\mathrm{thr}}^{\mathrm{e},\mu,\cdots}(h)$ are the respective Cherenkov energy thresholds, $y_\gamma^{\mathrm{e},\mu,\cdots}(h,E)$ are the related Cherenkov yields, and

$$f_{\mathrm{e},\mu,...}(X,E) = \frac{1}{N_{\mathrm{e},\mu,...}} \frac{\mathrm{d}N_{\mathrm{e},\mu,...}}{\mathrm{d}\ln E} \tag{3.13}$$

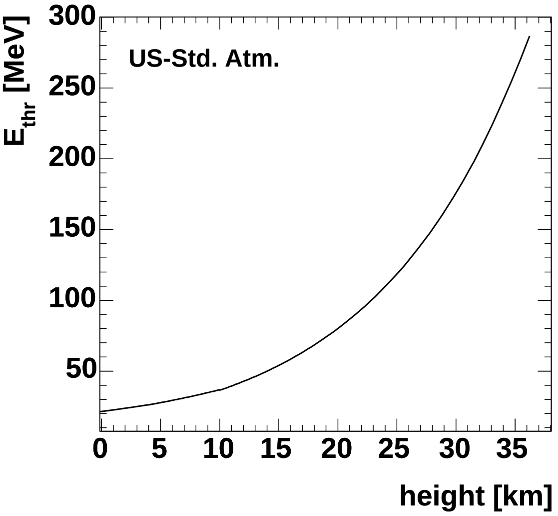

Figure 3.4: The Cherenkov threshold energy is decreasing with decreasing height because of the increasing index of refraction, Eq. 3.10. The dependence is calculated for electrons. At large altitudes the threshold energy amounts several hundreds of MeV, whereas at sea level it decreases down to about 20 MeV.

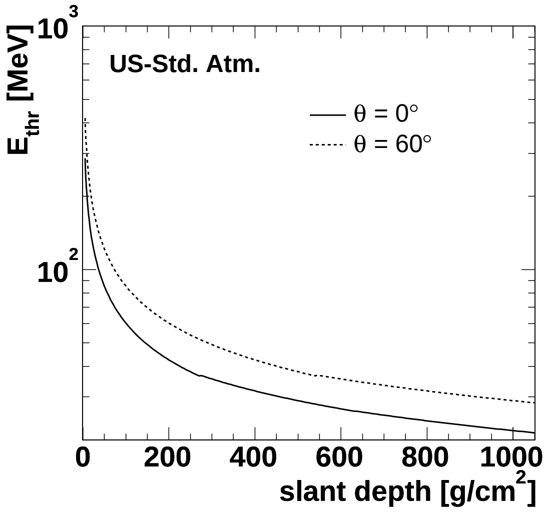

Figure 3.5: The Cherenkov threshold energy is decreasing with increasing atmospheric depth. The dependence is displayed for the vertical as well as for an inclined profile. As can be seen, differences due to inclination are so large that for the example of 60° at 1000 g/cm^2 deviations are in the order of nearly 50%.

are the corresponding normalised differential energy spectra at depth X, related to different charged particle types. In high-energy showers, more than 95 % of all charged particles are electrons. For example, in the case of a proton shower of 10^{19} eV, 99 % at shower maximum and still 97 % at Auger detector level are electrons. For an iron shower of the same energy the corresponding values are smaller but still 98 % and 95 % respectively. Thus, in a good approximation practically all charged particles can be assumed to be electrons. The total number of Cherenkov photons produced per slant depth in a shower at depth X is approximated by the following ansatz:

$$\frac{\mathrm{d}N_\gamma}{\mathrm{d}X}(X,h) = \int_{\ln E_{\mathrm{thr}}}^{\infty} N_{\mathrm{ch}}(X)\ y_\gamma(h,E)\ f_{\mathrm{e}}(X,E)\ \mathrm{d}\ln E\ . \tag{3.14}$$

Here $N_{\mathrm{ch}}(X)$ is the charged particle number as function of slant depth X, $E_{\mathrm{thr}}(h)$ and $y_\gamma(h,E)$ are the energy threshold and the yield according to electrons respectively, and

$$f_{\mathrm{e}}(X,E) = \frac{1}{N_{\mathrm{e}}}\ \frac{\mathrm{d}N_{\mathrm{e}}}{\mathrm{d}\ln E} \tag{3.15}$$

is the normalised differential energy distribution at depth X. For a given shower geometry, $h = h(X)$ follows from the atmospheric model assumed, c.f. Sec. 2.1.

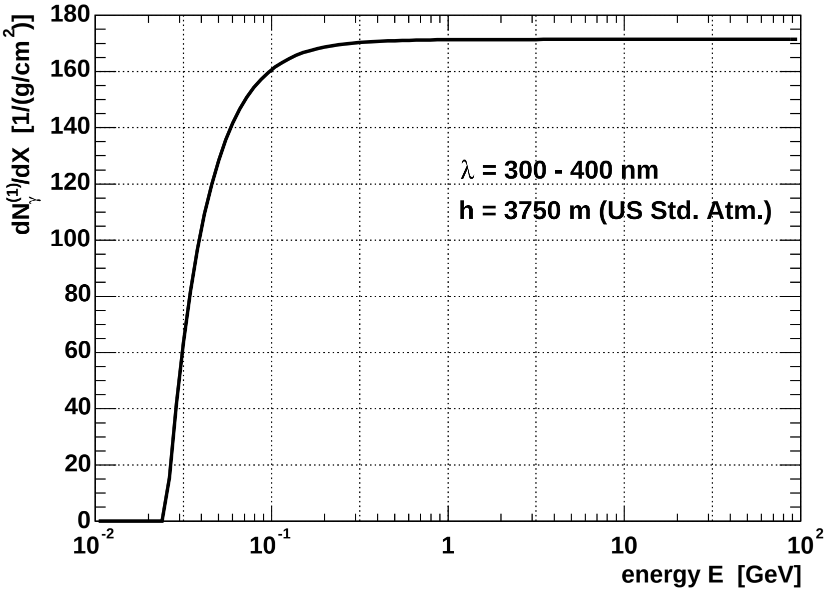

Figure 3.6: Threshold dependence of Cherenkov yield, Eq. (3.8). The number of photons produced by one electron within the wavelength band of interest for fluorescence observations at given height is calculated as function of the particle's energy. Above the threshold energy of about 25 MeV corresponding to the given height, the produced photon number increases fast until saturation is reached close to 170 photons per g/cm^2 above about 300 MeV.

This ansatz works considerably well, which is shown in Chap. 4. The Cherenkov yield shows the well-known sharp threshold dependence, as shown in Fig. 3.6.

Regarding the background subtraction from the fluorescence detector signal, $N(X)$ is the quantity which is derived from the measured light profile. Consequently, in order to find an analytical description of the total number of Cherenkov photons produced by extensive air showers according ansatz (3.14), one solely has to find a proper parameterisation of (3.15), which is presented in Chap. 4.

The total number of Cherenkov photons produced by extensive air showers per angular bin $\mathrm{d}N_\gamma/\mathrm{d}X\mathrm{d}\theta$ is then derived, under the assumption of factorisation, from (3.14) as

$$\frac{\mathrm{d}N_\gamma}{\mathrm{d}X\mathrm{d}\theta}(\theta,X,h) \;=\; A_\gamma(\theta,X,h) \;\cdot\; \frac{\mathrm{d}N_\gamma}{\mathrm{d}X}(X,h)\;, \tag{3.16}$$

where θ is the angle with respect to the shower axis and $A_\gamma(\theta,X,h)$ is the Cherenkov photon angular distribution normalised to one photon

$$A_\gamma(\theta,X,h) \;=\; \frac{1}{N_\gamma}\frac{\mathrm{d}N_\gamma}{\mathrm{d}\theta}(\theta,X,h)\;, \quad \text{with} \int_0^{180^\circ} A_\gamma(\theta,X,h)\;\mathrm{d}\theta = 1\;. \tag{3.17}$$

A_γ is quite unknown and hence also has to be parameterised, which is presented in Chap. 5. Finally, using proper parameterisations of the normalised electron energy spectrum as well as of the normalised Cherenkov photon angular distribution, the Cherenkov photon production by extensive air showers per slant depth and per angule with respect to the shower axis is given by

$$\boxed{\frac{\mathrm{d}N_\gamma}{\mathrm{d}X\mathrm{d}\theta}(\theta, X, h) \;=\; A_\gamma(\theta, X, h) \int_{\ln E_{\mathrm{thr}}}^{\infty} N_{\mathrm{ch}}(X)\; y_\gamma(h, E)\; f_{\mathrm{e}}(X, E)\; \mathrm{d}\ln E} \tag{3.18}$$

Employing this ansatz, the Cherenkov signal in a detector, e.g. the Auger fluorescence detector, can be predicted. Of course the attenuation and scattering effects of the atmosphere have to be taken into account.

3.2.2 Direct and Scattered Cherenkov Light

After its production while propagating towards the detector, the Cherenkov light (as well as the fluorescence light) is affected by the atmosphere. Normally there are two main effects occurring, attenuation and scattering. The first is due to both, purely absorptive as well as scattering processes, by which photons disperse out of the field of view. Within the wavelength band of interest for observations of roughly 300-400 nm, attenuation is essentially caused by scattering at aerosol particles, Mie Scattering, as well as at the air molecules, the Rayleigh scattering [Sokolsky 1989]. Light signals seen by the fluorescence detector are both enhanced as well as diminished. Scattering on the one hand removes light from a direct produced Cherenkov beam pointing to the detector while it enhances the source brightness by scattering Cherenkov photons which originally would not have reached the detector. The amount of photons which remain on their original path after emission and reach the detector, thus are neither scattered nor absorbed, are called *direct Cherenkov light.* The part of photons, which reaches the detector, because of being scattered into the field of view, and which is not absorbed during their path through the atmosphere, is called *scattered Cherenkov light.*

Mie Scattering

Mie scattering denotes scattering of light by aerosol particles whose sizes are comparable to the wavelength of the light. In principle the optical properties of such particles can be calculated based on Maxwell's equation using Mie's theory. The difficulties arise from the variety of properties of aerosols, e.g. their size distribution, maybe varying with altitude, weather conditions and composition of pollutants. Thus, if the aerosol concentration is large, no reliable theoretical predictions for atmospheric attenuation can be made. Therefore, the Auger sites and, in general, places for building up observatories using the fluorescence technique are chosen to have minimal aerosol contamination, see e.g. [Auger-DR 1997]. In this case Mie scattering constitutes only a minor correction to the light measured by the fluorescence detector. Estimates for such circumstances are based on a simplified model [Elterman & Toolin 1965], where Mie scattering is assumed to fall off exponentially with altitude

$$\frac{\mathrm{d}N_\gamma}{\mathrm{d}l} \approx -\frac{N_\gamma}{l_{\mathrm{M}}}\; \mathrm{e}^{-h/h_{\mathrm{M}}}\;, \tag{3.19}$$

where $h_{\mathrm{M}} \approx 1.2\,\mathrm{km}$ is the aerosol scale height and $l_{\mathrm{M}} \approx 14\,\mathrm{km}$ the Mie scattering mean free path at 400 nm [Sokolsky 1989]. The angular distribution is strongly peaked forward and can be described approximately by an exponential

$$\frac{\mathrm{d}^2 N_\gamma}{\mathrm{d}l \mathrm{d}\Omega} \approx a \cdot \mathrm{e}^{-\theta/\theta_\mathrm{M}} \left| \frac{\mathrm{d}N_\gamma}{\mathrm{d}l} \right| , \tag{3.20}$$

where $a = 0.80$ and $\theta_\mathrm{M} = 26.7°$. The model presented here is quite general and thus has to be understood as approximation. It is used by previous experiments using the fluorescence detector technique, see e.g. [Baltrusaitis et al. 1985]. The above given value for $h_\mathrm{M} \approx 1.2\,\mathrm{km}$ has newly been measured to be $\approx 7.5\,\mathrm{km}$ for the Auger southern site [Matthews & Clay 2001]. Mie scattering is mainly important for small angles between the shower axis and the detector.

Rayleigh Scattering

If the scattering centres are small compared to the wavelength Rayleigh scattering applies, which is a special case of the more general theory of Mie [Hutzinger 1982]. The cross-section depends strongly on the wavelength already pointed out by Lord Rayleigh in the 19th century [Rayleigh 1899]:

$$\frac{\mathrm{d}\sigma}{\mathrm{d}\Omega} \sim \frac{1}{\lambda^4} . \tag{3.21}$$

Since the scattering mean free path is $X_\mathrm{R} = 2970\,\mathrm{g/cm}^2$ at $\lambda = 400\,\mathrm{nm}$, the number of photons scattered off the beam per unit length is given by [Elterman & Toolin 1965]

$$\frac{\mathrm{d}N_\gamma}{\mathrm{d}l} = -\frac{\rho(h) N_\gamma}{X_\mathrm{R}} \left(\frac{400\,\mathrm{nm}}{\lambda} \right)^4 , \tag{3.22}$$

where $\rho(h)$ follows from the atmospheric model assumed. Using the Rayleigh phase function (see e.g. [Buchholtz 1995])

$$P_\mathrm{R} = 3/4 \; (1 + \cos^2 \theta) , \tag{3.23}$$

the angular distribution can then be written as

$$\frac{\mathrm{d}^2 N_\gamma}{\mathrm{d}l \mathrm{d}\Omega} = \frac{3}{16\pi} \left| \frac{\mathrm{d}N_\gamma}{\mathrm{d}l} \right| (1 + \cos^2 \theta) , \tag{3.24}$$

where θ is the scattering angle and no angular spread of the initial photons is assumed. Since the angular dependence of the Rayleigh scattering is rather weak, it is important for all angles of the shower axis to the detector.

Attenuation

The different angular distributions of both effects, Mie and Rayleigh scattering respectively, imply different impacts on the received light signals. At small angles Mie dominates over Rayleigh scattering and vice versa for large angles ($> 90°$). The fraction of photons not Mie dispersed off the beam directed to the detector is derived by (3.19). Assuming the light source to be at height h_1 and the detector at h_2, then by integration ($h_2 < h_1$) the Mie transmission factor T_M reads

$$T_\mathrm{M} \;=\; \exp\left[\frac{h_\mathrm{M}}{l_\mathrm{M}\cos\vartheta}\left(\exp\left[-\frac{h_1}{h_\mathrm{M}}\right]-\exp\left[-\frac{h_2}{h_\mathrm{M}}\right]\right)\right] \;, \tag{3.25}$$

where ϑ is the angle between the vertical and the line of sight. Since $\rho \mathrm{d}l = \mathrm{d}X$ the corresponding Rayleigh transmission factor T_R of light propagating from a point at a certain slant depth X_1 to a point at slant depth X_2 can be calculated from (3.22):

$$T_\mathrm{R} \;=\; \exp\left[-\frac{|X_1 - X_2|}{X_\mathrm{R}}\left(\frac{400\,\mathrm{nm}}{\lambda}\right)^4\right] \;. \tag{3.26}$$

Here, the slant depth corresponding to the path between the two points ($|X_1 - X_2|$) are crucial. For the total transmission, taking both effects into account, then follows

$$T \;=\; T_\mathrm{M}\, T_\mathrm{R} \;. \tag{3.27}$$

Finally, the amount of photons reaching the detector under a certain angle Φ is given by

$$\frac{\mathrm{d}N_\gamma}{\mathrm{d}X\mathrm{d}\Phi} \;=\; \frac{\mathrm{d}N_\gamma}{\mathrm{d}X\mathrm{d}\theta} \cdot T_\mathrm{M}\, T_\mathrm{R} \;, \tag{3.28}$$

where the photon beam is produced under the angle θ regarding the shower axis, whereas Φ is the angle between the photon beam and the line of sight of the detector.

The simple multiplication of the individual transmission factors is only valid assuming negligible multiple scattering. The importance of the contribution of multiply scattered Cherenkov photons is currently under investigation by the Cracow Auger group. Their preliminary result shows that multiple scattered photons contribute a sizable amount of light but spread over a wide area of the sky. The contribution to the intensity of the shower image is rather small, being of the order of 1 % [Pękala et al. 2003].

Within the Auger Collaboration there are many investigations ongoing to quantify Rayleigh cross-sections as well as aerosol properties much more accurately. For instance an aerosol transmission uncertainty of less than ~ 10 % [Matthews & Clay 2001] should be achieved. There is also ongoing work on atmospheric monitoring in order to measure transmission factors T_M and T_R using LIDAR[1] systems [Rizi 2002]. Detailed information about the LIDAR system in the Auger Observatory may be found in [Mussa et al. 2004]. A good overview of the present knowledge about Rayleigh cross-sections is given in [Abendschein & Matthews 2003]. A new general calculation of Rayleigh scattering for the atmosphere can be found in [Buchholtz 1995] using realistic estimates of the refractive index. Furthermore, appropriate phase functions of both, Mie and Rayleigh scattering, are under investigation [Mostafa et al. 2003].

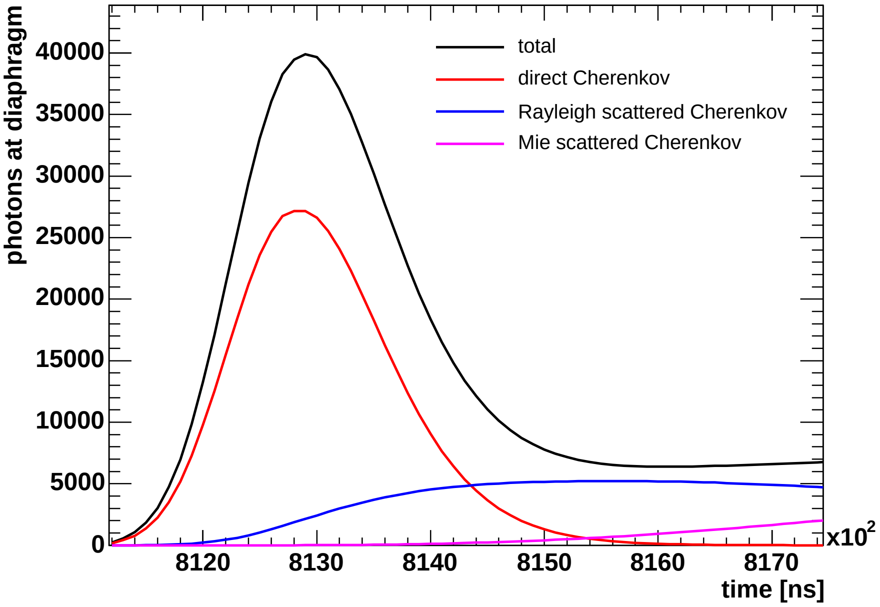

Figure 3.7: Light signal in the fluorescence detector seen by one Auger fluorescence telescope, simulated with FDSim [Prado et al. 2004]. (proton, $\sim 10^{20}$ eV, small viewing angle) The respecting direct and scattered Cherenkov light contributions are calculated analytically with the new Cherenkov model introduced in this work. In the example shown a large direct Cherenkov contribution is contained in the total light signal due to the small viewing angle. The direct Cherenkov light contribution can amount the order of the fluorescence light (and even more), depending on geometrical constellation. Because of the small viewing angle and a small observation distance, the duration of the detected light profile is relatively small, see also Fig. 3.8. ([Engel 2004])

3.2.3 Cherenkov Signal in the Auger Fluorescence Detector

The fluorescence detector of the Pierre Auger Observatory measures the light flux within a wavelength band of about 300-400 nm, c.f. Chap. 2. For the properties of fluorescence light produced in extensive air showers and the important features with respect to the fluorescence technique see [Bunner 1967, Kakimoto et al. 1996, Nagano et al. 2003].

In Fig. 3.7 and Fig. 3.7 respectively, the simulated total light flux for two exemplary air showers seen by one telescope of the fluorescence detector is shown. The simulation has been done using FDSim [Prado et al. 2004] for two extreme shower geometries in terms of the expected Cherenkov light signal. The total photon flux at the diafragm is plotted versus time slots of 100 ns each. Additionally, the estimated contributions of direct and scattered Cherenkov light are plotted. Here, the direct and scattered curves are calculated using the new Cherenkov model introduced in this work, which is discussed in Chap. 4 and Chap. 5 respectively. The amount of Cherenkov light reaching at the diafragm of the fluorescence detector depends strongly on the geometry of the shower. In the case shown in Fig. 3.7, the shower develops towards the detector. Therefore, even the direct Cherenkov light is of the same order of magnitude as the fluorescence light. It is expected that the amount of direct Cherenkov light is developing in time proportional to the total light, as it is also,

---

[1] Light Detection and Ranging

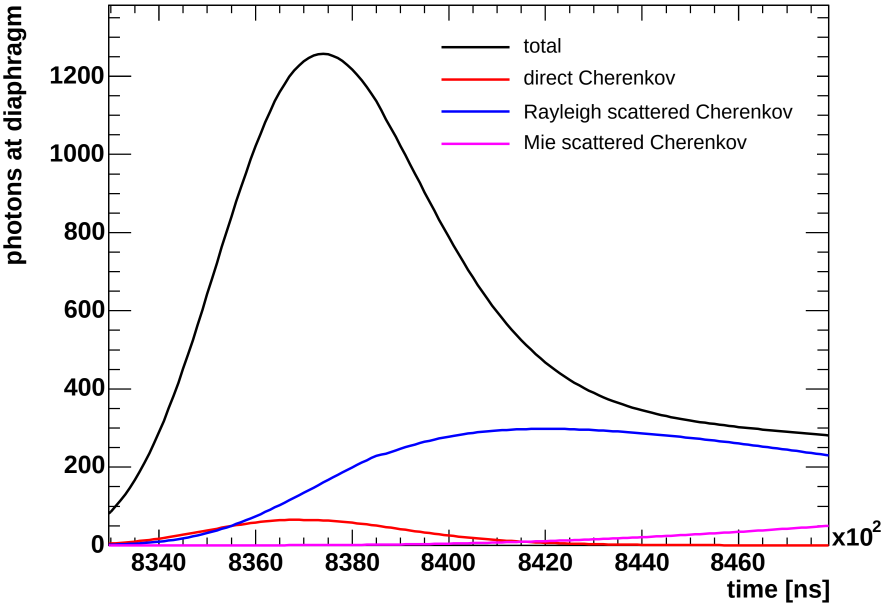

Figure 3.8: Simulated Light signal in the fluorescence detector - example II. The light signal in a Auger fluorescence telescope simulated with FDSim [Prado et al. 2004] (proton, $\sim 10^{20}$ eV, small viewing angle). The respecting direct and scattered Cherenkov light contributions are calculated analytically with the new Cherenkov model introduced in this work. In the example shown relatively small direct Cherenkov contribution is contained in the total light signal, since the shower is observed under a large viewing angle. The scattered Cherenkov light contribution to the total detected signal depends only weak on the viewing angle. Because of a large viewing angle and observation distance, the duration of the detected light profile is relatively large, see also Fig. 3.7. ([Engel 2004])

like the fluorescence, proportional to the shower size. Because the scattered Cherenkov light travels a longer path to the detector it arrives delayed compared with the fluorescence light. The simulated shower in Fig. 3.8 develops more or less parallel to the focal plane of the PMT camera. Since the scattered Cherenkov light contribution to the total detected signal depends only weak on the viewing angle, the amount of scattered Cherenkov light reaching the detector is more or less of same order as compared to the situation in Fig. 3.7. Because of a large viewing angle and observation distance, the duration of the detected light profile is relatively large, and vice versa in the case of a small viewing angle and smaller distance.

From Fig. 3.7 and Fig. 3.8 it is clear, that, first of all, the Cherenkov contribution is a non-negligible background in the fluorescence detector signal, see also discussion in [Nerling 2004]. Secondly, not only the total amount of light is increased, but also the time dependence of the light curve is changed as compared to the pure fluorescence signal. A further discussion of the dependence on shower geometry is given in Chap. 6.

Chapter 4

Parameterisation of the Electron Energy Distribution in Extensive Air Showers

As pointed out in Chap. 3, in order to calculate the total number of Cherenkov photons produced by extensive air showers one has to know the longitudinal electron energy distributions. Moreover, such parameterisation is very useful also for other cosmic ray applications, wherever the energy distribution of electrons is of interest. Examples apart from Cherenkov calculations are so-called fast hybrid simulation codes[1] like e.g. CONEX [Kalmykov et al. 2003], which is a program also for simulating shower fluorescence signals currently under development in the Karlsruhe Auger group. Having a proper parameterisation of longitudinal development of electron energy spectra also the longitudinal energy deposit profile can be calculated analytically using a conversion factor of the mean energy deposit per charged particle in a shower. From the energy deposit profile, one is able to deduce the fluorescence light profile, if the fluorescence yield is proportional as it is assumed to be [Nagano et al. 2003].
In this chapter, after specification of the Monte Carlo program used, a new universal parameterisation of the electron energy distribution is presented. This distribution is then compared with other and finally applied to the calculation of the total number of Cherenkov photons produced in extensive air showers.

4.1 Monte Carlo Simulations

To find a proper parameterisation of the electron energy spectrum, the cosmic ray simulation code CORSIKA [Knapp & Heck 1998] has been used to obtain such distributions for showers of different combinations of primary energy, zenith angle and mass. Furthermore CORSIKA

---

[1] Hybrid simulation codes combine Monte Carlo simulations, which are based on single particle tracking, with analytical treatment in order to reduce the very huge computing time necessary for full simulations of extensive air showers at Auger energies. Actually, CONEX will generate itself particle energy spectra, merely temporarily it has reverted to the parameterisation presented [Pierog 2004]. However, apart from CONEX other Hybrid simulation codes are used, like e.g. the "Bartol" approach [Alvarez-Muniz et al. 2002], which do not generate electron spectra itself, for others see references in [Drescher 2004].

has been utilised to calculate the longitudinal profile of Cherenkov photon production in order to compare the results with the analytical calculation (3.14) based on the longitudinal profile of charged particles and electron energy distributions. For the work presented CORSIKA version `6.137` in combination with the hadronic interaction models QGSJET 01 [Kalmykov et al. 1997] for high and GEISHA 2002 [Fesefeldt 1985, Cassel & Bower 2002] for low energies is used. Since shower simulations at the highest energies are very CPU-time consuming, optimum thinning [Kobal 2001, Risse et al. 2001] of 10^{-6} and appropriately chosen maximum weight is applied unless otherwise noted. The `UPWARD` option is enabled, by which also the upward going electromagnetic particles are followed[2]. This feature is important for the purpose of this work because Cherenkov production goes with particle number, regardless whether they are moving up or downwards. The option `AUGCERLONG` gives the longitudinal Cherenkov spectrum even though increases the CPU-time enormously. Furthermore, the `AUGERHIST` option has been used, which produces a series of `HBOOK` histograms. These are filled with simulated information (like e.g. kinetic energy) of different particle types at up to 20 horizontal layers. This option allows to study various longitudinal shower parameters. In the case of this work, namely the electron energy spectrum, the angular spectrum of electrons, as well as produced Cherenkov photons with respect to the shower axis have been simulated. For more details of the chosen CORSIKA options see [Heck et al. 1998]. low-energy cuts of 100 MeV for hadrons and muons, and of 1 MeV for electrons and gammas have been applied, unless otherwise noted.

The usage of the `UPWARD` option is necessary for the purpose of Cherenkov calculations, as upward going charged particles also produce Cherenkov light unless their energies are below the energy threshold for the Cherenkov effect. However, when using the `UPWARD` option, one has to be aware that counting particles in terms of traversing (horizontal) layers, particles might be counted multiply, depending on how often, and under which angles single particles are scattered when traversing the atmosphere. Anyhow, those electrons which have to be taken into account for Cherenkov production are of energies larger than 20 MeV. Due to their relative large energy, the mean scatter angle with respect to the shower axis of electrons producing Cherenkov photons is small. Therefore, electrons considered in the purpose of this work are rarely counted twice or multiply. This result has been obtained by systematic studies of comparing electron energy spectra simulated with the `UPWARD` option enabled and without, and further by studies of the energy dependent angular distribution of electrons with respect to the shower axis, see Fig. A.1. Furthermore, this result of the fraction of upward going electrons of energies above the Cherenkov threshold being negligible in terms of Cherenkov calculations is well summarised in Fig. A.2 [Risse 2003].

---

[2] In CORSIKA particles are counted at horizontal layers which can be specified by the user. By default, particles under angles larger than 90° are not followed anymore. However, by applying the `UPWARD` option, these particles are treated in the electromagnetic shower component.

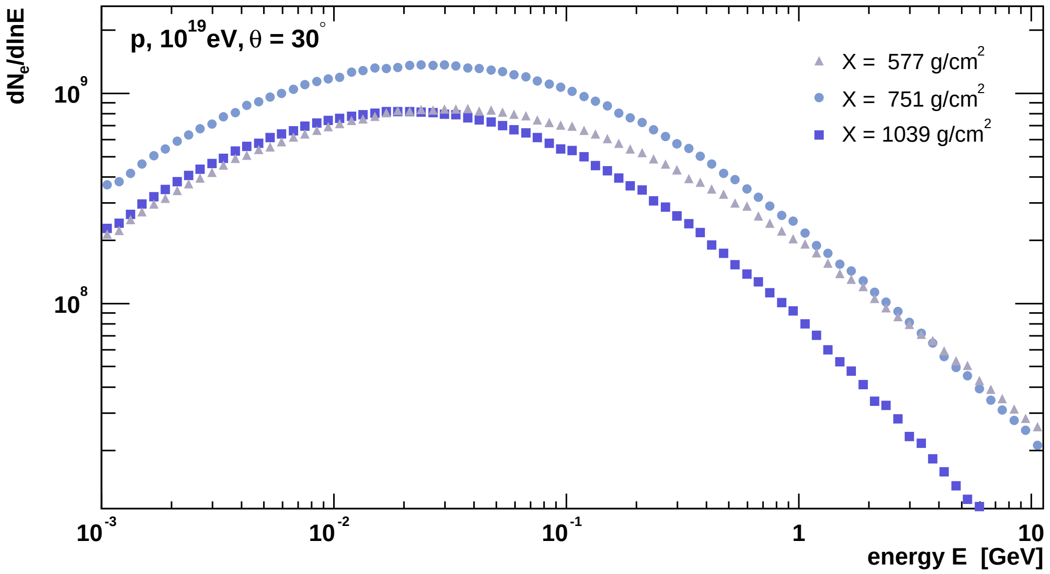

Figure 4.1: Simulated electron energy spectra at three different slant depths of an individual proton shower of 10^{19} eV and a zenith angle of 30°. The number of electrons is changing with increasing slant depth, since different slant depths correspond to different stages of shower development.

4.2 Electron Energy Spectra

In the following a new universal parameterisation of the electron energy distribution as a function of shower age is introduced. This parameterisation also takes into account different low-energy cuts. In the second part the parameterisation is compared to other and applied for calculating the total number of Cherenkov photons produced by extensive air showers.

4.2.1 Interpolation in Shower Age

In order to study the longitudinal development of the electron energy distribution in extensive air showers, 20 vertical depth layers with equal mass-overlay difference of $50\,\mathrm{g/cm^2}$ up to sea level have been defined for the CORSIKA simulated showers. In this manner electron energy distributions have been histogram-med in vertical depth steps of $50\,\mathrm{g/cm^2}$ up to $X_\mathrm{v} = 1000\,\mathrm{g/cm^2}$. One has to convert these vertical depth levels X_v into slant depth X

$$X = X_\mathrm{v}/\cos\theta \;, \quad \text{for inclined showers with } \theta \neq 0^\circ. \tag{4.1}$$

The conversion given here is only approximate, but works well for $\theta \leq 60^\circ$. Exemplarily for one individual shower, electron energy distributions are shown for three different slant depths in Fig. 4.1. The same spectra are plotted again in Fig. 4.2, but here they have been normalised to unity above the low-energy cut E_cut of the simulation. The energy spectra f_e are normalised according to

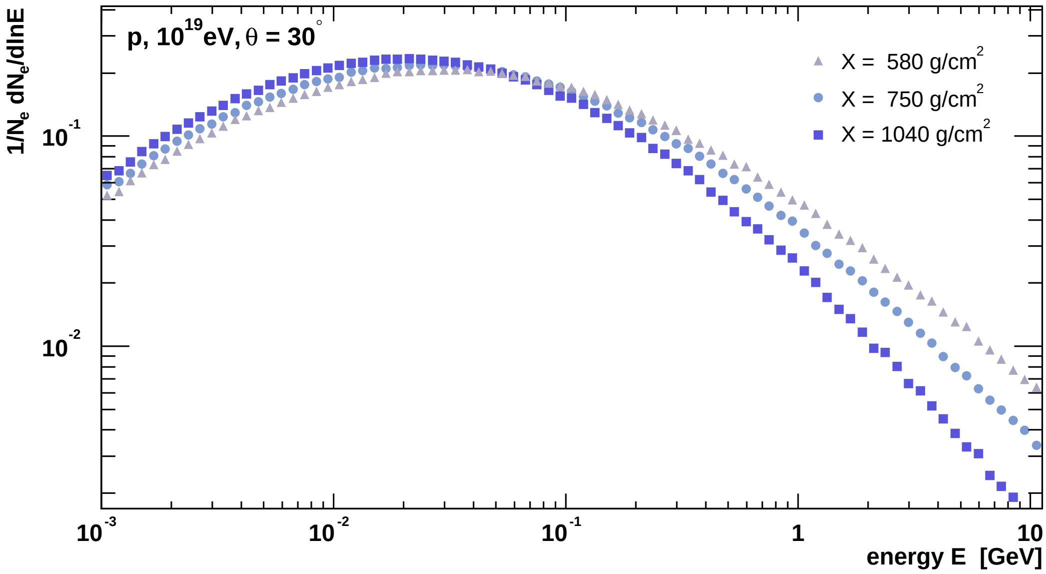

Figure 4.2: Simulated electron energy spectra at three different slant depths of an individual proton shower of 10^{19} eV and a zenith angle of 30°. The same spectra as shown in Fig. 4.1 have been normalised according to Eq. (4.2). With ongoing shower development the maximum of the distribution moves towards lower energies, c.f. Fig. 4.3, for discussion see text.

$$f_{\mathrm{e}}(E) = \frac{1}{N_{\mathrm{e}}}\frac{\mathrm{d}N_{\mathrm{e}}}{\mathrm{d}\ln E}\ , \quad \text{with} \quad \int_{\ln E_{\mathrm{cut}}}^{\infty} f_{\mathrm{e}}(E)\ \mathrm{d}\ln E \ = \ 1\ . \tag{4.2}$$

The number of electrons per energy bin is changing with slant depth. This is expected, since different slant depths correspond to different stages of shower development, namely different shower ages (see also Sec. 2.1). The definition of shower age, as it is used in the following, is a function of slant depth X for a given shower maximum X_{max}

$$s(X) := \frac{3}{1 + 2X_{\mathrm{max}}/X}\ . \tag{4.3}$$

In Fig. 4.3 the longitudinal shower development is plotted in terms of charged particles versus slant depth of this individual proton shower. The marked shower ages correspond to the energy spectra shown in Fig. 4.1 and Fig. 4.2 respectively. The spectra shown in Fig. 4.2 show a shift of the maximum towards lower energies with increasing slant depth, in other words with ongoing shower development. High energetic particles more and more are slowed down due to bremsstrahlung, c.f. Chap. 2. Furthermore, at the lowest slant depth level considered here ($X = 580\,\mathrm{g/cm^2}$), one finds less electrons than at the level of $750\,\mathrm{g/cm^2}$, whereas one finds least at the deepest level ($X = 1040\,\mathrm{g/cm^2}$). At the third slant depth level in Fig. 4.1 the shower has evolved past its maximum and so the number of charged particles is decreasing.

For one individual shower one can, of course, determine the associated age s for each slant depth X. But, in order to study longitudinal electron energy distributions in general,

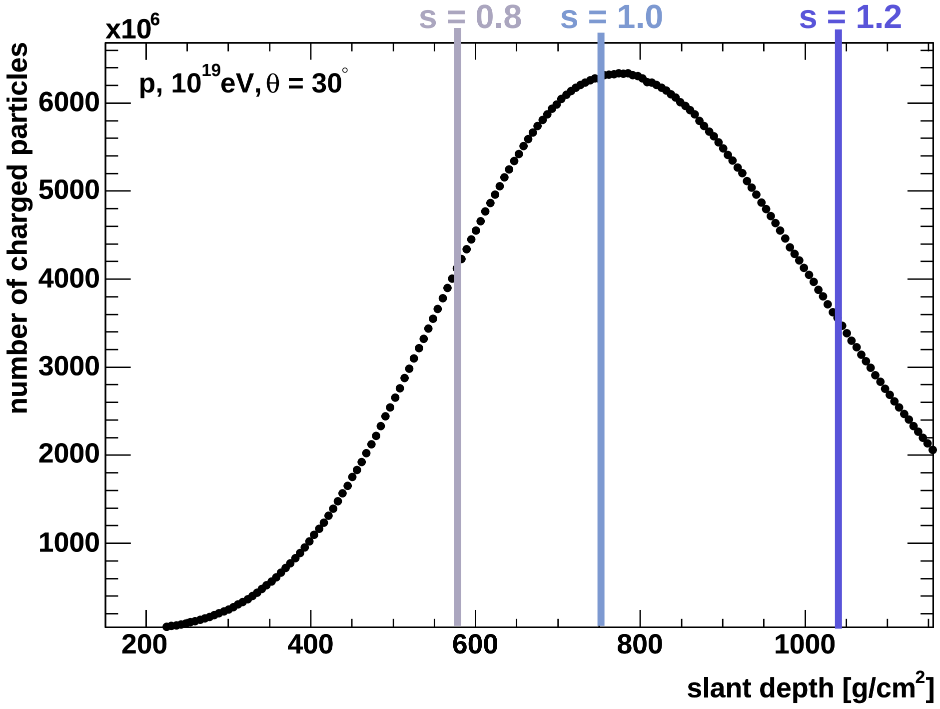

Figure 4.3: Longitudinal shower development of one individual shower. The simulated longitudinal development of shower size versus slant depth is displayed for an individual proton shower of 10^{19} eV. Three different shower age levels are marked, for which the corresponding electron energy spectra are shown in Fig. 4.1 and Fig. 4.2.

due to shower-to-shower fluctuations, slant depth levels on its own are not comparable regarding shower physics. In Fig. 4.4 such shower-to-shower fluctuations are illustrated. Here the number of charged particles of individual showers differs up to about 15 % at shower maximum. Moreover, for a certain slant depth, each shower has reached a different age, in other words, the showers have different X_{max}, which is the crucial quantity for determining the individual shower age system. Thus, normalised electron energy spectra are not expected to be comparable in terms of slant depth levels.

Fig. 4.5 shows the same showers' longitudinal profiles as function of shower age. In this reference system the individual longitudinal shower profiles differ much less. Near the shower maximum between $s = 0.8$ and $s = 1.2$ they show almost the same shape. Remaining differences are due to shower-to-shower fluctuations, like point of first interaction and respective heights of hadronic interactions. Consequently, it is promising to study the longitudinal development of electron energy distributions in shower age. Therefore the normalised histogrammed energy spectra derived from CORSIKA have been interpolated linearly in s on a shower-by-shower basis.

Assuming s to be the age value of interest, then the corresponding interpolated histogram H_{s} is given by

$$H_{\mathrm{s}} = \frac{s - s_{\mathrm{low}}}{s_{\mathrm{up}} - s_{low}} \cdot (H_{\mathrm{up}} - H_{\mathrm{low}}) + H_{\mathrm{up}} \ , \qquad (4.4)$$

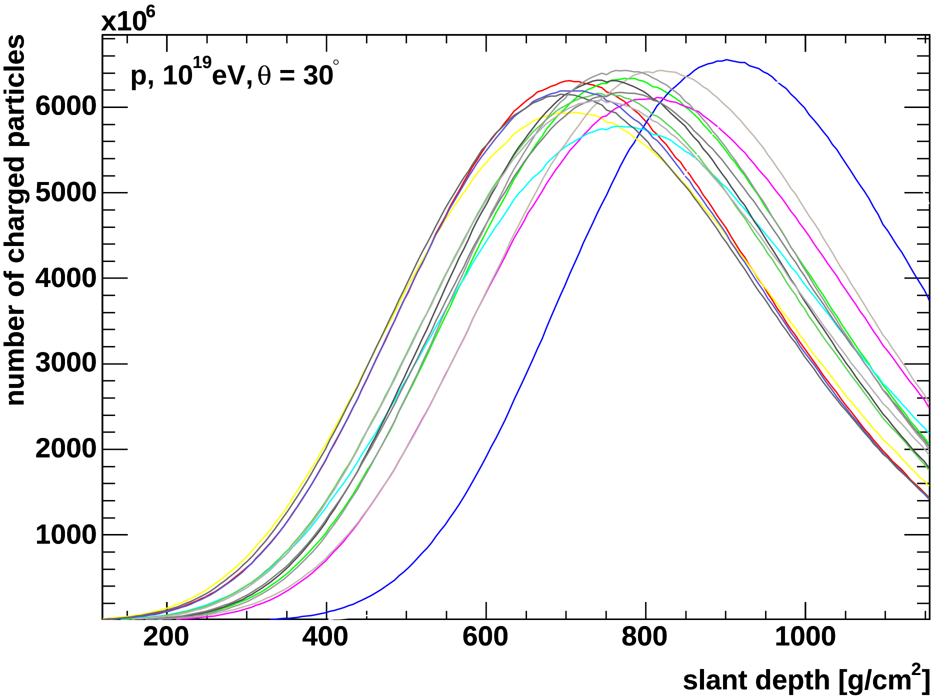

Figure 4.4: Number of charged particles versus slant depth for individual proton showers of 10^{19} eV. Showers fluctuate in their development, which is reflected in different shower maxima as well as different shower sizes at maximum.

where H_{low} and H_{up} are histograms of neighbouring slant depth levels of corresponding ages s_{low} and s_{up}, for which $s_{\mathrm{low}} < s < s_{\mathrm{up}}$. In this manner, histograms H_{s} for age values between $s = 0.8$ and $s = 1.2$ have been obtained for each shower. For $s < 0.7$, the shower-to-shower fluctuations are very large, and hence the showers are useless for fitting, see also Fig. 4.5. The upper limit of $s = 1.2$ is due to the fact, that (vertical) showers of such energies penetrate deep in the atmosphere, so that ages larger than $s = 1.2$ are reached for many showers only deeper than 1000 g/cm^2 (corresponding to sea level for vertical showers).

Several interpolated electron energy distributions are shown for proton showers of 10^{19} eV in Fig. 4.6. They do not differ very much from shower-to-shower. The differences increase with increasing energy, since the higher the energy, the less electrons one finds (for the age region considered). Increasing statistical fluctuations with decreasing particle numbers even at the highest energies are expected due to thinning.

The relative differences of these normalised energy spectra to the average are shown for three shower ages in Fig. 4.7. In the low-energy region differences are up to about 5 %, whereas at 100 GeV they amount up to about 25 %. The fluctuations are small in the energy range from the maximum (which is located at about 30 MeV for young showers of $s = 0.8$ and moves to about 20 MeV for $s = 1.2$) up to 100 MeV ($s = 0.8$) and 200 MeV ($s = 1.2$) respectively, the fluctuations get minimal and account only 2-3 %. For primary energies of 10^{18} eV and 10^{20} eV

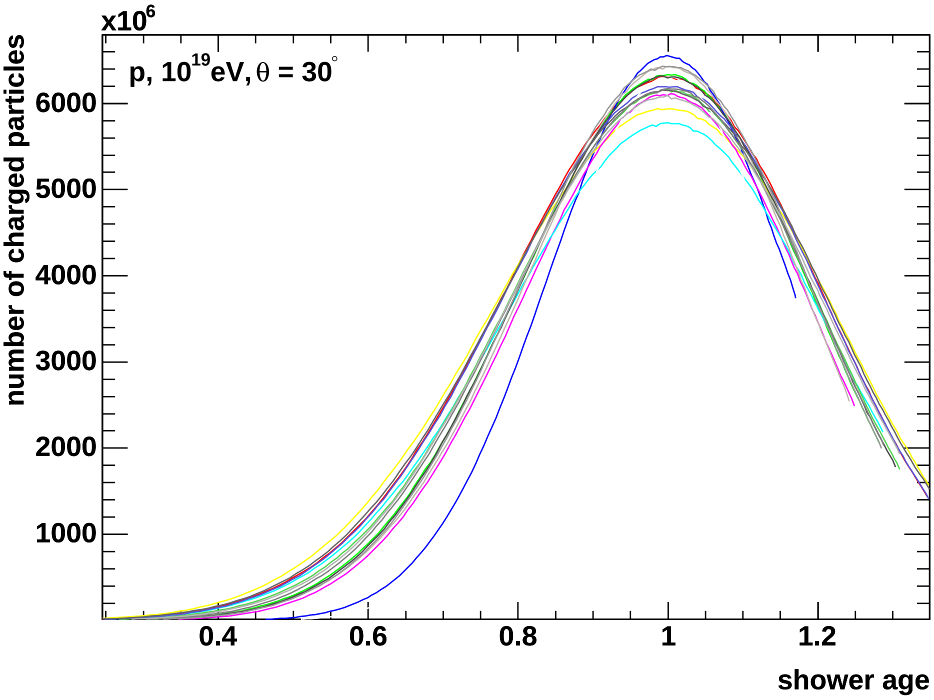

Figure 4.5: Number of charged particles versus shower age for individual proton showers of 10^{19} eV. Using shower age, individual showers are comparable. Remaining differences are due to shower-to-shower fluctuations of first interaction and respective heights of hadronic interactions.

as well as for different primary particles, namely iron and gamma-ray showers[3], shower-to-shower fluctuations are of the same order. The respective relative differences of individual showers to their average for all primary particles and energies regarded, are shown in Fig. A.3 - A.7 in Appendix A.

---

[3] In the case of gamma-ray showers simulations were done for $10^{19.5}$ eV instead of 10^{20} eV as otherwise the Landau-Pomeranchuk-Migdal effect [Heck & Knapp 1998] occurs, which causes an effective reduction of the pair production and bremsstrahlung cross-sections at high energy. Increase of penetration depth and larger fluctuations are the consequences.

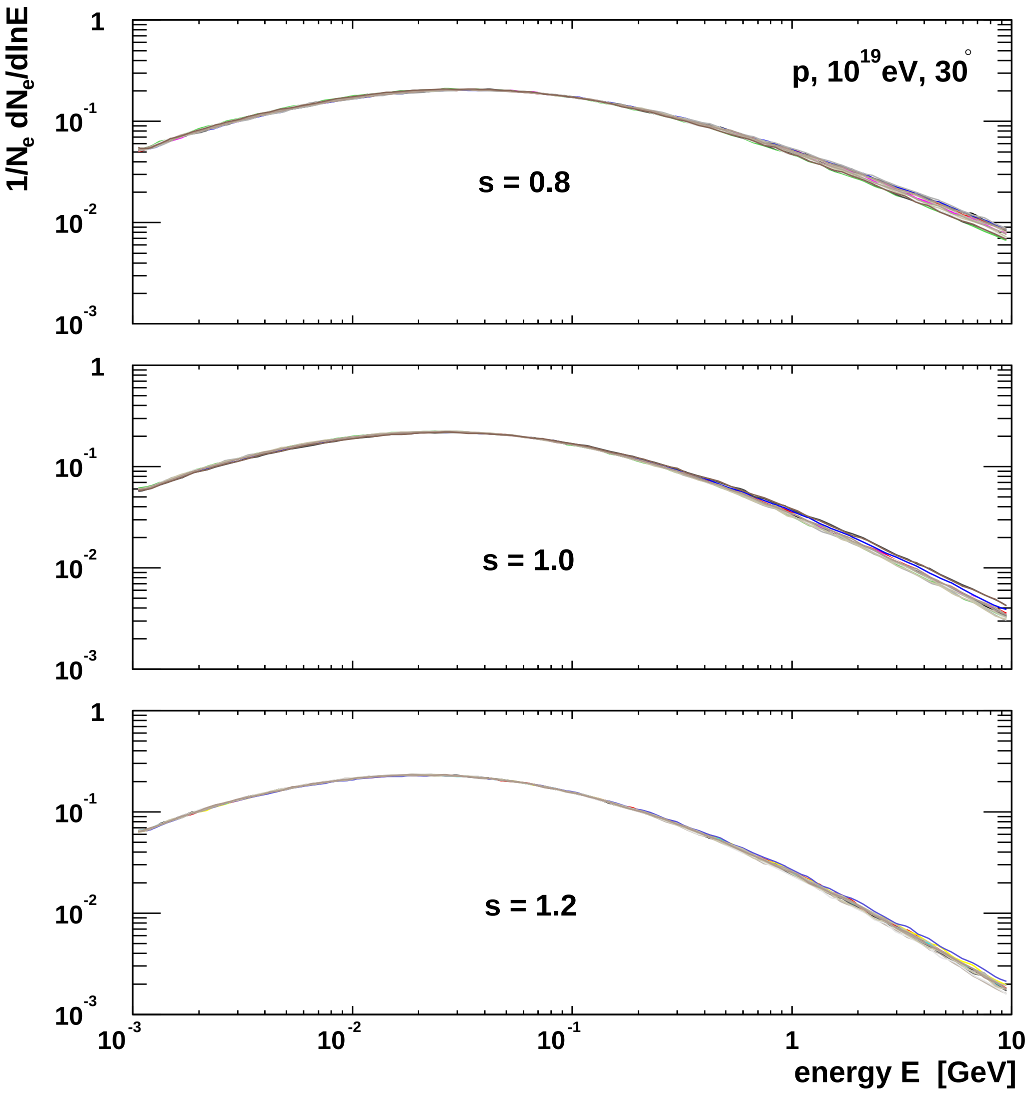

Figure 4.6: Electron energy spectra of individual showers of have been normalised according to Eq. (4.2) and interpolated in shower age according to Eq. (4.4). The resultant distributions of individual proton showers of 10^{19} eV are shown for three different shower ages $s = 0.8$, $s = 1.0$, and $s = 1.2$. For different primary energies (10^{18} eV, 10^{20} eV) and masses (iron, gamma-ray) the result is similar. The energy distributions of individual showers do not differ much in shower age. Increasing statistical fluctuations with decreasing particle number are expected due to thinning. Shower-to-shower fluctuations increase with increasing energy, c.f. Fig. 4.7.

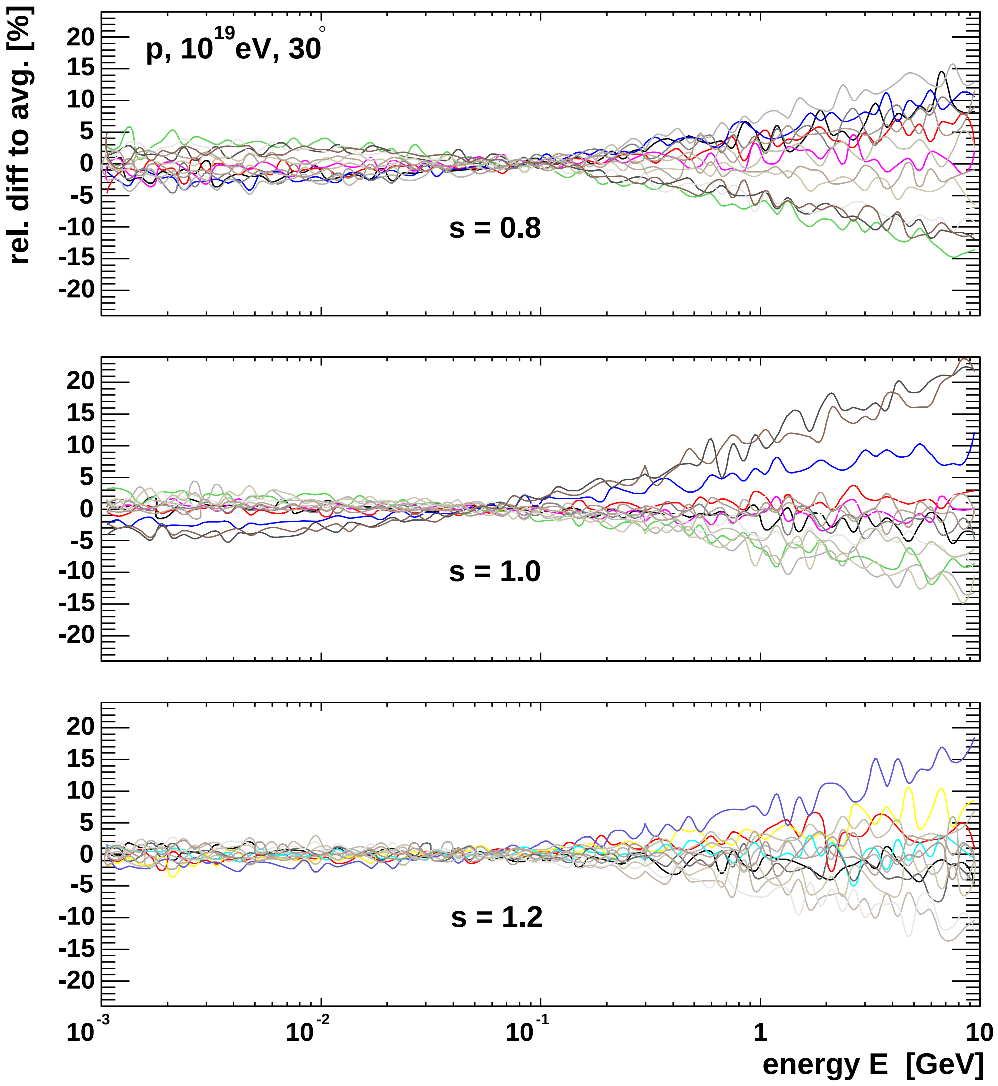

Figure 4.7: Shower-to-shower fluctuations of electron energy spectra (normalised according to Eq. (4.2)) are demonstrated for three different shower ages $s = 0.8$, $s = 1.0$, and $s = 1.2$. The relative differences of the electron energy spectra to the mean spectrum have been calculated by averaging the spectra of 15 proton showers (10^{19} eV). Up to 300-400 MeV (depending on shower age) fluctuations are smaller than about 5 %. Shower-to-shower fluctuations increase with increasing energy and amount up to 25 % at 10 GeV. For different primary energies (10^{18}, 10^{20} eV) and different primary particles (iron, gamma-ray), shower-to-shower fluctuations are of the same order, see Fig. A.3 - A.7.

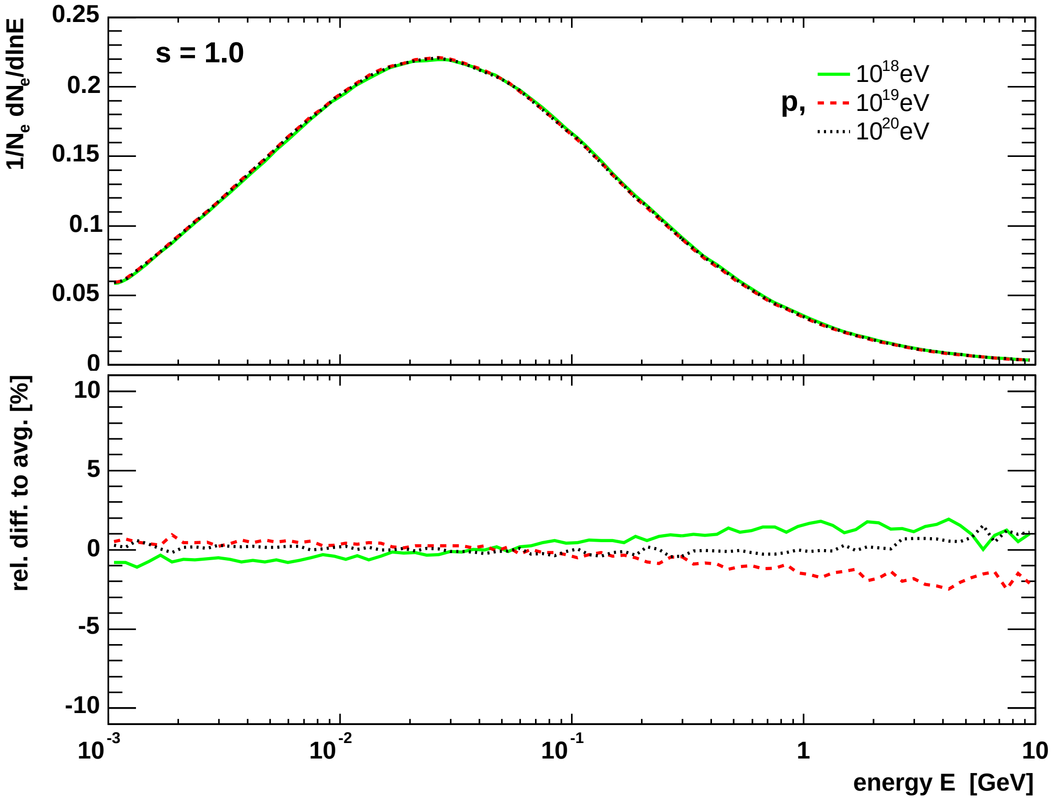

Figure 4.8: Universality of electron energy distributions for proton showers of different primary energy. Mean proton showers of $10^{18}, 10^{19}$ and 10^{20} eV do not show significant differences of their electron energy distributions in shower age, here shown for $s = 1.0$; for other shower ages see Fig. A.8 in Appendix A.

4.2.2 Universality

In the previous section it has been shown that - interpolated in shower age - electron energy distributions of individual showers of a certain primary particle and a certain primary energy fluctuate around the average comparably. In Fig. 4.8 the mean electron energy distribution of proton showers with different primary energies, namely $10^{18}, 10^{19}$ and 10^{20} eV, are compared. In shower age, apart from shower-to-shower fluctuations, proton showers of the highest energies do not differ significantly with respect to their electron energy distributions. The corresponding relative differences of mean electron distributions to the average are shown in the lower panel of Fig. 4.8. For shower ages between 0.8 and 1.2 and electron energies up to about 400 MeV deviations are on the 1 % level. For larger energies the relative differences to the average increase up to about 2 % at electron energies of 10 GeV.

For other primary particles, namely iron and gamma-rays, the same investigation is presented in Fig. 4.9. Here the result is similar, neither the mean iron nor the mean gamma-ray shower differ significantly from each other. The relative differences of the mean electron energy distributions in iron and gamma-ray showers of different primary energy to their average show the same tendencies and same order of magnitude of a few percent. Obviously the

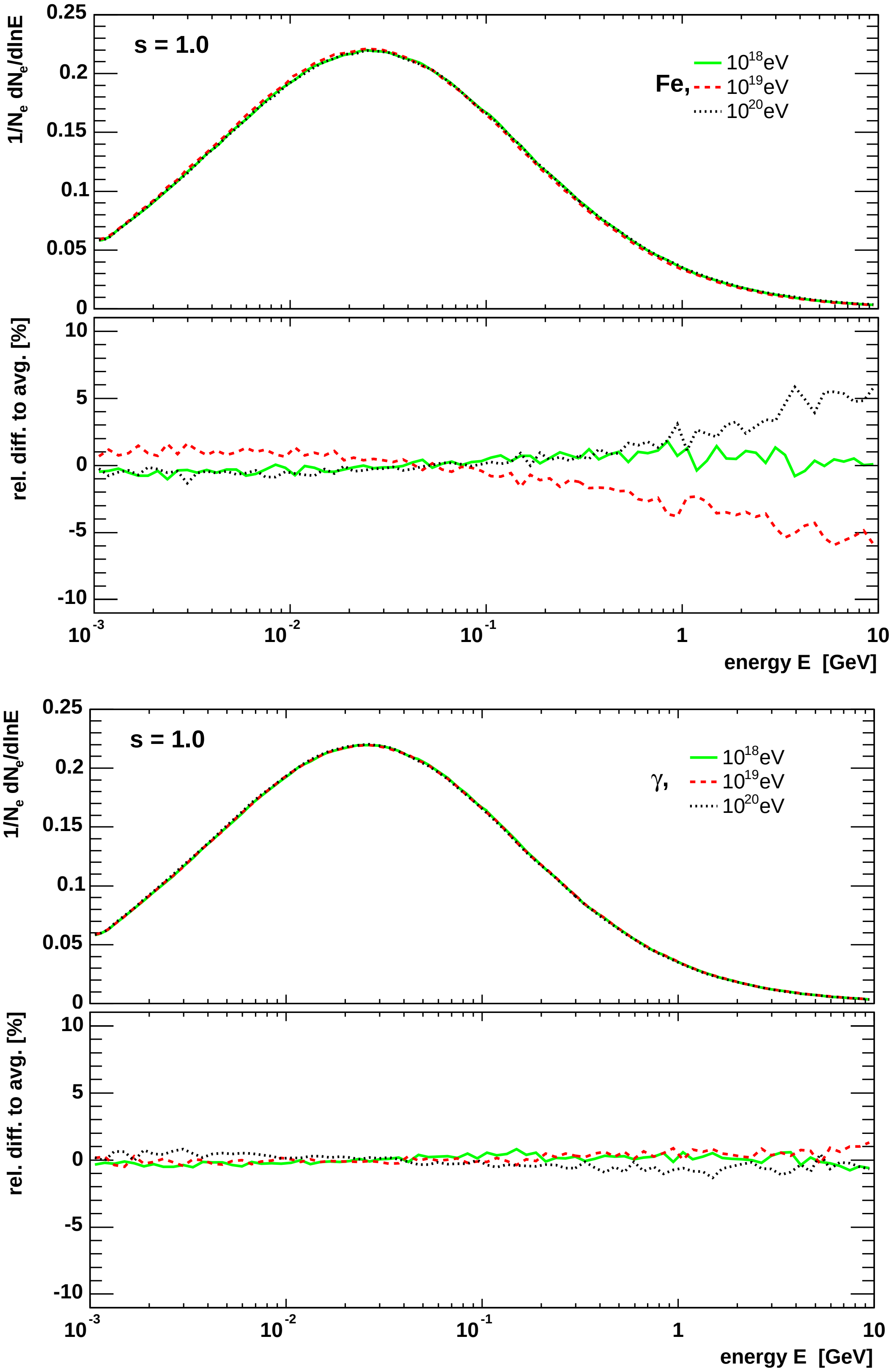

Figure 4.9: Universality of electron energy distributions for iron induced and gamma-ray showers of different primary energy (upper and lower panel respectively). Mean showers of $10^{18}, 10^{19}$ and $10^{20}/10^{19.5}$ eV do not show significant differences of their electron energy distributions in shower age, here shown for $s = 1.0$; for other shower ages see Fig. A.9 and Fig. A.10 in Appendix A.

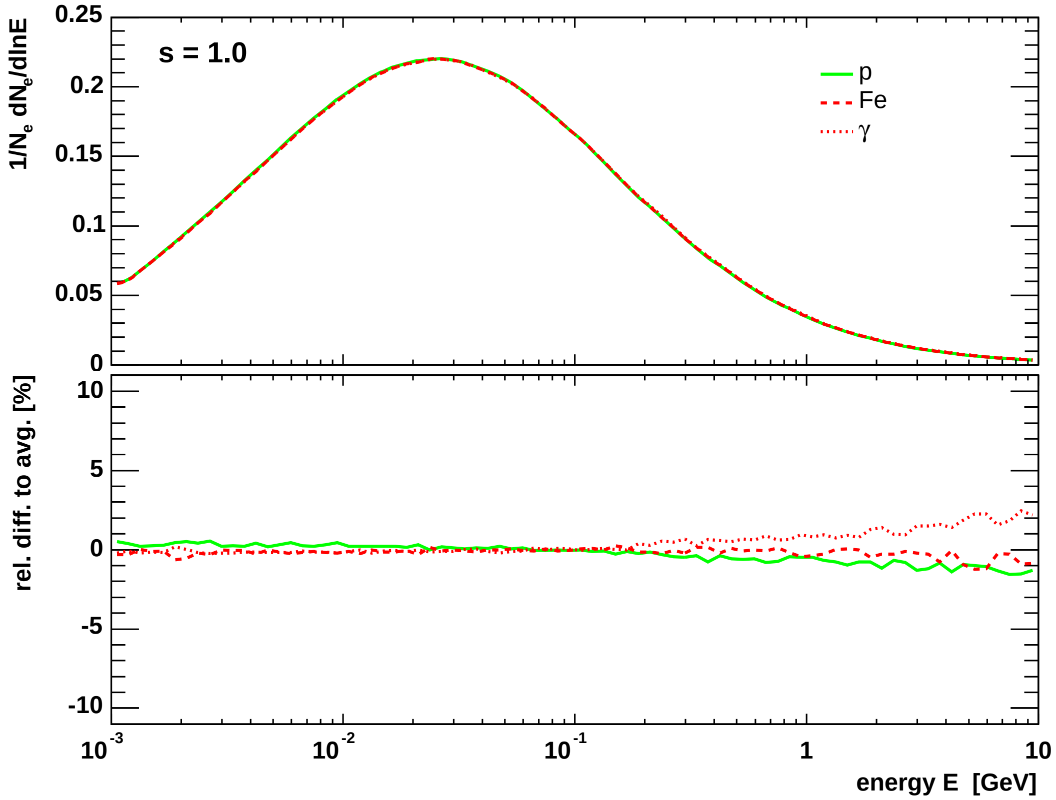

Figure 4.10: Universality of mean electron energy distributions in showers of different primary particles (averaged are the respective mean distributions of showers of 10^{18}, 10^{19}, and 10^{20} eV). Mean showers of proton, iron and gammas do not show significant differences of their electron energy distributions in shower age, here shown for $s = 1.0$; for other ages see Fig. 4.11 and Fig. 4.12 respectively.

deviations in the case of gamma-ray showers are smaller, which is expected since gamma-ray showers consist solely in an electromagnetic cascade and therefore have smaller intrinsical fluctuations[4]. Also for iron showers compared to proton showers one would expect less fluctuations, but the sample of iron showers for this comparison is relatively small compared to proton. Coming back to the larger deviations above 400 MeV, one finds relatively small particle densities in the GeVregion. The statistics are limited due to thinning in this energy region. That is the reason why the set of simulated showers of which the average has been build, might be too small in order to interprete discrepancies of the percent level.

In Fig. 4.10 the mean electron energy distributions of showers of different primary particles, namely proton, iron and gamma, now also averaged over the three different above-mentioned energies are compared at shower maximum. The relative differences to their averages are very small. In the low-energy region they are smaller than 0.5 % while above 400 MeV they increase up to about 2 % at 10 GeV.

For the younger and older showers shown in Fig. 4.11 and Fig. 4.12 respectively, the

---

[4] Since the hadronic interaction length is about 2.5 times the radiation length, and due to the fact that pure electromagnetic shower are not 're-feeded' from a hadronic cascade, gamma-ray showers fluctuate less.

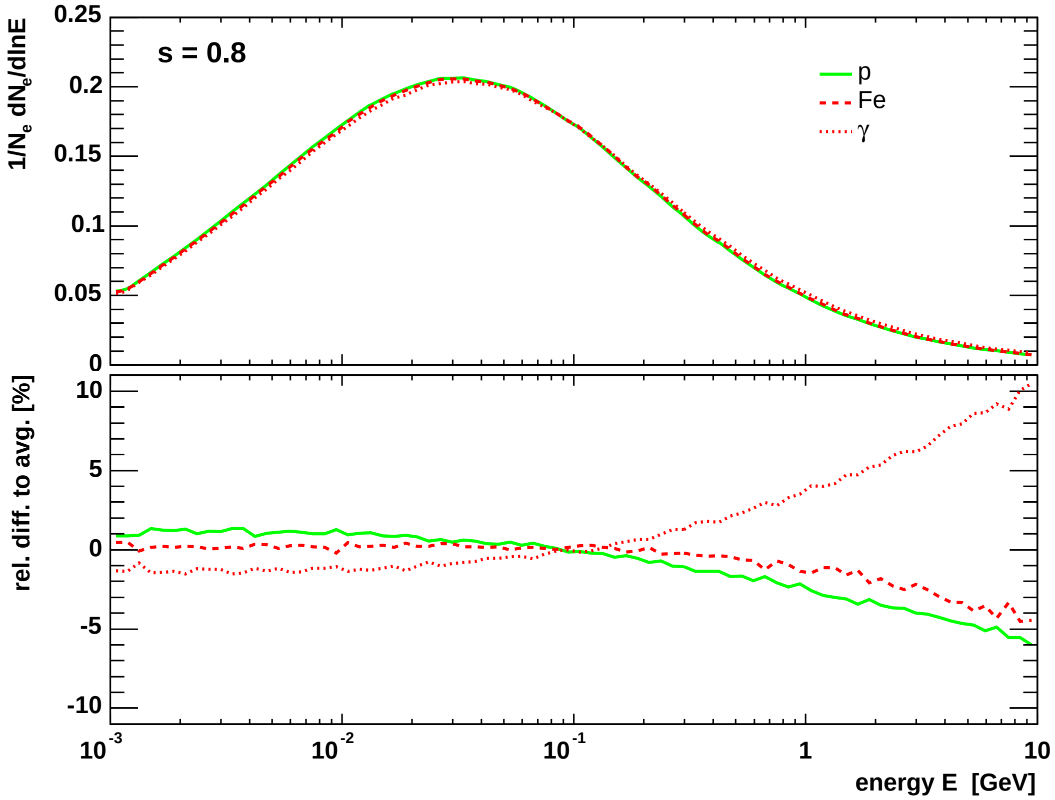

Figure 4.11: Universality of electron energy distributions in showers of different primary particles (averaged are the respective mean distributions of showers of 10^{18}, 10^{19}, and 10^{20} eV), here shown for $s = 0.8$. Mean showers of proton and iron do not show significant differences in their electron energy distributions in shower age, but purely electromagnetic do compared to hadronic ones. The average built is biased by the mean gamma-ray shower, see text for discussion. For other ages see Fig. 4.10 and Fig. 4.12 respectively.

deviations are larger compared to those at shower maximum (Fig. 4.10), but still in the order of 2 % up to 400 MeV. For increasing electron energies differences also increase up to about 5 % in the case of proton and iron, but up to about 10 % for the mean gamma-ray shower. This is the effect of averaging two hadron showers and one gamma shower. As already argued above, gamma-ray shower are quite different from hadronic ones, as they do not have a hadronic component, which 're-feeds' the electromagnetic cascade, and because the electromagnetic interaction length is much shorter. Therefore, already at all states of shower development all energy of the primary gamma-ray has gone to electromagnetic particles. More high-energetic electrons are expected as compared to a hadronic shower, where at early states a good fraction of the primary energy is still carried by hadrons.

This reason also holds for old showers but vice versa. Old gamma-ray showers are not 're-feeded' by a hadronic component and thus, one finds less electrons in the GeVregion. Iron showers also develop systematically different from proton showers. Differences might be expected due to higher hadronic cross-sections during first interactions, by which iron showers are developing faster than proton initiated ones. Subsequent to first interactions, also in a

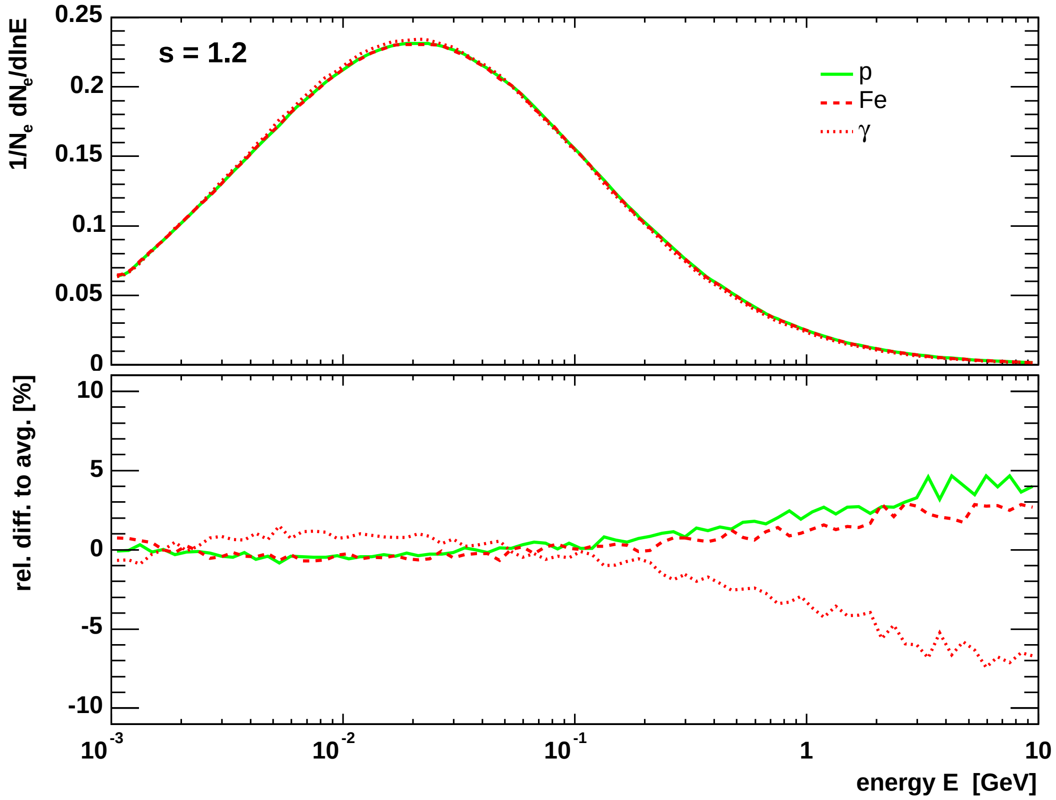

Figure 4.12: Universality of electron energy distributions in showers of different primary particles (averaged are the respective mean distributions of showers of 10^{18}, 10^{19}, and 10^{20} eV), here shown for $s = 1.2$. Mean showers of proton and iron do not show significant differences in their electron energy distributions in shower age, but purely electromagnetic do compared to hadronic ones. The average built is biased by the mean gamma-ray shower, see text for discussion. For other ages see Fig. 4.11 and Fig. 4.10 respectively.

iron induced shower one has free nucleons. This is the reason why actually the differences between iron and proton showers are smaller regarding both, in energy as well as in mass. Lastly the reference mean shower is biased by the gamma-ray showers. That is why gamma-ray showers have not been used for fitting the parameterisation of the angular distribution of produced Cherenkov photons, c.f. Chap. 5.

In conclusion, the spectral shape of electron energy distributions in air showers of the highest energies are in the considered energy range within a few percent universal in shower age. They do depend neither on primary energy nor on primary mass, see also [Nerling et al. 2003] and the independent work by [Giller et al. 2004]. Consequently, a parameterisation as a function of shower age, valid for a large range of primary energies and masses, is possible. A parameterisation in shower age for pure electromagnetic showers had already been introduced by [Hillas 1982]. A new parameterisation based on CORSIKA simulated showers of the highest energies is introduced next, applying this universality to describe both hadronic and electromagnetic showers.

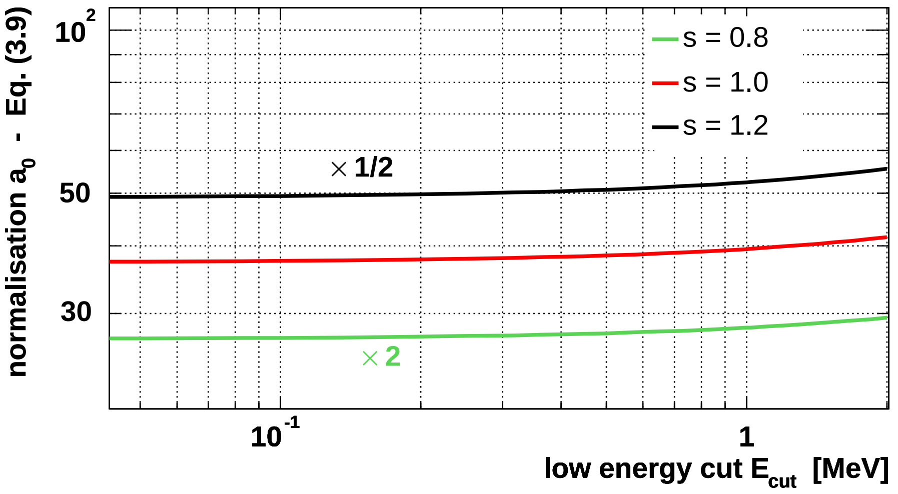

Figure 4.13: Normalisation of the parameterisation Eq. (4.7) of normalised electron energy spectra - dependence on low-energy cut, Eq. (4.9). The coefficient a_0 changes in dependence of the applied low-energy cut $E_{\rm cut}$. For the $E_{\rm cut}$-range considered changes can be as large as about 10 %.

4.2.3 Parameterisation

The new parameterisation introduced here, describing the CORSIKA simulated energy spectra, has been derived by the following simple functional form:

$$f(E,s) = \frac{E}{(E+a_1)(E+a_2)^s} \; . \tag{4.5}$$

This ansatz is motivated by the high energy limit of the energy behaviour of electrons in the cascade theory under approximation A [Rossi & Greisen 1941]:

$$\frac{\mathrm{d}N}{\mathrm{d}\ln E} \sim \frac{1}{E^{s+1}} \; . \tag{4.6}$$

In air shower simulation programs like CORSIKA one always uses a lower energy threshold $E_{\rm cut}$ for electrons (and photons), c.f. Sec. 4.1. Therefore, in applications like for example calculating the Cherenkov light for a simulated shower profile, one has to calculate a normalisation constant a_0 according to the threshold used in the corresponding shower simulation. The new parameterisation of the normalised electron energy spectrum proposed is [Nerling et al. 2003]:

$$\boxed{f_{\rm e}\;(E,s) \;=\; a_0 \;\cdot\; \frac{E}{(E+a_1)\;(E+a_2)^s}} \tag{4.7}$$

A mean electron energy distribution has been derived for each shower age state by averaging over numerous individual showers of different primary particles, namely proton, iron and gamma-ray, as well as the three different primary energies (for each primary mass), 10^{18}, 10^{19}, and 10^{20} eV, for which the universality of the electron energy distribution has been shown. By

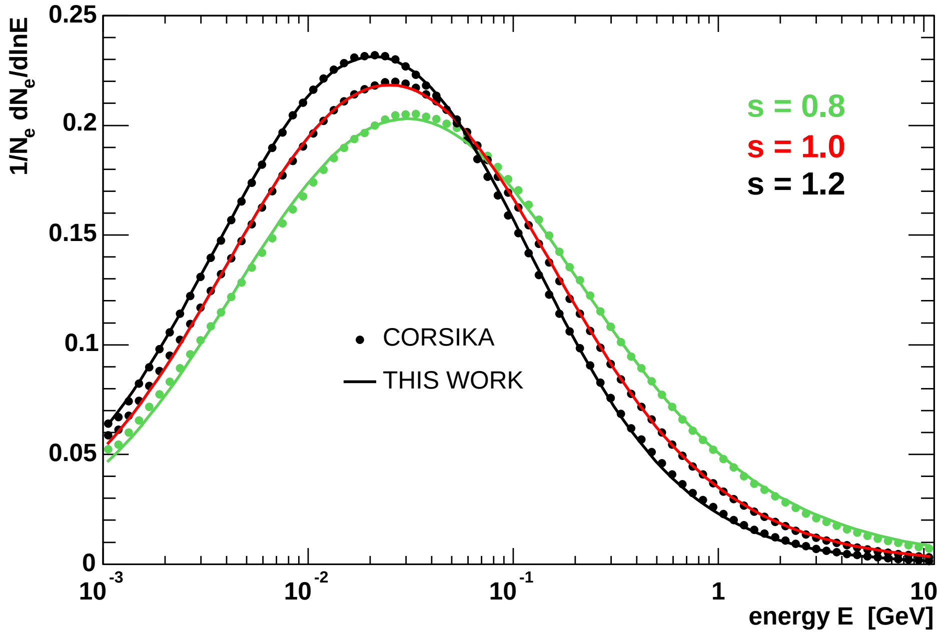

Figure 4.14: Description of Monte Carlo simulations by the proposed new parameterisation. The markers represent the CORSIKA result for an individual proton shower of 10^{19} eV and a zenith angle of 30° for three different shower ages. The straight lines represent the parameterisation (Eq. (4.7)), a good description over the whole range of 1 MeV up to 10 GeV is achieved.

minimising (4.5) to these average electron energy distributions in shower age s using MINUIT [James 1994], the parameters a_1 and a_2 of Eq. (4.7) have been derived for E in MeV:

$$\begin{aligned} a_1 &= 6.42522 - 1.53183 \cdot s \\ a_2 &= 168.168 - 42.1368 \cdot s \; , \quad (E \text{ in MeV}). \end{aligned} \tag{4.8}$$

The normalisation a_0 follows automatically through integration of (4.5) in $\ln E$ for each value of shower age s and a given low-energy cut E_{cut}:

$$\frac{1}{a_0} = \int_{\ln E_{\text{cut}}}^{\infty} f(E, s) \, \mathrm{d} \ln E \; . \tag{4.9}$$

The dependence of the normalisation a_0 on the low-energy cut (Eq. (4.9)) is displayed in Fig. 4.13 for three different shower ages. In the lower energy range well below about 500 keV, this dependence might be negligible, but for larger cut-offs, changes of the normalisation increase up to about 10 % in the energy cut range considered (50 keV - 2 MeV). Particularly with respect to calculations of Cherenkov light based on ansatz (3.18), but also for deriving energy deposit profiles in order to compute fluorescence light production, the normalisation a_0 is needed. Since the number of charged particles provided by the simulations refers only to the particles above the threshold E_{cut}, the dependence of the normalisation of f_{e} on E_{cut} is required to be consistent with the shower size profile. Neither the previous nor the other parameterisation, which are discussed and compared to the parameterisation (4.7) in the next section, take into account different low-energy cuts.

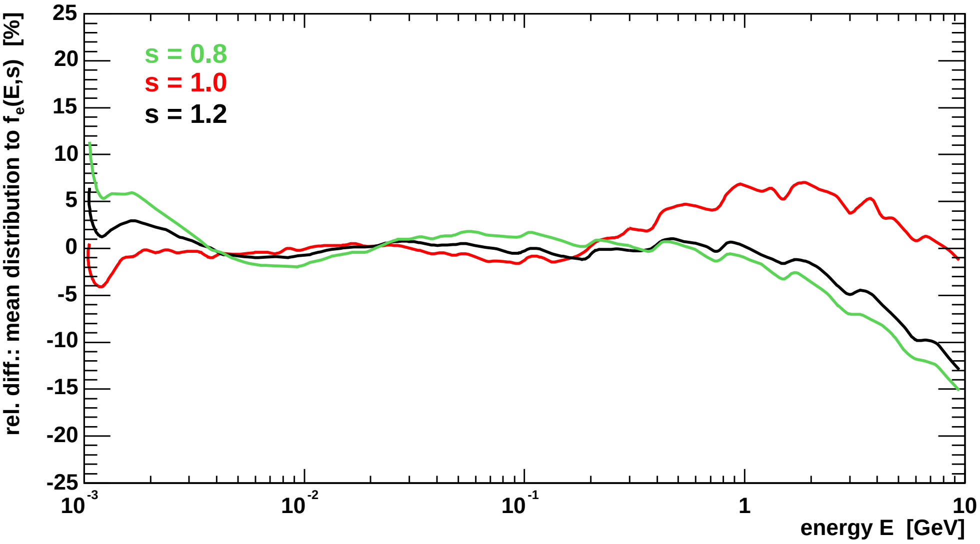

Figure 4.15: Relative differences between the mean normalised electron energy spectra and the new parameterisation (Eq. (4.7)) for different ages. Positive values correspond to an overestimation of the energy spectrum. A very good description is achieved in the range from a few MeV up to 1 GeV, where differences are well below 5 %. In the GeV-range deviations are increasing with energy up to 15 % at 10 GeV and $s = 0.8$.

The comparison of the parameterisation (4.7) with normalised electron energy distributions of an individual proton shower of 10^{19} eV derived from CORSIKA simulations is shown for three different shower ages in Fig. 4.14. As can be seen, using the s-dependence of a_1 and a_2 as given in (4.8) and the normalisation determined by (4.9), the simulated electron spectra are reproduced well over the whole range. In Fig. 4.15 the quality of the fit is shown for different shower ages. The deviations are well below 5 % in the range of a few MeV up to about 1 GeV. For electron energies in the GeV-range the differences are much larger, increasing with energy up to 15 %.

In Fig. 4.16 the quality of description of individual showers by the parameterisation (4.7) is shown. A good description is obtained for energies up to 1 GeV for all shower ages considered. For higher energies, differences increase up to about 25 %. Further, one rediscovers in this display the same systematic for a certain shower age as in Fig. 4.15. The relative differences according to individual showers fluctuate around zero in the order of shower-to-shower fluctuations similar to those shown and discussed in Sec. 4.2.1. Thus, the same accuracy of prediction is obtained for different primary energies and different primary masses.

However, given the fact that the parameterisation (4.7) is of quite simple functional form and is applied here over a wide energy range covering four orders of magnitude, the predicted energy distributions describe well the results of the CORSIKA simulations.

For Cherenkov calculations following ansatz (3.18) the energy region of primary interest is the MeV-range. Thus, for this purpose the already reached quality of description by the new approach (4.7) is absolutely satisfactory. This result is discussed in detail in Sec. 4.3, where the new parameterisation (4.7) is applied for the calculation of the longitudinal Cherenkov production.

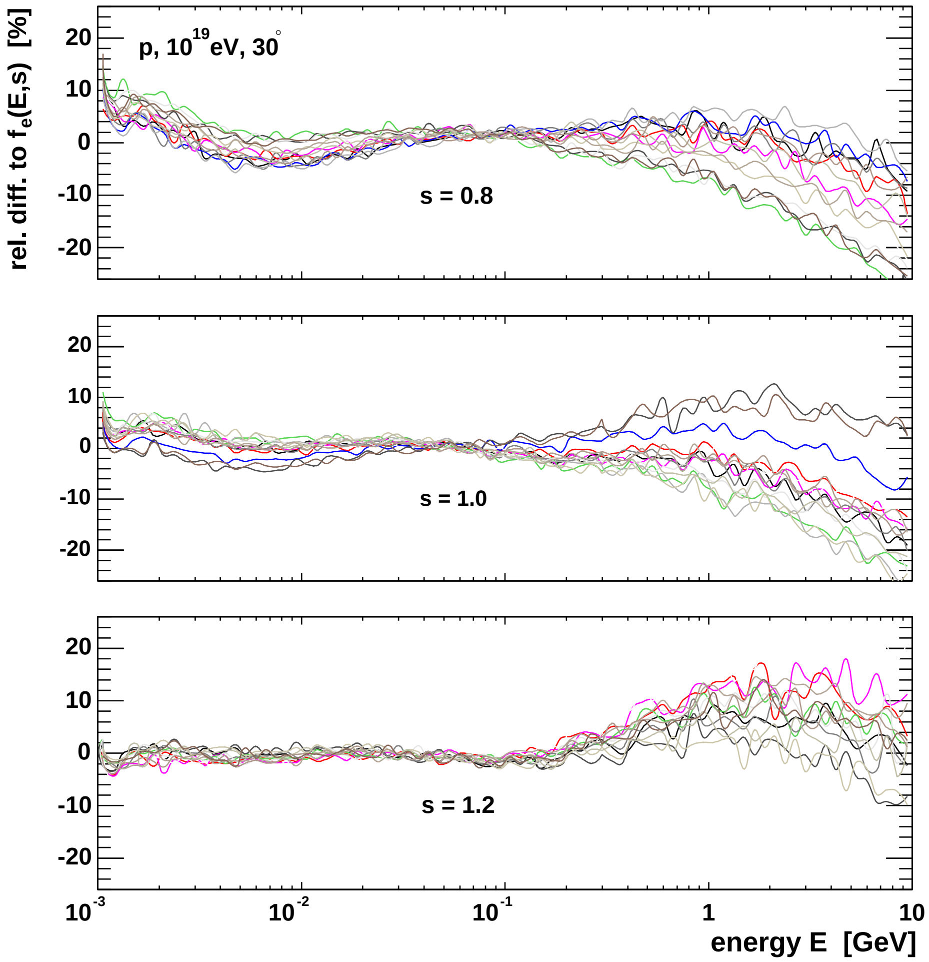

Figure 4.16: Relative differences between normalised electron energy spectra of individual showers and the new parameterisation (Eq. (4.7)) for different ages. Positive values correspond to an overestimation of the energy spectrum. The description achieved for all shower ages considered is better than a few percent for energies up to 1 GeV. For higher energies deviations increase up to 25 %. Systematic features in differences for each shower age are the same as in Fig. 4.15 and result from the quality of the fit. The fluctuations of individual showers with regard to the parameterisation are in the order of shower-to-shower fluctuations, c.f. Sec. 4.2.1. The same accuracy of prediction is achieved for different primary masses and energies.

The discrepancy above the MeV-range has still to be investigated and ansatz (4.7) is to be extended to larger energies. Especially for general applications in the form of fast hybrid simulation codes, the whole energy range is important. In such approaches the goal is to replace CPU consuming single particle tracking by such analytical descriptions. Ideas for extension as well as their physical motivations are discussed finally in the outlook in Chap. 7.

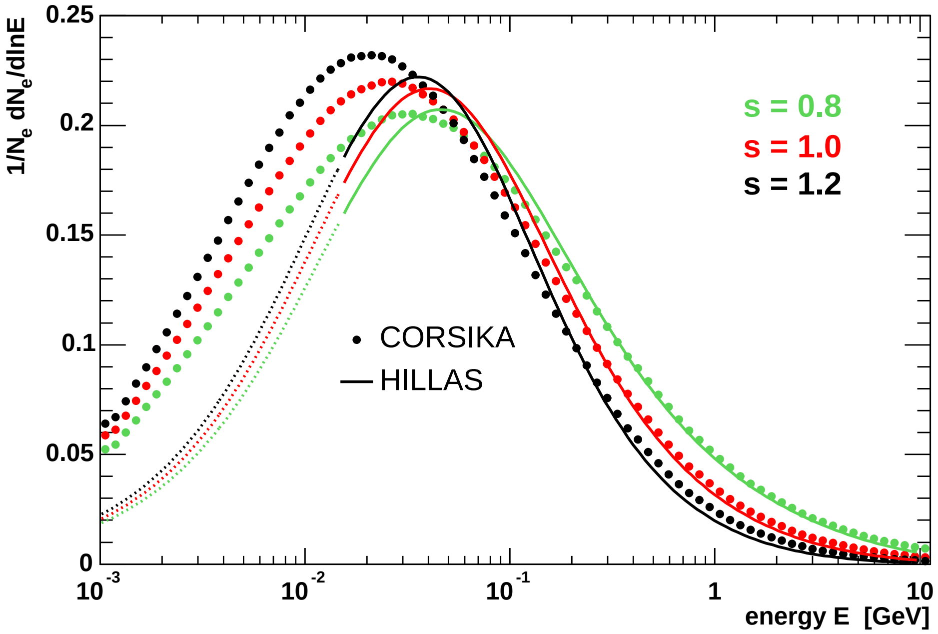

Figure 4.17: Comparison of Hillas' parameterisation [Hillas 1982] and simulated normalised electron energy spectra derived from CORSIKA. The parameterisation is plotted as dotted lines below 15 MeV, which is the lower validity limit given for this analytical description. The comparison is shown here for the same individual proton shower (10^{19} eV, 30°) as shown for the new parameterisation in Fig. 4.14.

4.2.4 Comparison with other Parameterisations

A parameterisation of the normalised integral electron energy spectrum, depending only on the shower age, was provided by Hillas based on 100 GeV photon shower simulations using a low-energy particle cut-off of 50 keV [Hillas 1982]. Traditionally this approximation is used to calculate the Cherenkov contamination of fluorescence light signals from high-energy showers, as for example by HiRes/Fly's Eye [Baltrusaitis et al. 1985, Abu-Zayyad et al. 2001].

In Fig. 4.17 electron distributions obtained by this historical parameterisation are compared to the CORSIKA results for different shower ages. Given the fact that this parameterisation was obtained for low-energy primary photons, a larger disagreement above energies of 15 MeV, which is the lower validity limit given in [Hillas 1982], might have been expected.

Another analytical form for the normalised differential electron energy spectra has been developed independently from this work by Giller et al. [Giller et al. 2003, Giller et al. 2004]. The parameterisation proposed by the Lodz group is [Giller et al. 2004]:

$$\frac{1}{N_e}\frac{\mathrm{d}N}{\mathrm{d}\ln E} = C(s)\cdot\left[1 - a\cdot\exp\left(-d(s)\frac{E}{E_{cr}}\right)\right]\left(1+\frac{E}{E_c}\right)^{-[s+b\cdot\ln(\frac{E}{cE_c})]} , \tag{4.10}$$

where E_c is the critical energy, see Sec. 2.1.2, and $a = 1.005$, $b = 0.06$, $c = 189$, $d(s) = 7.06s+12.48$, and $C(s) = 0.111\cdot s+0.134$ in the region $0.7 \leq s \leq 1.3$. Note that the parameter values are different in [Giller et al. 2003] and [Giller et al. 2004]. Moreover, another set of parameters for Eq. (4.10) has been announced within the Auger Collaboration [Giller 2004]:

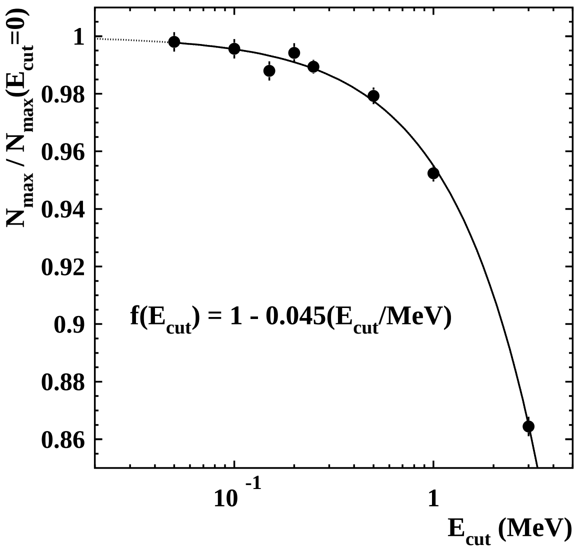

Figure 4.18: Dependence of shower size at maximum on simulation energy threshold. The ratio of the mean shower size at shower maximum N_{max} to that extrapolated to $E_{cut} = 0$ is shown for different simulation thresholds. For the E_{cut}-range considered, differences in N_{max} can reach up to about 10 %. A parameterisation of this ratio as a function of E_{cut} is given. ([Risse et al. 2001])

$a = 1.017$, $b = 0.0735$, $c = 356$, $d(s) = 6.159s + 9.954$ and $C(s) = 0.109 \cdot s + 0.135$, which is considered in addition.

As pointed out in the previous section, the dependence of the normalisation of such a parameterisation on a low-energy cut is not negligible. Especially for calculations of Cherenkov light based on ansatz (3.18), the dependence of the normalisation is needed, to be consistent with the shower size profile provided by the simulation. The Hillas as well as the Giller et al. approaches neglect this E_{cut} dependence. Whereas Hillas gives 50 keV as low energy cut, the parameterisation of Giller et al. is claimed to be valid for $E_{cut} = 0$. For typical values of low-energy cuts applied in simulations, the change of the proper normalisation can be up to about 10 %, see Fig. 4.13. Therefore, and since the energy threshold used in the simulations for the Giller et al. fits are not known, there is some ambiguity in the comparison that will be shown. In the following, the parameterisations of Hillas and Giller et al. are normalised the same way as the newly developed parameterisation, see Eq. (4.9). In the case of the integral distribution provided by Hillas, CORSIKA simulated electron spectra have to be renormalised in order to compare properly. This renormalisation is done according to the dependence of shower particle content on simulation energy threshold, as displayed in Fig. 4.18.

Therefore, in order to take into account differences in low-energy particle cut-offs, the Hillas approach F_{Hillas} is compared after renormalisation to F'_{Hillas} as given by [Risse et al. 2001]

$$F'_{\mathrm{Hillas}} = F_{\mathrm{Hillas}} \cdot \frac{1}{1 - 0.045(E_{cut}/\,\mathrm{MeV})}\,, \tag{4.11}$$

where E_{cut} is the respective low-energy cut-off used in the simulations. Wherever a low-energy cut-off different from 50 keV has been applied in the CORSIKA simulations, this renormalisation is done for comparisons with Hillas' approach throughout the presented work.

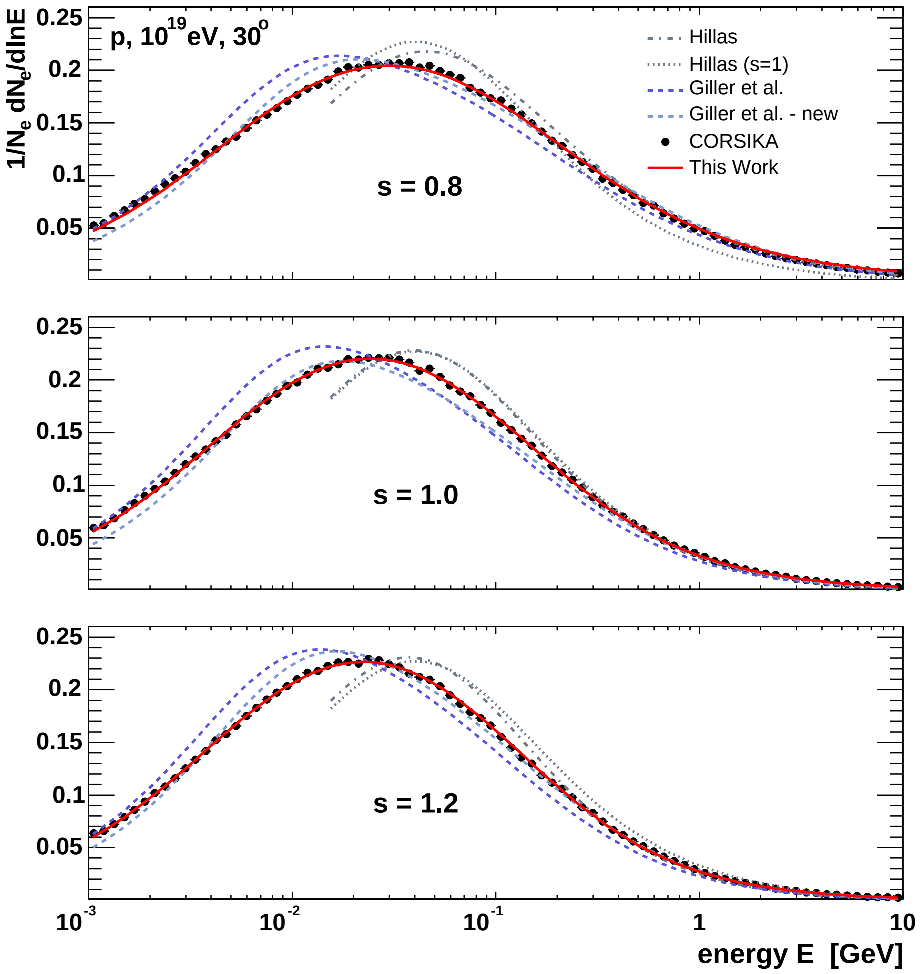

Figure 4.19: Comparison of different parameterisations of normalised electron energy spectra with respect to CORSIKA, $E_{\mathrm{cut}} = 1$ MeV. The different approaches are marked by dashed-dotted lines for [Hillas 1982] and dotted lines for its simplification like used by the HiRes/Fly's Eye collaboration [Baltrusaitis et al. 1985, Abu-Zayyad et al. 2001], dashed lines for [Giller et al. 2004, Giller 2004], and straight lines for [Nerling et al. 2003], whereas the Monte Carlo result is given by the markers. The approach provided by Hillas is only plotted above its lower validity limit. The comparison is shown here for an individual proton shower (10^{19}eV, $30°$) for three different shower ages. The result is similar for different primary masses, energies and zenith angles, see Fig. A.11 - A.26 in Appendix A.

In the following the parameterisations of all three authors, namely Hillas [Hillas 1982], Giller et al. [Giller et al. 2004, Giller 2004] and this work are compared with CORSIKA predictions. In the case of Hillas, a simplified application of the parameterisation is shown additionally. This simplification in the form of using only the electron energy distribution for $s = 1$ over the whole range of shower development has been applied by the HiRes/Fly's Eye collaboration [Baltrusaitis et al. 1985, Abu-Zayyad et al. 2001] and therefore also might be of interest. For the other approach, the set of parameters published in [Giller et al. 2004] is denoted as "Giller et al." and their revised parameters as "Giller et al. - new".

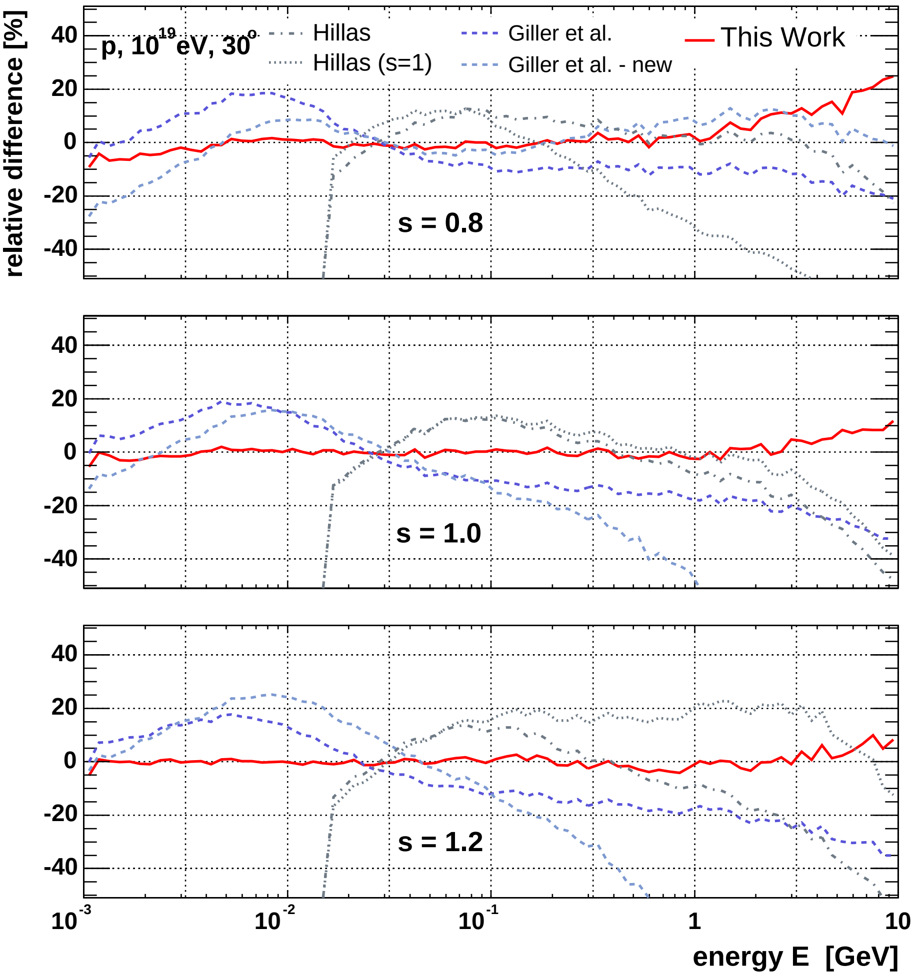

Figure 4.20: Comparison of relative differences of different parameterisations of the electron energy distribution with respect to CORSIKA. Positive values correspond to an overestimation of the simulated energy spectrum. The different approaches are marked by dashed-dotted lines for [Hillas 1982] and dotted lines for its simplification as it is used by the HiRes/Fly's Eye collaboration [Baltrusaitis et al. 1985, Abu-Zayyad et al. 2001], dashed lines for [Giller et al. 2004, Giller 2004], and straight lines for [Nerling et al. 2003]. For the approach provided by Hillas, the relative differences are only plotted above the lower validity limit. The comparison is shown here for an individual proton shower of 10^{19}eV and a zenith angle of 30°, and for three different shower ages, for discussion see text. The result is similar for different primary masses, energies and zenith angles, see Appendix A.

The different normalised electron energy distributions are displayed for three different shower ages in Fig. 4.19. The analytically calculated predictions are represented by lines, the distributions derived from CORSIKA are given by markers. The dotted and dashed dotted lines respectively representing Hillas' parameterisation are only compared above the lower validity limit of 15 MeV. As can bee seen, the predicted maxima of the distributions differ by about 50 % (20 %) in the case of Giller et al. (Giller et al.-new) and by about 40 % for Hillas respectively at shower maximum from the CORSIKA predictions. The parameterisation proposed in this work gives a very good overall description of the CORSIKA results.

In Fig. 4.20 the respective over- and underestimations versus the electron's energy are illustrated. There, the relative differences of the different approaches with respect to CORSIKA are shown for the same levels of shower development. In the range of a few MeV up to about 30 MeV the Giller approach over-estimates the Monte Carlo result by up to 20 %, whereas it tends to underestimate above 30 MeV (accepting the case of using their improved set of parameters for $s = 0.8$). The underestimation for higher energies is in the order of up to 25 % increasing with electron energies using the published set of parameters, whereas their new set of parameters leeds to even larger inaccuracies at shower maximum and beyond. The work of Hillas going back to 1982 predicts too few electrons below approximately 30 MeV. The relative differences reaches 10 % at the validity limit of 15 MeV. It then overestimates the Monte Carlo predictions by up to 15 % for particle energies close to 300 MeV, whereas beyond underestimation increasing with energy takes place by up to about 50 %. The ansatz of this work predicts the CORSIKA results within a few percent for the whole MeV-range, whereas uncertainties increase beyond a few GeV up to about 10 % at shower maximum and beyond.

In conclusion, a significant improvement in the description of 20 % over the whole energy range is achieved if the parameterisation (Eq. (4.7)) developed in this dissertation is used. In what extent this new parameterisation of normalised electron energy spectra improves the accuracy in calculating the total number of Cherenkov photons produced in extensive air showers, is discussed in the next section.

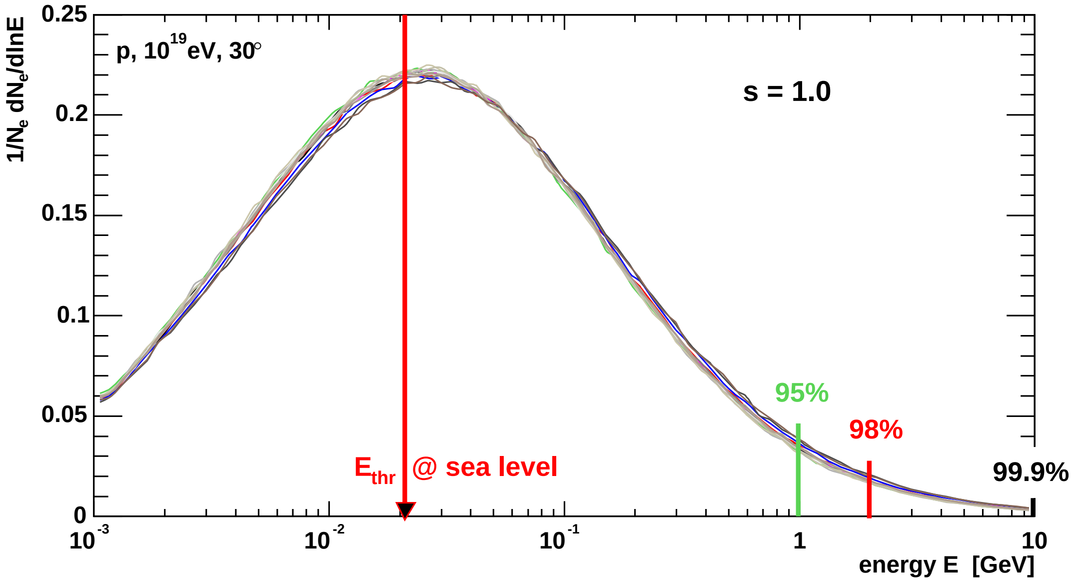

Figure 4.21: Electron energy distributions of interpolated proton showers. The energy region of interest for Cherenkov calculation is marked. At sea level the Cherenkov production threshold energy amounts $E_{\mathrm{thr}} = 22$ MeV (US-Std.Atm.), c.f. Fig. 3.4 and Fig. 3.5 respectively. Between E_{thr} and 1 GeV one finds 95 % of electrons producing Cherenkov photons, up to 2 GeV 98 % and in order to take into account more than 99 % of the contributing particles, the spectrum up to 10 GeV is important.

4.3 Calculation of the Total Number of Produced Cherenkov Photons

For calculating analytically the total number of Cherenkov photons produced per slant depth in extensive air showers following ansatz 3.14, a parameterisation of the normalised electron energy distribution has to be applied. In the following, the new parameterisation Eq. (4.7) is applied for this calculation and the result is compared to the Monte Carlo calculation. In addition, the accuracy of predictions of longitudinal Cherenkov photon production with respect to CORSIKA is compared to applying both further approaches.

4.3.1 Electron Energy Region of Interest for Cherenkov Calculations

As discussed in Chap. 3, electrons in extensive air showers emit Cherenkov photons only at energies above the threshold E_{thr}, which is a function of the refractive index in air. Since in general older stages of shower development take place in denser atmospheric layers, this threshold decreases with increasing shower age. Assuming the mean shower E_{thr} is about 30 MeV for shower age $s = 0.8$ and goes down to 25 MeV ($s = 1.0$), 24 MeV ($s = 1.2$) and finally 22 MeV at sea level, c.f. Fig. 3.4 and Fig. 3.5 respectively. This implies that for Cherenkov applications the energy region above 20 MeV is most important. Furthermore, the electron energy distribution decreases in the high energy region. Since the amount of

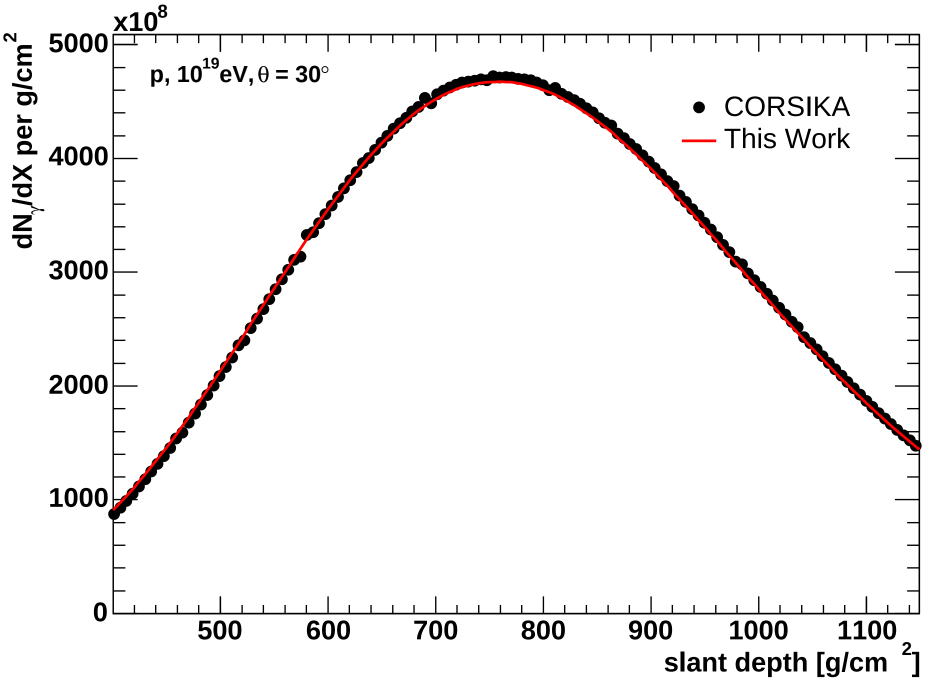

Figure 4.22: Total number of Cherenkov photons produced per slant depth within an individual extensive air showers simulated with CORSIKA and analytically calculated by ansatz (3.14). For the analytical prediction the new parameterisation of electron energy distributions Eq. (4.7) is applied. The accuracy of prediction based on (3.14) utilising (4.7) compared to the Monte Carlo simulations is better than 2 %.

produced Cherenkov photons depends on particle number, the high energy region does not contribute much to the Cherenkov production. Relative to all electrons above E_{thr}, 95 % of the electrons have energies $< 1\,\mathrm{GeV}$ at sea level (90 % at altitudes where the mean shower reaches $s = 0.8$).

In order to take into account 98 % of all electrons above the energy threshold one has to integrate Eq. (3.14) up to 2 GeV, and integrating up to 10 GeV delivers 99.9 %, see Fig. 4.21 Thus for calculating the total number of Cherenkov photons produced by air showers using ansatz Eq. (3.14), not the complete electron energy distribution is needed. The region from 20-30 MeV up to 10 GeV is most important, whereas the large range of 1-10 GeV contains only roughly 5 % of the electrons to be considered.

4.3.2 Comparison with Monte Carlo Simulations

Since Eq. (4.7) predicts the normalised electron energy distributions compared with the Monte Carlo within a few percent in the energy region of interest, it should be sufficiently applicable for computations following ansatz (3.14). In Fig. 4.22 the result of this analytical calculation for an individual shower and the according photon profile derived from simulations is illustrated. In the case of the analytical approach, the number of charged particles as a function of slant depths is provided by CORSIKA. Using the approach presented in this work, the total number of produced photons are predicted within 2 %. For different primary masses,

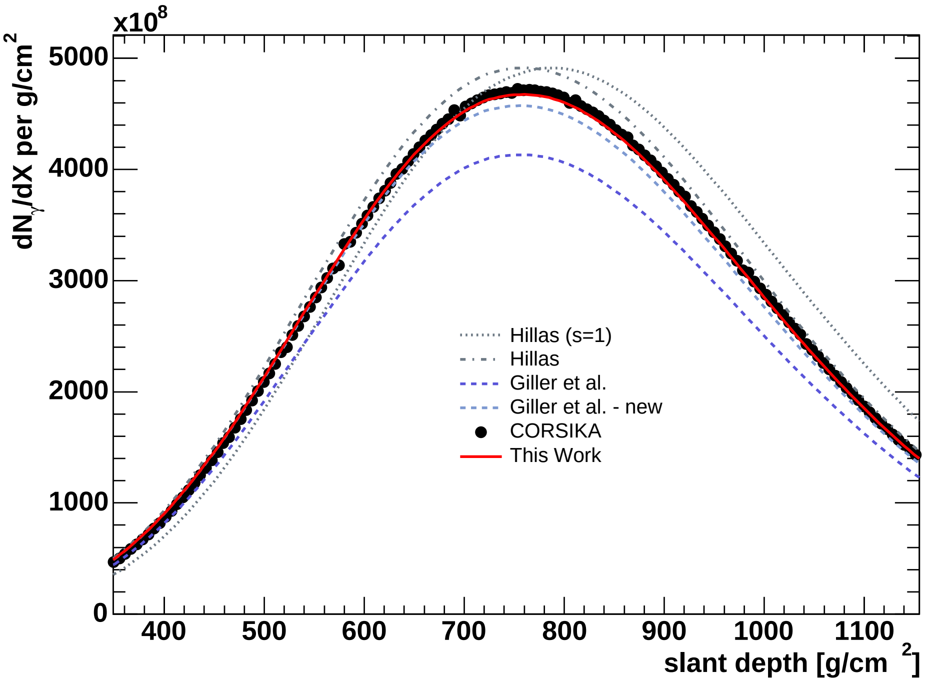

Figure 4.23: Comparison of total number of Cherenkov photons produced per slant depth within an individual extensive air showers simulated with CORSIKA and analytically calculated by ansatz (3.14) using different parameterisations of electron energy distributions. The different approaches are marked by dashed-dotted lines for [Hillas 1982] and dotted lines for its simplification as it is used by the HiRes/Fly's Eye collaboration [Baltrusaitis et al. 1985, Abu-Zayyad et al. 2001], dashed lines for [Giller et al. 2004, Giller 2004], and straight lines for [Nerling et al. 2003]. The comparison is shown here for an individual proton shower (10^{19}eV, 30°) for three shower ages, for discussion see text. The result is similar for different primary masses, energies and zenith angles.

primary energies and zenith angles the accuracy of prediction is similar, see Fig. A.27 and Fig. A.28 in Appendix A.

4.3.3 Comparison with other parameterisations

In Sec. 4.2.4 three different parameterisations of the normalised electron energy distribution in extensive air showers have been presented and their accuracies of description of Monte Carlo simulated spectra using CORSIKA have been compared. In Fig. 4.23 the total numbers of produced Cherenkov photons versus slant depth calculated based on ansatz (3.14) using these different approaches are displayed as well as the CORSIKA result.

The utilisation of a simplified Hillas parameterisation, noted by 'Hillas s=1', which has been used by the HiRes/Fly's Eye collaboration [Abu-Zayyad et al. 2001], results in a shift of the predicted profile maximum by about 40 g/cm^2 for the individual proton shower shown. This affect is due to the simplification in terms of neglecting the shower age dependence, namely they assume the shape of electron energy distribution at shower maximum for all stages of shower development, see Fig. 4.20. Thus, when taking into account also the age

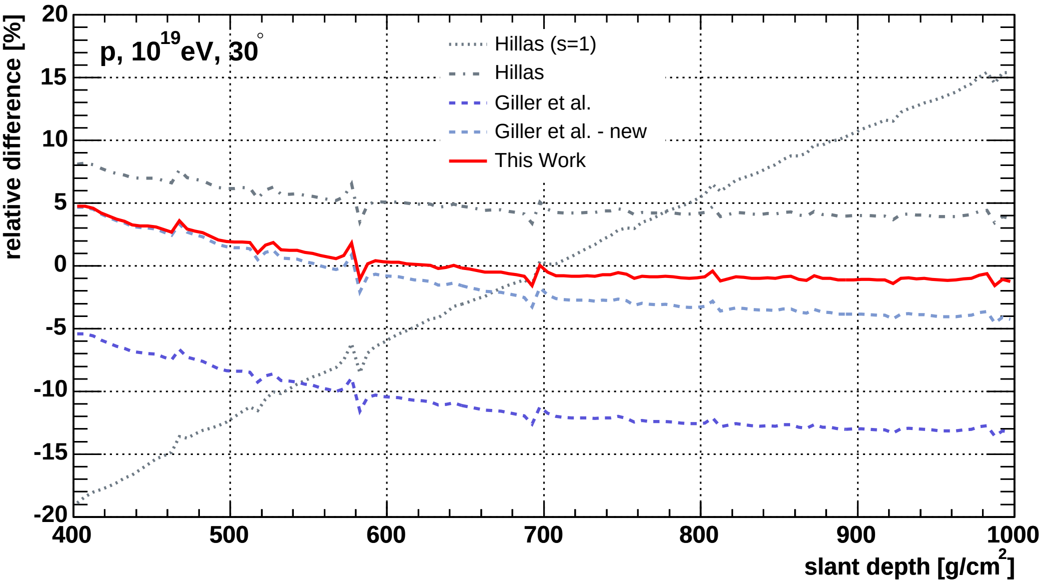

Figure 4.24: Comparison of relative differences in total number of Cherenkov photons produced per slant depth within an individual extensive air showers simulated with CORSIKA and analytically calculated by ansatz (3.14) using different parameterisations of electron energy distributions. The different approaches are marked by dashed-dotted lines for [Hillas 1982] and dotted lines for its simplification like used by the HiRes/Fly's Eye collaboration [Baltrusaitis et al. 1985], dashed lines for [Giller et al. 2004, Giller 2004], and straight lines for [Nerling et al. 2003]. For the approach provided by Hillas, the relative differences are only plotted above the lower validity limit. The comparison is shown here for the same individual proton shower (10^{19}eV, 30°) as considered in Fig. 4.23, and for three different shower ages, for discussion see text. The result is similar for different primary masses, energies and zenith angles, see Appendix A.

dependence of shower size and the change of the energy threshold for Cherenkov production with altitude, this simplification results in an under-estimation of Cherenkov photons produced for the younger shower, but an over-estimation beyond the shower maximum, see Fig. 4.24.

There, the relative differences, with respect to CORSIKA, of calculated longitudinal photon profiles under application of all different approaches considered are presented. Using Hillas' approach results in a slight over-estimation of produced photons over the whole shown slant depth range by roughly 5 %, whereas the analytical calculation proposed by Giller et al. implicates an under-estimation of up to about 10 %. Their new set of parameters improves the prediction of Cherenkov photons strongly regarding the published ones over the whole shower development. However, compared to the previous parameterisation provided by Hillas, using the analytical form proposed by Giller et al., the prediction of produced Cherenkov photons is improved for the young shower, but not that much beyond the shower maximum.

In conclusion, it is amazing how well the number of produced Cherenkov photons is described by [Hillas 1982] compared to the CORSIKA result, even though the small deviations of about 5 % turns out to be achieved somehow by chance, since over- and under-estimations of electron spectra above the Cherenkov threshold seems to cancel out.

Compared to this previous approach, an improvement of up to 5 % for stages of shower development before the shower maximum is achieved when applying 'Giller et al. - new' [Giller et al. 2004, Giller 2004].

In the case of utilising the work presented here [Nerling et al. 2003], the photon profile is predicted in agreement to the Monte Carlo simulations within 2 % for the whole range of shower age around the shower maximum. This is the range of interest for applying the fluorescence technique, like e.g. the Pierre Auger Observatory. In comparison to the previous work by Hillas the accuracy of prediction is graded by about 5 % when using the new approach.

Chapter 5

Parameterisation of the Angular Distribution of Cherenkov Photons

In Chap. 3 it has been pointed out that, for determining the Cherenkov contribution to correct light profiles measured using the fluorescence technique, the angular distribution regarding the shower axis is mandatory. In this chapter a new parameterisation based on CORSIKA simulations is introduced. This parameterisation takes into account two dependencies, namely on the refractive index and on the shower age.

5.1 Monte Carlo Simulations

The CORSIKA program is used to derive Cherenkov photon angular distributions at different atmospheric depth levels for showers of various primary properties. The applied options and corresponding settings used are the same as described in Sec. 4.1. Unless otherwise noted, an optimised thinning of 10^{-6} is chosen and as low energy cuts 100 MeV for hadrons and muons, and 1 MeV for electrons and gamma-rays are applied. The Cherenkov photon spectra derived in this manner are displayed for different slant depth levels in the upper panel of Fig. 5.1. In the lower panel of Fig. 5.1 the same spectra of this individual shower are plotted again, but here they are normalised to one photon. In the following such normalised distributions are investigated in order to find a appropriate analytical description of (3.16) in dependence on the stage of shower development.

5.2 Dependence on Refractive Index

The angular distribution of Cherenkov photons with respect to the shower axis is derived by convoluting the angular distribution of underlying electrons with the Cherenkov angle $\theta_{\check{C}}$, which is the angle with respect to the emitting charged particle's trajectory given by Eq. (3.2). In Fig. 5.2 normalised photon angular distributions of an individual shower are displayed for three different heights.

The angular distributions of the underlying electrons are mostly determined by Coulomb scattering (single, plural and multiple scattering). The corresponding cross-sections depend

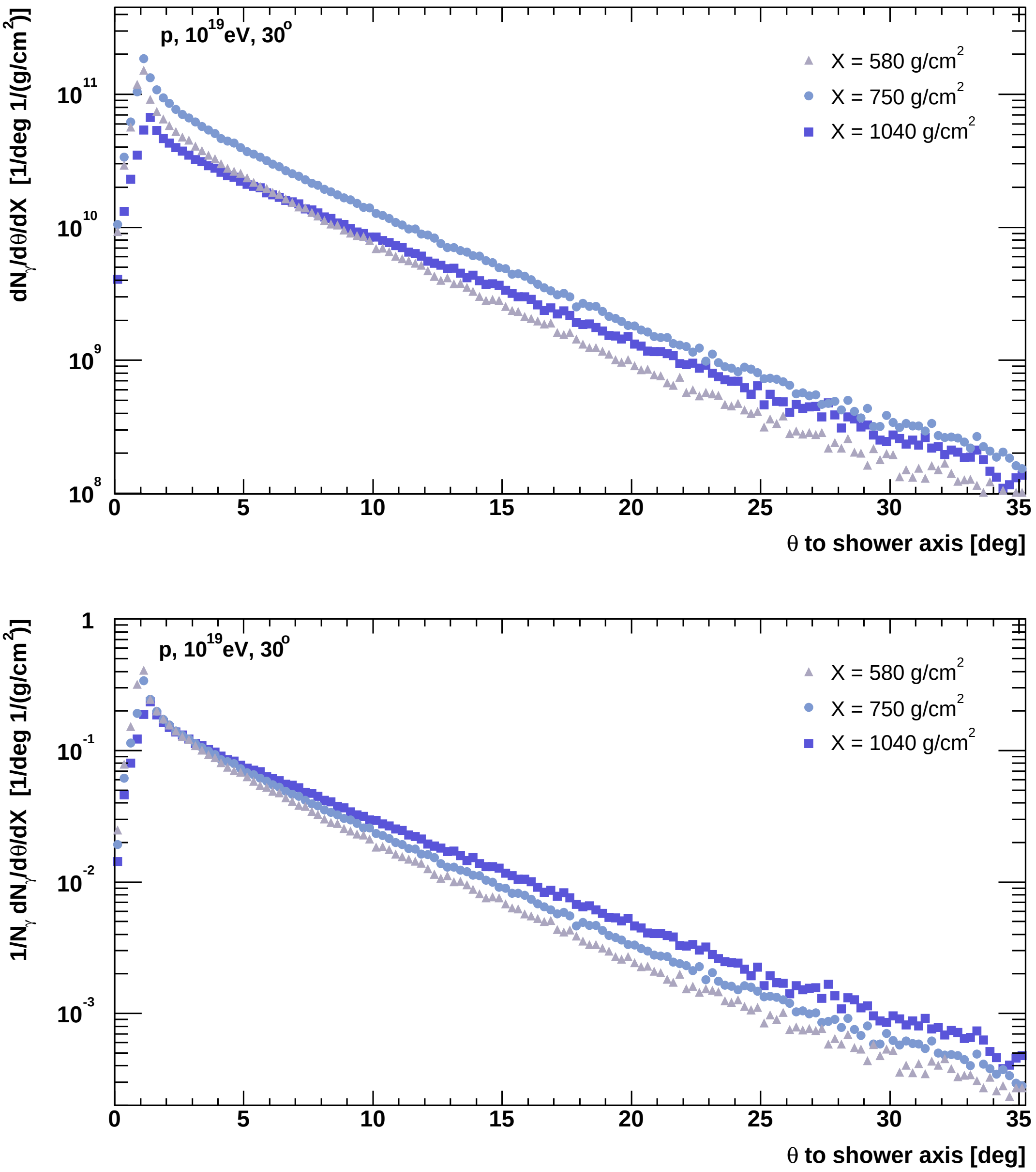

Figure 5.1: Simulated angular spectra of produced Cherenkov photons at three different slant depths of an individual proton shower (10^{19} eV, $30°$ inclination). Upper panel: The photon number is correlated with shower size, since the number of produced Cherenkov photons is proportional to particle number, c.f. Chap. 3. Lower panel: The same spectra as in the upper panel have been normalised to one photon. With ongoing shower development the slope of the distributions above about 1-2° gets less steep, for discussion see text.

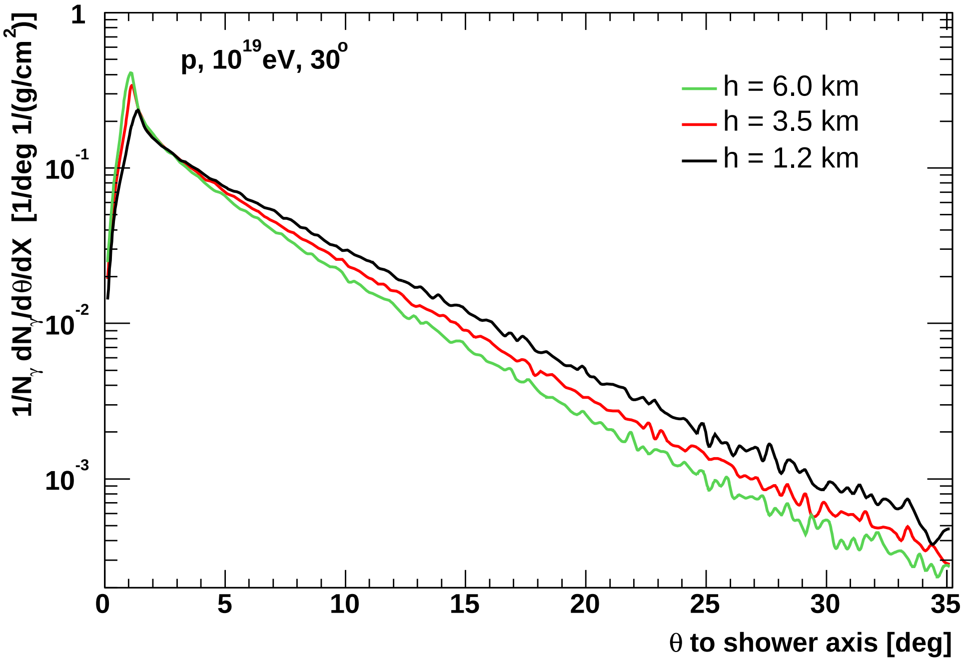

Figure 5.2: Cherenkov photon angular distribution at three different heights for an individual proton shower (10^{19} eV, 30°). The different maximum positions of $\sim 1.5°$ of the distributions at different heights reflect the Cherenkov emission angle (Eq. (3.2)), which depends on the refractive index, c.f. Chap. 3. The exponential shape for angles above $\sim 2.5°$ is implicated by the angular distribution of underlying electrons, whereas the change of slope with decreasing height is implicated by the dependence of the threshold energy for Cherenkov production (Eq. (3.10)) on the refractive index, c.f. Fig. 3.4; for discussion see text.

strongly on energy. The higher the particle's energy the smaller is the scattering. Thus, the electron angular distribution is correlated with energy: The higher the electron energy, the smaller is their (mean) angle with respect to the shower axis. Of course, only electrons of energies above the energy threshold for Cherenkov emission E_{thr} are of interest here. This implies that the higher E_{thr} the smaller is the mean angle (with respect to the shower axis) of electrons producing Cherenkov light. Finally, since the Cherenkov energy threshold is - via the refractive index - a function of altitude, see Fig. 3.3, also the angular distribution of Cherenkov photons depends on the index of refraction. This dependence can be seen in Fig. 5.2. With decreasing height or with increasing index of refraction, one finds more and more photons at larger angles to the shower axis, whereas one finds less photons at angles smaller than about 2.5°.

Above this angle of about 2.5°, the distributions are quite linear on logarithmic scale. The slope decreases with increasing atmospheric density, for which the index of refraction is larger, and thus, the energy threshold for Cherenkov production is lower. Therefore the mean angle of the electrons involved in Cherenkov production is larger at low altitudes.

It is common to describe the dependence of the angular distribution of Cherenkov light by a simple exponential function, where the scaling angle is a function of the Cherenkov energy

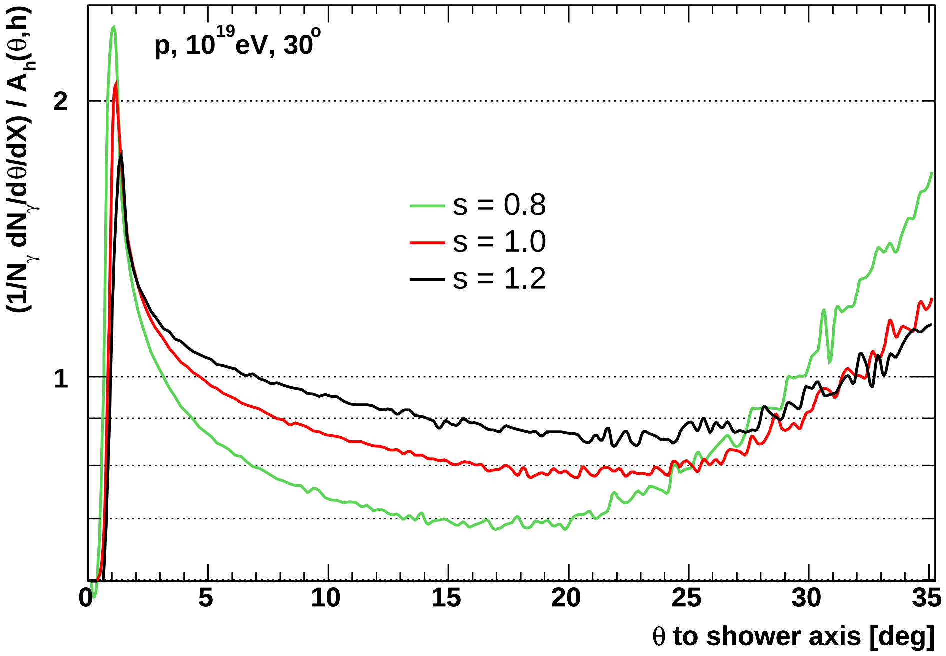

Figure 5.3: Simulated Cherenkov photon angular distributions at three different shower age levels divided by their dependence on the refractive index (5.1) (individual proton shower, 10^{19} eV, 30°). The angular distribution of produced Cherenkov photons in extensive air showers depends on shower age. With ongoing shower age the curvature is less pronounced; for discussion see text.

threshold:

$$A_\gamma(h,\theta) = 1/\theta_0 \cdot e^{-\theta/\theta_0} \ . \tag{5.1}$$

Parameterisations of θ_0 as a function of local Cherenkov threshold energy E_{thr} has been calculated by several authors. One recent calculation was done by [Elbert et al. 1983]:

$$\theta_0 = a\,E_{\text{thr}}^{-b}\ , \text{ with} \tag{5.2}$$

$$(a,b) = (0.83, 0.67)\ . \tag{5.3}$$

Traditionally this approximation is applied for calculating the Cherenkov contamination of fluorescence light signals from high energy showers, see e.g. [Baltrusaitis et al. 1985, Abu-Zayyad et al. 2001].

5.3 Dependence on Shower Age

The angular distribution of produced Cherenkov photons is given by the energy dependent electron angular distribution, when folding in the Cherenkov light yield (Eq. 3.8). Already in the previous section, for interpreting the shape due to the dependence on the refractive index, this 'microscopic picture' has been very useful. Since electron energy spectra develop with shower age the part of electrons above the Cherenkov threshold E_{thr} also changes with shower age.

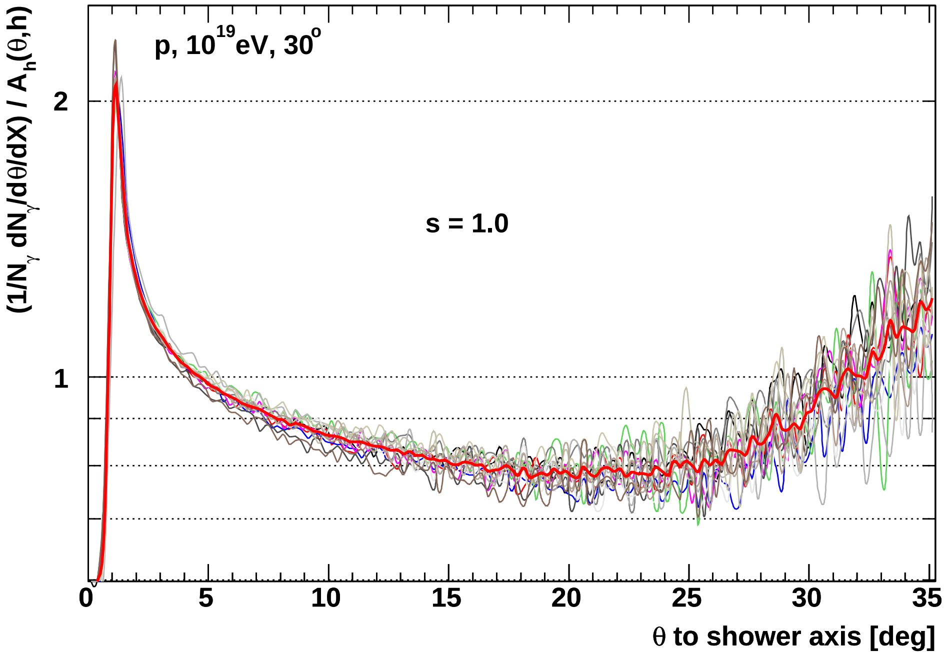

Figure 5.4: Simulated Cherenkov photon angular distributions at shower maximum divided by their dependence on the refractive index (5.1) (15 individual proton showers, 10^{19} eV, 30°). The angular distribution of produced Cherenkov photons in extensive air showers depend on shower age. Within statistical fluctuations due to thinning all 15 individual showers show the same age dependence, c.f. Fig. 5.3.

Further, there is a correlation between the electron energy and their mean angle (with respect to the shower axis) as described in the previous section. Consequently, on the one hand the photon angular distributions depend on altitude, due to the dependence of E_{thr} on the refractive index, and on the other hand there is an additional dependence on shower age, because the fraction of electrons above E_{thr} and their energy spectrum depends on shower age.

In Fig. 5.3, the latter dependence of the Cherenkov photon angular distribution is displayed. There, the normalised photon angular distribution divided by the assumed height dependence due to the refractive index (Eq. (5.1)) is plotted versus the angle θ with respect to the shower axis. The systematic change depending on shower age is clearly seen: The older the shower, the less concave the distributions are.

Additionally, in Fig. 5.4 the same distribution is shown for a set of individual showers and their average at shower maximum. All showers exhibit the same age dependence within the statistical fluctuations due to thinning.

5.4 Parameterisation

In the previous sections it has been derived that two effects have to be taken into account in order to parameterise the Cherenkov photon angular distribution with respect to the shower axis. One is related with the state of development (shower age) and the other with the height of the emission point. The first accounts for so-called shower-to-shower fluctuations, namely the point of first interaction. The latter includes the inhomogeneity of the medium, which in this context is the gradient of the refractive index.

In order to take into account both effects, the dependence on refractive index as well as on the shower age, simply a factorised ansatz is chosen for the analytical description of Eq. (3.17):

$$\begin{aligned} A_\gamma(\theta, h, s) &= A_\gamma(s) \cdot A_\gamma(\theta, h) \\ &= a_\mathrm{s}(s) \ \cdot \ 1/\theta_\mathrm{c}(h)\ e^{-\theta/\theta_\mathrm{c}(h)} \ , \end{aligned} \tag{5.4}$$

where $a_\mathrm{s}(s)$ is a polynomial of second order in shower age and the second, exponential term on the right depends on altitude only. The most important range up to about 30° is described well by (5.4). In order to enlarge the range of validity up to 60° ansatz (5.4) has to be extended by a second term to:

$$\boxed{A_\gamma(\theta, h, s) = a_\mathrm{s}(s)\,\frac{1}{\theta_\mathrm{c}(h)}\,e^{-\theta/\theta_\mathrm{c}(h)} + b_\mathrm{s}(s)\,\frac{1}{\theta_\mathrm{cc}(h)}\,e^{-\theta/\theta_\mathrm{cc}(h)}} \tag{5.5}$$

In this expression, the age dependence is included by polynomials of third order

$$a_\mathrm{s}(s) = a_0 + a_1 \cdot s + a_2 \cdot s^2 \tag{5.6}$$

$$b_\mathrm{s}(s) = b_0 + b_1 \cdot s + b_2 \cdot s^2 \ , \tag{5.7}$$

and the height dependence is taken into account by the exponential factors

$$\theta_\mathrm{c}(h) = \alpha \cdot E_\mathrm{thr}^{-\beta} \quad \text{, with } E_\mathrm{thr} \text{ in MeV} \tag{5.8}$$

$$\theta_\mathrm{cc}(h) = \gamma \cdot \theta_\mathrm{c}(h) \quad \text{, with } \gamma = \alpha' + \beta' \cdot s \ . \tag{5.9}$$

As shown in Fig. 5.5, the CORSIKA spectra are predicted properly using the following parameters that have been found by a global fit to many individual showers:

$$\begin{aligned} (a_0, a_1, a_2) &= (4.2489 \cdot 10^{-1}, 5.8371 \cdot 10^{-1}, -8.2373 \cdot 10^{-2}) \\ (b_0, b_1, b_2) &= (5.5108 \cdot 10^{-2}, -9.5587 \cdot 10^{-2}, 5.6952 \cdot 10^{-2}) \\ (\alpha, \beta) &= (0.62694, 0.60590) \\ (\alpha', \beta') &= (10.509, -4.9644) \ . \end{aligned} \tag{5.10}$$

Indeed, numerous parameters are necessary to describe the angular distribution of Cherenkov photons produced in extensive air showers. But given the fact, that the state of shower development as well as the height of the Cherenkov photon emission region have to be accounted for, Eq. (5.5) is of rather simple form.

Since individual showers develop earlier or later in the atmosphere and further, are more or less inclined, each individual shower development takes place under different conditions,

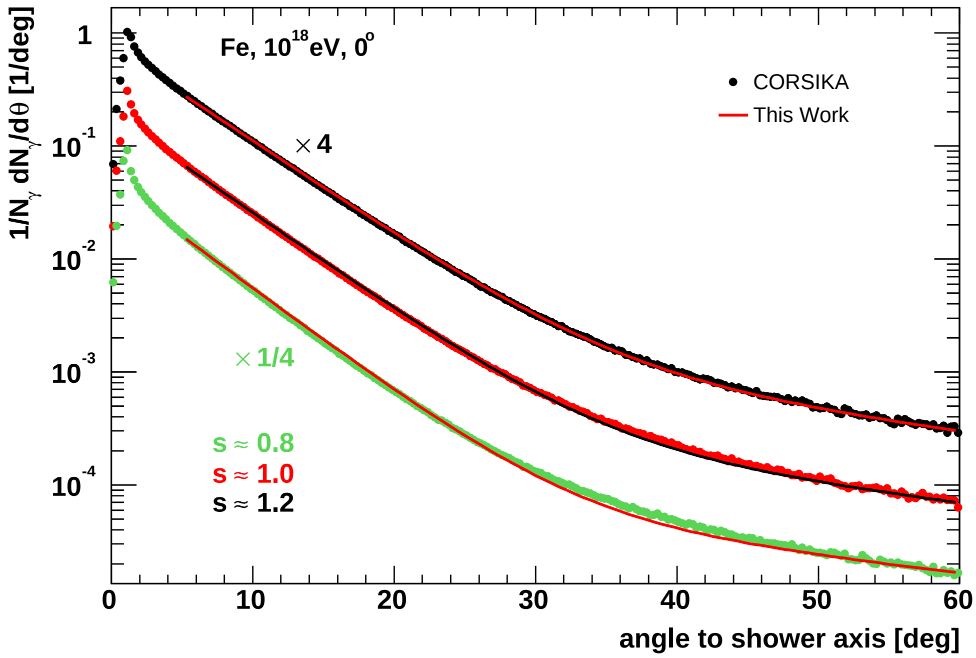

Figure 5.5: Cherenkov photon angular distribution with respect to the shower axis of an individual iron shower, 10^{18} eV, $0°$, simulated with optimum thinning 10^{-8}.

namely different mapping between shower ages and refractive indices. These varying conditions result in different angular distributions of produced Cherenkov photons. Therefore, the parameters of Eq. (5.5) have been derived by minimising the multi-dimensional parameter space of numerous photon angular distributions for a set of different individual showers (various zenith angles and shower maximum values, different primary masses and energies).

It should be noted, that the parameters (α, β) of Eq. (5.8) within the exponential term of ansatz (5.4) accounting for the height dependence, are different from the traditionally used values (5.3). The parameters used here are newly calculated based on CORSIKA simulations.

The parameterisation Eq. (5.5) describes the Monte Carlo simulations reasonably over a large range from $5°$ up to $60°$ for the shower age region $0.8 \leq s \leq 1.2$, see Fig. 5.5.

In Fig. 5.6, the relative differences between the analytical predictions by the parametrisation (5.5) and the Monte Carlo result are plotted for three shower ages for the same shower as in Fig. 5.5. For the young shower, deviations occur up to 15 % for the whole angle range, while they stay well below about 5 % up to 25°. At shower maximum the best accuracy is achieved. Beyond the shower maximum the description is even better, there an agreement within 2-3 % is achieved. Further examples of comparisons between simulated individual showers and Eq. (5.5), especially different inclination angles and depths of maximum values, are shown in the next section.

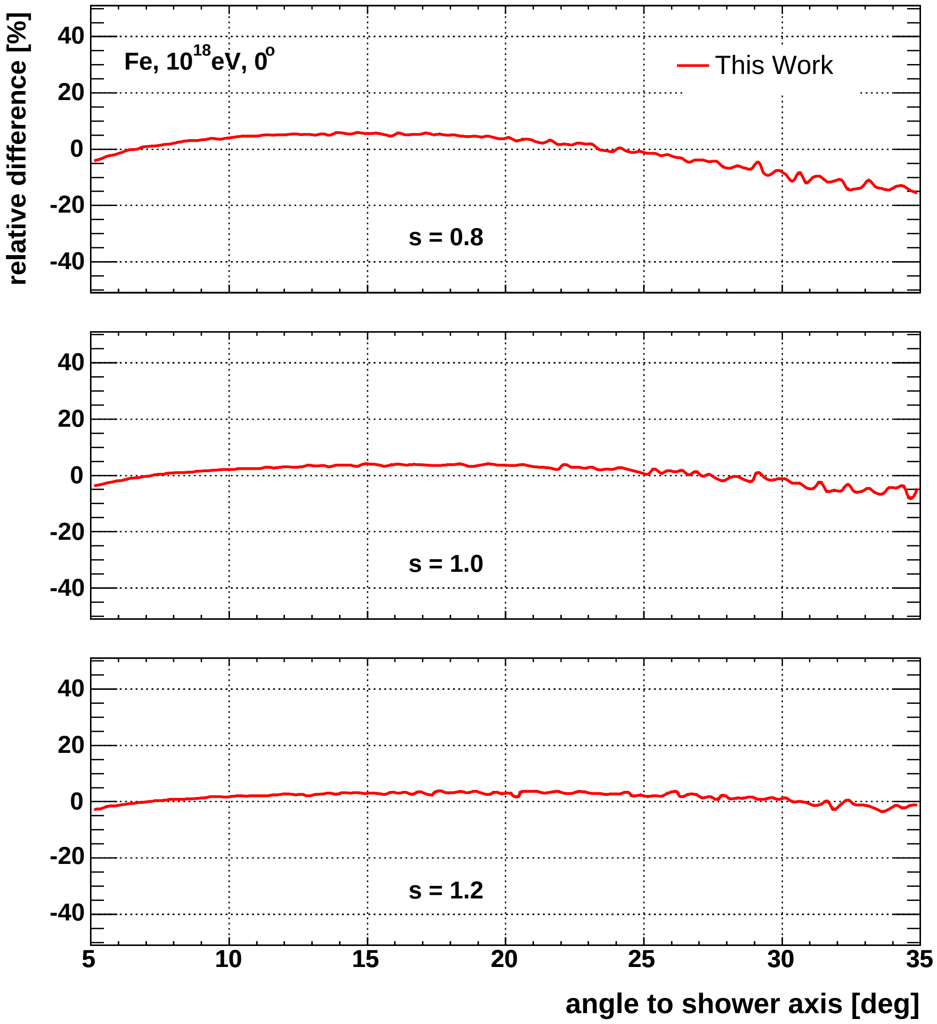

Figure 5.6: Relative difference between the parametrisation Eq. (5.5) and simulated Cherenkov photon angular distribution of an individual iron shower, 10^{18} eV, $0°$, optimum thinning 10^{-8}.

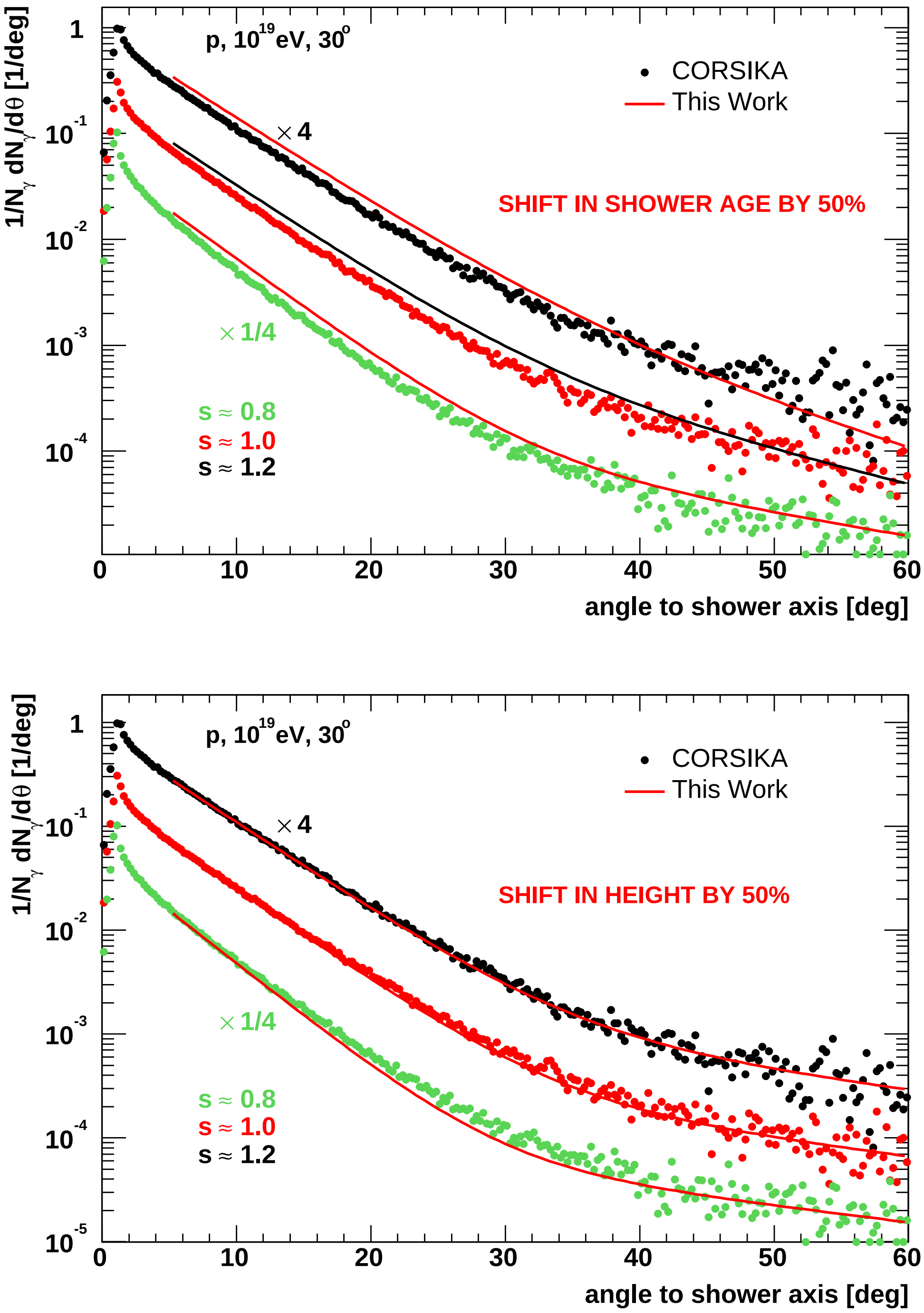

Figure 5.7: Upper panel: Demonstration of the sensitivity to shower age. The input age is shifted by 50 % off the correct value. Due to the over-estimated age the resulting curvature of the analytical curve (Eq. (4.7)) is too less pronounced, c.f. Fig. 5.3. Lower panel: Demonstration of the sensitivity to the refractive index. The input height is shifted by 50 % off the correct value. The over-estimated height results in a higher energy threshold for Cherenkov production, causing the analytical prediction (Eq. (4.7)) to be steeper, c.f. Fig. 5.2.

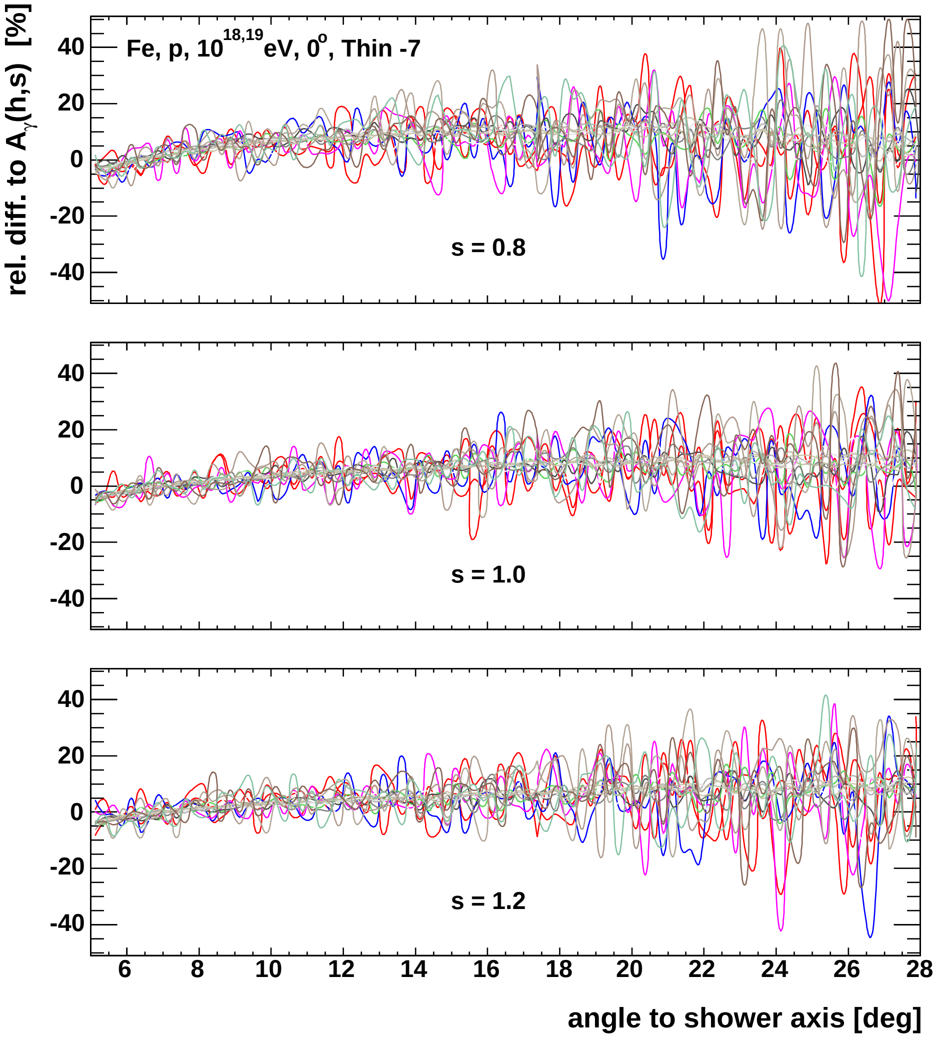

Figure 5.8: Quality of fit A. Shown are the relative differences between the parameterisation Eq. (5.5) and simulated Cherenkov photon angular distributions of many individual iron and proton showers, 10^{18}, 10^{19} eV, $0°$, optimum thinning 10^{-7}. The statistical fluctuations are due to thinning, see Fig. 5.8.

Fig. 5.7 exemplify the importance of respecting both effects, height dependence as well as the dependence on shower age. There, exemplarily for one individual shower, the height (upper panel) and the refractive index (lower panel) respectively as input for the parameterisation are shifted by 50 % off the correct values. It is seen that in both cases this results in a large systematic discrepancy between the analytical prediction and simulation results. Since the wrong input age for the parameterisation has been chosen too large, i.e. the shower is assumed to be older, the resulting curvature of the analytical curve is too less pronounced, as expected from Fig. 5.3. The over-estimated height results in a higher energy threshold for Cherenkov production, causing the distribution to be steeper. Thus, in this case Eq. (5.5) predicts too few photons under larger angles to the shower axis, which is also expected from the height dependence shown in Fig. 5.2.

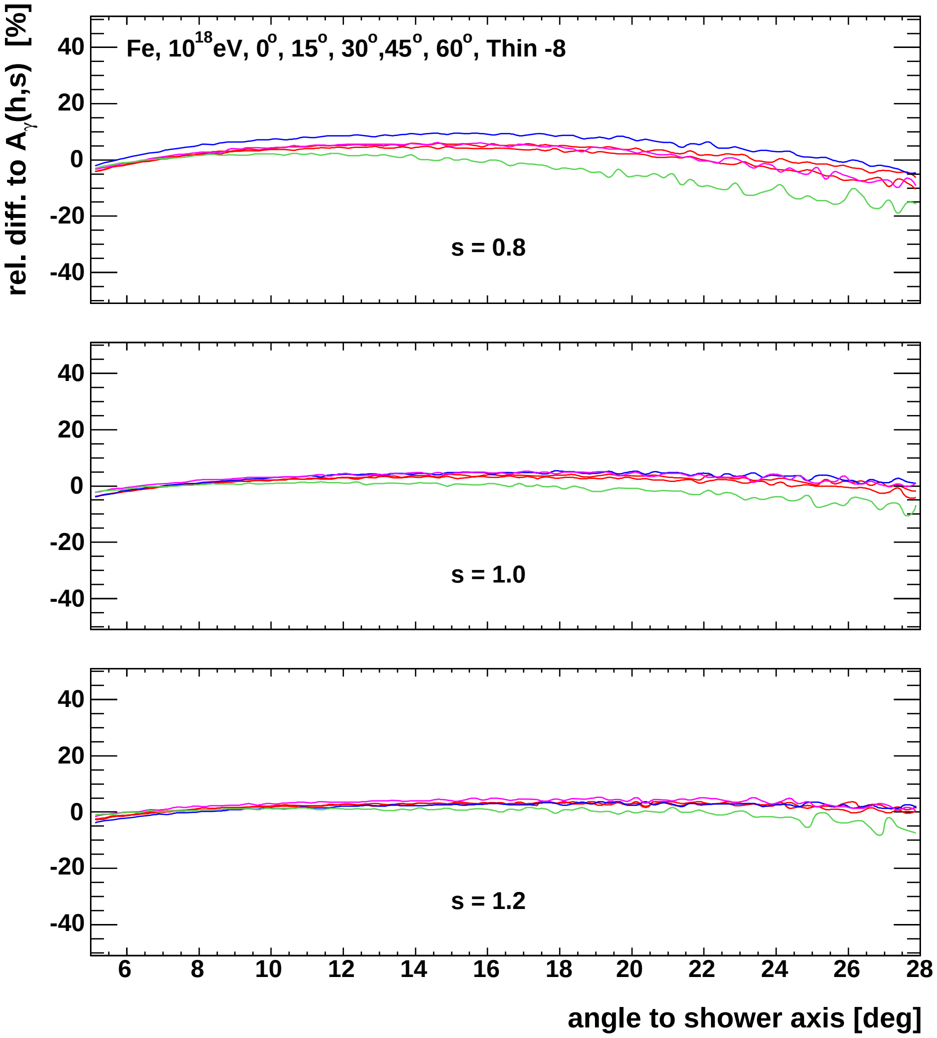

Figure 5.9: Quality of fit B. Shown are the relative differences between the parameterisation Eq. (5.5) and simulated Cherenkov photon angular distributions of many individual iron showers, 10^{18} eV, 0°, optimum thinning 10^{-8}. Due to the high quality thinning level, statistical fluctuations are minimum, see also Fig. 5.8. Using Eq. 5.5 the Monte Carlo results are reproduced within 10 % for $s = 0.8$, 5 % at shower maximum and better than 3 % for $s = 1.2$.

The quality of description achieved by Eq. (5.5) is shown in Fig. 5.8 and Fig. 5.9 respectively. In both cases relative differences between angular distributions of simulated individual showers and parameterisation (5.5) are displayed at three different ages. In Fig. 5.8 this is shown for numerous individual showers of different primary masses and energies. Here all showers are vertical and optimum thinning of 10^{-7} has been used for the simulation. It is seen that a dense band of showers occurs within about 10 %, whereas some statistical fluctuations reach up to 50 %. With increasing angle to the shower axis the number of underlying electrons decreases (see Sec. 2.1.2) and thus also the statistical fluctuations increase.

That these statistical fluctuations are due to thinning is verified by Fig. 5.9. Here thinning of 10^{-8} is applied and the fluctuations are reduced enormously. The simulation of a single

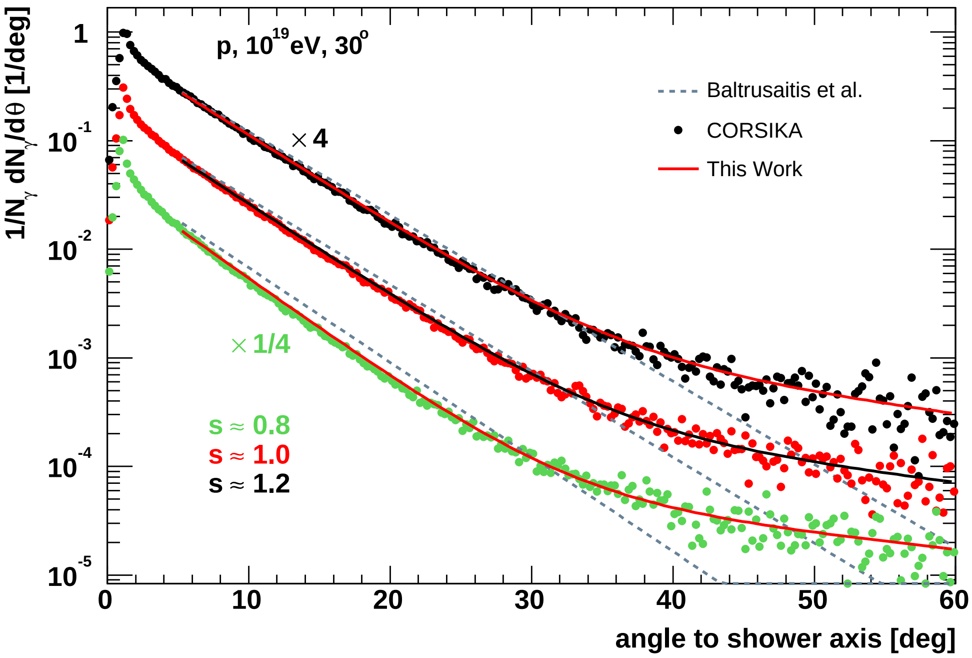

Figure 5.10: Comparison of analytical approaches and simulated Cherenkov photon angular distribution using CORSIKA, proton, 10^{19} eV, 30°; for discussion see text. (for iron, 10^{18} eV, 0°, thinning -8, see Fig. B.1/B.2 in Appendix B)

shower with this thinning level takes about 1 month of CPU time. Unlike Fig. 5.8 here the relative differences to the parameterisation are shown only for iron showers of 10^{18} eV, but for five different inclination angles. As one can see, except for statistical fluctuations, the Monte Carlo results are reproduced within 10 % in the case of young showers, at shower maximum agreement is achieved within 5 % and beyond the maximum at shower age of 1.2 differences stay well below 3 %.

5.5 Comparison with other Parameterisation

A parameterisation of the angular distribution of Cherenkov photons produced by extensive air showers was already given in [Elbert et al. 1983] accounting only for the height dependence. This calculation is based on equations of electron angular distributions provided by [Hillas 1982]. In this approach, the angular distribution of Cherenkov photons produced within extensive air showers relative to the shower axis is given by Eq. (5.1):

$$\begin{aligned} A_\gamma(h,\theta) &= 1/\theta_0 \cdot e^{-\theta/\theta_0} \\ \theta_0 &= a\,E_{\rm thr}^{-b}\,, \text{ with} \\ (a,b) &= (0.83, 0.67)\,. \end{aligned} \tag{5.11}$$

Traditionally this approximation is used to calculate the Cherenkov contamination of fluorescence light signals from high-energy showers, see for example [Baltrusaitis et al. 1985,

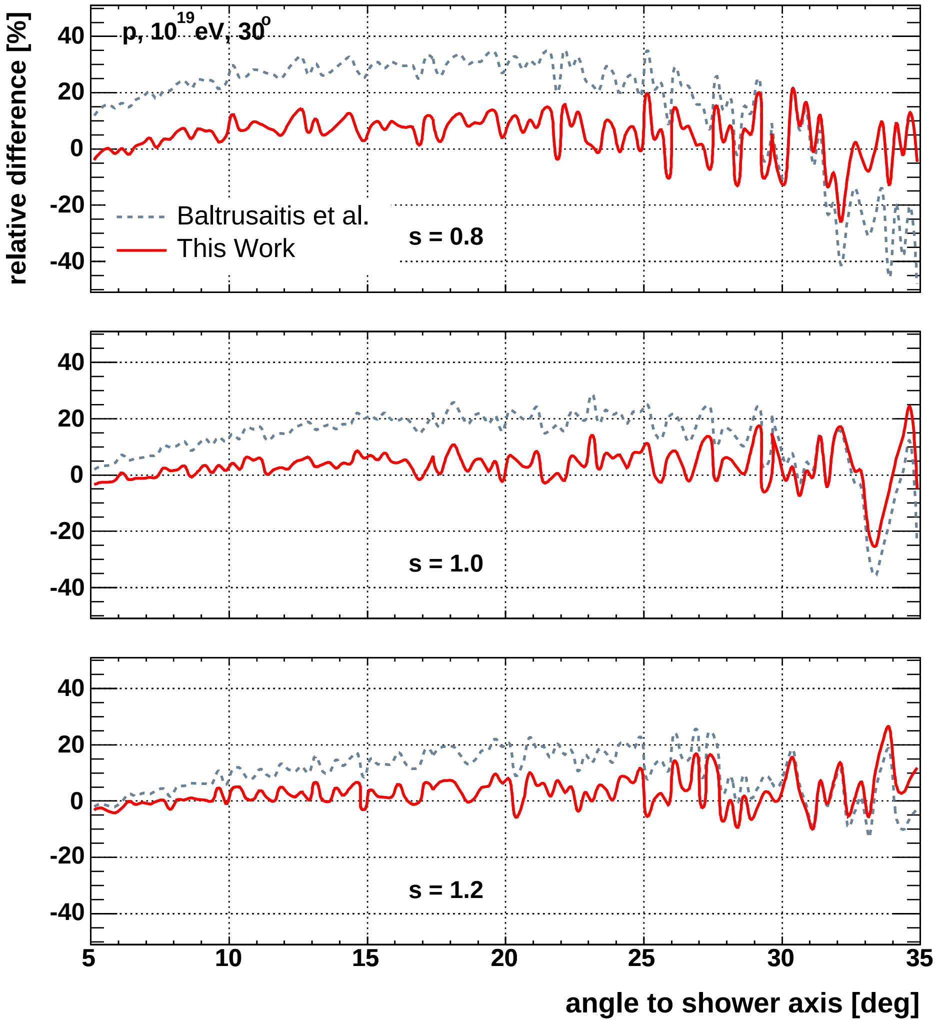

Figure 5.11: Relative differences between analytical approaches and simulated Cherenkov photon angular distribution using CORSIKA, proton, 10^{19} eV, 30°; for discussion see text.

Abu-Zayyad et al. 2001]. In the following the photon angular distribution obtained by this previous parameterisation, by the new parameterisation (Eq. (5.5)) and results derived from CORSIKA are compared.

In Fig. 5.10 this comparison is done for a typical proton shower of 10^{19} eV; typical means that it has a shower maximum close to the mean depth of shower maximum. From Fig. 2.8 and Fig. 2.9 respectively, it is seen that the mean depth of shower maximum $X_{\max}$ is about 750 g/cm^2 for proton showers of 10^{19} eV. An approximative description is achieved by Eq. (5.11) in the range of 5°-35°, whereas the new parameterisation (Eq. 5.5) is in agreement with the Monte Carlo simulations up to 60°.

The quantitative comparison of the predictions is illustrated in Fig. 5.11 up to 35° for this typical proton shower. Apart from statistical fluctuations due to thinning, the HiRes/Fly's Eye approach is in agreement with the Monte Carlo simulations within about 20 % at shower

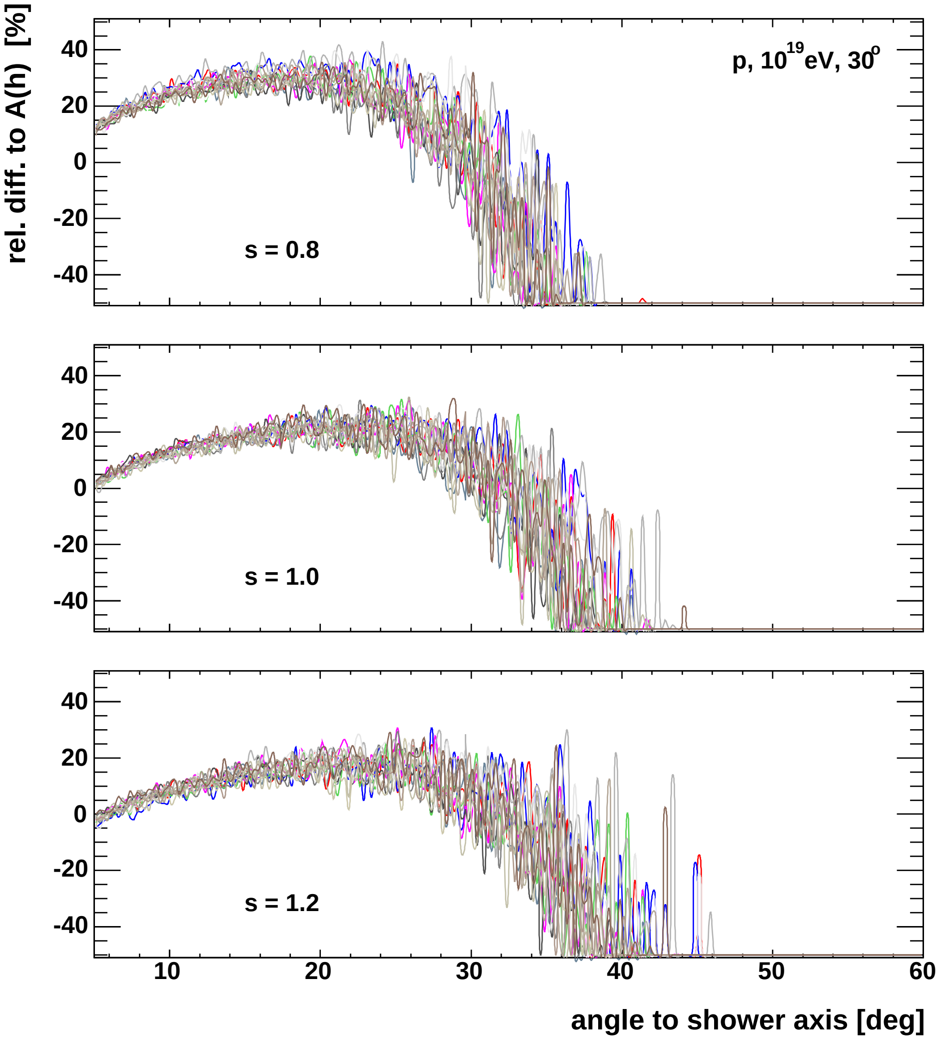

Figure 5.12: Systematic deviations of the HiRes/Fly's Eye approach (Eq. (5.11)) with respect to CORSIKA. Applying the traditionally used approach differences show systematic deviations. Systematic anomaly amounts up to about 15 % at $\sim 25^{\circ}$ for s = 1.2, 20 % at shower maximum, and 30 % for s = 0.8. For angles with respect to the shower axis larger than 35°-40° systematic disagreements exceed 50 %, c.f. Fig. 5.13.

maximum (30 % for s=0.8, 15 % for s=1.2), whereas the new approach agrees within 5 % at the maximum (10 % for s=0.8, 10 % for s=1.2). Furthermore, it describes the simulations for larger angles up to 60°, but this is here not discussed quantitatively, because of the statistical fluctuations due to thinning. The quality of description by Eq. (5.5) at larger angles up to 60° with respect to the shower axis has already been demonstrated previously.

To investigate possible systematic disagreements, relative differences are shown for numerous individual proton showers over the whole range up to 60° in Fig. 5.13. In Fig. 5.12 the HiRes/Fly's Eye approach is applied. Here the differences clearly show systematic discrepancies. While this systematic anomaly amounts up to about 15 % at around 25° for s=1.2, it constitutes 20 % at shower maximum and even 30 % for the young shower of s=0.8. For

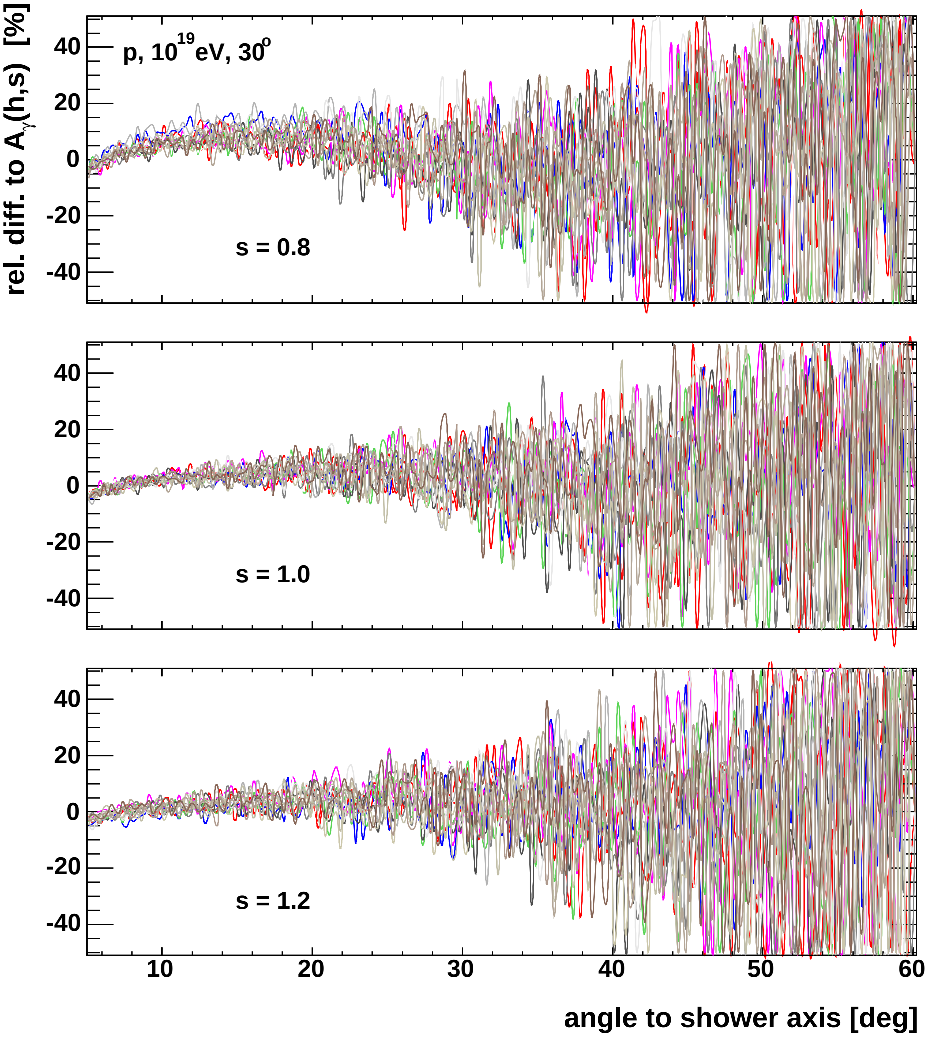

Figure 5.13: Systematic deviations of new approach (Eq. (5.5)) with respect to CORSIKA. Applying the new approach (Eq. (5.5)) the Monte Carlo results are predicted without any significant systematic deviations over the whole range up to 60°, c.f. Fig. 5.13.

angles with respect to the shower axis larger than 35°-40° systematic disagreements exceed 50 %. These systematic disagreements disappear nearly completely when using the new parameterisation, as can be seen in Fig. 5.13. The small differences of 3 % for s = 1.2, 5 % at shower maximum and 10 % for s = 0.8 are related to the quality of the fit, see Fig. 5.9. This can be optimised by fitting Eq. (5.5) to a larger set of well simulated showers using optimum thinning of 10^{-8}. However, Fig. 5.13 shows, that the new parameterisation accounts for the underlying physics, since Cherenkov photon angular distributions are predicted without any significant systematic deviations.

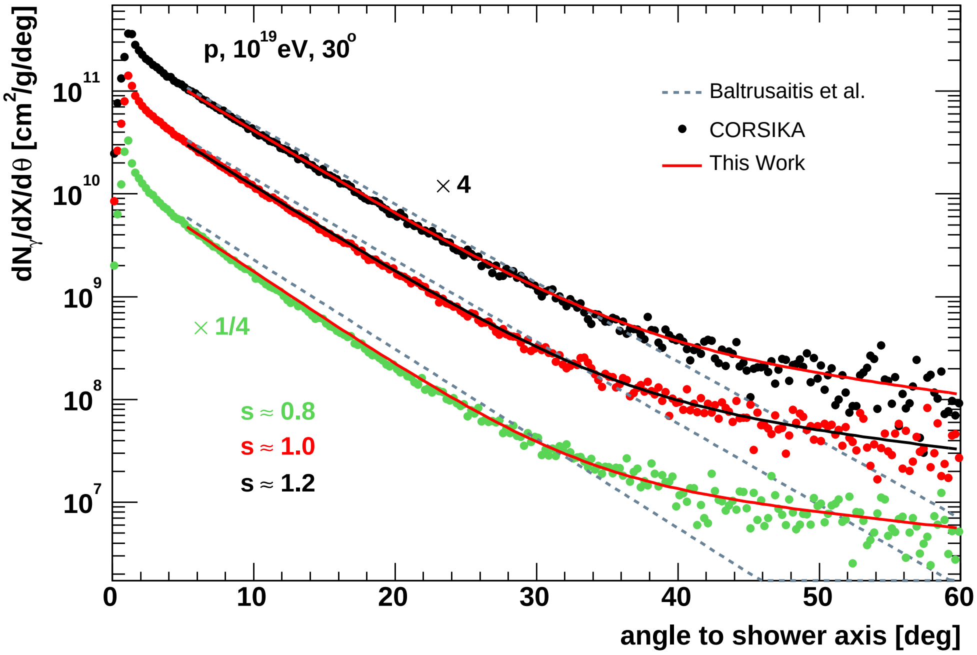

Figure 5.14: Comparison of the Cherenkov model with Monte Carlo simulations for a mean shower (proton, 10^{19} eV, 30°). The Cherenkov model is based on ansatz 3.18 applying the new parameterisations of normalised electron energy distribution (Eq. (4.7)) and normalised Cherenkov photon distribution (Eq. (5.5)). The new approach is compared to the traditionally used, see e.g. [Baltrusaitis et al. 1985, Abu-Zayyad et al. 2001].

5.6 Test of the Cherenkov Model with Monte Carlo Simulations

For analytical calculation of the Cherenkov light produced in extensive air showers, ansatz (3.18) has been introduced, see Chap. 3. The two Parameterisations needed for complete computation, namely the *normalised* electron energy spectrum $f_e(E, s)$ (Eq. (4.7)) and the *normalised* angular distribution of produced Cherenkov photons $A_\gamma(\theta, h, s)$ (Eq. (5.5)) in extensive air showers have been provided in Chap. 4 and Sec. 5.4 respectively. In the following the accuracy of prediction by the full new Cherenkov model, i.e. the total number of Cherenkov photons produced in extensive air showers per slant depth and per angular interval with respect to the shower axis is compared to Monte Carlo simulations.

In Fig. 5.14 the total number of Cherenkov photons produced per slant depth and angular interval is shown. Analytical results are compared to the results derived from CORSIKA. Additionally the previous analytical Cherenkov model going back to Hillas is shown, as it is traditionally used for calculating the Cherenkov contribution in fluorescence light signals from high-energy showers, see for example [Baltrusaitis et al. 1985, Abu-Zayyad et al. 2001]. The computations of photon distributions are shown for three different shower ages. The new model predicts the total photon numbers in good agreement with CORSIKA over the whole

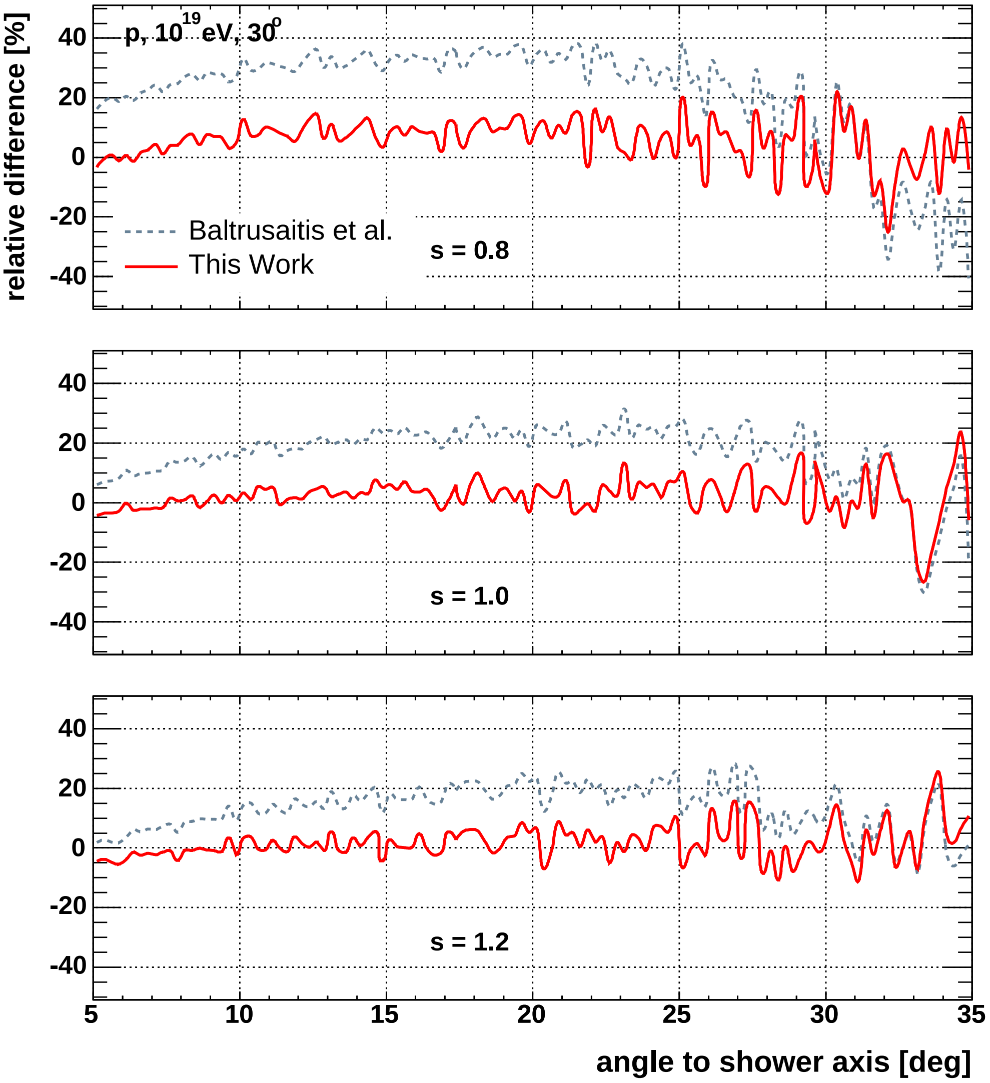

Figure 5.15: Relative difference: Full Cherenkov Model versus Monte Carlo result, mean shower (proton, 10^{19} eV, 30°), for quality of descriptions see also Fig. 5.16.

angular range up to 60°. In comparison, the traditional approach overestimates the photon number at angles smaller than about 30° for all ages. For larger angles to the shower axis this previous approach does not reproduce the simulated spectra at all, which might have been expected, since 30° is the upper validity limit given in [Baltrusaitis et al. 1985].

In Fig. 5.15 and Fig. 5.16 respectively the quality of prediction compared to CORSIKA is illustrated for either models for an individual mean proton shower and an early developing iron shower with different zenith angle. Apart from different primary parameters the difference between both of them is, that the former shows the quality study for a shower simulated with an optimised thinning of 10^{-6}, whereas for the latter a much better thinning of 10^{-8} has been applied. Also here, the statistical fluctuations in the former difference plot are due to thinning,

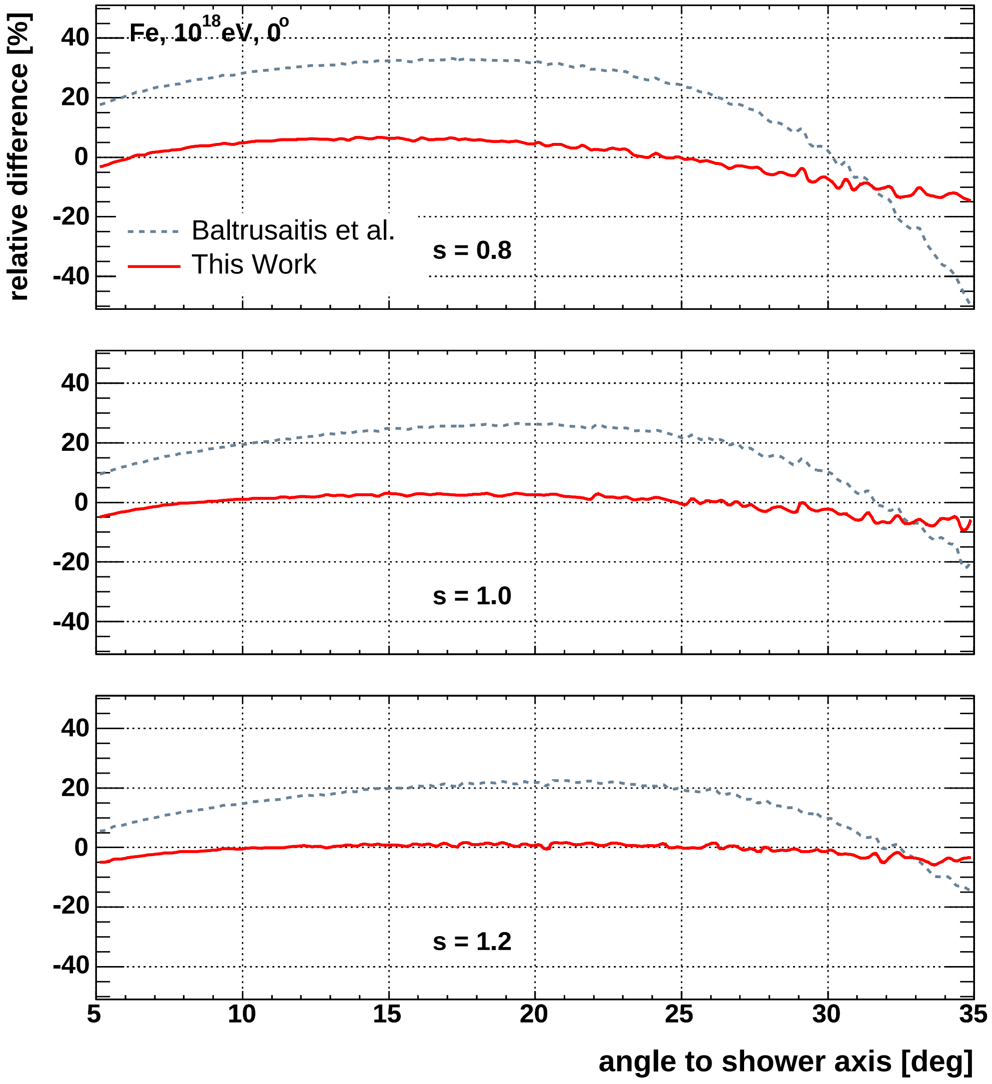

Figure 5.16: Relative difference: Full Cherenkov Model versus Monte Carlo result, very early developing shower (iron, 10^{18} eV, 0°, optimum thinning 10^{-8}). The total number of Cherenkov photons produced per slant depth and angular interval with respect to the shower axis is in agreement with the result derived from CORSIKA within 10 % (s=0.8), 5 % (s=1.0) and 3 % (s=1.2) respectively. In comparison to the traditionally used approach, see e.g. [Baltrusaitis et al. 1985], an improvement in description of up to 20-30 % depending on shower age is achieved.

wherefore this kind of fluctuations nearly vanishes in the latter illustration, since the statistics are much better. From Fig. 5.16 it can be seen, that the previous model overestimates the photon number by up to about 30 % for the young shower, 25 % at shower maximum, and by 20 % beyond. A significant improvement is achieved using the new approach, which predicts the result derived from simulations better than 10 % (s=0.8), 5 % (s=1.0) and 3 % (s=1.2) respectively. Similar accuracy is also achieved for different primary masses, energies and inclinations, c.f. Fig. B.3 et seq.

In conclusion, calculating the number of Cherenkov photons produced per slant depth and angle with respect to the shower axis via the new Cherenkov model presented, consisting in ansatz (3.18) applying the new Parameterisations of normalised electron energy distribution (Eq. (4.7)) as well as normalised Cherenkov photon angular distribution (Eq. (5.5)), is in agreement on a few percent level with the Monte Carlo. In comparison to the previous approach, the prediction of total photon numbers compared to CORSIKA is systematically improved by up to 20-30 % depending on shower age. Moreover, the new model is able to predict Cherenkov photon production for angles with respect to the shower axis larger than 30°, it works sufficiently up to 60°.

Chapter 6

Application to Auger data

In this chapter, the impact of the new Cherenkov calculation, consisting in ansatz Eq. (3.18) under utilisation of Eq. (4.7) and Eq. (5.5) on the Auger event reconstruction is studied. Therefore, the collaboration's DPA (data processing and analysis framework) Offline [Nellen et al. 2004] has been applied for the reconstruction of various primary parameters. Using the whole data set from September 2003 until October 2004, the effects of the new Cherenkov treatment compared to the previous approach on reconstructed parameters on an event-by-event basis are presented. Measurements of interest are different reconstructed fractions of Cherenkov light of the total light detected by the fluorescence detector namely the fractions of direct, scattered as well as total Cherenkov light, c.f. Chap. 3, and furthermore the reconstructed primary parameters such as number of charged particles at shower maximum N_{max}, the primary energy E_{p} as well as the position of the shower maximum X_{max}.

6.1 Event Reconstruction and Selection

In Fig. 6.1-6.3, the mono-reconstruction (see Sec. 2.1) of a typical event measured by the Auger fluorescence detector is demonstrated. In Fig. 6.1, the fit of the shower detector plane, within which the reconstructed shower axis is derived by fitting the trigger times of triggered pixels considered versus the elevation angle, the so-called time fit, see Fig. 6.2. Finally, the electron profile, which in a good approximation corresponds to the shower size profile, c.f. Chap. 3, is calculated from the light profile after subtraction of the analytically calculated Cherenkov background, see Fig. 6.3 and Fig. 6.4 respectively.

The primary parameters are derived directly from the reconstructed shower size profile, c.f. Chap. 2.1.2, which itself is calculated via the fluorescence yield after detector properties (quantum efficiencies of photomultipliers etc., derived from the so-called Drum Calibration [Brack et al. 2004]) have been taken into account. In order to apply the Gaisser-Hillas fit [Gaisser & Hillas 1977] to the measured light profile for determination of the shower size profile, the amount of Cherenkov light included within the light profile detected has to be calculated and subtracted correctly.

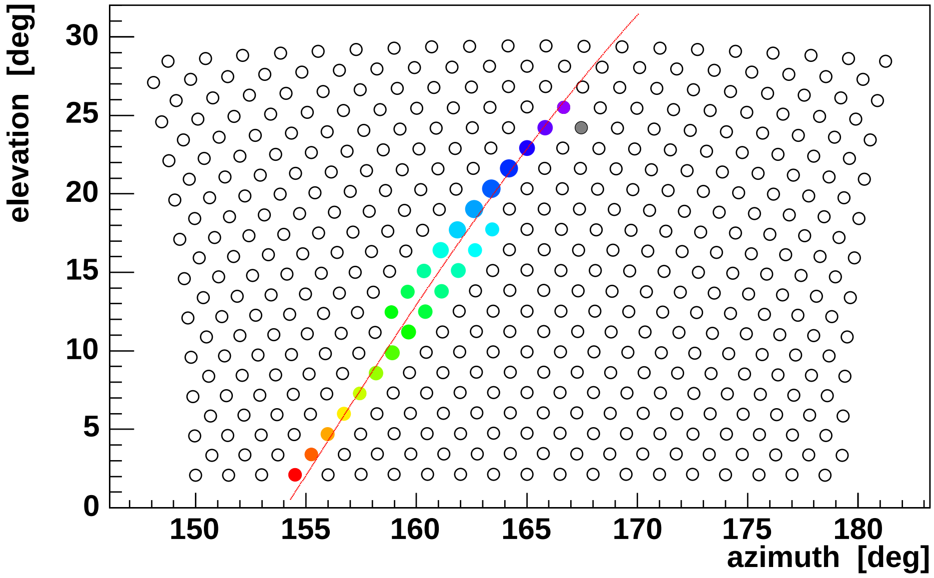

Figure 6.1: Fit of the shower detector plane. The shower detector plane contains the detector and the shower axis, see also Fig. 6.2. The directions of triggered pixels considered are fitted for determination of the shower detector plane. The time order information is represented by the colour code (blue - early, red - late, for uncoloured hardcopy: here, blue to red from up to down).

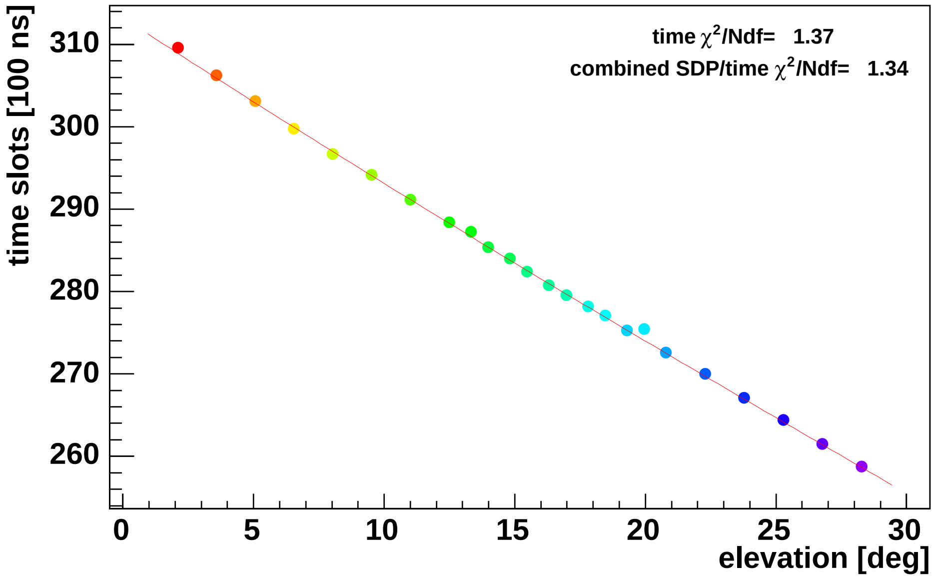

Figure 6.2: Fit of shower axis, the so-called time fit. The reconstructed shower axis is derived by fitting the trigger times of triggered pixels considered versus the elevation angle within the shower detector plane, see also Fig. 6.1. The time order information is represented by the colour code (blue - early, red - late, for uncoloured hardcopy: see time information given by ordinate).

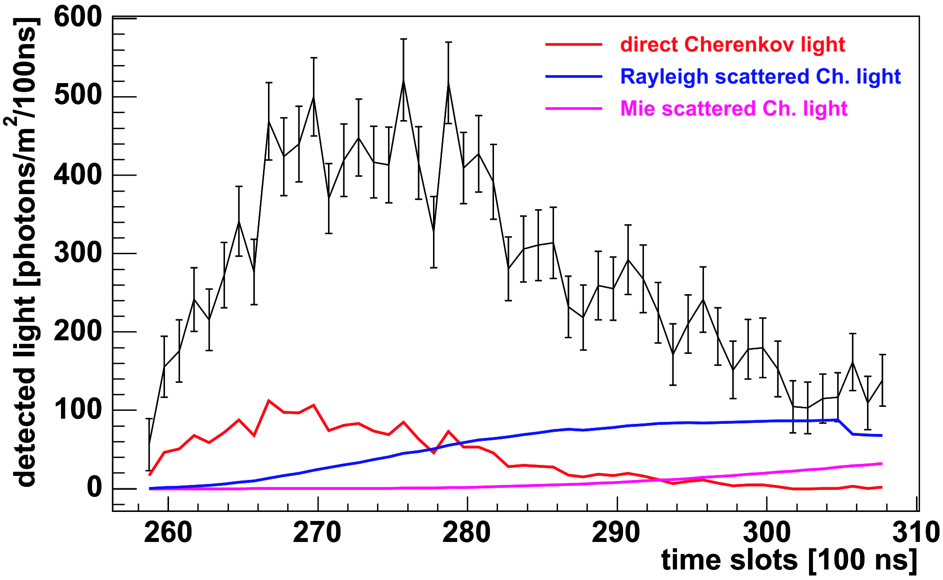

Figure 6.3: Measured light flux. The data in the form of total light measured per sampling time and the appropriate calculated Cherenkov contributions for a typical individual event are shown. In black the number of detected photons are represented, whereas the according calculated profile of direct Cherenkov light is given in red, the Mie scattered in pink and the Rayleigh scattered Cherenkov light profile in blue are given additionally, for details of these different scattered contributions see Chap. 3.

Coming back to Fig. 6.3, where the total light measured per time and the appropriate calculated Cherenkov contributions for this typical event are displayed. The number of totally detected photons and the according calculated profiles of the direct Cherenkov light, the Mie scattered and the Rayleigh scattered Cherenkov light are represented, for details of these different scattered contributions see Chap. 3. For analytical calculation of all these different kinds of Cherenkov background the previous and in the meantime also the new Cherenkov model is implemented and available for use in the DPA, the implementation has been done in collaboration with the Tourin Auger group [Chiosso & Melo 2004].

Since the number of Cherenkov photons produced is proportional to shower size, like it holds also for the fluorescence photon production, the profile of direct Cherenkov photons is expected to develop comparable to the total light flux, as it can be seen for the example shown here. The scattered contributions of light reach the detector later, since these photons traverse a larger way from their origin through the atmosphere until they reach the aperture. The direct Cherenkov light is strongly peaked forward, whereas the fluorescence light is emitted isotropically. Rayleigh scattering is the dominant process for the Cherenkov contribution in light signals seen by the fluorescence telescopes, whereas the amount of Cherenkov photons Mie scattered into the fluorescence detector's field of view is of less importance. The Rayleigh scattered Cherenkov photons are nearly isotropic, since the underlying process, Thomson scattering, is proportional to $(1 + \cos^2\theta)$, see Chap. 3. The fraction of direct Cherenkov light contained in the (total) light profile measured is strongly depending on the shower geometry with respect to the detector. in contrast, the fraction of scattered Cherenkov light contaminates the fluorescence detector signal for all shower geometries.

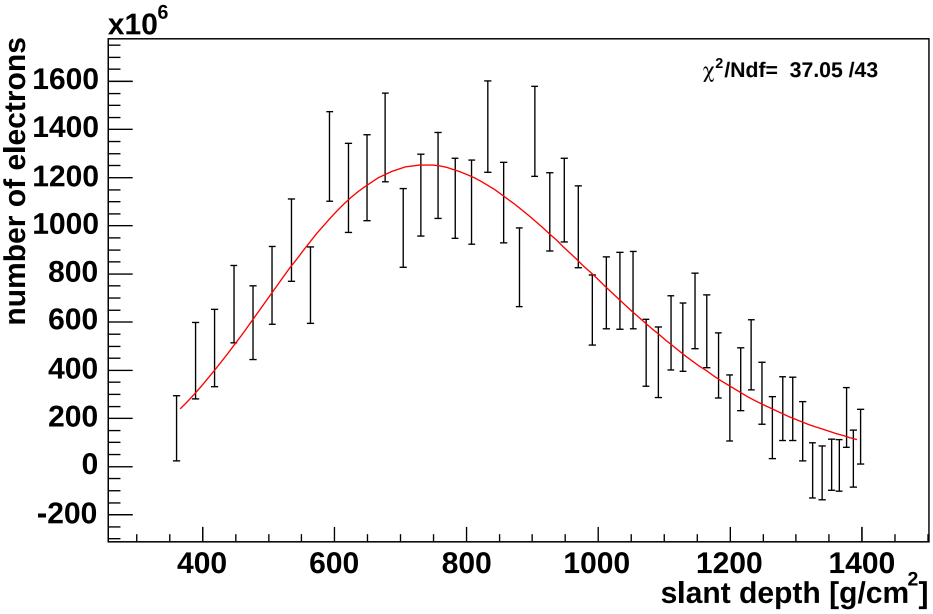

Figure 6.4: After subtraction of the analytically calculated amount of Cherenkov light included within the detected light profile, the electron profile is estimated and the Gaisser-Hillas fit [Gaisser & Hillas 1977] is applied for determination of the primary parameters.

For the study of differences in reconstructed event properties as a result of replacing the current Cherenkov model with the new one, all Auger fluorescence data currently available have been analysed (09/03-10/04). To ensure a reasonable reconstruction quality, the following selection criteria are applied to the data:

- number of reconstructed pixels > 2.
- quality of Gaisser-Hillas fit:
  $\chi^2/Ndf < 3$ (90 % residual).
- estimated statistical uncertainty of reconstructed energy:
  $E_{\mathrm{p_{err}}}/E_{\mathrm{p}} < 0.3$ (75 % residual).
- estimated statistical uncertainty of reconstructed position of shower maximum:
  $X_{\mathrm{max_{err}}}/X_{\mathrm{max}} < 0.3$ (90 % residual).

The numbers in parenthesis state the corresponding selection efficiencies. After this selection, 6746 individual showers measured by the fluorescence detector are remaining for the event-by-event study. The differences in reconstructed event properties ΔRec are always calculated like:

$$\Delta\mathrm{Rec} := \mathrm{Rec}_{(\text{New Cherenkov Model Applied})} - \mathrm{Rec}_{(\text{Old Cherenkov Model Applied})} ,$$

and relative differences discussed are always relative to the new model. Even though the scattered Cherenkov contribution only depends weakly on the shower geometry with respect to the detector, the direct Cherenkov light depends strongly on it and thus finally the total Cherenkov signal does as well. This is why, the changes in reconstructed N_{max}, E_{p} and X_{max}

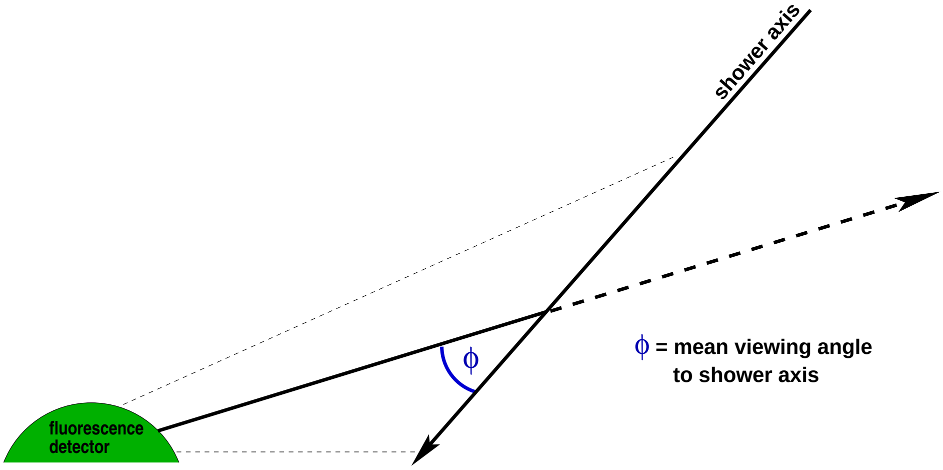

Figure 6.5: Definition of mean viewing angle to shower axis. The mean viewing angle is defined as the angle determined by the normal vector of the triggered pixel having the mean trigger time with respect to the total observation time and the shower axis.

are expected to be dependent on the accordant viewing angle, under which each individual event has been observed by the fluorescence detector.

In Fig. 6.5 the viewing angle to which will be referred to in the following is defined. Actually the viewing angle, under which an event is seen by the fluorescence detector changes with shower development. Therefore, as mean viewing angle determined by the normal vector of the triggered pixel having the mean trigger time with respect to the total observation time is chosen for the studies presented below.

6.2 Reconstructed Fraction of Cherenkov light

In the current version of Offline [Nellen et al. 2004] the Cherenkov light contained in measured light profiles is estimated analytically using an iterative algorithm. The measured light profile is assumed to be purely fluorescence light at the first step. Then the Gaisser-Hillas longitudinal fit is applied. Based on the resulting shower size profile, the shower geometry, the maximum and the shower age is derived. Using these input variables the Cherenkov contribution is estimated analytically and subsequently subtracted. The results in the form of primary parameters are determined within four iterations, presumed the profile fit has converged [Dawson 2003].

Changes in the reconstruction of primary parameters due to the new Cherenkov model originate from differences in the reconstructed amount of Cherenkov light contained in the total light profile, c.f. Fig. 6.3. The fraction of Cherenkov light is given by

$$f_{\mathrm{Ch.}} = \frac{N_{\gamma}^{\mathrm{Ch.}}}{N_{\gamma}^{\mathrm{Fl.}} + N_{\gamma}^{\mathrm{Ch.}}} \ . \tag{6.1}$$

In Fig. 6.6 the fractions of total Cherenkov light of events passing the quality cuts mentioned above are shown versus the mean viewing angle, under which the showers have been

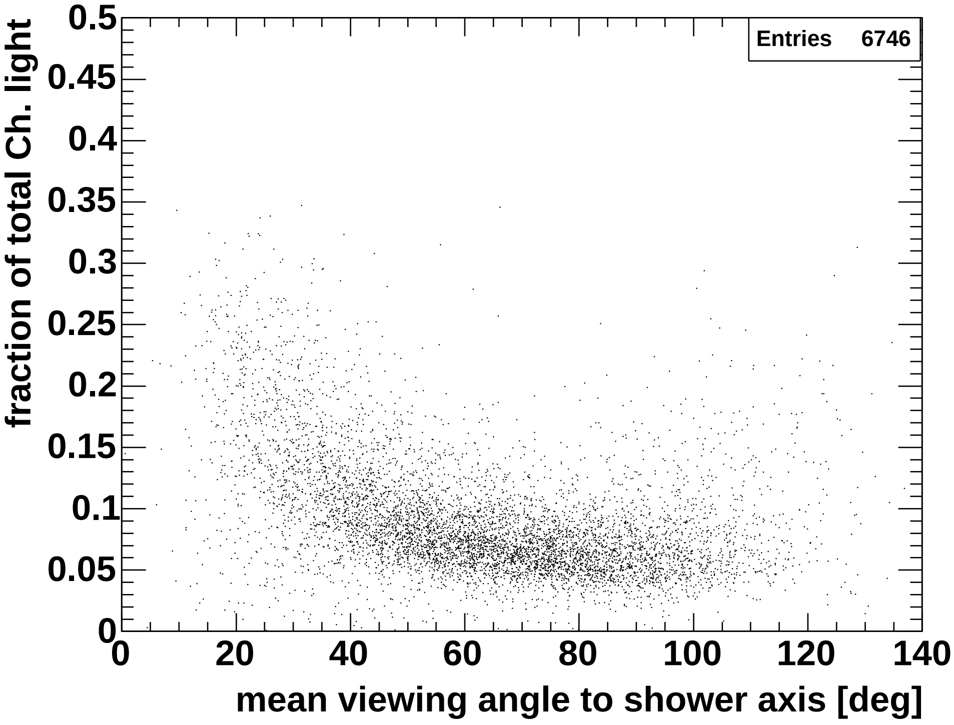

Figure 6.6: Current reconstruction efficiency with respect to fraction of Cherenkov light.

seen by the fluorescence detector. With decreasing viewing angle the Cherenkov contribution increases, which is expected since the more the shower is directed towards the detector, the more of the in forward direction emitted direct Cherenkov light is reaching it. When showers are developing under viewing angles near to 90° (more or less parallel to the camera plane), showers typically have fractions of total Cherenkov light of 5-10 %.

Further, it should be noted from this figure, that light profiles containing more than 35 % of Cherenkov contribution, are not passing the full reconstruction chain in combination with the relatively weak quality cuts chosen. This seems to be a problem of the current Cherenkov subtraction algorithm assuming at first step the raw light profile measured not to include any Cherenkov light at all. Since Cherenkov contamination can be easily larger than only 35 % [Nerling 2004], see also Fig. 3.7, this has still to be improved systematically in order to increase the reconstruction efficiency in general.

In Fig. 6.7 the reconstructed fraction of direct Cherenkov light versus the mean viewing angle is displayed applying the new and old Cherenkov calculation respectively as well as the corresponding relative differences. The general effect of a decreasing fraction of direct Cherenkov light with increasing viewing angle is identified for both models, whereas the decrease is less steep in the case of the reconstruction with the new model. Compared to the new approach, for viewing angles larger than about 25° the old Cherenkov model results in an over-estimation of direct Cherenkov fraction, which increases systematically with increasing viewing angle up to about +100 % for angles larger than roughly 60°. For angles smaller than

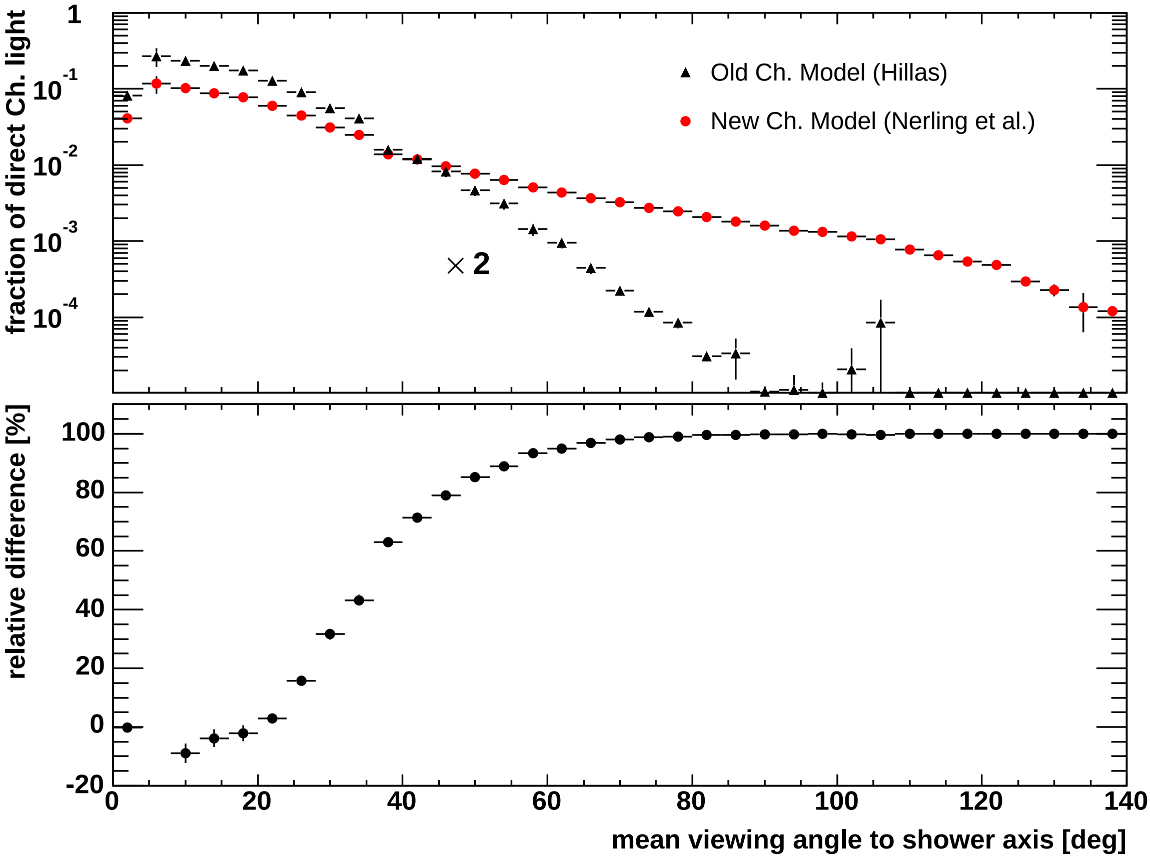

Figure 6.7: Reconstructed fraction of direct Cherenkov light contribution. Data points based on the previous Cherenkov model are scaled by a factor of two, for discussion see text.

25°, the new model predicts up to about -10 % less direct Cherenkov light. The data points in the bins closest to 0° and 140° are not to be taken seriously, since these bins contain only one event (c.f. Fig. 6.6) wherefore no statistical uncertainty could be calculated. Fig. 6.6. The result of predicting smaller fraction of direct Cherenkov light when using the new model for angles up to nearly 30° but larger contributions for angles beyond 30° as well as the amount of relative differences are completely in agreement with the Monte Carlo simulations comparisons presented in Chap. 5.6.

The similar study has been done for the fractions of scattered Cherenkov light, which is illustrated in Fig. 6.8. The scattered Cherenkov light is expected not to show such a large dependence on the viewing angle as the direct one. Since the dominant dispersion effect, namely Rayleigh scattering, is proportional to $(1+\cos^2\theta)$ one expects only a slight modulated dependence proportional to $\cos^2\theta$. Such modulation is recognised easily, both data curves reach their minimum at about 90° and increase towards 0° as well as towards 180°. Actually,

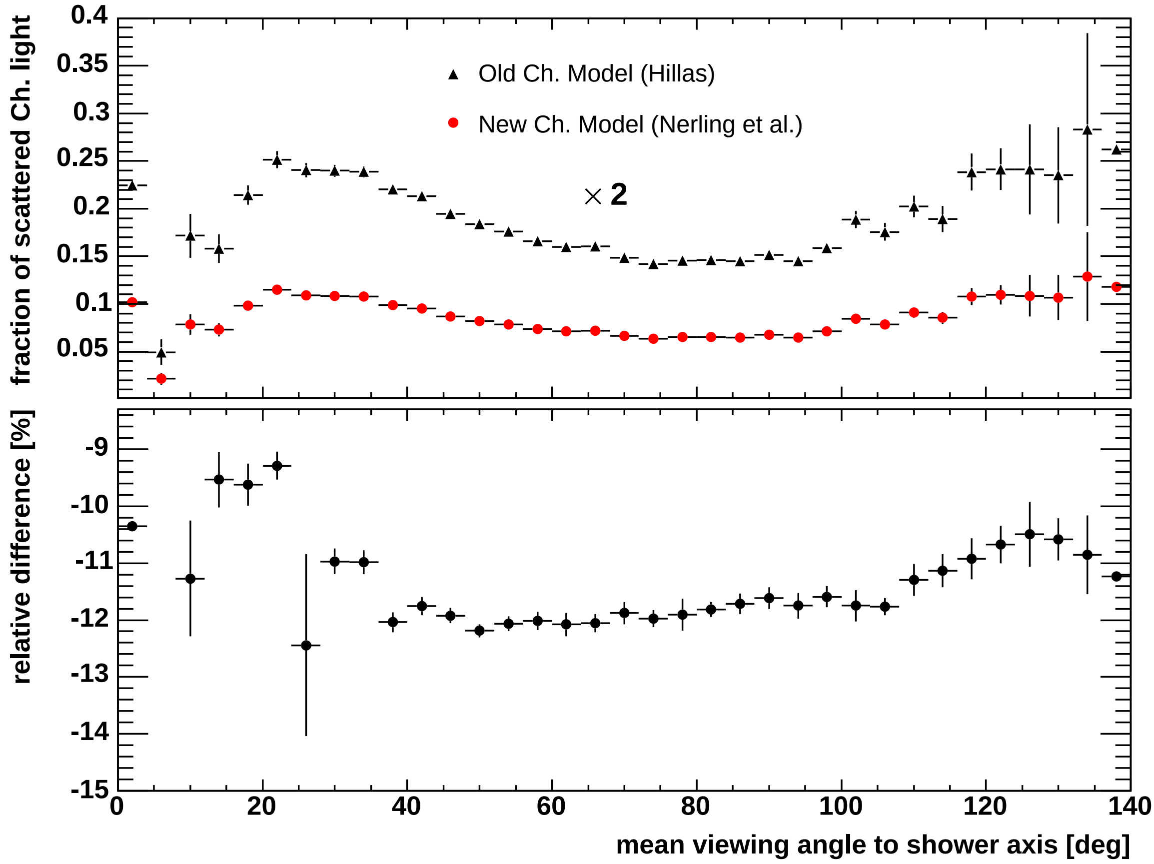

Figure 6.8: Reconstructed fraction of Scattered Cherenkov Light Contribution. Data points based on the previous Cherenkov model are scaled by a factor of two, for discussion see text.

they both do not really reach their maximum for angles where $\cos\theta = 1$, but for both of these extreme angular regions statistics are too small (see error bars and Fig. 6.6). For the angular region of very small viewing angles the Cherenkov subtraction algorithm again might be the source of non-realistic estimates of Cherenkov fractions. However, at angles of about 20° and 120° respectively, the fractions have already increased up to almost a factor of two compared to those corresponding to 90°. The relative differences (lower panel) show that the application of the new model results in less scattered Cherenkov light contribution of about -10 %, depending only slightly on viewing angle. This result agrees also with the Monte Carlo studies insofar as the improvement by the new approach in predicting the CORSIKA results is only about -5 % concerning the total number of Cherenkov photons produced, see Chap. 4, and larger, namely up to about -30 %, for the angular distribution of Cherenkov photons produced, see Chap. 5. Therefore, due to the new Cherenkov model large changes in direct Cherenkov light contributions are expected, but merely lower impact on the scattered part.

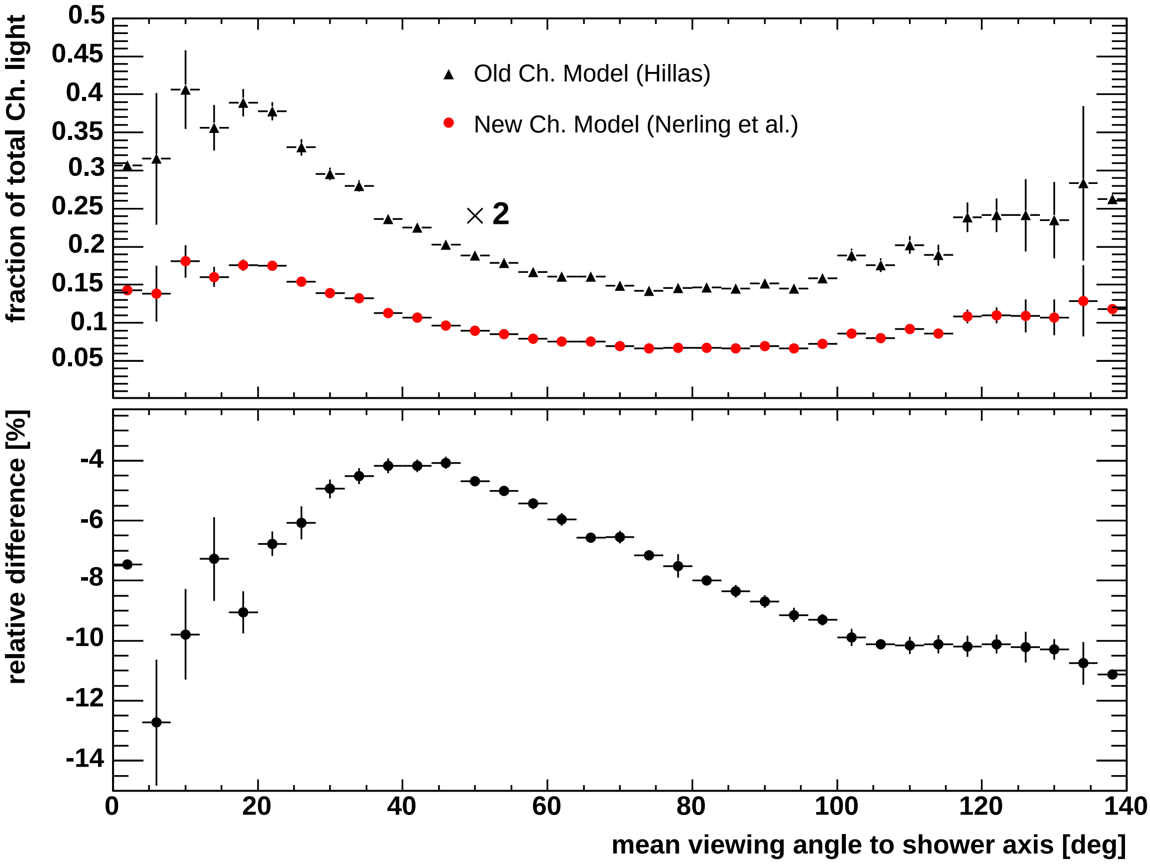

Figure 6.9: Reconstructed fraction of Total Cherenkov Light Contribution. Data points based on the previous Cherenkov model are scaled by a factor of two, for discussion see text.

In Fig. 6.9 the impact on fraction of total Cherenkov light is displayed. Since, the total Cherenkov light is derived just by adding both, the direct and the scattered Cherenkov light, just the superposition of previous discussed data curves are expected. In fact, one can recognise the same picture as Fig. 6.8 when adding the fractions of direct Cherenkov light. In the large angular region, where the direct contribution is small, changes are small as well, whereas in the region of smaller viewing angles differences compared to Fig. 6.8 are appropriately larger. It can be concluded that the usage of the new model results in smaller fractions of the total Cherenkov light over the whole angular range, whereas above 40° changes increase with increasing angle up to about -10 % and below 40° the same with decreasing angle.

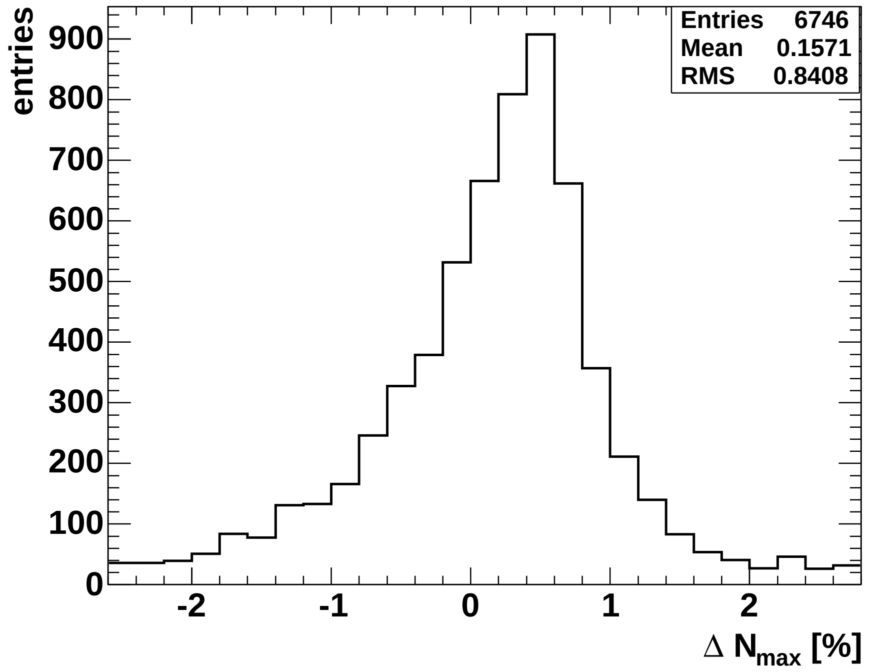

Figure 6.10: Impact of new Cherenkov model on reconstructed N_{max} averaged over phase space, for discussion see text.

6.3 Impact on Reconstruction of Primary Parameters

It has been shown, that the impact on fraction of Cherenkov light by using the new approach of analytical Cherenkov calculation instead of the previous one is neither independent of viewing angle nor negligible. The further step of interest is, how large differences in reconstruction of primary parameters are due to the utilisation of the new Cherenkov model.

Number of Charged Particles at Shower Maximum

The according study for the reconstructed number of charged particles at shower maximum N_{max} is presented in Fig. 6.10 and Fig. 6.11 respectively. The first show the distribution, from which the mean difference in N_{max} with respect to the whole data set, whereas the latter shows the underlying angular dependence of impact. On average, using the new Cherenkov calculation N_{max} is reconstructed to be about $+0.2\,\%$ larger compared to usage of the previous model. Thus on average, the impact is not very large, but of course it is expected to depend on viewing angle, since N_{max} is directly derived from the reconstructed shower size profile, namely it is the value of its maximum. Therefore, in the case of showers comprising a larger direct Cherenkov fraction, the impact on reconstructed maximum of longitudinal shower size distribution is expected to be the larger the smaller the viewing angle is.

In fact, this is the result presented in Fig. 6.11, where the relative differences in N_{max} resulting from usage of the different Cherenkov models are plotted versus the viewing angle

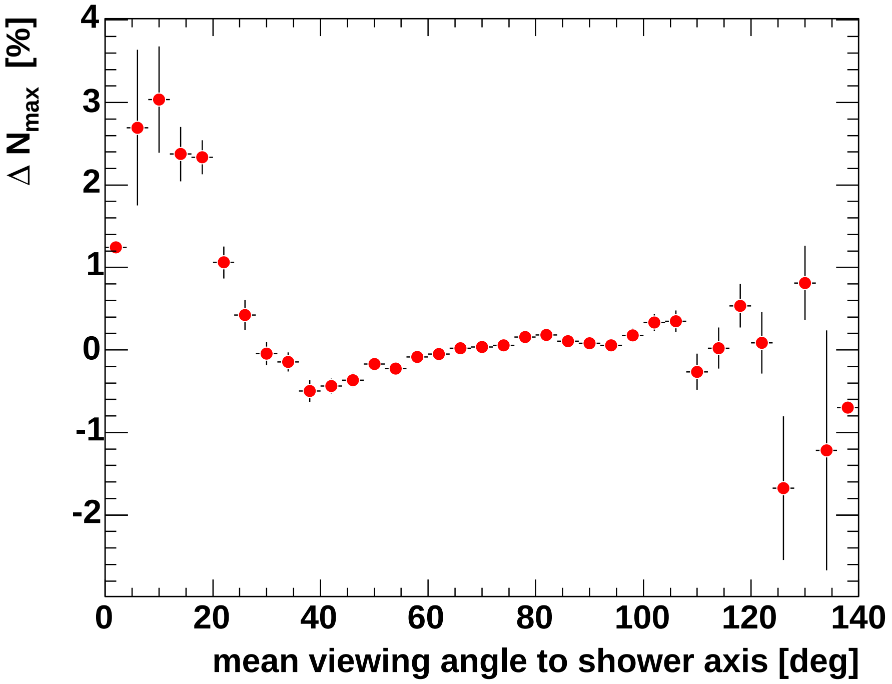

Figure 6.11: Impact of new Cherenkov model on reconstructed $N_{\max}$ versus viewing angle, for discussion see text.

with respect to the shower axis. The differences are well below ± 1 % for larger angles to shower axis. For angles smaller than 30°, there is a systematic increase with decreasing viewing angle up to about +3 %. The higher the fraction of (direct) Cherenkov light is in a shower, the higher the change in reconstructed $N_{\max}$ is. This is the reason why it is emphasised, that if showers having larger (total) Cherenkov contribution than 35 % were reconstructed, the impact on $N_{\max}$ reconstruction is expected to be larger than +3 %.

The same study has been done for the reconstructed primary energy E_{p} and is presented in Fig. 6.12 and Fig. 6.13 respectively. The mean impact on energy reconstruction, as can be seen from the ΔE_{p} distribution, amounts about +0.4 %. Again in this case, the mean change due to the new Cherenkov model is even below a percent, but since the reconstructed energy is derived by integrating the reconstructed shower size profile, the impact on the integrated longitudinal shower size distribution is expected to be the larger the smaller the viewing angle is. Fig. 6.13 confirms this expectation, the relative differences in energy reconstruction, going back to application of the new model instead of the old one, show such dependence. Differences do not exceed ± 1 % for larger viewing angles, whereas below about 30°, deviations increase systematically with decreasing angle. For this angular region the primary energy is reconstructed significantly higher by up to about +2.5 %. Here, the same explanation holds again, the more a shower is contaminated by Cherenkov light, the bigger the impact through the new Cherenkov calculation on the reconstructed energies.

Finally, the effect on the reconstructed position of shower maximum $X_{\max}$, when using the new instead of the previous analytical Cherenkov description, is illustrated in Fig. 6.14

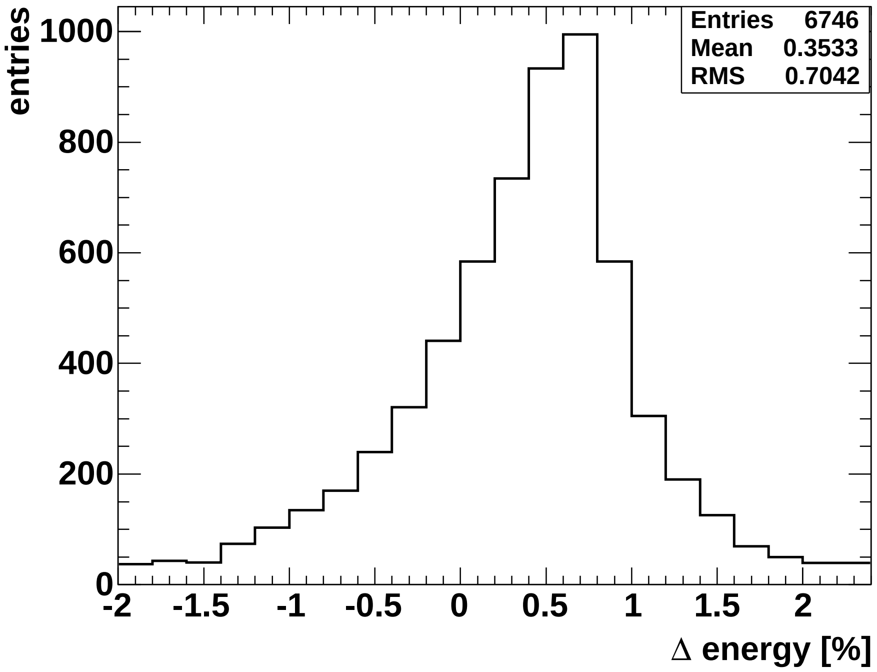

Figure 6.12: Impact of new Cherenkov model on energy reconstruction averaged over phase space, for discussion see text.

and Fig. 6.15 respectively. Since for composition studies absolute values are crucial, the differences ΔX_{max} are considered in terms of grammage rather than percentage. On average, reconstructed shower maxima are shifted by $+3.5\,\mathrm{g/cm^2}$ towards deeper penetration.

With respect to the mean viewing angle, there is a significant change of sign in resultant impacts on X_{max}. Having in mind Fig. 6.3 it is clear, that the position of the reconstructed shower size profile is affected by the constellation of direct and scattered Cherenkov light. When the fraction of direct Cherenkov light is large (small viewing angles), rather the position of maximum of the size profile is shifted to lower slant depth values by subtraction of the Cherenkov light curves from the raw light profile. In the opposite case of small direct Cherenkov contribution the same argumentation holds, but vice versa. As the amount of scattered Cherenkov light, being nearly isotropically distributed, stays more or less stable, i.e. only slightly depending on viewing angle, a small fraction of direct Cherenkov light rather leeds to a shift towards larger slant depths. Absolute differences do not exceed ± 1 % for larger viewing angles, whereas below about 30°, deviations increase systematically with decreasing angle.

In conclusion, the usage of the new Cherenkov calculation, instead of the previous one, for the Auger event reconstruction results in significant changes in reconstructed shower properties. It results in a smaller fraction of Cherenkov light in measured raw light profiles by about -4 % to -10 % depending on viewing angle. Consequently, the number of charged particles, primary energy and the position of shower maximum are reconstructed to be larger by +0.2 %, +0.4 % and $3.5\,\mathrm{g/cm^2}$ respectively, averaged over phase space. In dependence

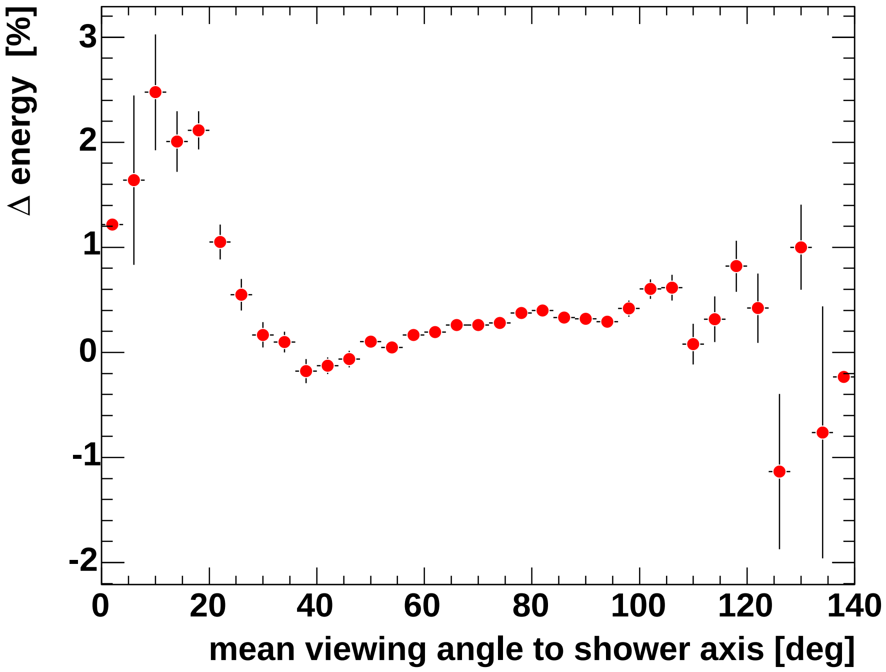

Figure 6.13: Impact of new Cherenkov model on energy reconstruction versus viewing angle, for discussion see text.

of the viewing angles with respect to the fluorescence telescope, impacts are larger. Here, the affect on reconstructed N_{max} can be as large as $+3\,\%$ and on reconstructed energy up to $+\ 2.5\,\%$ for small viewing angles for which the Cherenkov contribution increases. In the case of reconstructed X_{max}, differences range between $+6\,\mathrm{g/cm^2}$ for large viewing angles and $-6\,\mathrm{g/cm^2}$ for showers developing towards the fluorescence detector. The results presented are quantitatively as well as qualitatively totally in agreement with the comparison studies with respect to the Monte Carlo. It has to be emphasised, that the current reconstruction chain as it has been used for this study do not work for shower light profiles containing Cherenkov fraction larger than $35\,\%$. The impact on reconstructed primary properties due to the new Cherenkov model are expected to be larger for those showers.

At least for shower reconstructions on an event by event basis in the case of very interesting cosmic rays of the highest energies, the up to now solution of Cherenkov subtraction algorithm is needed to be improved. Moreover, to ensure that the new Cherenkov calculation is improving the prediction of reality, it is planned to check that differences in mono-reconstructed primary properties of stereo observed events are cancelled completely out or at least are decreased when using the new Cherenkov model. Possibly, one can even measure the Cherenkov light produced by extensive air showers in the case of events observed in stereo mode.

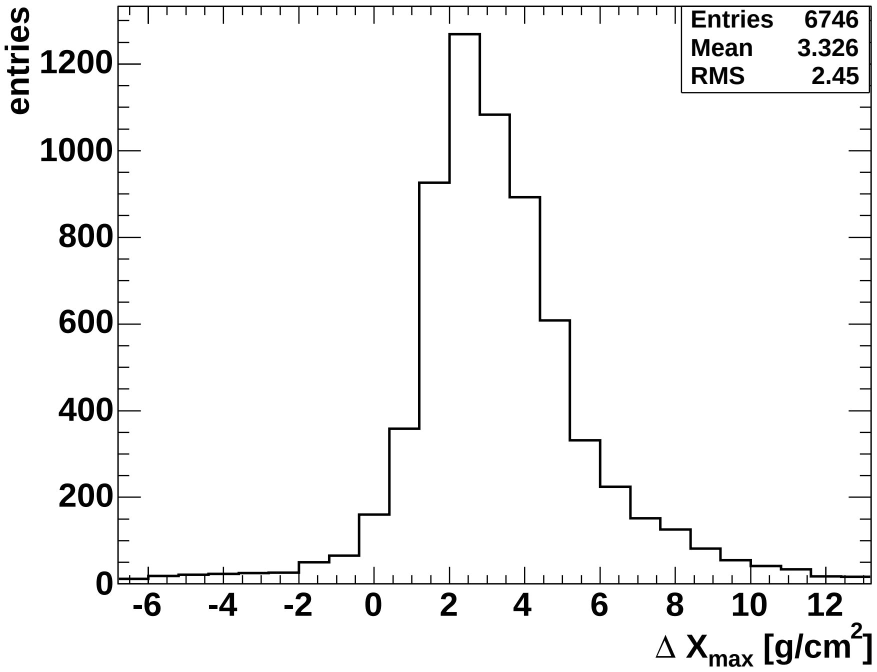

Figure 6.14: Impact of new Cherenkov model on reconstructed $X_{\rm max}$ averaged over phase space, for discussion see text.

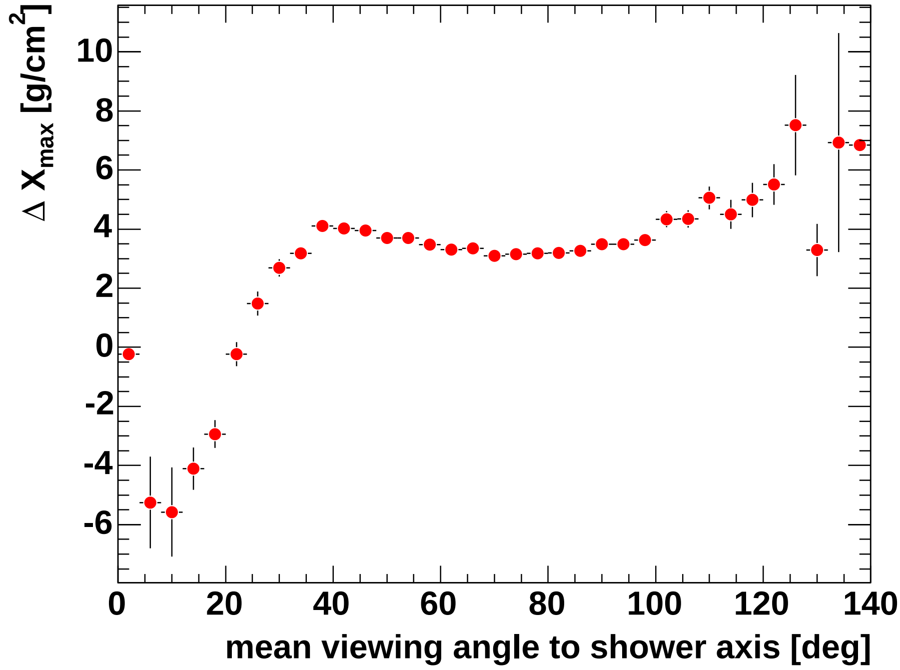

Figure 6.15: Impact of new Cherenkov model on reconstructed $X_{\rm max}$ versus viewing angle, for discussion see text.

Chapter 7

Summary & Outlook

Within this thesis Cherenkov light production in extensive air showers has been investigated with the aim of improving the event reconstruction of optically detected ultrahigh-energy air showers.

In the first part of this work, a new approximation for the analytical description of Cherenkov light production in extensive air showers has been developed. This approximation is based on parameterisations of the electron energy distribution and the angular distribution of produced Cherenkov photons with respect to the shower axis. The main results of this work are the following:

- It has been shown that, for ultrahigh-energy cosmic rays of energies above 10^{18} eV, the electron energy distribution in air showers is universal. The distribution neither depends significantly on primary mass nor on primary energy.
- On the basis of CORSIKA simulations, a new parameterisation of the differential electron energy distribution in extensive air showers has been derived. This parameterisation depends only on shower age and not on primary particle type and energy. It accounts for a given low energy threshold, as it always has to be used in air shower simulations and is needed in applications like e.g. calculating Cherenkov light for a given simulated longitudinal profile. For the energy and shower age range of interest, the achieved accuracy of prediction of the Monte Carlo data is better than a few percent. Applying this ansatz, including shower-to-shower fluctuations, the Monte Carlo simulated distribution is reproduced better than 25 % for the whole energy range from 1 MeV to 10 GeV, in the range of shower ages from $s = 0.8$ to $s = 1.2$.
- Using the proposed analytical function for the electron energy distribution, the total number of produced Cherenkov photons can be calculated with an accuracy better than 2 % relative to CORSIKA predictions in the whole shower age range important for the fluorescence technique. This is a significant improvement as compared to existing parameterisations.
- A new parameterisation of the angular distribution of produced Cherenkov photons in extensive air showers has been introduced. It has been shown that, for an efficient description of the Cherenkov photon angular distribution, the dependence on the refractive

index (originating from the height dependence of the energy threshold for Cherenkov production) and the dependence on the shower age (induced by the shower age dependence of underlying electron energy distributions) has to be taken into account. Again CORSIKA simulations were used to determine the parameters of this parameterisation and to verify its validity. Applying this parameterisation, showers are universally described, independent of their inclination angle, primary mass and energy. Including shower-to-shower fluctuations, the predictions based on this new ansatz are in agreement with the CORSIKA results within 5 % at shower maximum (10 % for s = 0.8 and 3 % for s = 1.2).

- The complete Cherenkov model introduced in this work, i.e. calculation of the total Cherenkov photon number produced per angular and depth interval, has been tested and compared to CORSIKA predictions. Applying this model, agreement with CORSIKA is achieved within a few percent. This has to be compared to deviations of up to 30 % found if previous models are used.
- The new Cherenkov model has been implemented and tested in the Auger data analysis framework, and is available for use in the event reconstruction within the Pierre Auger Collaboration.

In the second part of this work, the new Cherenkov light production model has been applied to the currently available Auger fluorescence data set (Sept. 2003 - Oct. 2004) in order to determine the impact of its application on the event reconstruction. The data has been reconstructed with the old and with the new Cherenkov model. Changes in the reconstructed primary parameters due to the new model have been analysed on an event-by-event-basis. They can be summarised as follows

- fraction of Cherenkov light $\Delta f_{\mathrm{Ch.}}$: -4 % to -10 %, depending on viewing angle.
- number of charged particles at shower maximum ΔN_{max}: +0.2 % , averaged over phase space.
- primary energy ΔE_{p}: +0.4 % , averaged over phase space.
- depth of shower maximum ΔX_{max}: +3.5 g/cm^2, averaged over phase space.

As already the change in the reconstructed fraction of total Cherenkov light depends on the viewing angle, the impact on reconstruction of primary parameters also depends on this angle. Based on the set of reconstructed events this dependence can be quantified as

- $\Delta N_{\mathrm{max}} \leq +3\,\%$,
- $\Delta E_{\mathrm{p}} \quad \leq +2.5\,\%$,
- $\Delta X_{\mathrm{max}} \leq \pm 6\,\mathrm{g/cm}^2$.

It is emphasised that the changes are relatively small, but significant and contribute to the systematic reconstruction uncertainties. They increase with the fraction of Cherenkov light contributing to the observed light profile for individual events. It is expected that showers with small viewing angles are considerably better reconstructed with the proposed Cherenkov light approximation than using previous ones. All changes of the reconstructed quantities are in agreement with the expected dependence on viewing angle based on the comparison with Monte Carlo results.

The current version of the data analysis chain only reconstructs events containing Cherenkov fractions of less than about 30 %. This indicates that the Cherenkov subtraction algorithm, as it is implemented presently, fails to converge for events with large Cherenkov light contribution. In particular showers observed with viewing angles smaller than 20° are affected by this shortcoming as the direct Cherenkov light is larger or of the same order as the fluorescence light. Moreover, the data analysis shows that the reconstructed number of charged particles at shower maximum is less sensitive to the Cherenkov background treatment than the reconstructed primary energy. Thus, the proposed approach of determining the primary energy rather from the quantity N_{max} than from the integrated reconstructed longitudinal shower size profile [Alvarez-Muniz et al. 2004] is supported by this result.

It would be worthwhile to use the advantage of stereo events being observed simultaneously with different fluorescence detectors, different viewing angles and geometries. Comparing the independently reconstructed shower profiles allows an experimental check of the validity of the proposed Cherenkov model. However, stereo studies of this type are currently hampered by the limited statistics of stereo events. Additionally, on the basis of stereo events, also a measurement of atmospheric properties like attenuation lengths should be possible by measuring the Cherenkov light detected from different detector sites at different distances. Analyses of this type will be very valuable once enough stereo events have been collected.

Future work on the Cherenkov model itself could focus on fitting larger sets of high quality simulated distributions, i.e. applying very good thinning, in order to improve the quality of the fits. In particular, for the parameterisation of the Cherenkov photon angular distribution, the range of shower zenith angles would be worthwhile to be extended. The used set of simulations is restricted to zenith angles smaller than 60° due to CORSIKA limitation.

It would be worthwhile studying to which degree the parameterisation of the electron energy spectra could be improved at higher energies by introducing a height dependence. This idea is supported by the observation of increasing deviations in the description for electron energies larger than a few GeV with increasing primary zenith angles. It is suspected that this systematic effect could be related to the dependence of the pion decay probability on zenith angle getting important at higher energies.

The investigation of the Cherenkov light production in extensive air showers presented is based on the classical treatment of the Cherenkov light effect. The quantum theoretically treatment of Cherenkov production [Ginsburg 1940, Tidman 1956], gives practically the same result with additional higher order terms, which are negligible for the purpose of this work, see e.g. [Zrelov 1970].

Finally, it is mentioned that also the idea of a mesonic Cherenkov effect based on relativistic quantum field theory has been considered [Wada 1949]. Such a Cherenkov-like effect is still investigated and has been extended to all four fundamental forces; for a generalised two-component Cherenkov-like effect some experimental evidence exist, see [Ion 2003]. Even though this would be a different field of research, for the farther future the mesonic Cherenkov effect could become important to be considered also for astroparticle physics.

Appendix A

Appendix: Electron Energy Spectra

A.1 Monte Carlo Simulations - Upward going particles

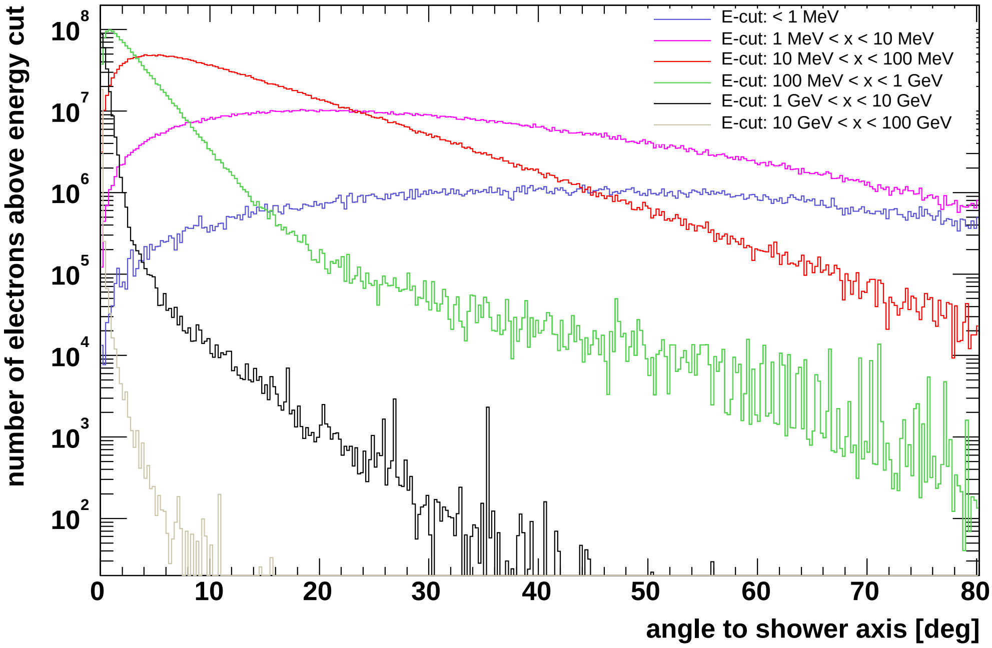

Figure A.1: Electron angular distribution with respect to shower axis at shower maximum. (proton, 10^{19} eV, $0°$). From the energy dependent angular distribution of electrons it can be seen, that for energies above the Cherenkov energy threshold (~ 20 MeV), the distribution is relatively steep. Only a small fraction of electrons above the Cherenkov threshold are found at angles larger $30°$, above which the problem of multiple counting occurs, when the `UPWARD` option is enabled, see also Fig. A.2. Thus, as long as not zenith angles close to $60°$ are chosen, the effect of undefined shower size, i.e. multiple counting, is negligable for the purpose of Cherenkov calculations. See for comparison also Fig. A.23/A.24 and Fig. A.25/A.26.

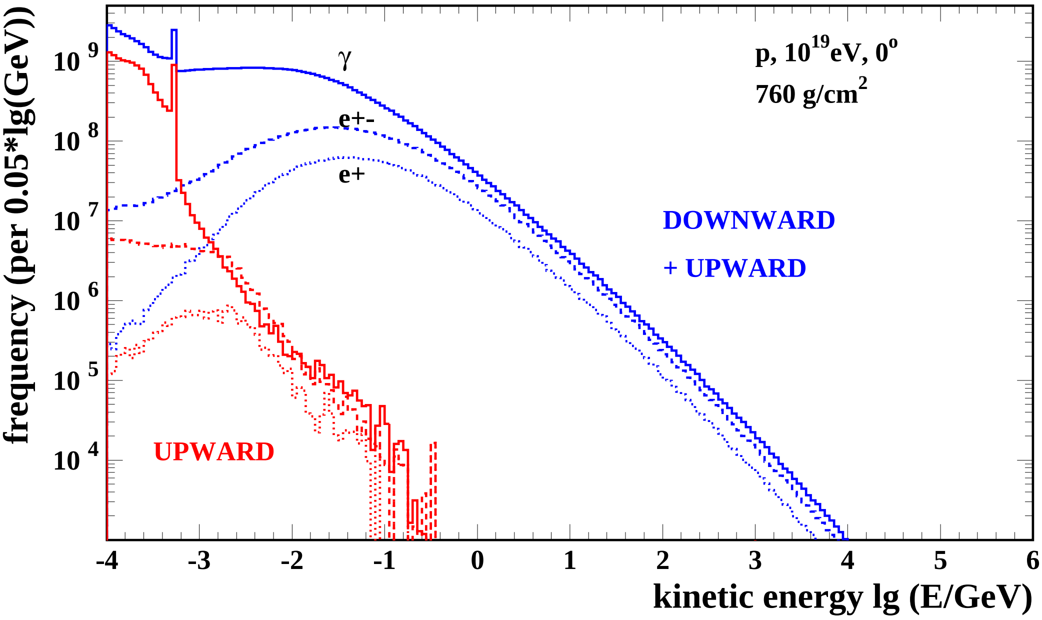

Figure A.2: Electron Energy Spectra - Comparison of upward and downward going particles. The fraction of upward going electrons in the energy range of interest for Cherenkov calculations (> 20 MeV $\approx -1.7\,\mathrm{lg}(E/\mathrm{GeV})$) is negligible. The peak at about 0.5 MeV ($\approx -3.3\,\mathrm{lg}\,(E/\mathrm{GeV})$) is due to annihilation. ([Risse 2003])

A.2 Interpolation in Shower Age

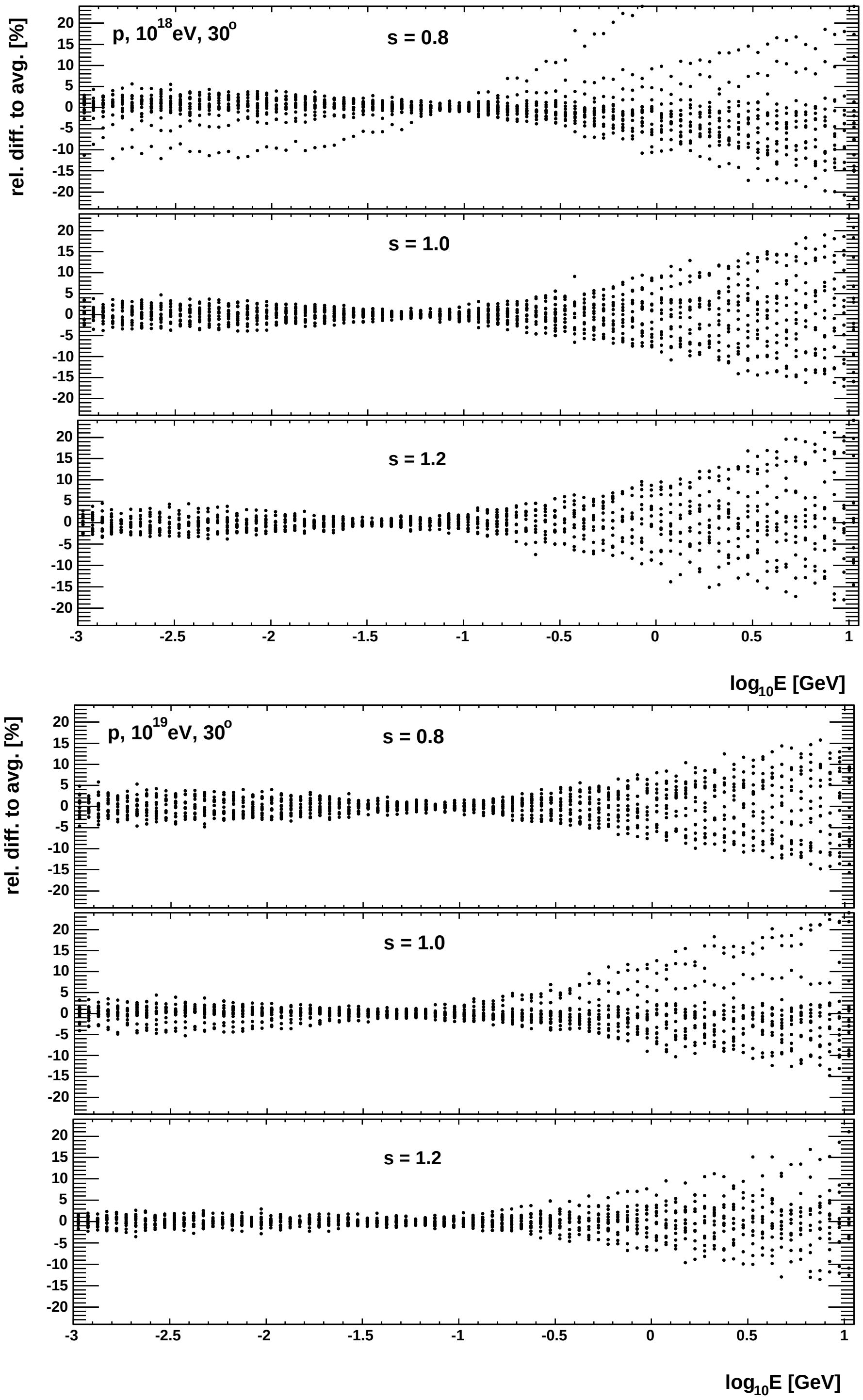

Figure A.3: Electron Energy Spectra. Shower-to-shower fluctuations of electron energy spectra (normalised according to Eq. (4.2)) are demonstrated for three different shower ages $s = 0.8$, $s = 1.0$, and $s = 1.2$. The relative differences of the electron energy spectra to the mean spectrum have been calculated by averaging the spectra of 15 proton showers (10^{18} eV/10^{19} eV).

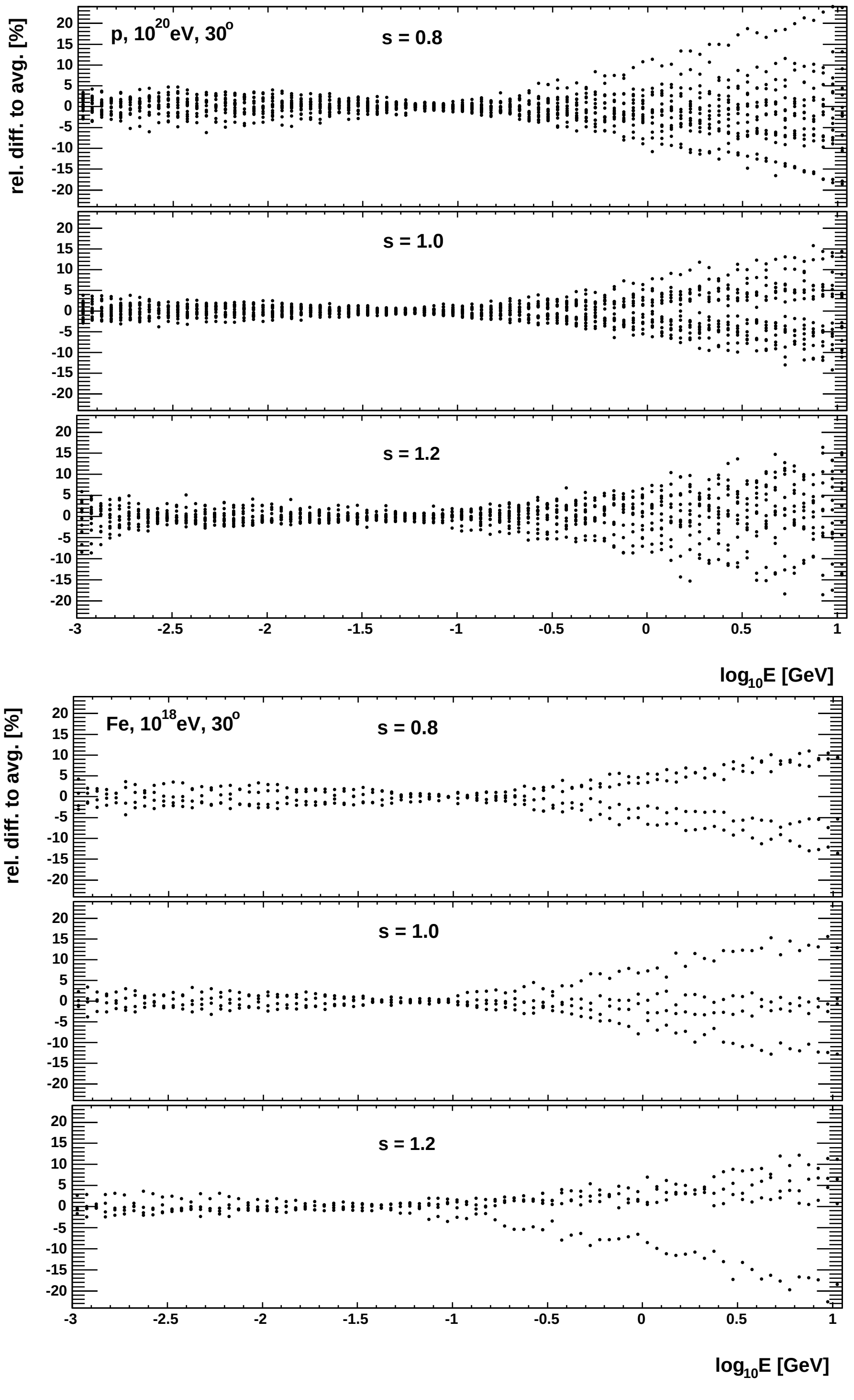

Figure A.4: Electron Energy Spectra. Shower-to-shower fluctuations of electron energy spectra (normalised according to Eq. (4.2)) are demonstrated for three different shower ages $s = 0.8$, $s = 1.0$, and $s = 1.2$. The relative differences of the electron energy spectra to the mean spectrum have been calculated by averaging the spectra of 15 proton/4 iron showers (10^{20} eV/ 10^{18} eV).

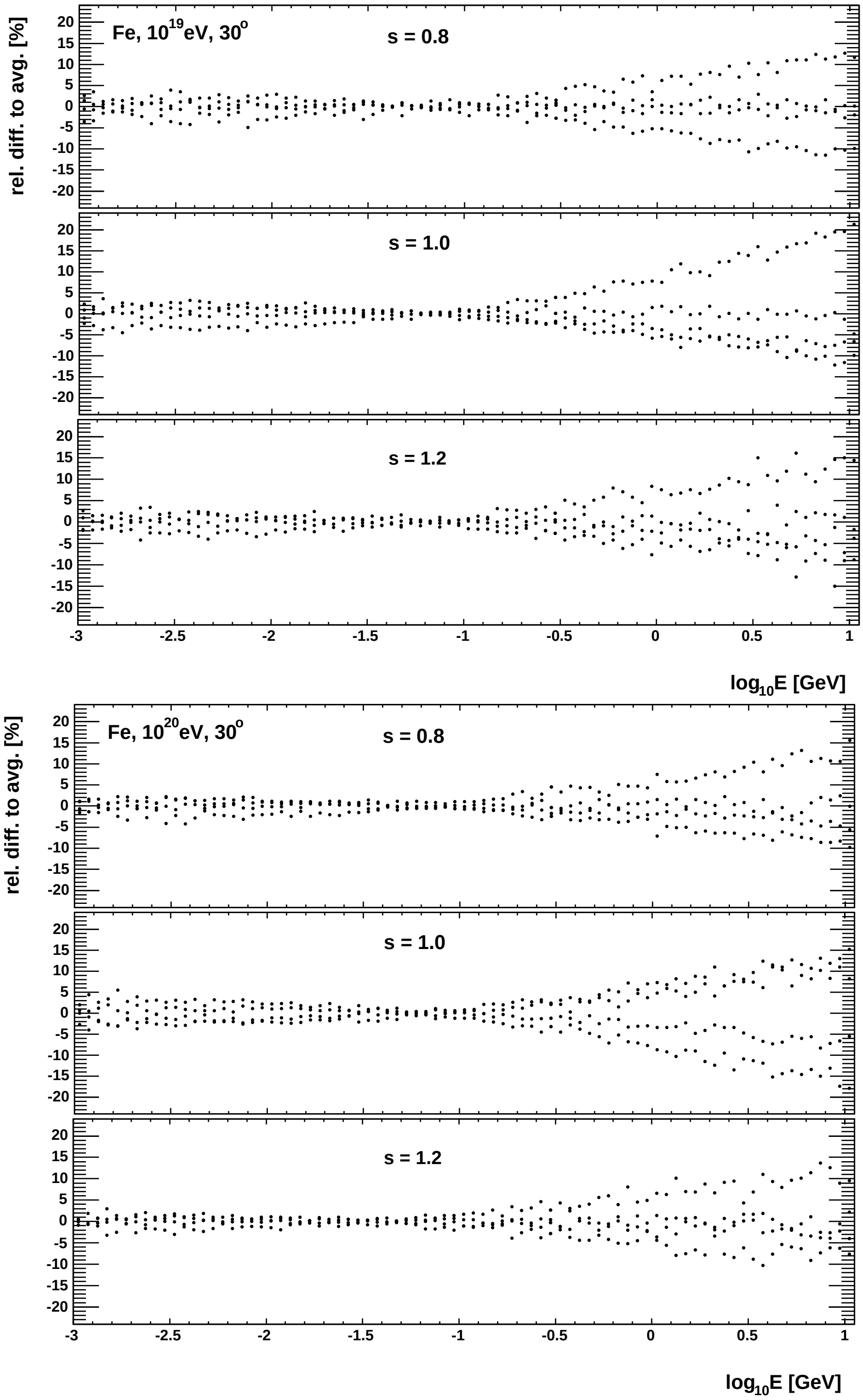

Figure A.5: Electron Energy Spectra. Shower-to-shower fluctuations of electron energy spectra (normalised according to Eq. (4.2)) are demonstrated for three different shower ages $s = 0.8$, $s = 1.0$, and $s = 1.2$. The relative differences of the electron energy spectra to the mean spectrum have been calculated by averaging the spectra of 4 iron showers (10^{19} eV/ 10^{20} eV).

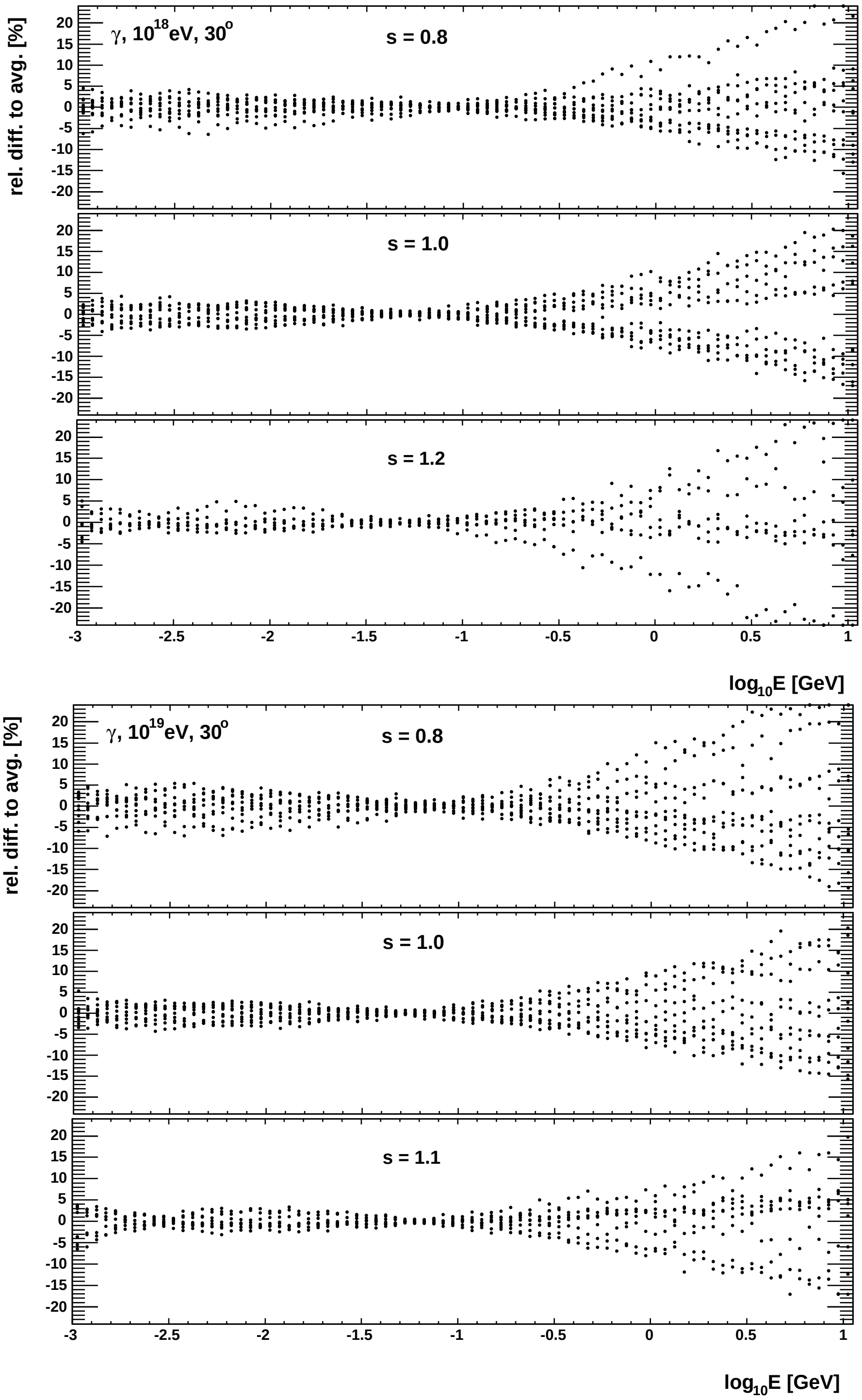

Figure A.6: Electron Energy Spectra. Shower-to-shower fluctuations of electron energy spectra (normalised according to Eq. (4.2)) are demonstrated for three different shower ages $s = 0.8$, $s = 1.0$, and $s = 1.2$ / 1.1. The relative differences of the electron energy spectra to the mean spectrum have been calculated by averaging the spectra of 10 gamma-ray showers (10^{18} eV/ 10^{19} eV).

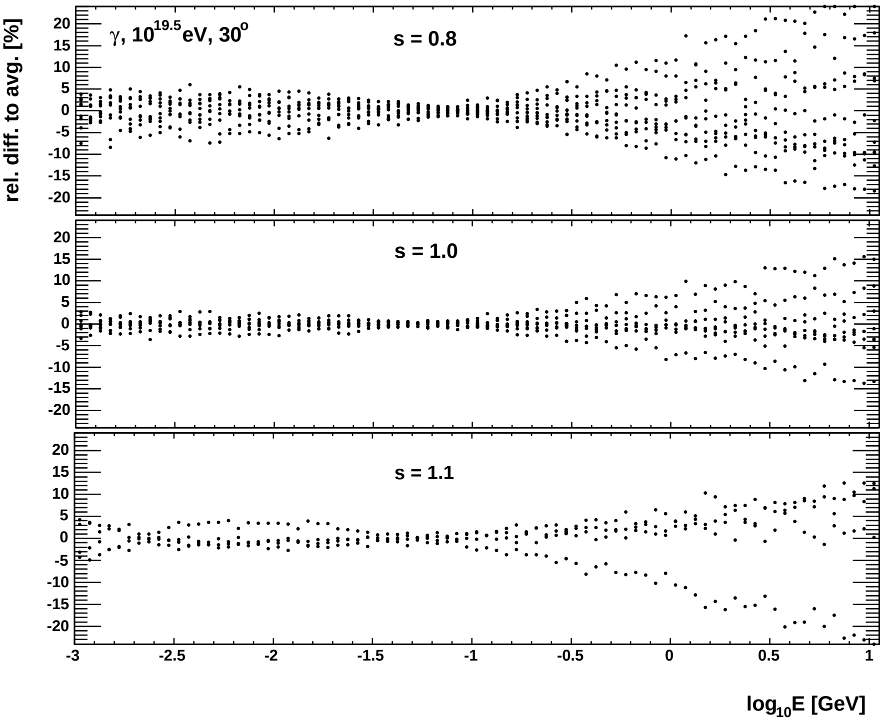

Figure A.7: Electron Energy Spectra. Shower-to-shower fluctuations of electron energy spectra (normalised according to Eq. (4.2)) are demonstrated for three different shower ages $s = 0.8$, $s = 1.0$, and $s = 1.1$. The relative differences of the electron energy spectra to the mean spectrum have been calculated by averaging the spectra of 10 gamma-ray showers ($10^{19.5}$ eV).

A.3 Universality

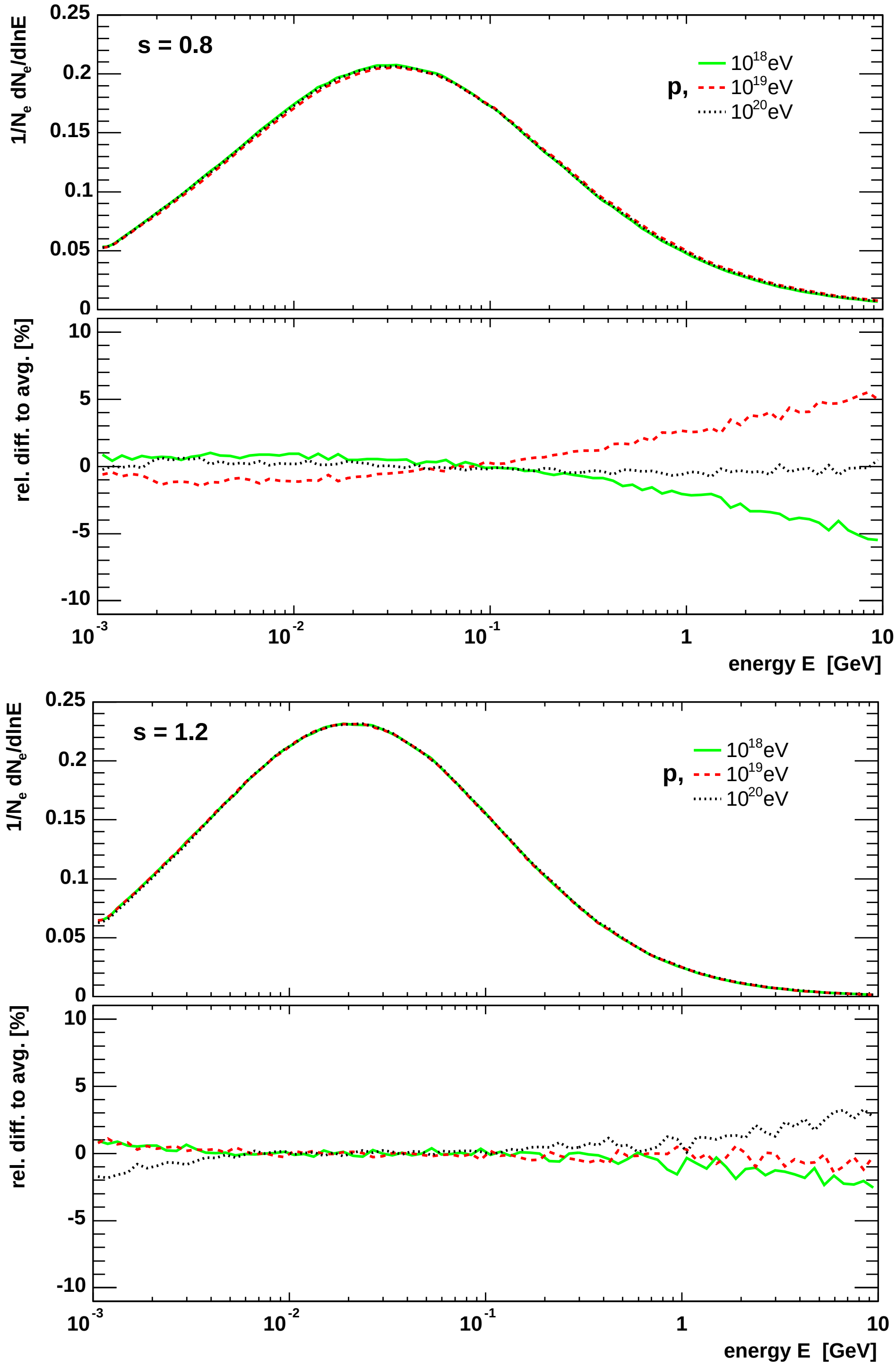

Figure A.8: Universality of electron energy distributions for proton showers of different primary energy. Mean proton showers of $10^{18}, 10^{19}$ and 10^{20} eV, here shown for $s = 0.8$ and $s = 1.2$.

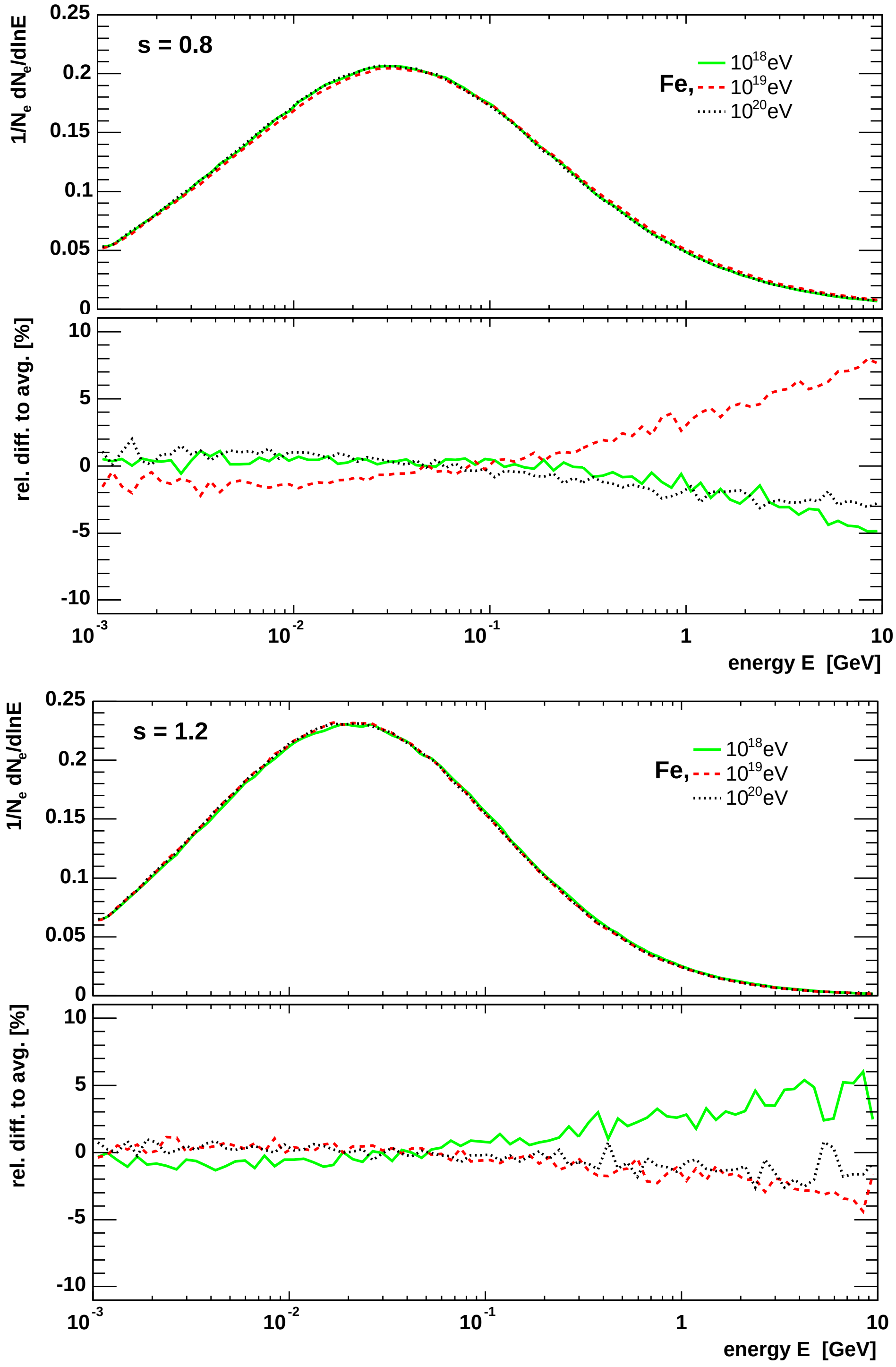

Figure A.9: Universality of electron energy distributions for proton showers of different primary energy. Mean iron showers of $10^{18}, 10^{19}$ and 10^{20} eV, here shown for $s = 0.8$ and $s = 1.2$.

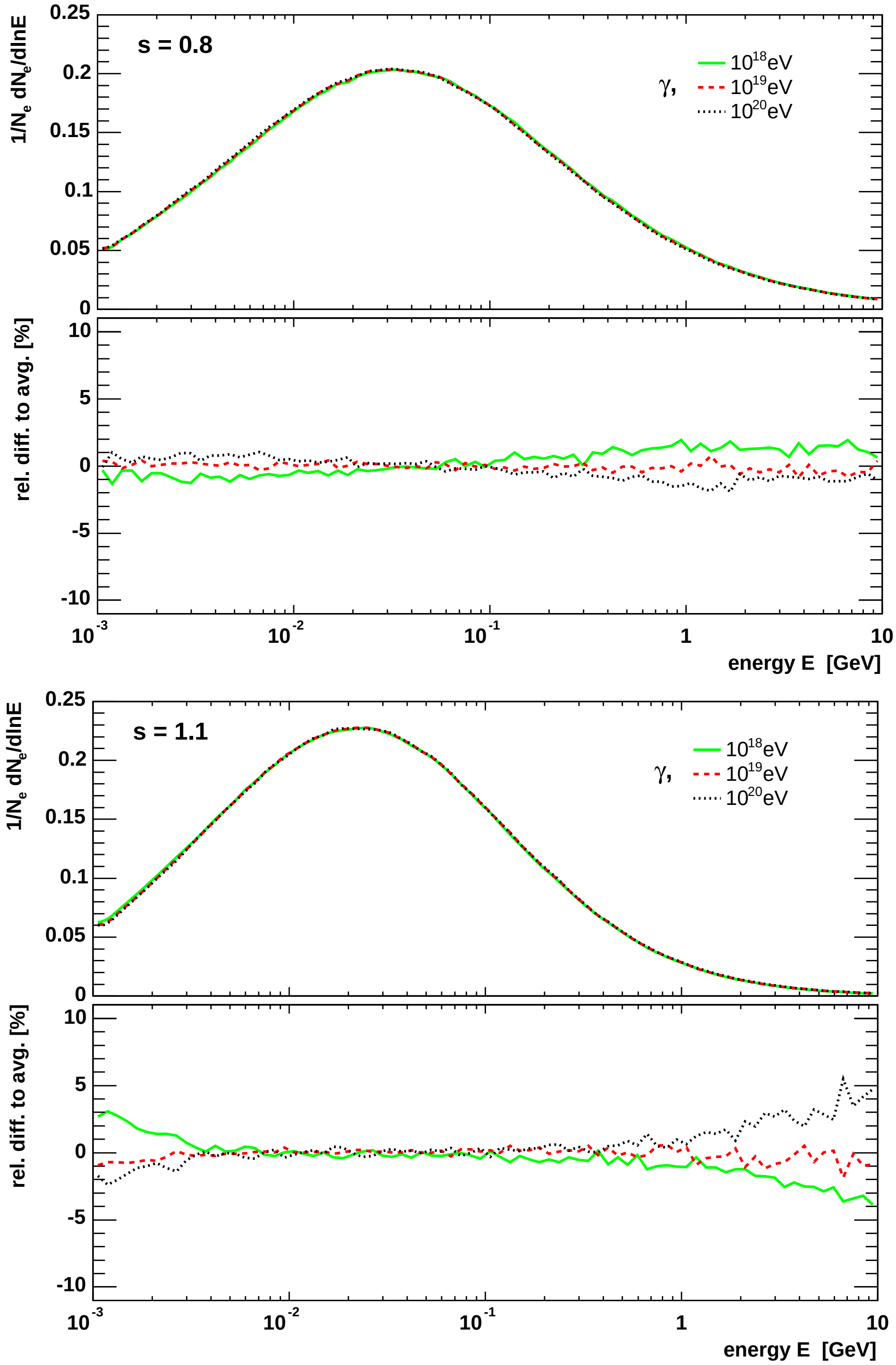

Figure A.10: Universality of electron energy distributions for proton showers of different primary energy. Mean gamma-ray showers of $10^{18}, 10^{19}$ and 10^{20} eV, here shown for $s = 0.8$ and $s = 1.2$.

A.4 Comparison to Other Parameterisations

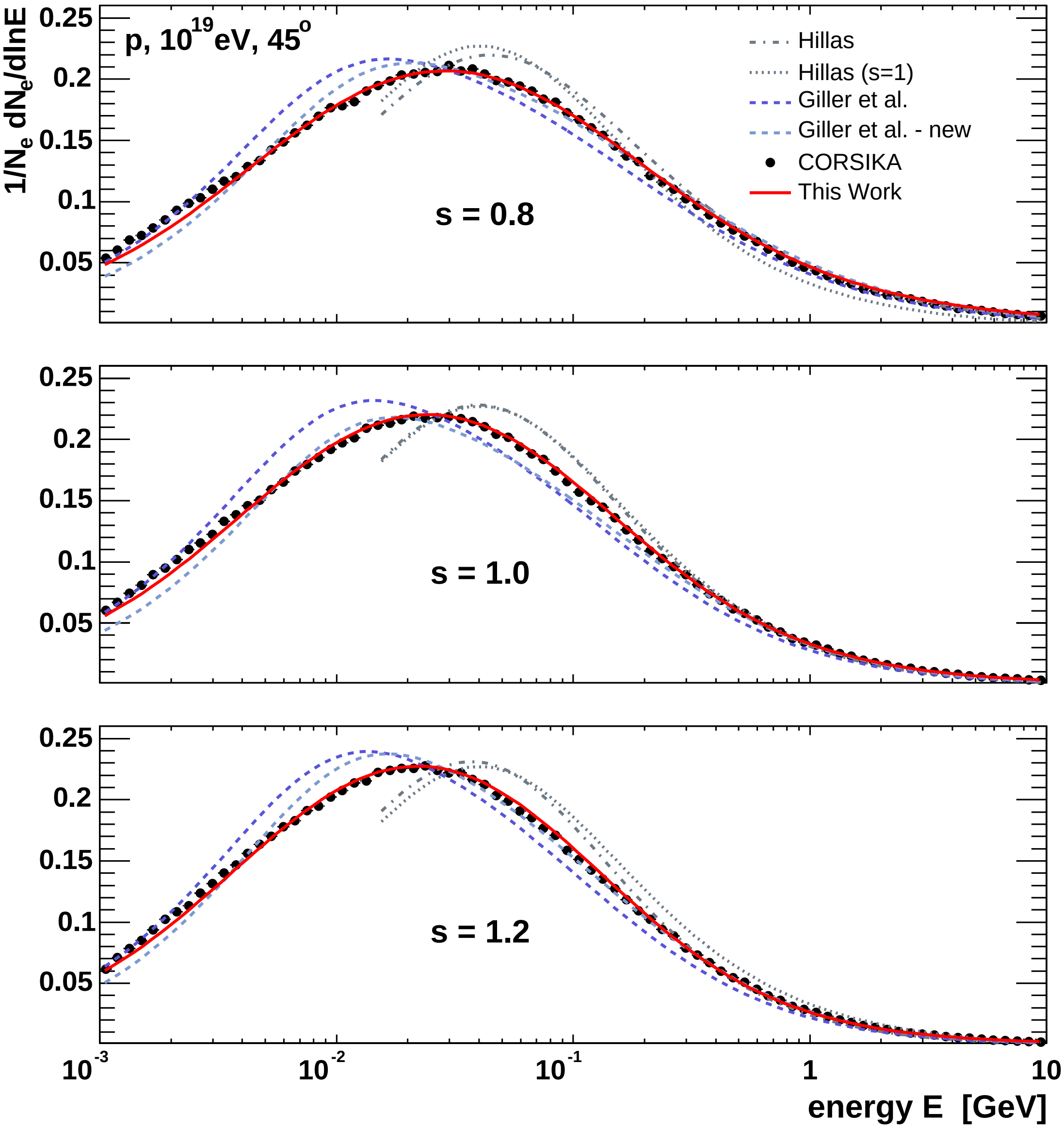

Figure A.11: Comparison to other parameterisations - proton, 10^{19} eV, $\theta = 45°$.

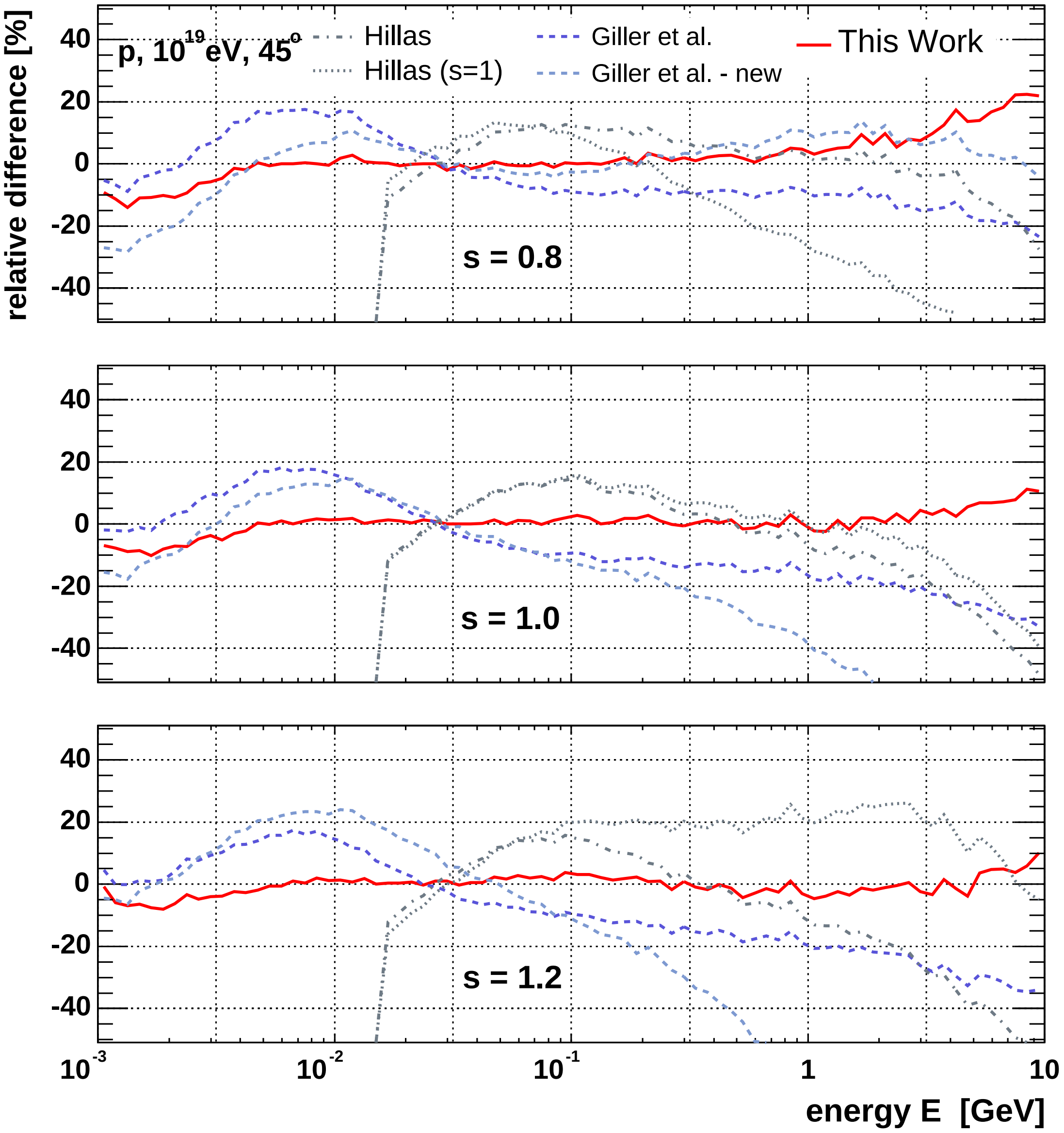

Figure A.12: Relative differences of different parameterisations to CORSIKA - proton, 10^{19} eV, $\theta = 45°$.

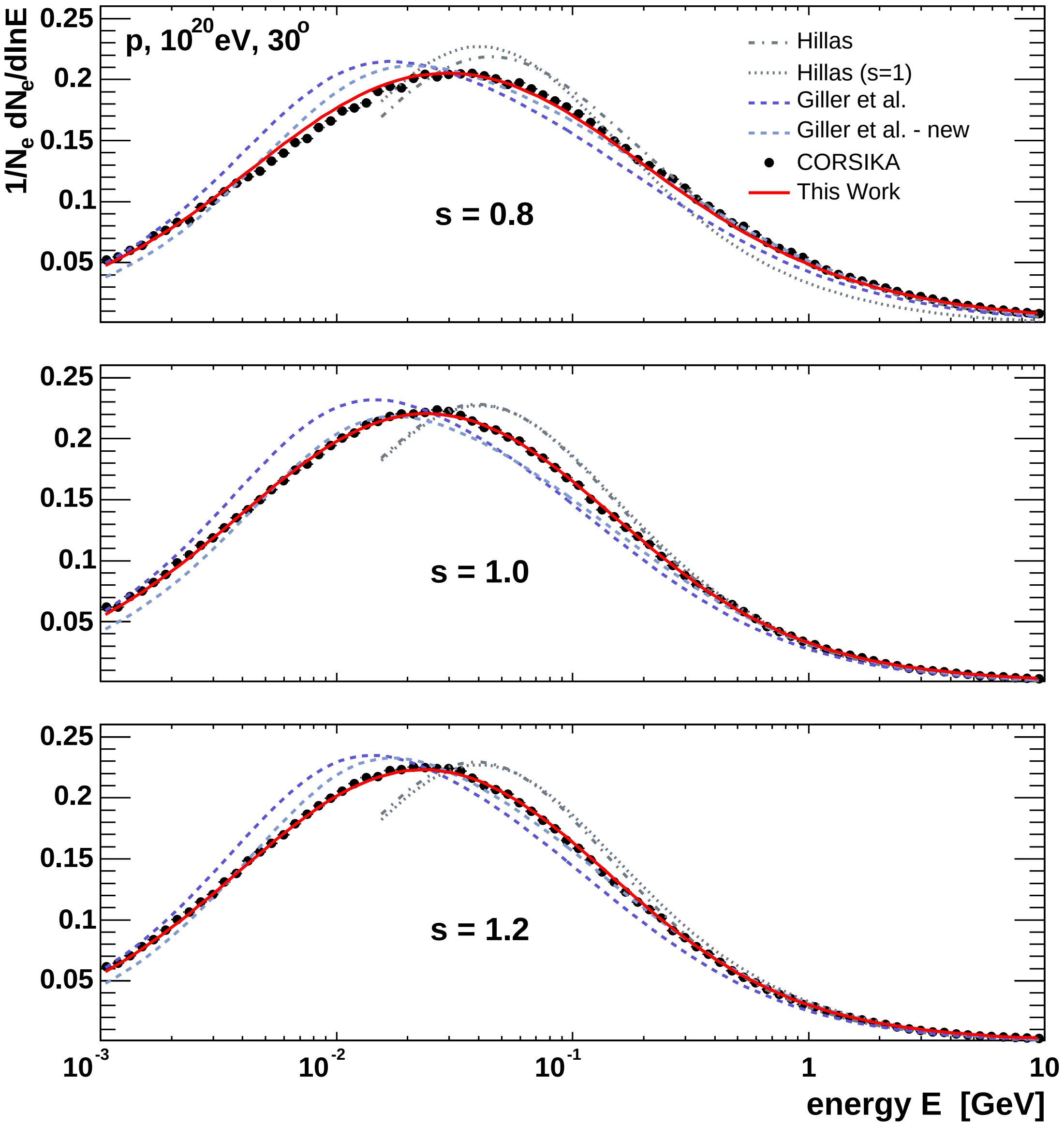

Figure A.13: Comparison to other parameterisations - proton, 10^{20} eV, $\theta = 30°$.

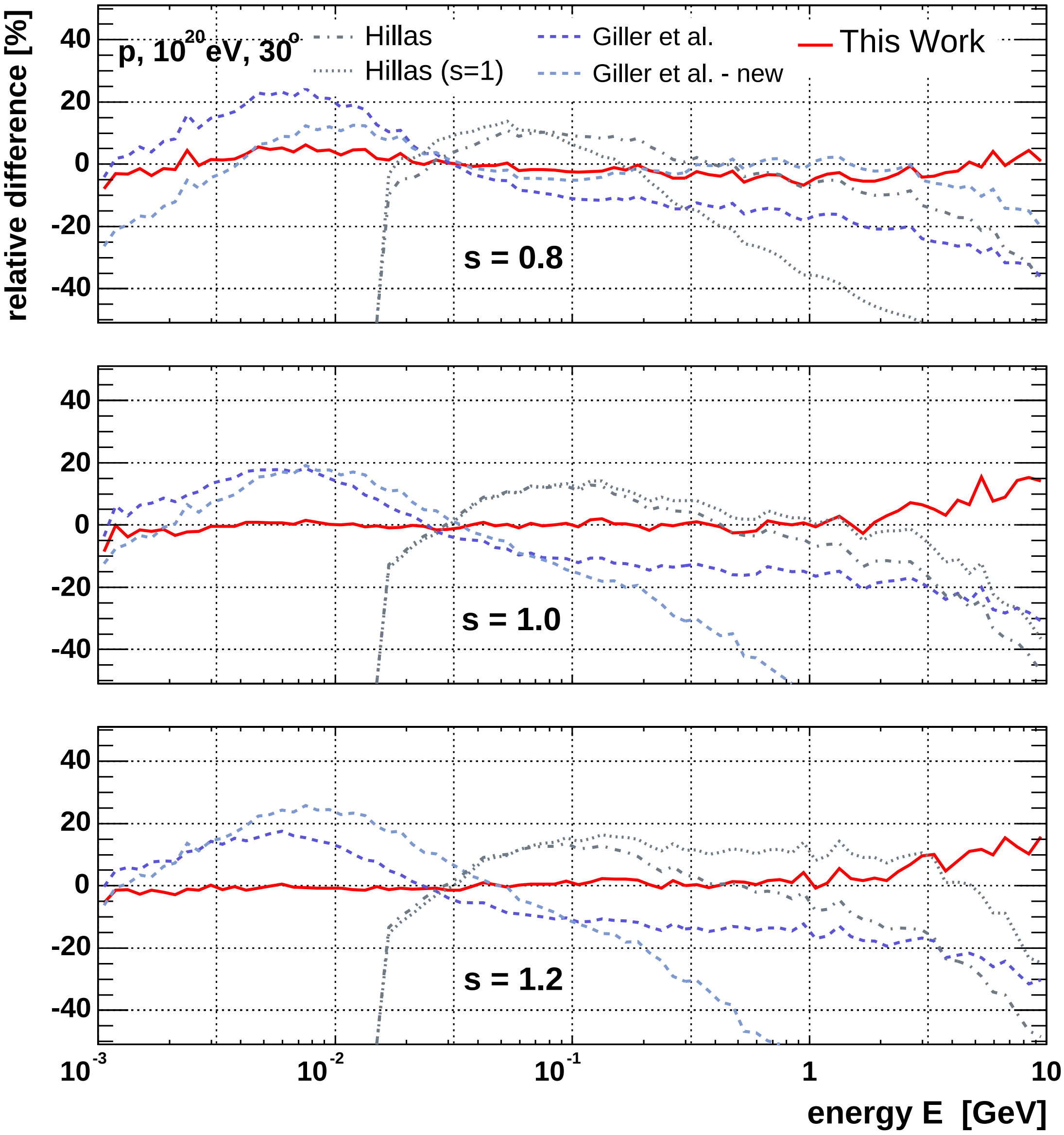

Figure A.14: Relative differences of different parameterisations to CORSIKA - proton, 10^{20} eV, $\theta = 30°$.

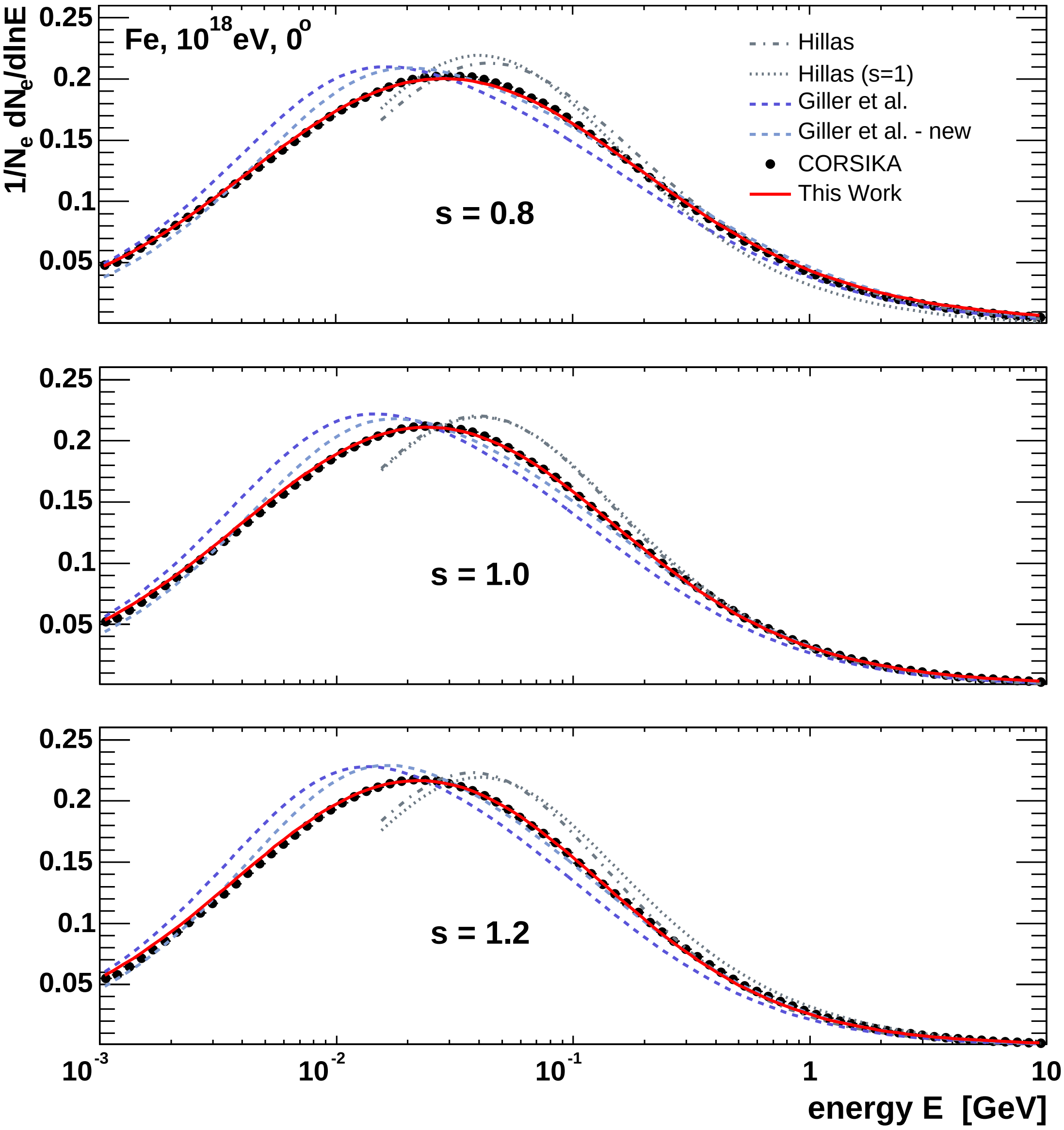

Figure A.15: Comparison to other parameterisations - iron, 10^{18} eV, $\theta = 0°$, opt. thinning 10^{-8}.

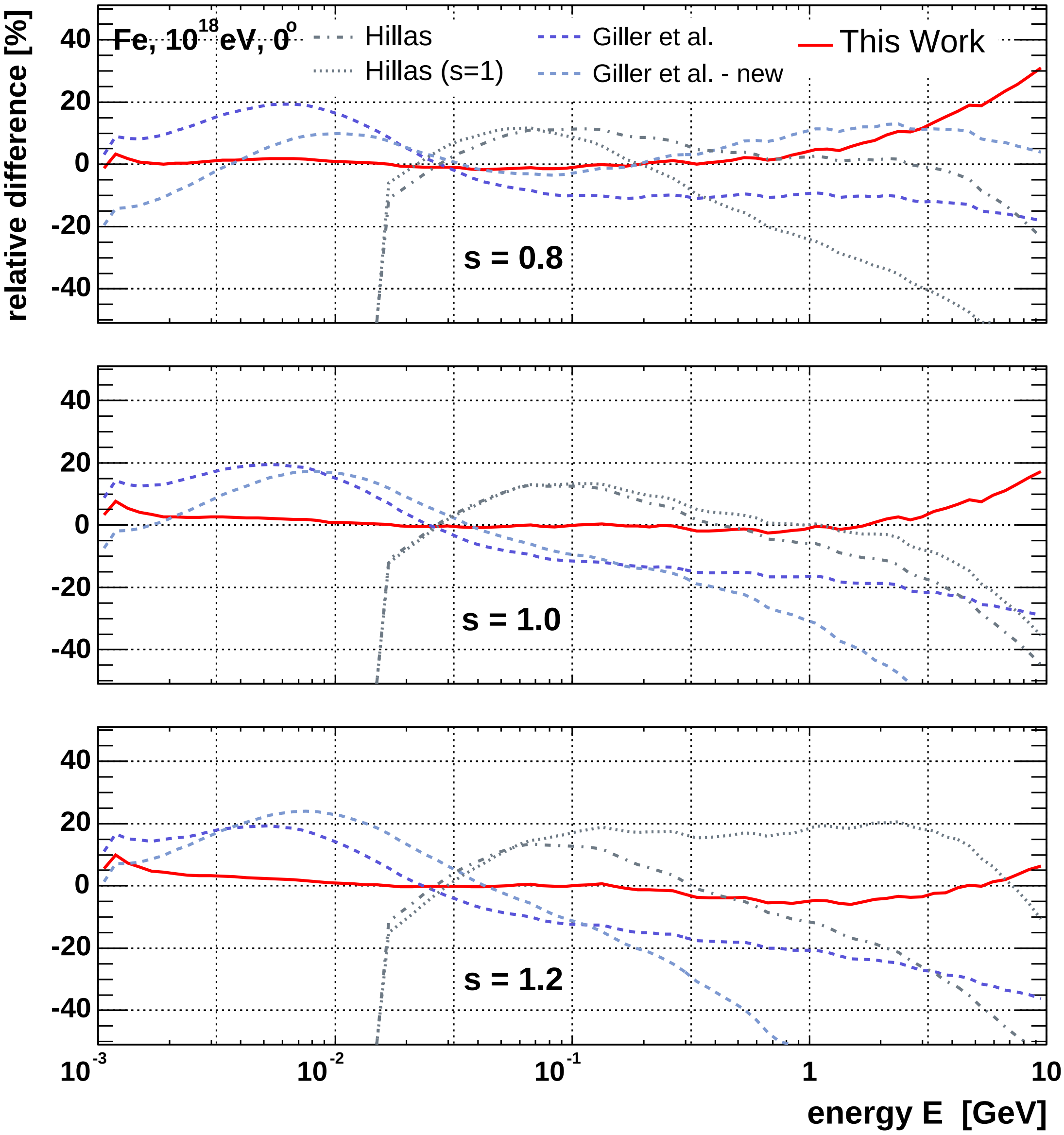

Figure A.16: Relative differences of different parameterisations to CORSIKA - iron, 10^{18} eV, $\theta = 0°$, opt. thinning 10^{-8}.

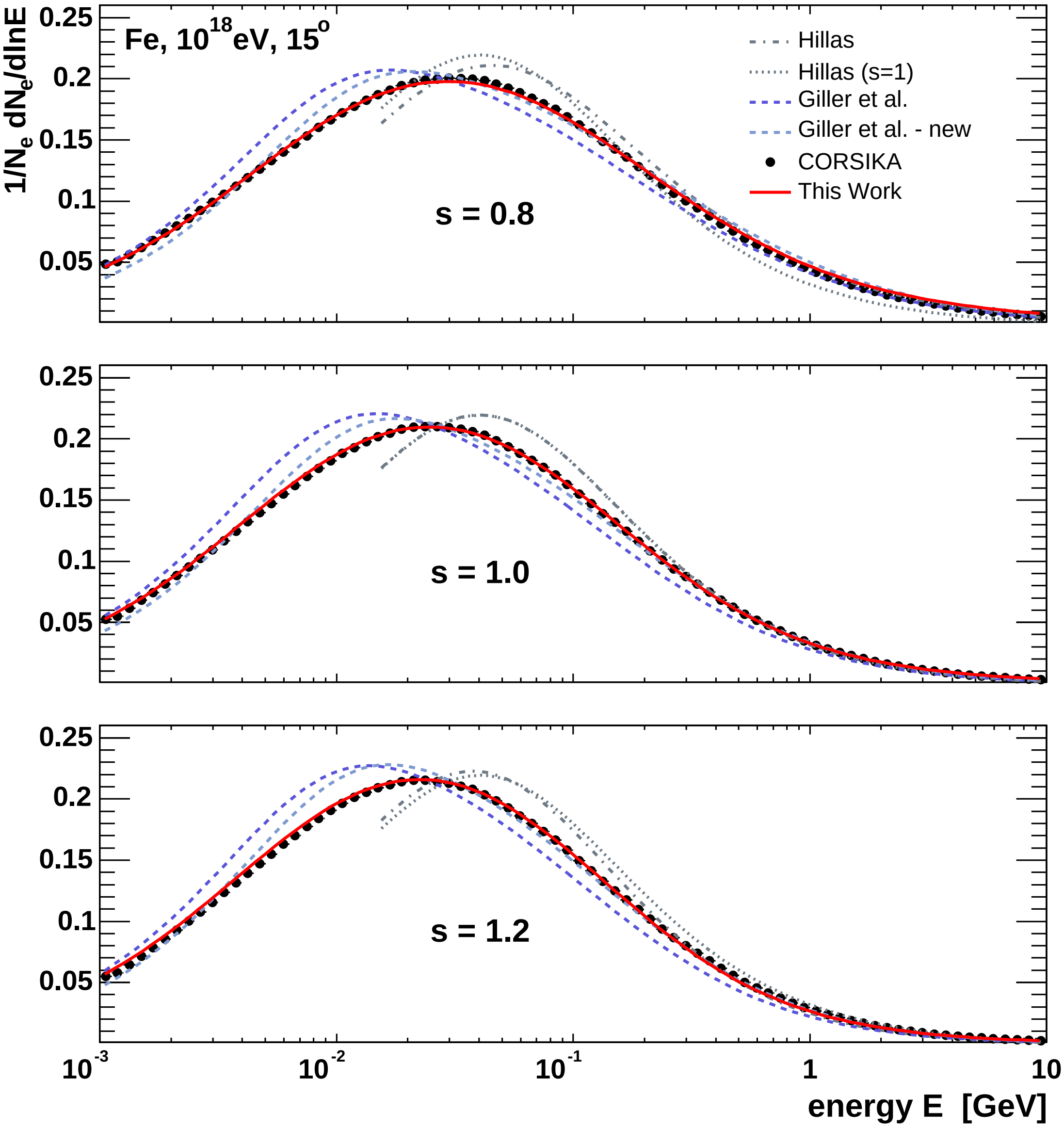

Figure A.17: Comparison to other parameterisations - iron, 10^{18} eV, $\theta = 15°$, opt. thinning 10^{-8}.

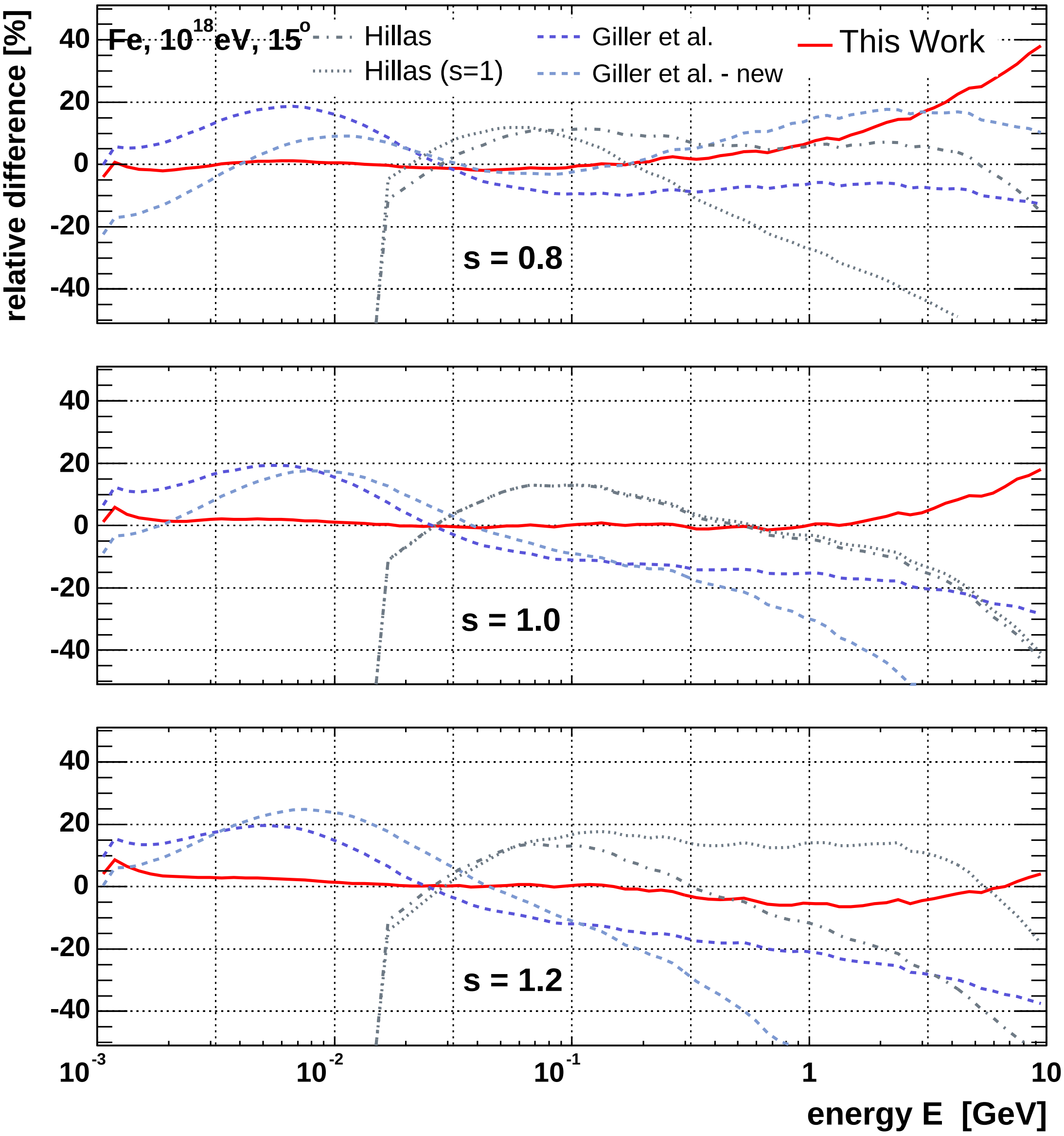

Figure A.18: Relative differences of different parameterisations to CORSIKA - iron, 10^{18} eV, $\theta = 15°$, opt. thinning 10^{-8}.

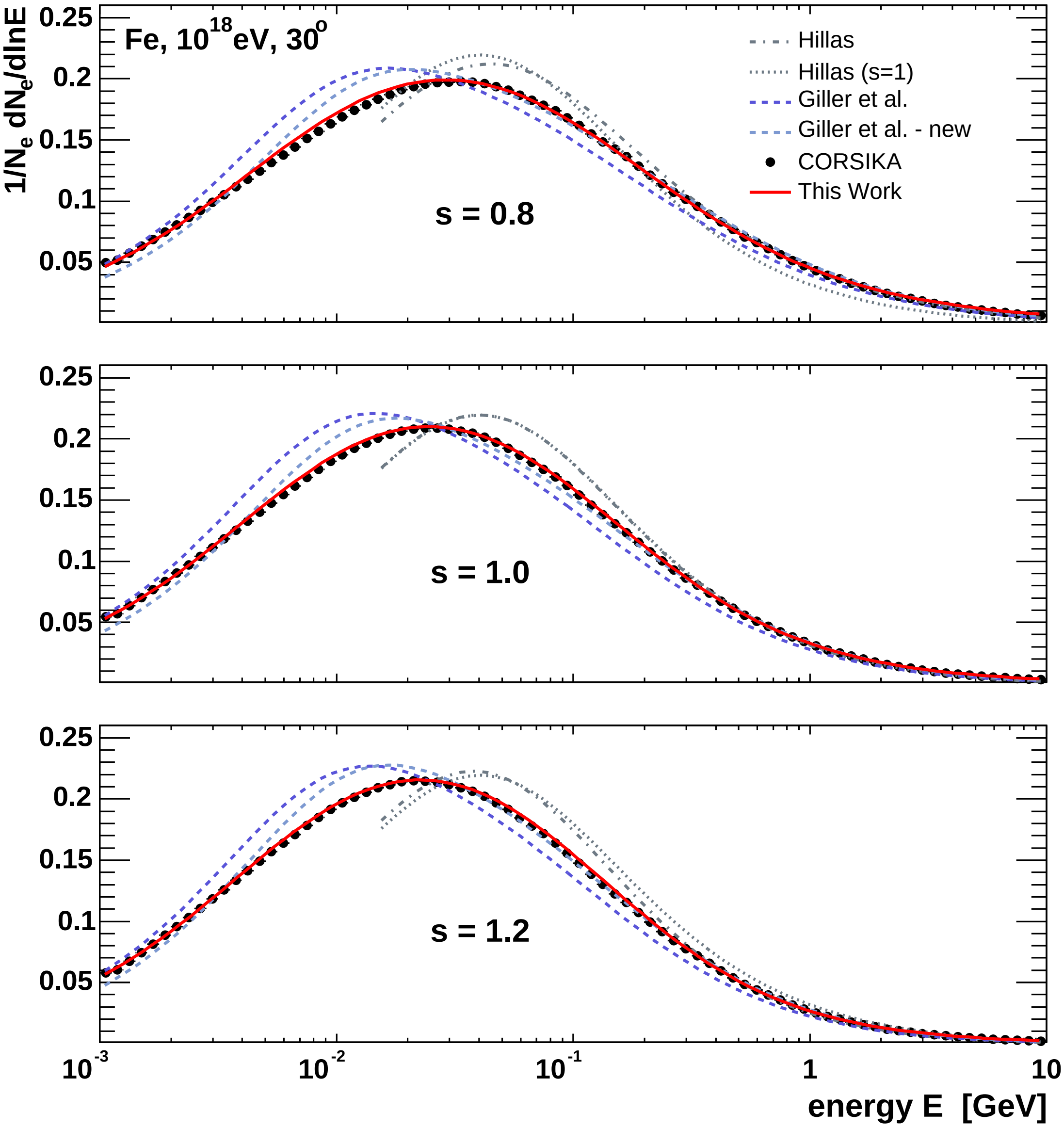

Figure A.19: Comparison to other parameterisations - iron, 10^{18} eV, $\theta = 30°$, opt. thinning 10^{-8}.

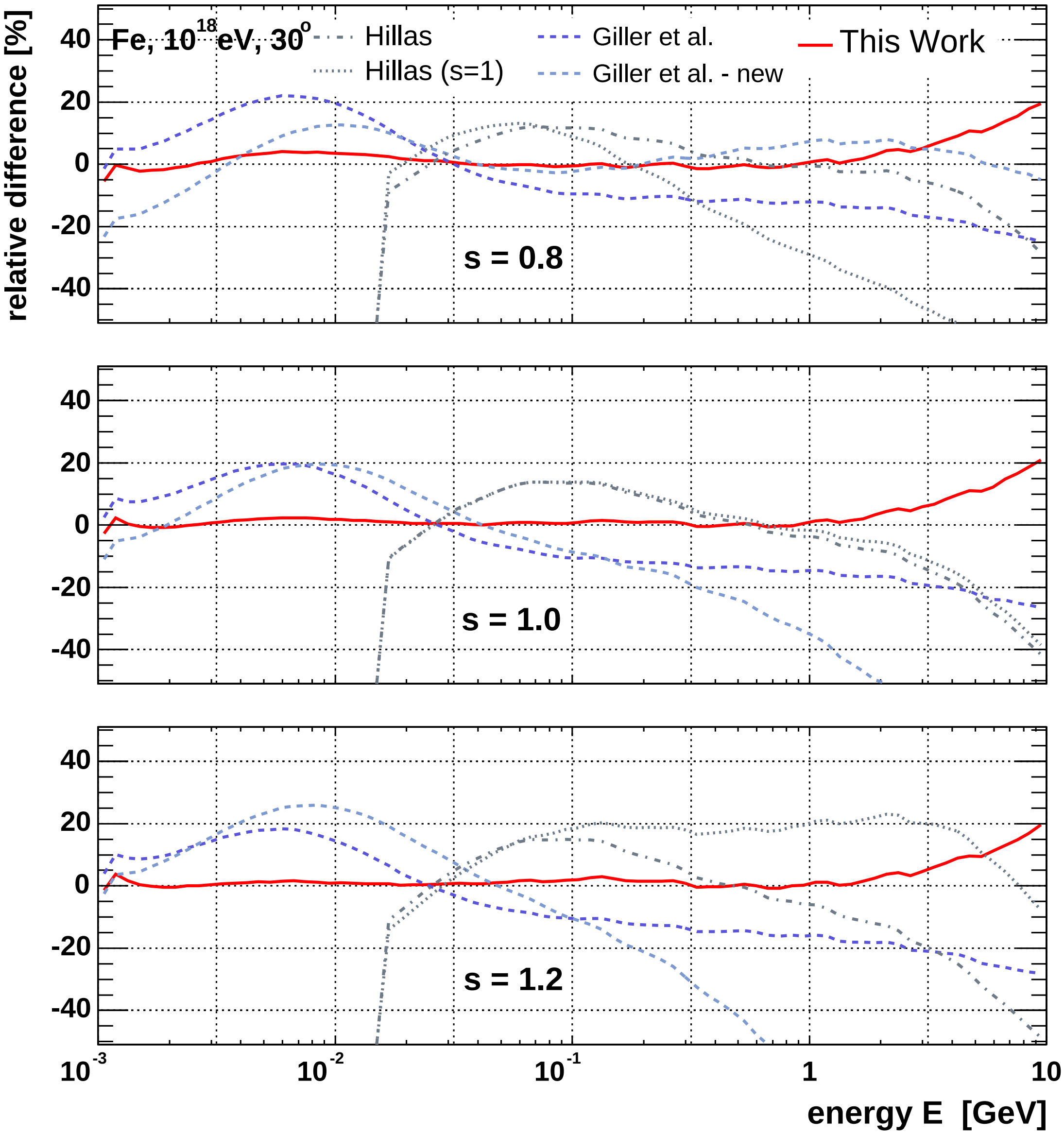

Figure A.20: Relative differences of different parameterisations to CORSIKA - iron, 10^{18} eV, $\theta = 30^{\circ}$, opt. thinning 10^{-8}.

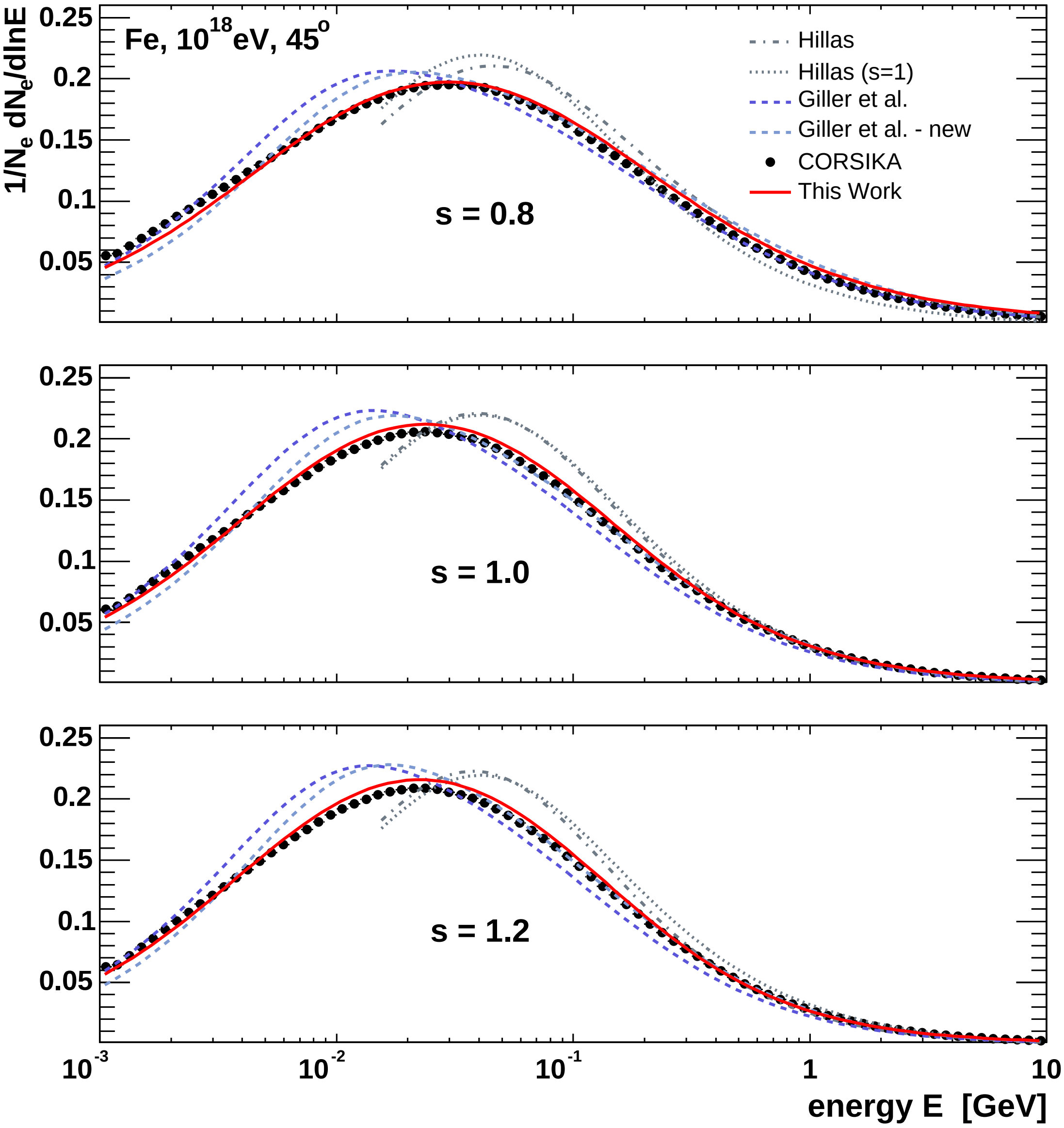

Figure A.21: Comparison to other parameterisations - iron, 10^{18} eV, $\theta = 45°$, opt. thinning 10^{-8}.

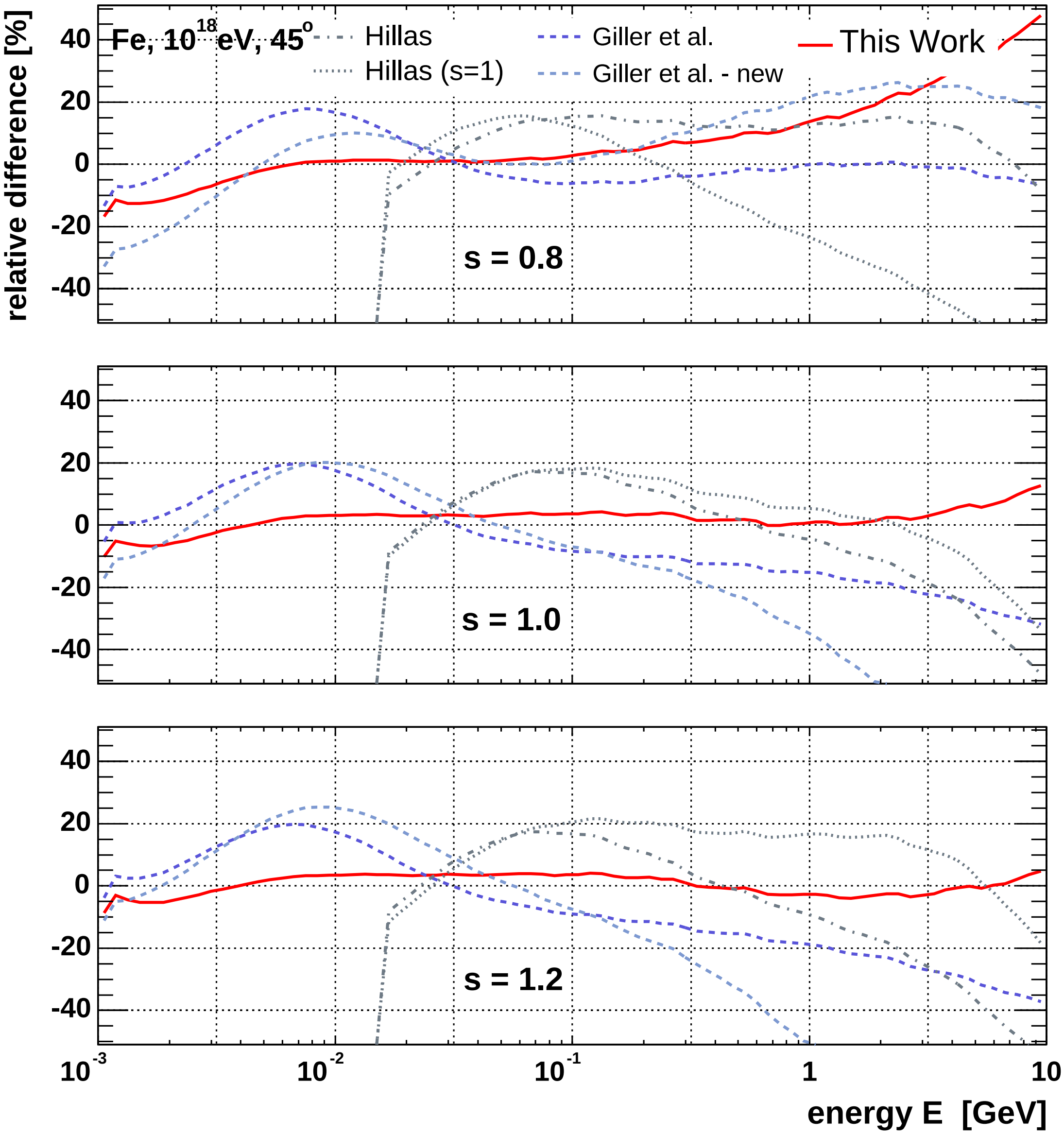

Figure A.22: Relative differences of different parameterisations to CORSIKA - iron, 10^{18} eV, $\theta = 45°$, opt. thinning 10^{-8}.

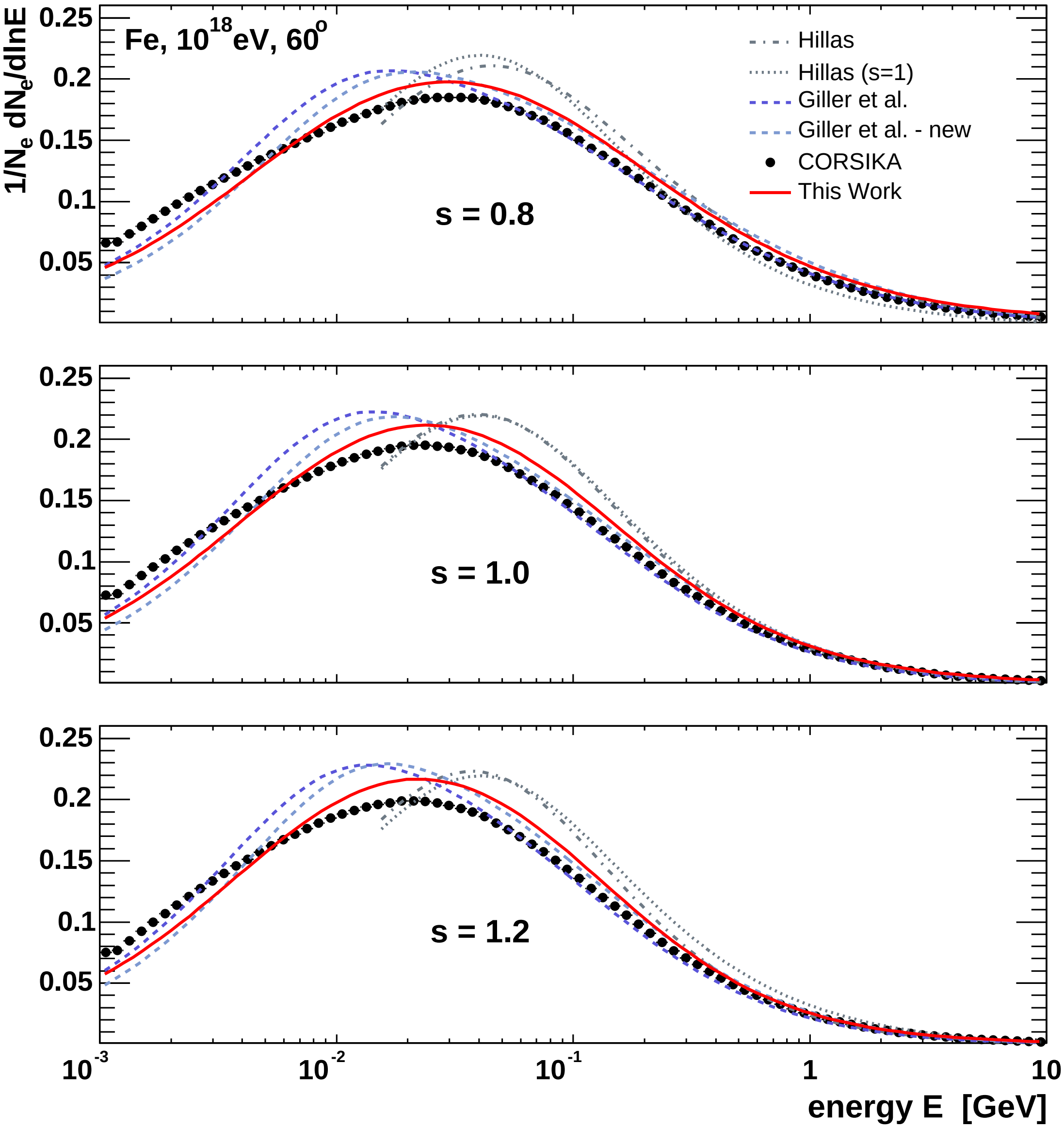

Figure A.23: Comparison to other parameterisations - iron, 10^{18} eV, $\theta = 60°$, opt. thinning 10^{-8}, CORSIKA simulation with enabled `UPWARD` option.

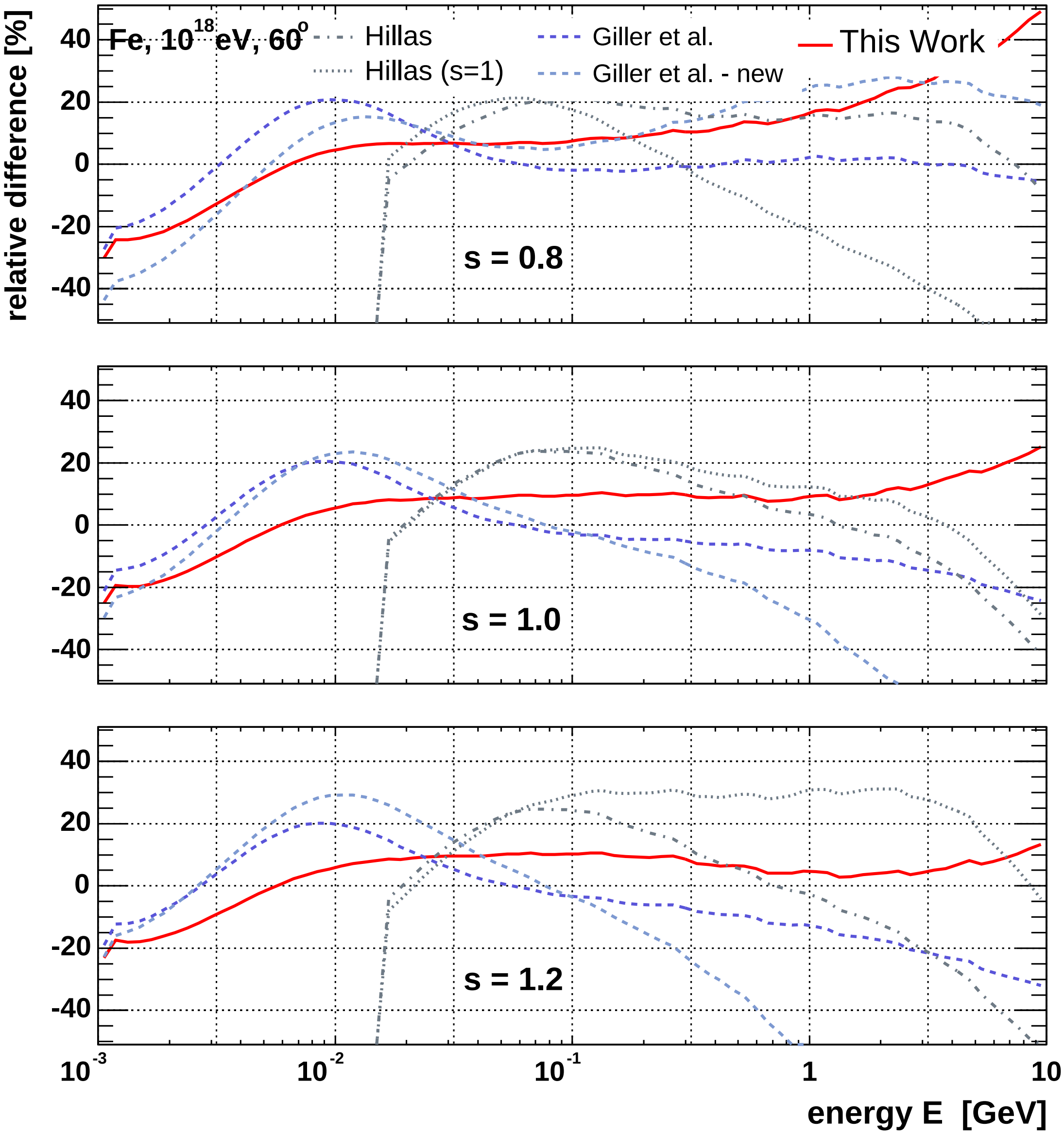

Figure A.24: Relative differences of different parameterisations to CORSIKA - iron, 10^{18} eV, $\theta = 60°$, opt. thinning 10^{-8}, CORSIKA simulation with enabled `UPWARD` option.

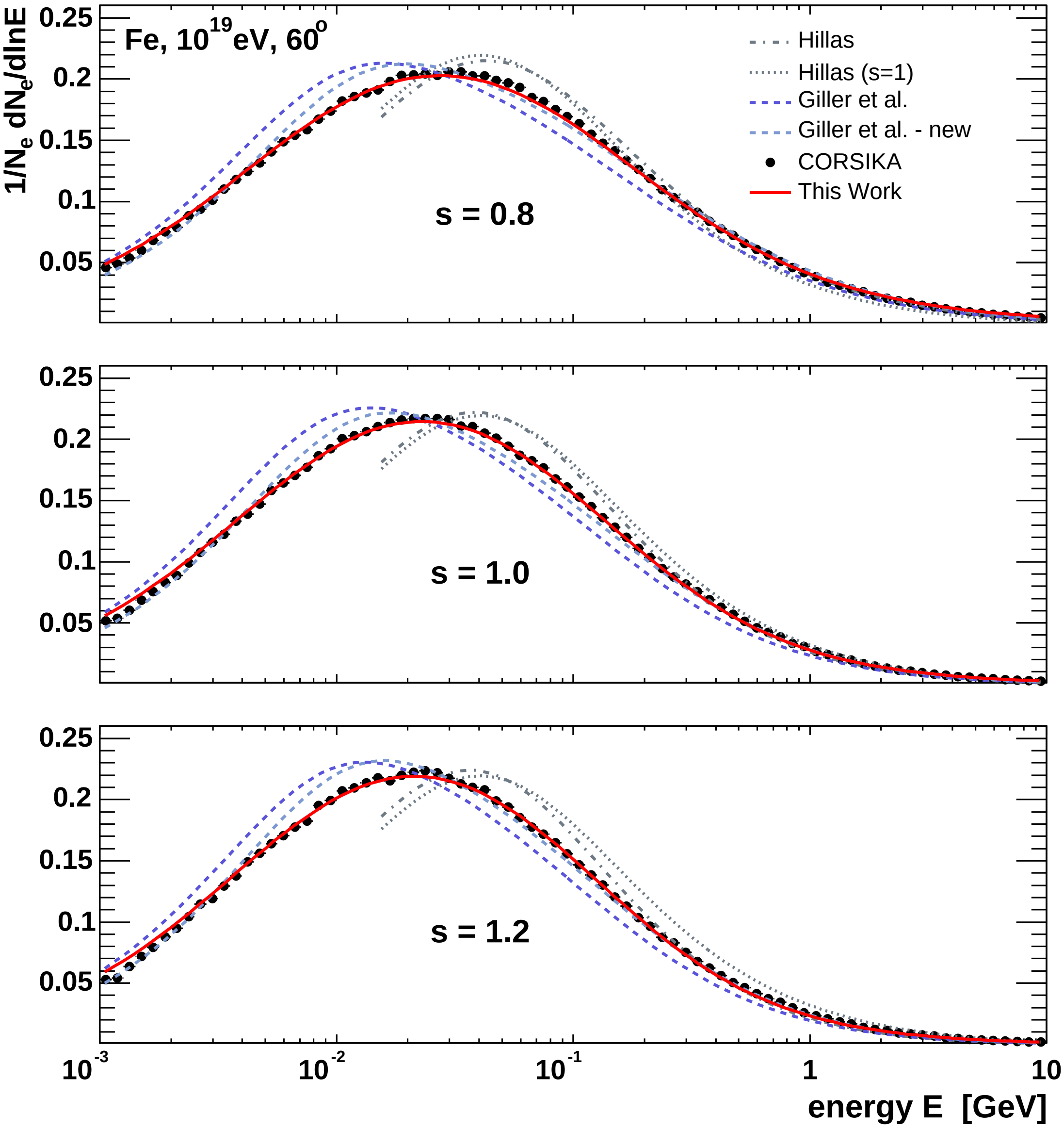

Figure A.25: Comparison to other parameterisations - iron, 10^{19} eV, $\theta = 60°$, CORSIKA simulation without enabled `UPWARD` option.

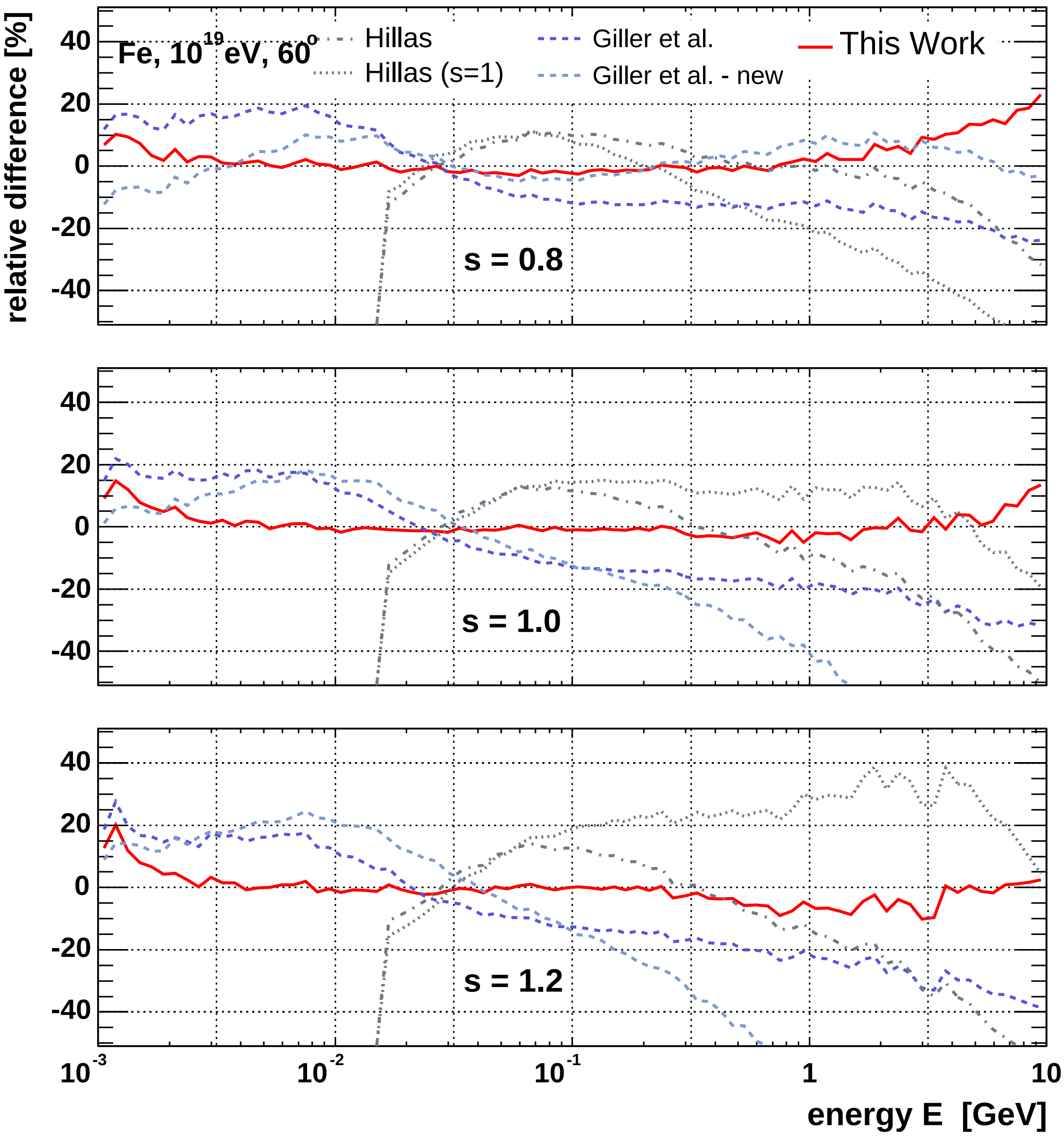

Figure A.26: Relative differences of different parameterisations to CORSIKA - iron, 10^{19} eV, $\theta = 60°$, CORSIKA simulation without enabled `UPWARD` option.

A.5 Calculation of the Total Number of Cherenkov Photons Produced

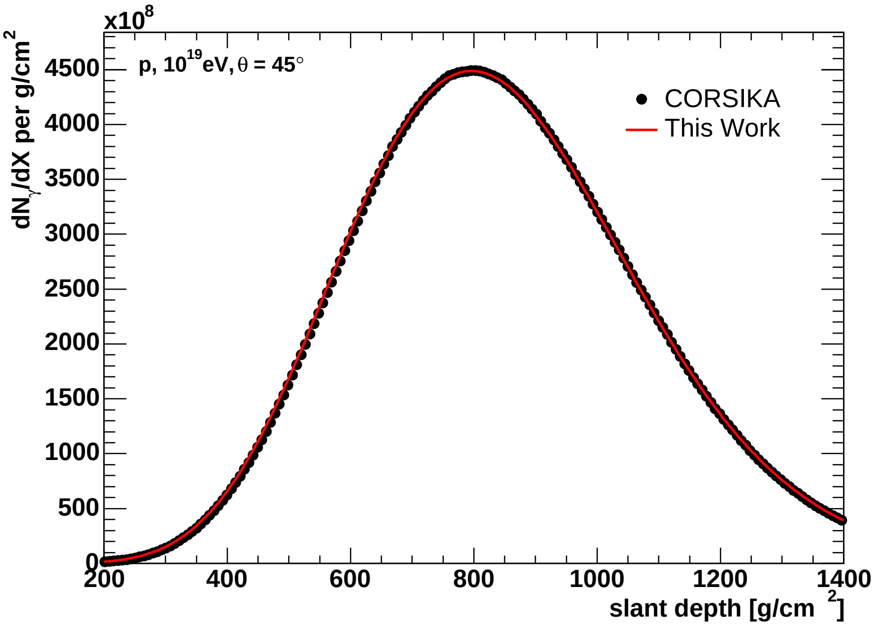

Figure A.27: Cherenkov Longitudinal Profile (proton, 10^{19} eV, $45°$).

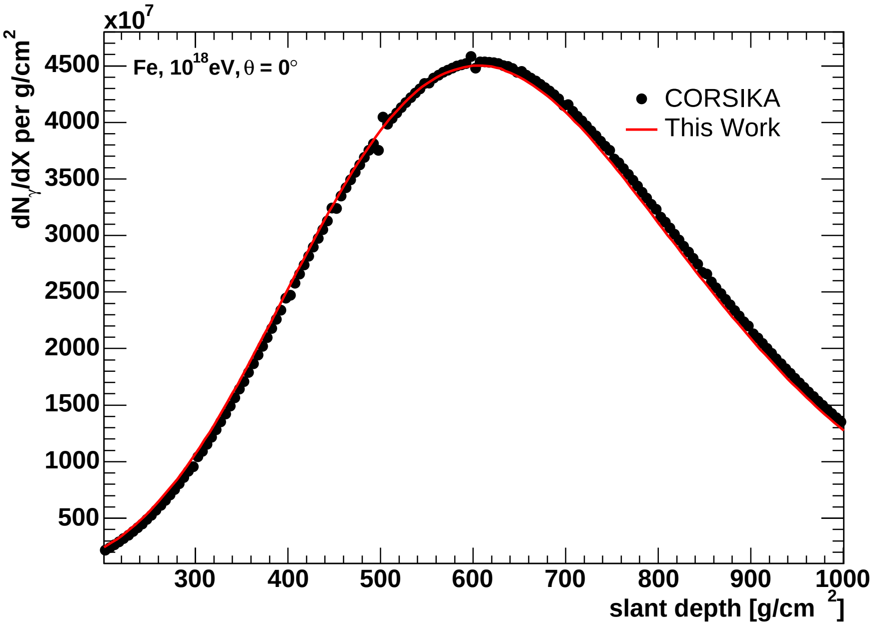

Figure A.28: Cherenkov Longitudinal Profile (iron, 10^{18} eV, $0°$, opt. thinning 10^{-8}).

Appendix B

Appendix: Test of Model with Simulations

Parameterisation of Angular Distribution of Cherenkov Photons

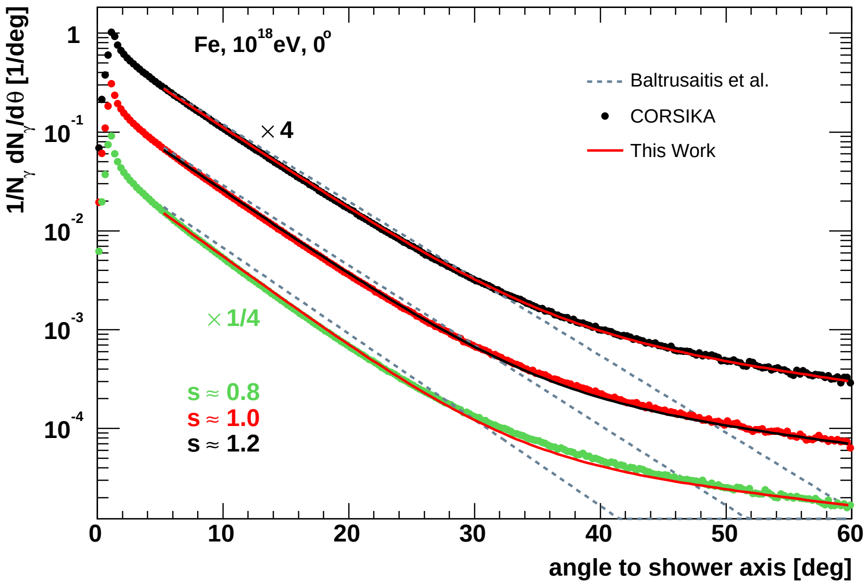

Figure B.1: Cherenkov Photon Angular distribution, previous [Baltrusaitis et al. 1985] and this work (iron, 10^{18} eV, 0°, opt. thinning 10^{-8}).

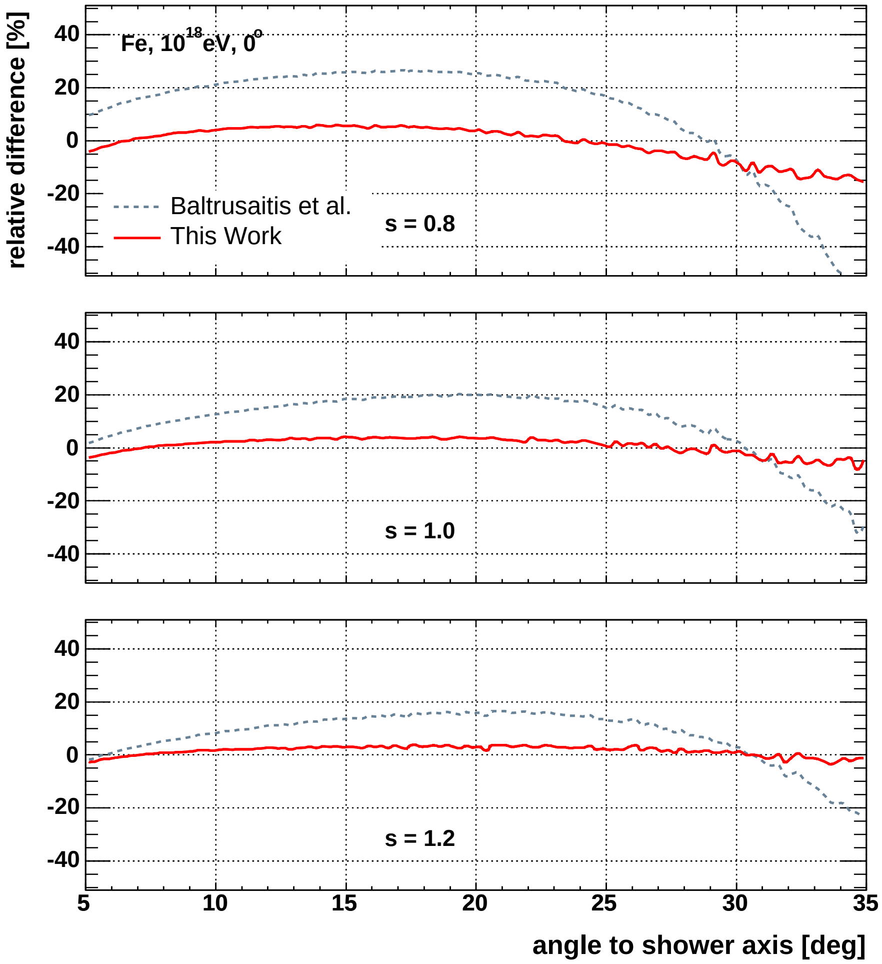

Figure B.2: Relative Difference: Cherenkov photon angular distribution, previous [Baltrusaitis et al. 1985] and this work relative to CORSIKA (iron, 10^{18} eV, 0°, opt. thinning 10^{-8}).

Parameterisation of Electron Energy Distribution for Calculation of the Total Number of Produced Cherenkov Photons

The new parametrisation of the normalised electron energy distribution proposed is:

$$\boxed{f_{\mathrm{e}}\,(E,s) \;=\; a_0 \;\cdot\; \frac{E}{(E+a_1)\;(E+a_2)^s}}\;. \tag{B.1}$$

The CORSIKA simulated electron energy spectra are described well by the following set of parameters:

$$\begin{aligned} a_1 &= 6.42522 - 1.53183 \cdot s \\ a_2 &= 168.168 - 42.1368 \cdot s \text{ , with } E \text{ in MeV.} \end{aligned} \tag{B.2}$$

Since (4.7) has already been implemented in the Auger analyse software Offline [Nellen et al. 2004] and numerical integration of (4.9) is quite CPU consuming, the normalisation a_0 for different E_{cut} has been parametrised in shower age s. a_0 is described by an exponential function in shower age

$$a_0 = k_0 \cdot \exp(k_1 \cdot s + k_2 \cdot s^2)\ , \tag{B.3}$$

where the parameters k_0, k_1 and k_2, calculated for six different threshold energies in the typical range for simulation energy thresholds of 50 keV - 2 MeV are linearly interpolated respectively extrapolated from the tabulated values. The C-code of the whole parametrisation including the parametrisation of the normalisation, as it is implemented in Offline:

```
double EDis_NewPara (double E_MeV, double Ecut_MeV, double s)
//===================================================================
//
//  diff. E-distr. of electrons (1/N dN/dlnE)
//  new parametrisation -> icrc2003, Nerling et al.
//
//  input:      E_MeV            energy[MeV]
//              s                shower age
//              Ecut_MeV         em energy cut in simulations[MeV]
//
//                                                (F.Nerling 07/2003)
//===================================================================
{
 double Ecut[6] = {2., 1. ,0.5, 0.25, 0.1, 0.05};
 double p0[6]   = {1.48071e-01, 1.45098e-01, 1.43458e-01,1.42589e-01,
                  1.42049e-01, 1.41866e-01};
 double p1[6]   = {6.22334,6.20114,6.18979 ,6.18413,6.18075, 6.17963 };
 double p2[6]   = {-5.89710e-01, -5.96851e-01,-6.01298e-01,-6.03838e-01,
                   -6.05484e-01,-6.06055e-01 };
 double k0, k1, k2;
```

```
 double f_para, a0, a1, a2;
 int i1,i2;

 a1 = 6.42522 - 1.53183*s;
 a2 = 168.168 - 42.1368*s;

 if(Ecut_MeV > Ecut[0]){
    i1 = 0;
    i2 = 1;
 }
 else {
    i1 = 4;
    i2 = 5;
    for(int i = 1; i < 6; i++){
        if(Ecut_MeV > Ecut[i]) {
           i1 = i-1;
           i2 = i;
           break;
        }
    }
 }
 k0 = p0[i1] + (p0[i2] - p0[i1])/(Ecut[i2] - Ecut[i1]) * (Ecut_MeV - Ecut[i1]);
 k1 = p1[i1] + (p1[i2] - p1[i1])/(Ecut[i2] - Ecut[i1]) * (Ecut_MeV - Ecut[i1]);
 k2 = p2[i1] + (p2[i2] - p2[i1])/(Ecut[i2] - Ecut[i1]) * (Ecut_MeV - Ecut[i1]);

 a0 = k0*exp( k1*s + k2* s*s);


 f_para = a0 * E_MeV/(E_MeV+a1)/pow(E_MeV+a2,s);

 return f_para;
}
```

Parameterisation of the Angular Distribution of Produced Cherenkov Photons

The new parametrisation of the angular distribution of Cherenkov photons produced in extensive air showers with respect to the shower axis:

$$\boxed{A_\gamma(\theta,h,s) \;=\; a_\mathrm{s}(s)\,\frac{1}{\theta_\mathrm{c}(h)}\,e^{-\theta/\theta_\mathrm{c}(h)} + b_\mathrm{s}(s)\,\frac{1}{\theta_\mathrm{cc}(h)}\,e^{-\theta/\theta_\mathrm{cc}(h)}} \qquad \text{(B.4)}$$

In this expression, the age dependence is included by polynomials of second order

$$a_\mathrm{s}(s) \;=\; a_0 + a_1\cdot s + a_2\cdot s^2 \qquad \text{(B.5)}$$

$$b_\mathrm{s}(s) \;=\; b_0 + b_1\cdot s + b_2\cdot s^2\ , \qquad \text{(B.6)}$$

and the height dependence is taken into account by the exponential factors

$$\theta_\mathrm{c}(h) \;=\; \alpha\cdot E_\mathrm{thr}^{-\beta} \quad ,\ \text{with } E_\mathrm{thr} \text{ in MeV} \qquad \text{(B.7)}$$

$$\theta_\mathrm{cc}(h) \;=\; \gamma\cdot\theta_\mathrm{c}(h) \quad ,\ \text{with } \gamma = \alpha' + \beta'\cdot s\ . \qquad \text{(B.8)}$$

As shown in Fig. 5.5, the CORSIKA spectra are predicted properly using the following parameters that have been found by a global fit to many individual showers:

$$\begin{aligned}(a_0, a_1, a_2) &= (4.2489 \cdot 10^{-1}, 5.8371 \cdot 10^{-1}, -8.2373 \cdot 10^{-2})\\(b_0, b_1, b_2) &= (5.5108 \cdot 10^{-2}, -9.5587 \cdot 10^{-2}, 5.6952 \cdot 10^{-2})\\(\alpha, \beta) &= (0.62694, 0.60590)\\(\alpha^{'}, \beta^{'}) &= (10.509, -4.9644)\ . \end{aligned} \tag{B.9}$$

The C-code of the parametrisation of the angular distribution, as it is implemented in Offline:

```
double ADis_NewPara (double x, double E_thr, double s)
//==================================================================
//
//  angular distr. of Ch.photons produced by EAS (1/Nch dNch/dtheta)
//
//
//  input:      x        angle theta to shower axis [deg]
//              E_thr    Ch.thr.energy [MeV]
//              s        shower age
//                                              (F.Nerling 06/2004)
//==================================================================
{
  double a0     =  4.2489e-01;
  double a1     =  5.8371e-01;
  double a2     = -8.2373e-02;
  double b0     =  5.5108e-02;
  double b1     = -9.5587e-02;
  double b2     =  5.6952e-02;
  double thc0   =  6.2694e-01;
  double thc1   = -6.0590e-01;
  double thcc0  =  1.0509e+01;
  double thcc1  = -4.9644e+00;
  double A = a0 + a1 * s + a2 * s*s;
  double B = b0 + b1 * s + b2 * s*s;
  double th_c = thc0 * pow(E_thr,thc1)/pi*180.;
  double c = thcc0+ thcc1 * s;
  double th_cc = c*th_c;

  return A * 1./th_c * exp(-1./th_c * x) + B * 1./th_cc * exp(-1./th_cc * x);
 }
```

Test of Full Cherenkov Model

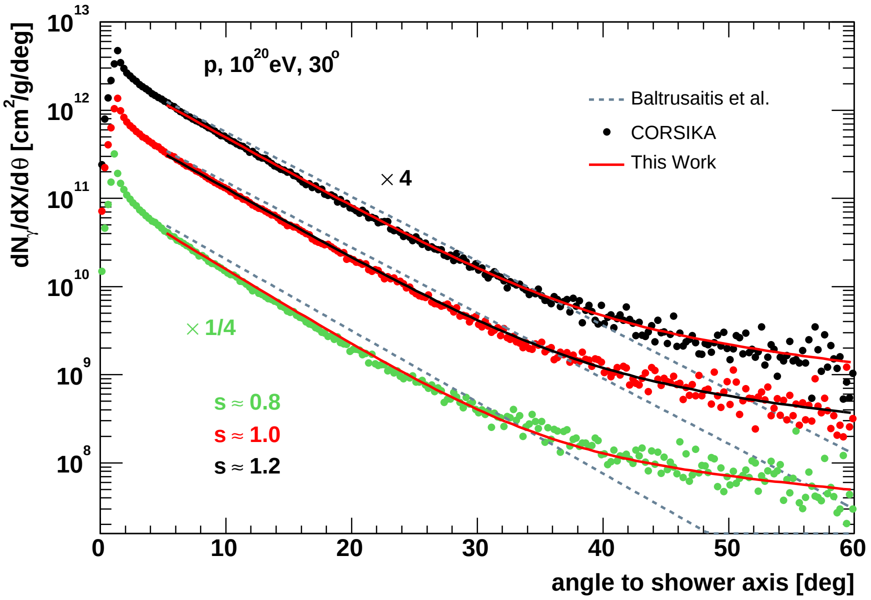

Figure B.3: Comparison of full Cherenkov model with Monte Carlo - very deep shower (proton, 10^{20} eV, $\theta_\mathrm{p} = 30°$). The calculation of the total number of Cherenkov photons produced in extensive air showers per slant depth and per angle with respect to the shower axis by ansatz (3.18) using the new parametrisations of normalised electron energy distribution and normalised Cherenkov photon distribution (Eq. (4.7) and Eq. (5.5)) as well as the previous approach are compared to the Monte Carlo simulations.

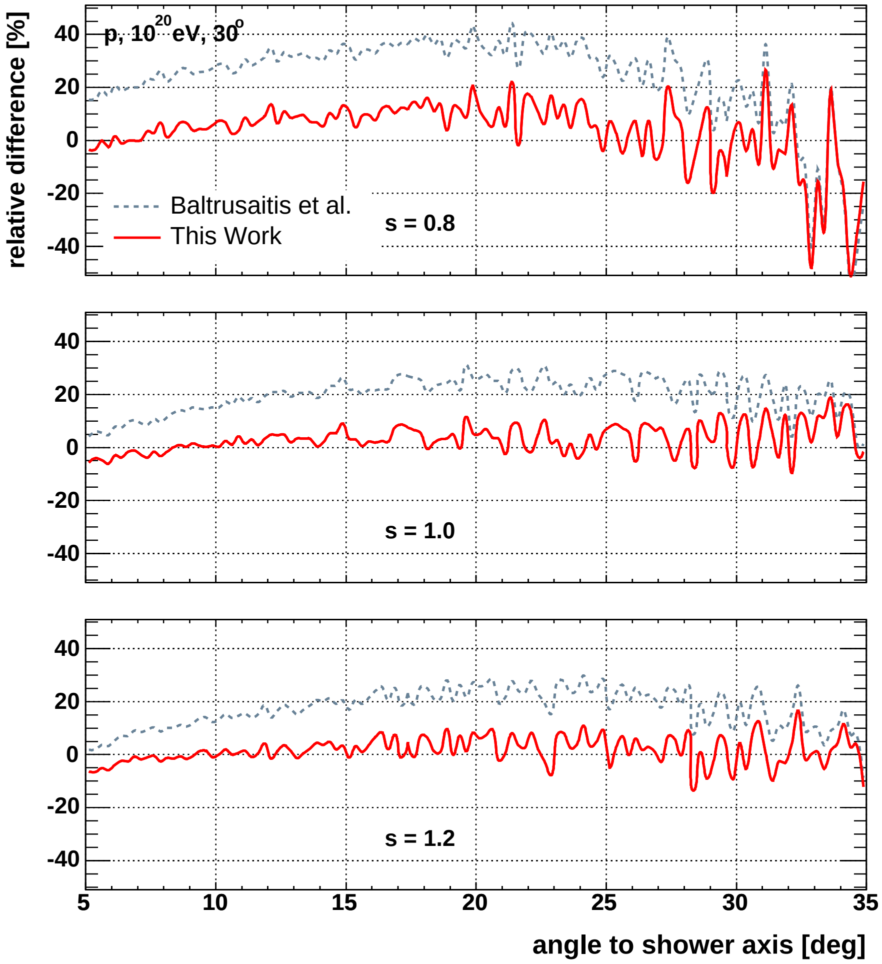

Figure B.4: Quality of prediction of total number of Cherenkov photons produced per slant depth and angle with respect to the shower axis, complete old and new model versus Monte Carlo simulations - very deep shower (proton, 10^{20} eV, $\theta_{\mathrm{p}} = 30°$).

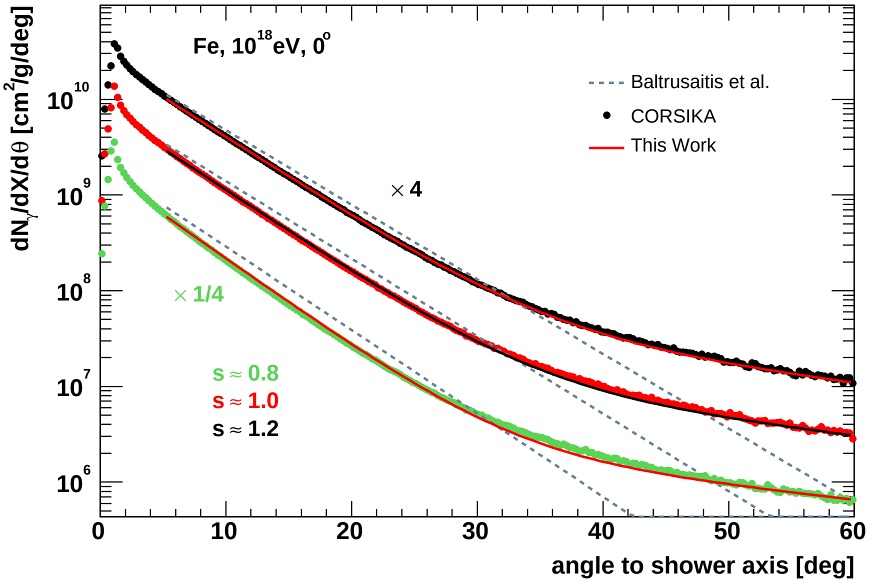

Figure B.5: Comparison of full Cherenkov model with Monte Carlo - very early developing shower (iron, 10^{18} eV, $\theta_\mathrm{p} = 0°$, opt. thinning 10^{-8}). The calculation of the total number of Cherenkov photons produced in extensive air showers per slant depth and per angle with respect to the shower axis by ansatz (3.18) using the new parametrisations of normalised electron energy distribution and normalised Cherenkov photon distribution (Eq. (4.7) and Eq. (5.5)) as well as the previous approach are compared to the Monte Carlo simulations.

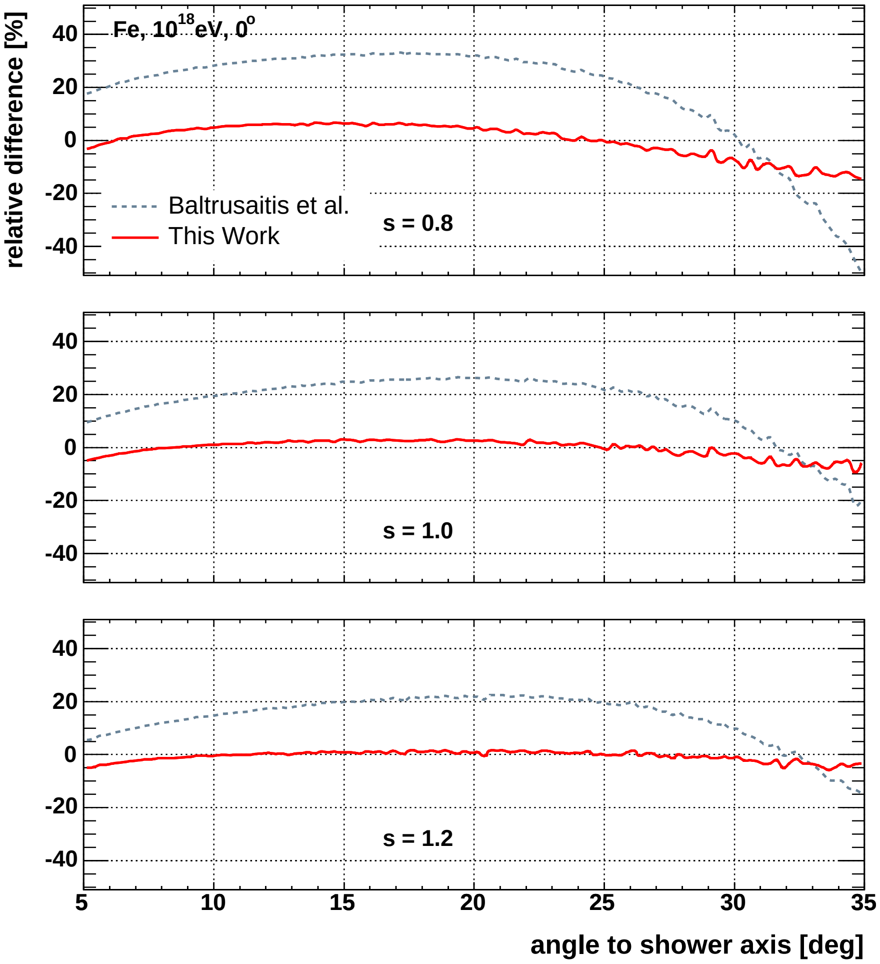

Figure B.6: Quality of prediction of total number of Cherenkov photons produced per slant depth and angle with respect to the shower axis, complete old and new model versus Monte Carlo simulations - very early developing shower, (iron, 10^{18} eV, $\theta_\mathrm{p} = 0°$, opt. thinning 10^{-8}).

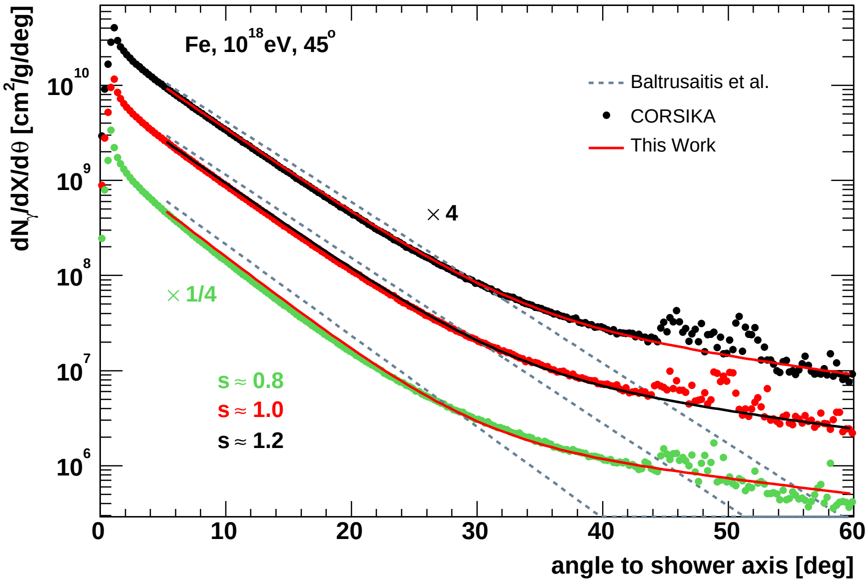

Figure B.7: Comparison of full Cherenkov model with Monte Carlo - different angle shower (iron, 10^{18} eV, $\theta_\mathrm{p} = 45°$). The calculation of the total number of Cherenkov photons produced in extensive air showers per slant depth and per angle with respect to the shower axis by ansatz (3.18) using the new parametrisations of normalised electron energy distribution and normalised Cherenkov photon distribution (Eq. (4.7) and Eq. (5.5)) as well as the previous approach are compared to the Monte Carlo simulations.

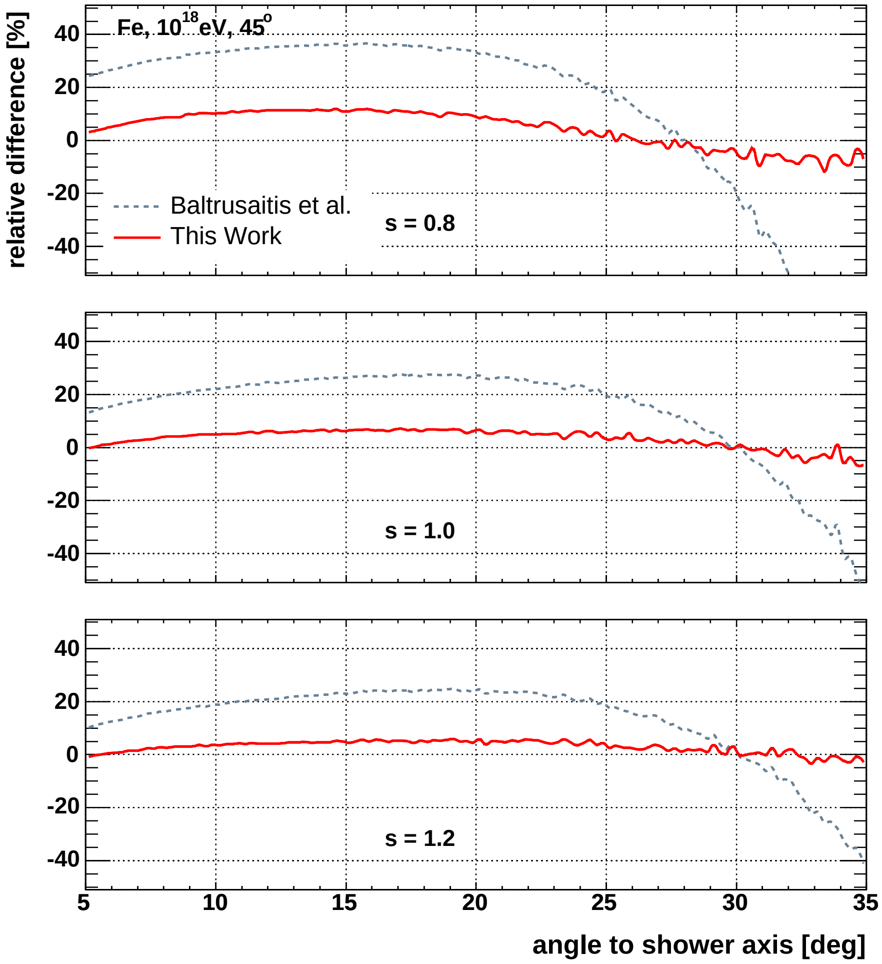

Figure B.8: Quality of prediction of total number of Cherenkov photons produced per slant depth and angle with respect to the shower axis, complete old and new model versus Monte Carlo simulations - different angle (iron, 10^{18} eV, $\theta_\mathrm{p} = 45°$, opt. thinning 10^{-8}).

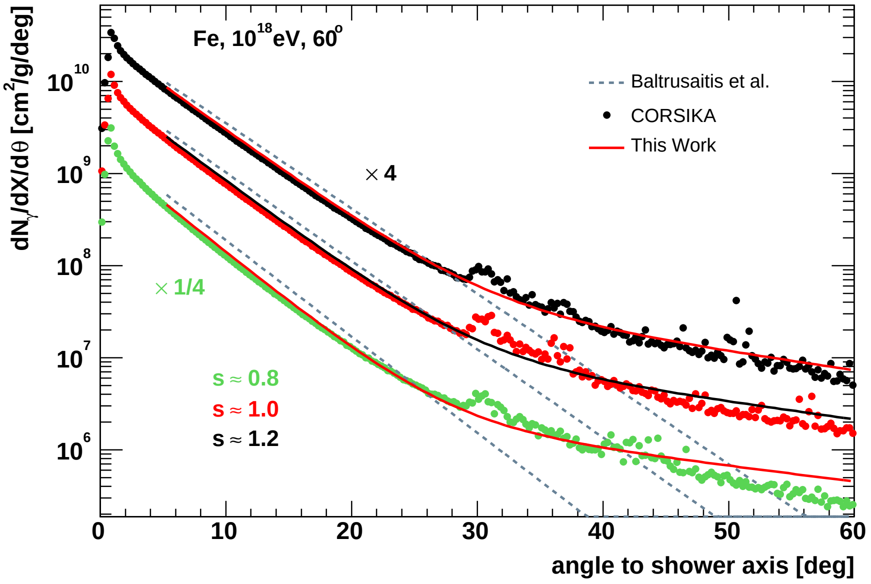

Figure B.9: Comparison of full Cherenkov model with Monte Carlo simulations - very large angle (iron, 10^{18} eV, $\theta_{\mathrm{p}} = 60^{\circ}$, opt. thinning 10^{-8}). The calculation of the total number of Cherenkov photons produced in extensive air showers per slant depth and per angle with respect to the shower axis by ansatz (3.18) using the new parametrisations of normalised electron energy distribution and normalised Cherenkov photon distribution (Eq. (4.7) and Eq. (5.5)) as well as the previous approach are compared to CORSIKA. The artefacts at about 30° are due to the horizontal layers for counting particles in CORSIKA. Particles and photons moving in parallel are not well defined, see also Fig. B.10, and brief discussion in the beginning of Chap. 4.

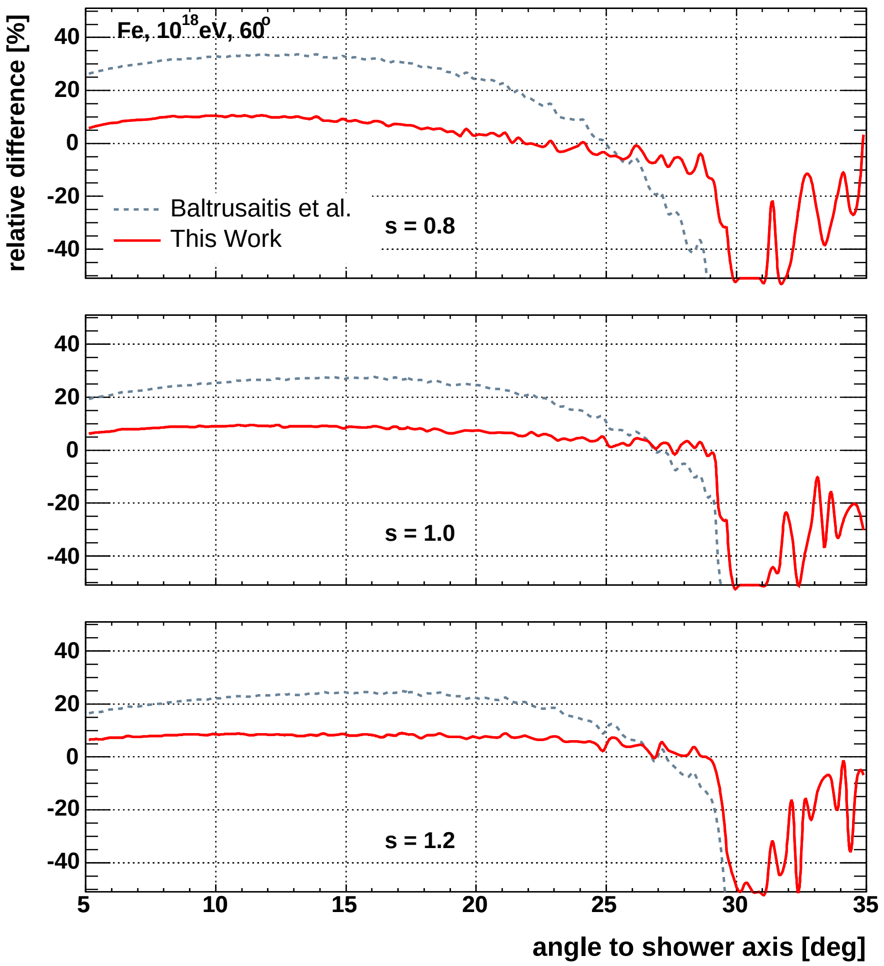

Figure B.10: Quality of prediction of total number of Cherenkov photons produced per slant depth and angle with respect to the shower axis, complete old and new model versus Monte Carlo simulations - very large angle, (iron, 10^{18} eV, $\theta_{\rm p} = 60°$). The large difference at about 30° are due to the horizontal layers for counting particles in CORSIKA. Particles and photons moving in parallel are not well defined, see also Fig. B.9, and brief discussion in the beginning of Chap. 4.

Bibliography

[Abbasi et. al. 2004] R.U. Abbasi HiRes Collaboration, astro-ph/0407622 (2004).

[Abendschein & Matthews 2003] A. Abendschein, J. A. J. Matthews, Auger technical note GAP-2003-059 (2003);
http://www.auger.org/admin/GAP_Notes/GAP2003/gap2003_059.pdf.

[AGASA Collaboration 2004] AGASA Collaboration, http://www-akeno.icrr.u-tokyo.ac.jp/AGASA/results.html (2004).

[Abraham et al. 2004] J. Abraham et al., Auger Collaboration, Nucl. Instr. and Meth. in Phys. Res. A 523, 50 (2004).

[Abu-Zayyad et al. 2000] T. Abu-Zayyad et al., HiRes Collaboration, Nucl. Instr. and Meth. in Phys. Res. A , 450, 253 (2000).

[Abu-Zayyad et al. 2001] T. Abu-Zayyad et al., HiRes Collaboration, Astropart. Phys., 16, 1 (2001).

[Abu-Zayyad et al. 2002] T. Abu-Zayyad et al., HiRes Collaboration, astro-ph/0208301 (2002).

[Abu-Zayyad et al. 2002] T. Abu-Zayyad et al., HiRes Collaboration, astro-ph/0208243 (2002).

[Alvarez-Muniz et al. 2002] J. Alvarez-Muniz et al., Phys. Rev. D, 66, 033011 (2002).

[Alvarez-Muniz et al. 2004] J. Alvarez-Muniz et al., Phys. Rev. D, 69, 103003 (2004).

[Anderson 1933] C.D. Anderson, Phys. Rev., 43, 491 (1933).

[Antoni et al. 2003] T. Antoni et al., KASCADE Collaboration, Nucl. Instr. and Meth. in Phys. Res. A, Vol. 513, Issue 3, 429 (2003).

[Apanasenko et al. 2001] A. Apanasenko et al., Astropart. Phys., 16, 13 (2001).

[Arisaka 2004] K. Arisaka, talk given at the 19th European Cosmic Ray Symposium (ECRS), Florence, Italy, August 30 - September 3 (2004).

[Arisaka et al. 2004] K. Arisaka et al., Auger technical note GAP-2004-037 (2004);

[Auger 1938]	P. AUGER, Rev. Mod. Phys., 11, 288 (1938).
[Auger-DR 1997]	AUGER COLLABORATION, Pierre Auger Project Design Report (1997); http://www.auger.org/admin/DesignReport/index.html.
[Auger-TDR 2002]	AUGER COLLABORATION, Technical Design Report (2002); http://tdpc01.fnal.gov/auger/org/tdr/index.html.
[Abraham et al. 2004]	AUGER COLLABORATION, http://www.auger.org (2004).
[Ave et al. 2001]	M. AVE et al., for the Auger Collaboration, Proc. 27th Int. Cosmic Ray Conf., Hamburg (Germany), 2, 707 (2001).
[Baltrusaitis et al. 1985]	R. M. BALTRUSAITIS et al., The Utah Fly's Eye Detector, Nucl. Instr. Meth. A240, 410 (1985).
[Belz et al. 2003]	J.W. BELZ et al., HiRes Collaboration, Proc. 28th Int. Cosmic Ray Conf., Tsukuba (Japan), 425 (2003).
[Bergmann et al. 2003a]	D.R. BERGMANN, et al., Mod. Phys. Lett. A, 18, 1235 (2003).
[Bergmann et al. 2003b]	D.R. BERGMANN, et al., Proc. 28th Int. Cosmic Ray Conf., Tsukuba (Japan), 2, 397 (2003).
[Bhattacharjee & Sigl 2000]	P. BHATTACHARJEE, G. SIGL, Phys. Rep. 327, 109 (2000).
[Bird et al. 1993]	D.J. BIRD et al., Fly's Eye Collaboration, Phys. Rev. , 71, 3401 (1993).
[Blümer 2003]	J. BLÜMER, for the Auger Collaboration, J. Phys. G, 29, 867 (2003).
[Boothby 1997]	K. BOOTHBY et al., Nucl. Phys. B (Proc. Suppl.), 52, 166 (1997).
[Boratav & Sigl 2004]	M. BORATAV, G. SIGL, C.R. Physique, 5 (2004).
[Brack et al. 2004]	J. BRACK et al., Astropart. Phys., 20, 653 (2004).
[Buchholtz 1995]	A. BUCHHOLTZ, Appl. Opt., 34, No. 15, 2765 (1995).
[Bunner 1967]	A. N. BUNNER, Cosmic Ray Detection by Atmospheric Fluorescence, PhD thesis, Cornell University, Ithaca, NY, USA (1967).
[Cassel & Bower 2002]	R.E. CASSELL, G. BOWER (SLAC), private communication to D. Heck (2002).
[Cester 2001]	R. CESTER, for the Auger Collaboration, Proc. 27th Int. Cosmic Ray Conf., Hamburg (Germany), 711 (2001).
[Cherenkov 1934]	P.A. CHERENKOV Dokl. Akad. Nauk, SSSR, 2, 451 (1934).

[Chiba et al. 1992]	N. CHIBA et al., Nucl. Instr. and Meth. in Phys. Res. A , 311, 338 (1992).
[Chiosso & Melo 2004]	M. CHIOSSO, D. MELO, private communication (2004).
[Cronin 1992]	J.W. CRONIN, Nucl. Phys. B (Proc. Suppl.), 28, 213 (1992).
[Cronin 1999]	J.W. CRONIN, Rev. Mod. Phys., 71, 165 (1999).
[Dawson 2003]	B. DAWSON, private communication (2003).
[Dawson 2004]	B. DAWSON, private communication (2004).
[Dawson et al. 1996]	B. DAWSON et al., Astropart. Phys., 5, 239 (1996).
[Dawson & Sommers 2001]	B. DAWSON, P. SOMMERS, for the Auger Collaboration, Proc. 27th Int. Cosmic Ray Conf., Hamburg (Germany), 2, 711 (2001).
[Dozkhenko & Pomanskii 1964]	O.I. DOZKHENKO, A.A. POMANSKII, Soviet Phys. JETP, 18, 187 (1964).
[Drescher 2004]	H.J. DRESCHER, astro-ph/0411144 (2004).
[Edlén 1966]	B. EDLÉN, Metrologia, 2, No. 2, 12 (1966).
[Eidelman et al. 2004]	S. EIDELMAN et al., PARTICLE DATA GROUP, Rev. Part. Phys., Phys. Lett. B, 592, I 1-4, 1 (2004).
[Elbert et al. 1983]	J. W. ELBERT et al., Proc. 18th Int. Cosmic Ray Conf., Bangalore (India), 6, 227 (1983).
[Elterman & Toolin 1965]	L. ELTERMAN, R.B. TOOLIN, Handbook of Geophysics and Space Environments, Ch. 7, Air Force Cambridge Research Labs, Office of Aerospace Research, USAF (1965).
[Engel 2004]	R. ENGEL, private communication (2004).
[Engel 1999]	R. ENGEL et al., Proc. 26th Int. Cosmic Ray Conf., Salt Lake City (USA) (1999).
[Engel & Klages 2004]	R. ENGEL, H. KLAGES, C.R. Physique, 5 (2004).
[Erber 1966]	T. ERBER, Rev. Mod. Phys., 38, 626 (1966).
[Fesefeldt 1985]	H. FESEFELDT, Report PITHA-85/02, RWTH Aachen (1985).
[Fermi 1949]	E. FERMI, Phys. Rev. , 75, 1169 (1949).
[Frank & Tamm 1937]	I.M. FRANK, I.E. TAMM, Dokl. Akad. Nauk, SSSR, 14, 107 (1937).
[Fukushima et al. 2000]	M. FUKUSHIMA et al., TA Collaboration, http://www-ta.icrr.u-tokyo.ac.jp (2000).

[Gaisser 1990] T. K. Gaisser, Cosmic Rays and Particle Physics, Cambridge University Press, Cambridge (1990).

[Gaisser & Hillas 1977] T. K. Gaisser, A. M. Hillas, Proc. 15th Int. Cosmic Ray Conf., Plovdiv (Bulgaria), 8, 353 (1977).

[Giller 2004] M. Giller, private communication (2004).

[Giller et al. 2003] M. Giller et al., Proc. 28th Int. Cosmic Ray Conf., Tsukuba (Japan), 2, 619 (2003).

[Giller et al. 2004] M. Giller et al., J. Phys. G 30, 97 (2004).

[Ginsburg 1940] V.L. Ginsburg, Zh. fiz. SSSR, 2, 441 (1940).

[Greisen 1956] K. Greisen, Prog. Cosmic Ray Phys., III, 1 (1956).

[Greisen 1964] K. Greisen, Phys. Rev. Lett., 16, 748 (1964).

[Greisen 1966] K. Greisen, Phys. Rev. Lett., Vol. 16, 748 (1966).

[Grigorov et al. 1971] N.L. Grigorov et al., Proc. 12th Int. Cosmic Ray Conf., (Hobart), 5, 1760 (1971).

[Hayashida et al. 1999] N. Hayashida et al., AGASA Collaboration, Astropart. Phys., 10, 303, astro-ph/9807045 (1999).

[Heck et al. 1998] D. Heck et al., CORSIKA: A Monte Carlo Code to Simulate Extensive Air Showers, Report FZKA 6019, Forschungszentrum Karlsruhe (1998).

[Heck & Knapp 1998] D. Heck, J. Knapp, Report FZKA 6097, Forschungszentrum Karlsruhe (1998).

[Heck 2003] D. Heck, private communication (2003).

[Heck 2004] D. Heck, private communication (2004).

[Hess 1912] V. Hess, Z. Phys. **13**, 1084 (1912).

[Hillas 2003] M.A. Hillas, Proc. 11th Int. Cosmic Ray Conf., Budapest (Hungary), 29, 355 (1969).

[Hillas 1982] A. M. Hillas, J. Phys., G 8, 1461 (1982).

[Hillas 1984] A. M. Hillas, Ann. Rev. of Astr. and Astrophys. 22, 425 (1984).

[Homola et al. 2003] P. Homola et al., astro-ph/0311442 (2003).

[Hutzinger 1982] O. Hutzinger (ed.), The Handbook of Environmental Chemistry, Vol.7 Part B, The Natural Environment and the Biogeochemical Cycles, Springer Verlag, Berlin (1982).

[Ion 2003] D.B. Ion, hep-ph/0302114 (2003); see also Nucl. Phys. B, 29, 547 (1971).

[Jackson 1975] J. D. Jackson, Classical Electrodynamics, John Wiley and Sons, Inc., New York (1975).

[James 1994] F. James, MINUIT Reference Manual, D506 (1994).

[Jelley 1958] J.V. Jelley, Čerenkov Radiation and its applications, Pergamon Press Ltd., London (1958).

[Kakimoto et al. 1996] F. Kakimoto et al., Nucl. Instr. and Meth. in Phys. Res. A, 372, 527 (1996).

[Kalmykov et al. 1997] N. N. Kalmykov, S. S. Ostapchenko, A. I. Pavlov, Nucl. Phys. B (Proc. Suppl.), 52, 17 (1997).

[Kalmykov et al. 2003] N. N. Kalmykov et al., Proc. 28th Int. Cosmic Ray Conf., Tsukuba (Japan), 2, 511 (2003).

[Kamata & Nishimura 1957] K. Kamata, J. Nishimura, Suppl. Prog. Theo. Phys., 4, 93 (1957).

[Kampert et al. 2004] K.-H. Kampert et al., KASCADE Collaboration, Nucl. Phys. B (Proc. Suppl.), 136, 273 (2004).

[Keilhauer et al. 2004] B. Keilhauer et al., Astropart. Phys. 22, 249 (2004).

[Knapp & Heck 1998] J. Knapp & D. Heck, Extensive Air Shower Simulation with CORSIKA: A User's Guide, Report KfK 5196B, Kernforschungszentrum Karlsruhe (1993); Auger technical note GAP-1998-012 (1998); for an up-to-date version see http://www-ik.fzk.de/corsika/usersguide/corsika_tech.html.

[Knapp & Heck 2003] J. Knapp & D. Heck, Astropart. Phys. 19, 77 (2003).

[Kobal 2001] M. Kobal, for the Auger Collaboration, Astropart. Phys. 15, 259 (2001).

[Linsley 1962] J. Linsley, Phys. Rev. Lett., 10, 146 (1962).

[Linsley 1988] J. Linsley, private communication by M. Hillas to G. Schatz (1988).

[Matthews & Clay 2001] J. A. J. Matthews, R. Clay, for the Auger Collaboration, Proc. 27th Int. Cosmic Ray Conf., Hamburg (Germany), 745 (2001).

[Mussa et al. 2004] R. Mussa et al., Nucl. Instr. and Meth. in Phys. Res. A, Vol. 518, 183-185 (2004).

[Mostafa et al. 2003] M. Mostafa, for the Auger Collaboration, Proc. 28th Int. Cosmic Ray Conf., Tsukuba (Japan), 2, 465 (2003).

[Nagano et al. 2003] M. Nagano et al., Astropart. Phys. 20, 293 (2003).

[Nagano & Watson 2000] M. Nagano, A. A. Watson, Rev. Mod. Phys., 72, No. 3, 689 (2000).

[Nellen et al. 2004] L. Nellen et al., The Offline Framework of the Pierre Auger Observatory, Subm. to Proc. CHEP 04, September 27 - October 1, 2004, Interlaken, Switzerland (2004).

[Nerling 2004] F. Nerling, for the Auger Collaboration, Aspects of the Reconstruction Chain for the Fluorescence Telescopes of the Pierre Auger Observatory, Proc. 13th ISCRA, Erice (Sicily), World Scientific, 251-259 (2004).

[Nerling et al. 2003] F. Nerling et al., Proc. 28th Int. Cosmic Ray Conf., Tsukuba (Japan), 2, 611 (2003)

[Oehlschläger 2004] J. Oehlschläger, private communication (2004).

[Owens 1967] J. C. Owens, Appl. Opt., 16, No. 1, 51, (1967).

[Pallavicini et al. 2003] M. Pallavicini et al., EUSO Collaboration, Nucl. Instr. and Meth. in Phys. Res. A, 502, 155 (2003).

[Peck & Reeder 1972] E. R. Peck, K. Reeder, J. Opt. Soc. Am., 62, 958 (1972).

[Pękala et al. 2003] J. Pękala et al., Proc. 28th Int. Cosmic Ray Conf., Tsukuba (Japan), 2, 551 (2003).

[Perkins 2003] D. P. Perkins, Particle Astrophysics, Oxford University Press, New York (2003).

[Pierog 2004] T. Pierog, private communication (2004).

[Prado et al. 2004] L. Prado et al., http://www.ifi.unicamp.br/AUGER (2004).

[Prosin 2003] V. Prosin, private communication to J. Knapp, July (2003).

[Risse 2003] M. Risse, private communication (2003).

[Risse et al. 2001] M. Risse et al., Proc. 27th Int. Cosmic Ray Conf., Hamburg (Germany), 2, 522 (2001).

[Risse et al. 2004] M. Risse et al., Astropart. Phys., 21, 479 (2004).

[Rayleigh 1899] Lord Rayleigh, Scientific Papers, Cambridge University Press, Vol.1, 87 (1899).

[Rizi 2002] V. Rizi et al., Auger technical note GAP-2002-004 (2002); http://www.auger.org/admin/GAP_Notes/GAP2002/gap2002_004.pdf.

[Rossi 1934] B. Rossi, Ric Sci. Suppl. 1, 570 (1934).

[Rossi & Greisen 1941] B. Rossi, K. Greisen, Phys. Mod. Rev., 13, 240, (1941).

[Sokolsky 1989] P. Sokolsky, Frontiers in Physics: Introduction to Ultra-high Energy Cosmic Ray Physics, Addison-Wesley Publishing Company, California / Redwood City (1989).

[Sokolsky et al. 1992] P. Sokolsky, P. Sommers, B.R. Dawson, Phys. Reports 217, 225 (1992).

[Sokolsky 2002] P. Sokolsky, eConf C 020620, FRAT04 (2002).

[Sommers 1995] P. Sommers, Astropart. Phys., 3, 349 (1995).

[Stanev et al. 2000] T. Stanev et al., Phys. Rev. D, 62, 93005, astro-ph/0003484 (2000).

[Takeda et al. 1998] M. Takeda et al., Phys. Rev., 81, 1163 (1998).

[Takeda et al. 1999] M. Takeda et al., AGASA Collaboration, Astropart. Phys., 522, 225, astro-ph/9902239 (1999).

[Takeda et al. 2003a] M. Takeda et al., AGASA Collaboration, Astropart. Phys., 19, 447 (2003).

[Takeda et al. 2003b] M. Takeda et al., AGASA Collaboration, Proc. 28th, Int. Cosmic Ray Conf., Tsukuba (Japan), 2, 381 (2003).

[Teshima 2003] M. Teshima, talk given at the XXXIII International Symposium on Multiparticle dynamics (ISMD), Cracow, Poland, September 5-11 (2003).

[Tidman 1956] D.A. Tidman, Nucl. Phys., 2, 289 (1956).

[Thomson 2004] G. Thomson, private communication to R. Engel (2004).

[Ulrich 2003] H. Ulrich et al., KASCADE Collaboration, Nucl. Phys. B (Proc. Suppl.), 122, 218 (2003).

[US-StdA 1976] National Aeronautics and Space Administration (NASA), U.S. Standard Atmosphere 1976, NASA-TM-X-74335 (1976).

[Wada 1949] W.W. Wada, Phys. Rev. Lett., 75, 981 (1949).

[Watson 2004] A.A. Watson, astro-ph/0410514 (2004).

[Weast 1986] R.C. Weast (ed.), Handbook of Chemistry and Physics, 67th Edition, E373, The Chemical Rubber Co., Cleveland (1986).

[Zatsepin & Kuz'min 1966] G. T. Zatsepin, V. A. Kuz'min, Sov. Phys. JETP Lett. (Engl. Transl.), 4, 78 (1966).

[Zrelov 1970]	V.P. ZRELOV, Cherenkov Radiation in High-energy Physics (Transl. Ltd. from Russian), Israel Program for Scientific Translations, Jerusalem (1970).